NUMERICAL METHODS AND TIME-DEPENDENT PHYSICAL MODELS FOR THE DESIGN AND DIAGNOSTIC OF PULSED-DC MAGNETRONS

by

TAMARA MOISEEV

November 9, 2005

NUMERICAL METHODS AND TIME-DEPENDENT PHYSICAL MODELS FOR THE DESIGN AND DIAGNOSTIC OF PULSED-DC MAGNETRONS

A thesis for the degree of

PHILOSOPHIAE DOCTOR

Presented to

DUBLIN CITY UNIVERSITY

by

TAMARA MOISEEV

School of Electronic Engineering

Dublin City University

Research Supervisor

Prof David C Cameron

External Examiner Prof Ulf Helmersson

Internal Examiner Dr Stephen Daniels

January 2006

I hereby certify that this material which I now submit for assessment on the programme of study leading to the award of Philosophiae Doctor is entirely my own work and has not been taken from the work of others save and to the extent that such work has been cited and acknowledged within the text of my work

Signed

Tamara Moiseev (Candidate) ID No 51162008, Date January 23rd, 2006

THESIS TITLE:

"NUMERICAL METHODS AND TIME-DEPENDENT PHYSICAL MODELS FOR THE DESIGN AND DIAGNOSTIC OF PULSED-DC MAGNETRONS"

Author: Tamara Moiseev

ABSTRACT:

Pulsed DC operation of magnetrons is a relatively new sputtering technique that significantly improves the properties of deposited layers. The understanding and control of phenomena taking place during pulsed DC sputtering requires new time-resolved methods of investigation.

This thesis presents a comprehensive development of new methods for magnetron design and time-resolved plasma diagnostic, based on Monte Carlo simulations and time-resolved plasma physical models derived for a pulsed DC opposed target magnetron discharge with rectangular geometry.

The numerical methods have been developed and benchmarked by the author through extensive numerical experiments. A representative set of application examples is included.

The time-resolved physical models for the pulse-on and pulse-off time discharge are based on the experimental data obtained by the author, which are presented as a basis for the interpretation.

The experimental data are obtained using new time-dependent diagnostic methods combining: I-V characteristics and waveforms, time and space-resolved Optical Emission Spectroscopy (OES) and time and space-resolved Ion Energy Spectra (IES).

The following original algorithms and new time-resolved plasma diagnostic methods are presented:

- Algorithm and method for Monte Carlo simulation of ion transport in the magnetron discharge, based on an original non-Runge-Kutta routine developed for calculating charged particles' trajectories in complex, position dependent, magnetic and electric fields. The Monte Carlo simulation is used for evaluating the intensity of the pre-sheath electric field through calculations of the travel time to targets of Ar ions. The time-scale for the sputtering and self-sputtering processes is also evaluated.

- A new method for time-resolved plasma diagnostic in pulsed DC discharges based on time and space-resolved OES using an acousto-optic spectrometer. The described method indicates the applicability conditions for electron temperature evaluations based on time-resolved OES, the procedure and interpretation of results.

  Based on time and space-resolved OES evaluations of electron temperatures, a model of the physical phenomena taking place in the pulsed DC discharge during the pulse-on time is developed.

- A new method for time-resolved analysis of the Ion Energy Spectra at the substrate region in pulsed DC discharges using a mass-energy analyser. Experimental results and data analysis are presented and an original physical model for plasma behaviour during the pulse-off time is developed, explaining the mechanism for the observed increase in the ion flux and energy at substrate during pulsed DC discharges.

  The described model explains for the first time the above effects and allows the control of the ion flux and energy at the substrate from the choice of the pulsed DC duty cycle.

The developed plasma models and time-resolved diagnostic methods are discussed for non-ferromagnetic (copper) and ferromagnetic (iron) targets and the observations are correlated in order to infer a global understanding of phenomena taking place in the pulsed DC discharge and at the substrate region.

ACKNOWLEDGMENTS

I wish to express my gratitude to all those whose support made possible the "making" of this thesis

First of all, I am extremely grateful to my supervisor, Prof David C Cameron, who allowed me to work on such a challenging project and has offered constant support in the lab at all levels, as well as invaluable advice at every step of the way

Although my work on this project took a turn towards plasma physics, I am very grateful to Dr Eugene Kennedy for his lessons in the use of the SEM and for his prompt support and interesting discussions Very many thanks to Dr Áine Allen for her advice and encouragement

A step forward in my training has been obtained thanks to Dr Noel O'Connor, who allowed me to attend his excellent lecture on C programming and to work as a demonstrator for the C computing Lab This experience led me to develop a whole range of original computer codes that are described in this thesis

I am very grateful to Prof Jeremy B Tatum from the Dept of Physics and Astronomy, University of Victoria, Canada, whose advice on optical lines widths came as invaluable support, at a time when nobody else could help

For providing technical support, my thanks go to Dr Claire Greenwood from Hiden Ltd UK and to Dr Till Wallendorf from IfU GmbH, Germany Their advice made a real difference, allowing higher accuracy measurements

Among the technical staff of DCU, I would like to express special thanks to Billy Roarty who provided constant help in the lab, on almost every issue in assembling the magnetron, assistance with electrical and electronic devices, vacuum pumps and electrical problems as well as ordering the necessary materials Many thanks go also to the DCU Mechanical Workshop for machining mechanical components of the magnetron

For their help with network and computer virus problems, my thanks go to Dr Stuart Woolley and to Robert Clare as well as to the Computer Helpdesk of DCU

Special thanks go to Dr Stephen Daniels for support with my participation fees to the GEC 57 conference and with colour printing of my thesis

I also have to thank to all others who contributed with their work and support at different levels to Breda McManus, Samantha Fahy and Sarah Hayes for their advice on "logistic" matters and to Gerard Considine for printing my conference posters

Despite the long hours of programming and endless work in the lab, the various unexpected delays and the lack of funding in the last 9 months, I enjoyed working on this project and I felt extremely privileged to work at DCU

Last but not least, I would like to thank to all my friends and especially to Kevin, Muriel, Peter, Cían and Ruth for making me feel at home in Ireland

TO

My mother, Irina Moiseev (née Gheorghiu)

for her courage and dedication and her faith in me

CONTENTS

1 INTRODUCTION 1

2 EQUIPMENT 4

2 1 Construction of the magnetron 5

2 1 1 Introduction 5

2 1 2 The magnetron construction 7

2 1 3 The design of the anti-arcing shields 10

2 2 The power supply 13

2 3 The Acousto-Optic Spectrometer 15

2 3 1 The operating principle 15

2 3 2 Operation modes 17

2 3 3 Performances 17

2 3 4 Fiber optic cables 19

2 4 The Quadrupole Mass-Energy Analyser 20

2 4 1 Tuning the EQP analyser 21

2 5 Overall view of the experimental system 23

3 NUMERICAL METHODS 26

3 1 Calculation of the magnetic field 27

3 1 1 The current sheet method 27

3 1 2 The C program structure 30

3 1 3 The magnetic pole configuration 30

3 1 4 The magnetic field distribution 31

3 1 5 Discussion and conclusions 35

3 2 ***3D*** Charged particles trajectories in time-dependent electric and magnetic fields 36

3 2 1 Introduction 36

3 2 2 Single particle motion 36

3 2 3 Motion in uniform fields 37

3 2 4 Electric Drifts 41

3 2 5 Magnetic Drifts 43

3 2 6 Adiabatic Invariants 45

3 2 7 The Trajectories Program Structure 47

3 2 8 Discussion and Conclusions 48

3 2 9 Examples of trajectories 50

3 3 Monte Carlo simulation of ions during pulsed DC magnetron operation 55
3 3 1 Monte Carlo simulations Why 55
3 3 2 The principle of Monte Carlo simulations 57
3 3 3 Integrating 3D trajectories in electric and Magnetic Fields 58
3 3 4 The transport process 60
3 3 5 The discharge Model 63
3 4 Monte Carlo simulation for Ar ions 70
3 4 1 The start data 70
3 4 2 The simulation for Ar ions 73
3 4 3 Results for Ar ions 74
3 5 Monte Carlo simulation for Cu ions 80
3 5 1 The self-sputtering time-scale 80
3 5 2 The simulation for Cu ions 80
3 5 3 The start data 81
3 5 4 Results for Ar ions 82
3 6 Conclusions on the simulation results 88

4 THEORETICAL BASIS FOR PLASMA DIAGNOSTICS 89
4 1 Equilibrium relations in plasma 90
4 1 1 Thermodynamic equilibrium (TE) 90
4 1 2 Concepts of Complete Thermodinamic Equilibrium (CTE) 91
4 1 3 Equilibrium relations 91
4 2 Non-equilibrium statistics of plasmas 93
4 2 1 Boltzmann and Focker-Plank kinetic equations 94
4 2 1 1 Macroscopic equations deduced from the kinetic Boltzmann equation 94
4 3 Theoretical basis for the diagnostic of pulse-on time plasma 96
4 3 1 Atomic spectroscopy basis 97
4 3 1 1 Atomic processes in plasmas 97
4 3 1 2 Electron impact excitation and de-excitation 98
4 3 1 3 Electron impact ionization and three-body recombination 99
4 3 1 4 The probability for direct electron impact ionization 100
4 3 2 The emission spectrum 100
4 3 2 1 Line broadening 101
4 3 2 2 Continuous spectra 103
4 3 2 3 Spectroscopic temperature measurements 104
4 3 2 4 Time-resolved spectra 105

4 4 Theoretical basis for the diagnostic of pulse-off time plasma 106

4 4 1 Charge-loss phenomena in plasmas 106

4 4 2 Diffusion and transport 106

4 4 3 Free Diffusion 107

4 4 4 Free Diffusion of Electrons and Ions 107

4 4 5 Ambipolar Flows 108

4 4 6 Conditions of Ambipolar Flow the Debye radius 109

4 4 7 Plasma Diffusion across Magnetic Fields 110

5 TIME-RESOLVED PLASMA DIAGNOSTIC METHODS 112

5 1 The I-V characteristics and the I and V waveforms 113

5 1 1 The I-V characteristics 113

5 1 1 1 Introduction 113

5 1 1 2 The experimental set-up 114

5 1 1 3 Typical I-V characteristics 114

5 1 1 4 Discussion on the I-V characteristics 116

5 1 1 5 Conclusions on the I-V characteristics 117

5 1 2 The I and V waveforms 118

5 1 2 1 Introduction 118

5 1 2 2 The experimental set-up 119

5 1 2 3 Voltage waveforms for Cu targets 119

5 1 2 4 Current waveforms for Cu targets 121

5 1 2 5 Typical waveforms for Fe targets 122

5 1 3 Conclusions 123

5 2 Optical Emission Spectroscopy (OES) 125

5 2 1 Introduction 125

5 2 2 Experimental set-up 126

5 2 3 Line spectra 128

5 2 4 Time-resolved OES 137

5 2 4 1 For the Cu targets configuration 137

5 2 4 2 For the Fe targets configuration 141

5 2 4 3 Conclusions 142

5 2 5 Time and space-resolved OES 143

5 2 5 1 Time and space-resolved OES for the Cu targets configuration 143

5 2 5 2 Time and space-resolved OES for the Fe targets configuration 146

5 2 5 3 Discussion and conclusions 149

5 3 Time and space–resolved electron temperatures 151

5 3 1 T_E Charts for Cu targets 151

5 3 1 1 Line width and intensity measurement 151

5 3 1 2 Noise and background determinations 152

5 3 1 3 Proofs for the LTE (PLTE) conditions 153

5 3 1 4 Line broadening 154

5 3 1 5 The electron temperature 155

5 3 2 T_F Charts for Fe targets 158

5 3 2 1 Line broadening 158

5 3 2 2 Corrections 158

5 3 2 3 The electron temperature chart 159

5 3 3 Conclusions 161

5 4 Time and space resolved Ion Energy Spectra (IES) 162

5 4 1 Introduction 162

5 4 2 Experimental set-up 162

5 4 3 The ion energy spectra (IES) 163

5 4 4 Discussion 165

5 4 5 The Space –resolved Ion Energy Spectra 167

5 4 6 The time-resolved method for IES analysis 168

5 4 7 The IES Statistics 169

5 4 8 Conclusions 172

6 TIME-RESOLVED PLASMA PHYSICAL MODELS OF THE PULSED DC DISCHARGE 173

6 1 Magnetron plasma model for the pulse-on time 174

6 1 1 Introduction 174

6 1 2 The Pulse-on time plasma model in the magnetron discharge with Cu targets 175

6 1 3 The discharge behaviour and validation of the model (Cu targets) 177

6 1 4 The Pulse-on time plasma model in the magnetron discharge with Fe targets 180

6 1 5 The discharge behaviour and validation of the model (Fe targets) 182

6 1 6 Conclusions 184

6 2 Magnetron plasma model for the pulse-off time 186

6 2 1 Introduction 186

6 2 2 Experiments and discussion 186

6 2 1 2 Current and Voltage waveforms 186

6 2 2 2 The IES 188

6 2 2 3 The space-resolved IES 189

6 2 3 Physical model for the pulse-off time ion flux and energy gain 189
6 2 3 1 The pulse-off time charge density gradients 189
6 2 3 2 The plasma-probe sheath model 191
6 2 3 3 The plasma-probe sheath behaviour and the IES 193
6 2 4 Validation of the model 194
6 2 4 1 From the space-resolved IES 194
6 2 4 2 From the IES statistics 195
6 2 4 3 The ion flux rate analysis 196
6 2 5 Conclusions 198

7 **FINAL CONCLUSIONS** **200**
7 1 Summary of the work 201
7 2 Summary of the experimental results 202
7 3 Considerations derived from the proposed models 205
7 3 1 The pre-sheath electric field 205
7 3 2 Magnetic field geometry and plasma parameters 206
7 3 3 The magnetic field and charge-loss effects 207
7 4 New and original results presented in this thesis 208
7 5 Possible directions for continuation of the work 209

8 **REFERENCES** **210**
8 1 References 211
8 2 List of published papers during thesis preparation 217
8 3 List of presentations at conferences during thesis preparation 217

LIST OF FIGURES

Fig 2 1 1 Magnetic field geometry and HV electrical connections for planar magnetrons,

Fig 2 1 2 The geometry and High Voltage bias connections for the Penning-type magnetron,

Fig 2 1 3 The geometry and High Voltage bias connections for opposed target (Penning –type) magnetrons with rectangular targets,

Fig 2 1 4 Overall construction of the magnetron with opposed rectangular targets used for the experiments,

Fig 2 1 5 The target assembly showing the insulator shields designed to shield the hot electrode from the unwanted deposition and prevent arcing and sputtering on unwanted surfaces,

Fig 2 1 6 Insulators for above the stem (holder),

Fig 2 1 7 Insulators for below the stem (holder),

Fig 2 1 8 (a) TARGET, thickness=9 5mm (Cu target) and 11 0 mm (Fe target),

Fig 2 1 8 (b) Countersink heads, h=5 5mm, M5 5, Φint=6 1 mm,

Fig 2 2 1 The RPG electrical connections to the discharge chamber

Fig 2 3 1 Schematics of the Acousto-optic system for quartz crystals,

Fig 2 3 2 Vector diagram of the momentum match condition (2 3 1) for collinear and non-collinear acoustic and optical waves

Fig 2 3 3 The passband and resolution for the AOS-4 ,

Fig 2 4 1 The standard HIDEN EQP 300 analyser system,

Fig 2 5 1 View of the magnetron,

Fig 2 5 2 View inside the magnetron chamber,

Fig 2 5 3 Overall view of the experimental set-up,

Fig 2 5 4 Overall schematic of the magnetron and the experimental set-up,

Fig 3 1 1 The current sheets producing a magnetic field equivalent to a rectangular magnet

Fig 3 1 2 Diagram of the algorithm for the calculation of the magnetic field

Fig 3 1 3 3D view of one magnet pole in the opposed target magnetron The opposed pole has a symmetrical structure, with opposed polarity of the magnetic field

Fig 3 1 4 The magnetic flux density B[T] distribution in the plane XOZ with the actual magnet arrays The blue lines represent the magnetic vector potential while the red lines represent the magnetic flux density

Fig 3 1 5 The magnetic field flux density B[T] distribution for the opposed target magnetron in the plane XOZ The targets are situated at top and bottom edges of the figure

Fig 3 1 6 3D view of the magnetic flux density B contour lines in the region between the targets, for the configuration with Cu targets

Fig 3 1 7 3D view of the magnetic flux density B contour lines in the region between the targets, for the configuration with Fe targets

Fig 3 1 8 3D comparative view of the magnetic flux density B contour lines for the two configurations (Cu targets, respectively Fe targets) The configuration with Cu targets has higher values Z[mm] is the distance between the targets

Fig 3 2 1 The displacements dx and dy in the initial (un-rotated) coordinate system where the gyration takes place around OZ axis,

Fig 3 2 2 The 3D rotation plane, magnetic field and initial and final gyration angles,

Fig 3 2 3 Flow diagram of the trajectories program

Fig 3 2 4 Trajectories (blue) with starting velocities along and opposed to the direction of an electric field E=1V/m with Bx=Bz=1 T ,

Fig 3 2 5 Trajectory in an electric field E=1 V/m for Bx=Bz=1 T and Vx=10000m/s It can be noticed how the trajectory "turns back" due to the electric field

Fig 3 2 6 Trajectory in Bx=Bz=1 T and E=1V/m The perfect resulting cycloid after the parallel velocity becomes zero due to the opposed electric field, can be noticed (blue colour)

Fig 3 2 7 Trajectory in a virtual magnetic field that increases continuously regardless of position Bx=Bx+0 001T, Bz=0 1T,

Fig 3 2 8 Trajectory in a virtual field One mirror effect can be noticed,

Fig 3 2 9 Trajectory in a virtual magnetic field as indicated in the figure,

Fig 3 2 10 Trajectory for a particle moving along the filed lines in a virtual field Two "mirror" events can be noticed

Fig 3 2 11 Real trajectory in the magnetron magnetic field given by the calculated mesh The electric field is E=1V/m The electron starts from the point (10,10,10) with Vx=Vy=Vz=10000 m/s

Fig 3 3 1 Concise diagram of the Monte Carlo simulation,

Fig 2 Elastic and charge-exchange cross-sections for Ar at 3mtorr (0 4Pa),

Fig 3 The Collision frequency as a function of energy for Ar at 3 mtorr (0 4Pa),

Fig 4 Mean Free Path as a function of energy for Ar at 3mtorr (0 4Pa),

Fig 3 3 5 The geometry set-up for the MC simulation The direction of the magnetic filed lines between the targets is shown in blue lines,

Fig 3 3 6 Contour lines of the total magnetic flux density between the targets,

Fig 3 3 7 Typical Current and Voltage waveforms on the cathodes during a 50kHz, 2016ns off time pulsed DC operation at a set current run of 2A,

Fig 3 3 8 The sheath thickness for pulse-off times from 496ns to 8016ns, 50kHz, I=2A, p=3mtorr, calculated from the Child-Langmuir law and the I-V waveforms

Fig 3 3 9 Sheath and pre-sheath models for the electric field behaviour (schematics),

Fig 3 3 10 Several types of pre-sheath electric field functions

Fig 3 4 1 Time-resolved OES and the power waveform for a 50Khz, pulse off time 2016ns, I=2A pulsed DC discharge at 3mtorr (0 4Pa) Argon pressure

Fig 3 4 2 3D relative Ar ion emission lines intensity in the bulk from time and space –resolved OES Time intervals 0 2 μs

Fig 3 4 3 The relative Ar ion emission lines intensity from time and space–resolved OES at 50Khz, 2016ns, 2A and the Power waveform on the cathodes Time resolution 0 2μs,

Fig 3 4 4 Ar ion transit times statistics for the linear pre-sheath field $E(z)=80*z$

Fig 3 4 5 Ar ion transit time statistics for the parabolic pre-sheath field $E(z)=3*z^2$,

Fig 3 4 6 Ar ion translation energy distribution for linear pre-sheath field The ions start from several layers Energy bin 10eV

Fig 3 4 7 Ar ion translation energy distribution for parabolic pre-sheath field The ions start from several layers Energy bin 10eV

Fig 3 4 8 Ar ion rotational energy distribution for linear pre-sheath field Energy bin 10eV

Fig 3 4 9 Ar ion rotational energy distribution for parabolic pre-sheath field Energy bin 10eV

Fig 3 4 10 Total energy distribution for rotation energy of Ar ions in linear pre-sheath field,

Fig 3 4 11 Total energy distribution for translation energy of Ar ions in linear pre-sheath field

Fig 3 4 12 Total energy distribution for rotational energy of Ar ions in parabolic pre-sheath field Ion simulation starts in different layers

Fig 3 4 13 Total energy distribution for translation energy of Ar ions in parabolic pre-sheath field Ion simulation starts in different layer

Fig 3 5 1 The relative (normalized) OES intensity for Cu I, 465nm line during the pulse The arrow indicates the start moment for the simulation

Fig 3 5 2 Cu ions transit times statistics for the linear pre-sheath field $E(z)=80*z$

Fig 3 5 3 Cu ions transit time statistics for the parabolic pre-sheath field $E(z)=3*z^2$

Fig 3 5 4 Cu ion translational energy distribution for linear pre-sheath field The ions start from several layers Energy bin 10eV

Fig 3 5 5 Cu ion translation energy distribution for parabolic pre-sheath field The ions start from several layers Energy bin 10eV

Fig 3 5 6 Cu ion rotational energy distribution for parabolic pre-sheath field The ions start from several layers Energy bin 10eV

Fig 3 5 7 Cu ion rotational energy distribution for linear pre-sheath field The ions start from several layers Energy bin 10eV

Fig 3 5 8 Total energy distribution for rotational energy of Cu ions in linear pre-sheath field

Fig 3 5 9 Total energy distribution for rotational energy of Cu ions in parabolic pre-sheath field

Fig 3 5 10 Total energy distribution for translation energy of Cu ions in linear pre-sheath field

Fig 3 5 11 Total energy distribution for translation energy of Cu ions in parabolic pre-sheath field,

Fig 5 1 1 The IV characteristics for DC operation at different pressures

Fıg 5 1 2 The IV charactenstucs at f=50kHz, w=4016ns for dıfferent pressures

Fıg 5 1 3 The IV charactenstıcs at p=3mtorr and f=100kHz for dıfferent values of the pulse-off tıme w

Fıg 5 1 4 The IV charactenstıcs at p=5mtorr and f=100kHz for dıfferent values of the pulse-off tıme w

Fıg 5 1 5 The IV charactenstıcs at p=3mtorr and pulse-off tıme w=496ns, for dıfferent values of the pulse frequency

Fıg 5 1 6 Typıcal I-V Charactenstıcs for Fe targets dunng DC and pulsed DC at p=2mtorr, 50kHz and dıfferent pulse-off tımes (w)

Fıg 5 1 7 The expenmental set-up for measunng the Current and Voltage waveforms

Fıg 5 1 8 Voltage waveforms for dıfferent currents at p=3mtorr, 50kHz

Fıg 5 1 9 Voltage waveforms at dıfferent Ar gas pressures for 50kHZ, I=1A

Fıg 5 1 10 Voltage waveforms wıth pressure at 200kHz and I=1A,, w=2016ns

Fıg 5 1 11 Voltage waveforms wıth pulse-off tıme at 50kHz, p=3mtorr, I=2A

Fıg 5 1 12 Current waveforms for several values of the set current run at 50kHz, p=3mtorr and w=4016ns

Fıg 5 1 13 Current waveforms wıth pressure at 50kHz, w=496ns, I=1A

Fıg 5 1 14 Current waveforms at Ar pressure p=3mtorr, f=50kHz, I=2A and dıfferent pulse wıdths

Fıg 5 1 15 Current and Voltage waveforms at 50kHz, w=4016ns, p=3mtorr I=2 A,

Fıg 5 1 16 Voltage waveforms for Fe targets at 2mtorr, 50kHz, 4016ns,

Fıg 5 1 17 Voltage waveforms wıth pressure at I=1 5A, 50kHz, 4016ns,

Fıg 5 1 18 Current waveforms at 2mtorr, 50kHz, w=4016ns for dıfferent set current run

Fıg 5 1 19 Current waveforms at two pressures for Fe targets, 50kHz, w=4016ns, I=1 5A

Fıg 5 1 20 Voltage waveforms for Fe targets for dıfferent pulse-off tımes at 50kHz, I=1 5A, p=2mtorr

Fıg 5 1 21 Current waveform for Fe targets for dıfferent pulse-off tımes at 50kHz, I=1 5A, p=2mtorr

Fıg 5 2 1 Cross-sectıon vıew ın the YOX plane wıth dırectıon of OES observatıon Probe posıtıonıng geometry A,

Fıg 5 2 2 Cross-sectıon vıew ın the ZOX plane wıth dırectıon of OES observatıon Probe posıtıonıng geometry,

Fıg 5 2 3 OES lıne Spectrum at 50KHz, w=496ns, pAr=1 mtorr,

Fıg 5 2 4 OES lıne spectrum at p=3mtorr, 50kHz, pulse-off tıme w=2016ns,

Fıg 5 2 5 OES lıne spectrum for Cu targets at 50kHz, pulse-off tıme w=4016ns and Ar gas pressure p=3mtorr Measurement wıth cable B

Fıg 5 2 6 Optıcal Emıssıon Lıne spectrum for Fe targets magnetron plasma f=50kHz,w=496ns, I=1 5A, p=2mtorr ,

Fig 5 2 7 The IV characteristics with Ar gas pressure at 50kHz, w=4016ns pulse DC discharge,

Fig 5 2 8 The IV characteristics with Ar gas pressure at 50kHz, w=2016ns pulse DC discharge,

Fig 5 2 9 Typical evolution of lines' radiance with current for two Ar II emission lines 460 965nm and 487 978nm at p=3mtorr, and 4016ns pulse-off time,

Fig 5 2 10 The evolution of the radiance for the Ar II 461nm line with current

Fig 5 2 11 The evolution of the radiance for the Ar II 487nm line with current

Fig 5 2 12 Typical IV waveforms for the Fe targets

Fig 5 2 13 OES line spectra for Fe targets OES Intensity with current at p=2mtorr, 50kHz, pulse-off time w=4016ns

Fig 5 2 14 Voltage and power waveforms along with the time-resolved OES signal for Ar II (487 9nm) and Cu I (465nm and 522nm) for a discharge at I=2A, f=50kHz, w=4016ns, pAr=3mtorr,

Fig 5 2 15 Time resolved O E S I=2A, f=50KHz, w=2016ns, pAr=3mtorr The dotted line indicates the expected "fall" of the excited Cu peak

Fig 5 2 16 Time-resolved OES at I=2A, f=100kHz, w=4016ns, p=3mtorr,

Fig 5 2 17 Time-resolved OES at I=2A, f=50kHz, w=496ns, pAr=3mtorr along with the power waveform

Fig 5 2 18 Time -resolved OES for Fe targets at 50kHz, w=4016ns, I=1 5A, p=2 mtorr

Fig 5 2 19 Time -resolved OES for Fe targets at 50kHz, w=2016ns, I=1 5A, p=2 mtorr

Fig 5 2 20 Time-resolved OES measurements at L=0 cm (discharge centre) for two Ar ion lines and one excited Ar atom line The time-resolved voltage waveform is superimposed

Fig 5 2 21 The relative Ar ion emission lines intensity from time and space-resolved OES at 50Khz, 2016ns, 2A and the Power waveform on the cathodes Time resolution 0 2μs, space resolution 1mm

Fig 5 2 22 The relative (normalized) OES intensity for Cu I, 465nm line during the pulse, from time and space-resolved OES at 50Khz, 2016ns, 2A and the Power waveform on the cathodes Time resolution 0 2μs, space resolution 1mm

Fig 5 2 23 Normalized relative intensity for Ar II 488nm line (up) and for Ar I 763nm line (bottom), space and time-resolved at 50kHz , 4016ns and p=3mtorr, for the Cu targets

Fig 5 2 24 Normalized relative intensity for Cu I 465nm line (up) and for Cu I 522nm line (bottom), space and time-resolved at 50kHz, 4016ns and p=3mtorr

Fig 5 2 25 Normalized relative intensity for Ar II 488nm line (up) and for Ar I 763nm line (bottom), space and time-resolved at I=1 5A, 50kHz, 4016ns and p=2mtorr, for the Fe targets

Fig 5 2 26 Normalized relative intensity for Fe I 372nm line (up) and for Fe I 492nm line (bottom), space and time-resolved at I=1 5A, 50kHz, 4016ns and p=2mtorr

Fig 5 2 27 Cu I, 465nm line, space and time resolved 3D image

Fig 5 2 28 Cu I, 522nm line, space and time resolved 3D image

Fig 5 2 29 Ar II, 488nm line, space and time resolved, for Cu targets 3D image

Fig 5 2 30 Ar I, 763nm line, space and time resolved for Cu targets 3D image,

Fig 5 2 31 Ar II, 488nm for Fe targets, 3D image

Fig 5 2 32 Ar I, 763nm for Fe targets, 3D image

Fig 5 2 33 Fe I, 492nm, 3D image,

Fig 5 2 34 Fe I, 392nm, 3D image,

Fig 5 3 1 The AOS-4 Pass-band and Resolution and the experimental widths for the Ar ion and atom lines The error bars indicate maximum deviation

Fig 5 3 2 Typical emission line spectrum in the discharge with Cu targets

Fig 5 3 3 Typical T_e evolution, along with the voltage waveform Values at z=0 (discharge centre)

Fig 5 3 4 Space and time-resolved electron temperature (3D view) during the pulse at 50kHz, pulse off time 4016ns, set current I=2A, argon pressure p= 3mtorr

Fig 5 3 5 Electron temperature contour lines evolution during the pulse at 50kHz, pulse off time 4016ns, set current I=2A, argon pressure p= 3mtorr

Fig 5 3 6 Optical Emission Line spectrum for Fe targets magnetron plasma at 50kHz,w=496ns, I=1 5A, p=2mtorr

Fig 5 3 7 Contour lines for the space and time–resolved electron temperature distribution for Fe targets

Fig 5 3 8 3D view of the Space and time–resolved electron temperature distribution for Fe targets

Fig 5 4 1 Geometry of the opposed target magnetron and the EQP probe

Fig 5 4 2 Ar ion energy spectra at 50kHz, I=2A, p=3mtorr, for different pulse-off time values for Cu targets

Fig 5 4 3 Cu ion energy spectra at f=50kHZ, I=2A, pAr=3mtorr, for different pulse-off time (w) values,

Fig 5 4 4 Ar ion energy spectra for Fe targets, for different pulse-off time (w) values

Fig 5 4 5 Fe ion energy spectra for Fe targets, for different pulse-off time (w) values,

Fig 5 4 6 DC ion energy spectra for Cu and Fe targets

Fig 5 4 7 Pulsed DC ion energy spectra at f=50kHz, off time=2016ns, for Cu and Fe targets,

Fig 5 4 8 Comparison of the energy density of the total ion current at the probe (substrate) for Cu and Fe targets

Fig 5 4 9 Ar IES as a function of the distance D of the probe from targets edge, for distances larger than 5cm The (*) arrows indicate the "step-like" edges in the ion energy distribution,

Fig 5 4 10 Ar IES as a function of the distance D of the probe from targets edge, for distances smaller than 5cm

Fig 5 4 11 The number of Ar and Cu ions collected by the energy analyser probe during the pulse-on time and during the pulse-off time, as a function of the pulse-off time

Fig 5 4 12 The Ar ion flux [Number of ions/collection time] collected by the probe during the pulse-on time and during pulse-off time as a function of the pulse-off time

Fig 5 4 13 Typical ion flux rate variation during the pulse-off time, calculated as d^2N/dt^2 (the variation of the ion flux (dN/dt) between two consecutive values of the pulse-off time)

Fig 6 1 1 Normalized relative intensity for Ar II 488nm line (up) and for Ar I 763nm line (bottom), space and time-resolved at 50kHz , 4016ns and p=3mtorr, for the Cu targets

Fig 6 1 2 Normalized relative intensity for Cu I 465nm line (up) and for Cu I 522nm line (bottom), space and time-resolved at 50kHz, 4016ns and p=3mtorr

Fig 6 1 3 Electron temperature contour lines evolution during the pulse at 50kHz, pulse off time 4016ns, set current I=2A, argon pressure p= 3mtorr

Fig 6 1 4 The time-resolved electron temperature during the pulse-on time at D=0 cm from the discharge centre along with the voltage waveform

Fig 6 1 5 Calculation of Ar and Cu direct electron impact ionization cross-sections Evolution with electron energy, using Thomson' formula presented in Chapter 4 3 1 [2]

Fig 6 1 6 Normalized relative intensity for Ar II 488nm line (up) and for Ar I 763nm line (bottom), space and time-resolved at I=1 5A, 50kHz, w=4016ns, p=2mtorr, for the Fe targets

Fig 6 1 7 Normalized relative intensity for Fe I 372nm line (up) and for Fe I 492nm line (bottom), space and time-resolved at I=1 5A, 50kHz, w=4016ns and p=2mtorr ,

Fig 6 1 8 Electron temperature space and time-resolved at I=1 5A, 50kHz, w=4016ns and p=2mtorr, for the Fe targets The values situated at distances below 1cm from the targets re extrapolated values

Fig 6 1 9 Te for Fe targets at D=3cm from the targets (z=2cm) along with the Voltage (-V) on the targets

Fig 6 1 10 Relative direct electron impact ionization cross-sections for Ar and Cu and Fe atoms Evolution with electron energy, using Thomson' formula,

Fig 6 2 1 Typical Voltage and Current waveforms at the targets at Ar gas pressure of 0 4Pa, and a pulsed DC operation at 2A, 50Khz, and 4016ns pulse-off time,

Fig 6 2 2a Voltage waveforms during the pulse-off time

Fig 6 2 2b Current waveforms during the pulse-off time,

Fig 6 2 3 Ar ion energy spectra at 50kHz, I=2A, p=3mtorr, for different pulse-off time values,

Fig 6 2 4 Cu ion energy spectra at f=50kHZ, I=2A, pAr=3mtorr, for different pulse-off time (w) values

Fig 6 2 5 Ar IES as a function of the distance D of the probe from targets edge, for distances larger than 5cm,

Fig 6 2 6 Ar IES as a function of the distance D of the probe from targets edge, for distances smaller than 5cm

Fig 6 2 7 Schematics of the plasma-probe sheath model Cross-section view of discharge chamber in plane XOY

Fıg 6 2 8 The number of Ar and Cu ıons collected by the energy analyser probe durıng the pulse-on tıme and durıng the pulse-off tıme, as a functıon of the pulse-off tıme,

Fıg 6 2 9 The Ar ıon flux [Number of ıons/collectıon tıme] collected by the probe durıng the pulse-on tıme and durıng pulse-off tıme as a functıon of the pulse-off tıme,

Fıg 6 2 10 Typıcal ıon flux rate vanatıon durıng the pulse-off tıme, calculated as d^2N/dt^2 (the vanatıon of the ıon flux (dN/dt) between two consecutıve values of the pulse-off tıme)

LIST OF TABLES

Table 3 4 1 Values of the travel time to targets for Ar ions

Table 3 5 1 Values of the travel time to targets for Cu ions

Table 4 1 List of atomic processes in plasmas

Table 4 2 The atomic processes, explained

Table 5 2 3 Transition data for the observed lines

CHAPTER 1 INTRODUCTION

The work presented in this thesis is devoted to the study of a Penning – type [1, 2, 3] (opposed target) magnetron with rectangular geometry under pulsed DC operation

Pulsed DC magnetron sputtering is a relatively new field in magnetron sputtering that has gained large interest in the last few years due to the significant improvement brought in the mechanical and structural properties of the deposited layers The pulsed DC bias of the targets also prevents charge build-up on insulating areas of the targets and arcing, thus allowing for sputtering of any materials, including insulators

Under the opposed target geometry, ferromagnetic materials can be easily sputtered making the opposed target magnetron under pulsed-DC operation suitable for a wide range of applications non-ferromagnetic, ferromagnetic, conducting and insulating materials can all be sputtered with comparable rates

The subject of magnetron sputtering has been approached in many experimental and theoretical studies leading to a general accepted theory of DC magnetron operation [4, 5, 6]

The experimental studies investigate the plasma parameters and their relationship to the magnetron operation and the properties of the deposited films The large list of references presented in Chapters 2-7 of the thesis indicates the importance of the field and the amplitude of the research interest devoted to these problems So far, plasma diagnostic methods rely almost exclusively on Langmuir probes and Laser-induced Fluorescence measurements and less on Optical Emission Spectroscopy or Ion Energy Spectra analysis The construction of Langmuir probes and the required numerical treatment increases in complexity and loses accuracy when magnetic fields are involved The study of layer's properties has the advantage of using the most modern investigation techniques SEM, AFM, XRD all devoted to revealing the structure of the layers and providing direct information on the improvement in their properties for pulsed-DC operation, that has been related to the increased ion flux and energy at the substrate

The theoretical studies aim at developing models to predict the behaviour of plasma components and parameters as well as the properties of the deposited layers using simulation codes based on Monte Carlo of fluid models or a combination of these These theoretical studies are enabled by simple start models like the behaviour of glow discharges that can be further extrapolated to magnetized discharges under DC operation

Pulsed DC operation involving time-dependent plasma parameters and new time-dependent behaviour of the plasma components poses more difficult problems in applying the suitable experimental and diagnostic techniques for deriving time-dependent physical models and developing the necessary theoretical models Recently, time and space-resolved studies of plasma parameters performed by Bradley et al in a planar magnetron reveal the behaviour of plasma parameters (electron temperature and density, plasma potential) [7, 8] This information needs to be correlated to suitable physical models of the pulsed DC magnetron discharge and sputtering process

Although simulation techniques can sometime provide information on the evolution of a system, without a well-formulated theoretical or physical model, such simulations cannot provide any useful prediction on the system's behaviour Recent numerical studies for the understanding of temporal evolution of plasma sheaths and pre-sheaths using Monte Carlo - Particle in Cell (MC-PIC) simulations have been devoted to Plasma Immersion Ion Implantation (PIII) applications, where magnetic fields are not involved [9]

Most of the experimental and theoretical studies devoted to pulsed DC magnetron operation do not provide the link between the observed phenomena, their physical causes and the pulsed DC operation of the magnetron Therefore, important issues in the field of pulsed-DC magnetron sputtering are still unsolved

- How to choose the pulsed frequency and duty cycle for optimum sputtering rate,
- How to control the self-sputtering process,
- How to control the ion flux and energy at the substrate using the pulsed DC operation,
- What is the temporal development of the sputtering process during the pulse,
- How is the magnetic field distribution affecting the ionization density and the sputtering, re-sputtering and self-sputtering processes

Finding an answer to such questions is therefore the aim of the present thesis

In the work performed and presented here, both the experimental and numerical approaches for the study of time-dependent magnetized plasmas have been investigated, developed and applied with the aim of revealing the physical models that govern the plasma behaviour and the sputtering process during the pulsed-DC operation

In order to approach the experimental investigation leading to time-dependent physical models of the pulsed DC magnetron discharge, new time-resolved plasma diagnostic methods are proposed and applied for both non-ferromagnetic and ferromagnetic material of the targets These plasma diagnostic methods are fairly easy to apply as well as accurate enough and independent of the presence of the magnetic field the time and space-resolved Optical Emission Spectroscopy (OES) and the Ion Energy Spectra (IES) measured at the substrate region

Another type of investigation performed here, based on a time-dependent Monte Carlo simulation of ion trajectories during the pulse, reveals information on the space distribution of the pre-sheath electric field which is the "motor" for the sputtering process, and its influence on the time-scales for the sputtering and self-sputtering processes and ion impact energies to the targets

This thesis presents therefore the following time-resolved diagnostic methods and the associated experimental data

- The Current -Voltage (IV) waveforms on the cathodes (Chapter 5 1),
- The time and space-resolved OES and time-space resolved electron temperatures (Chapter 5 2),
- The space-resolved IES and the IES temporal analysis and statistics (Chapter 5 4)

The above investigations allowed the development of two physical models describing the behaviour of pulsed DC discharges

-The physical model for the pulse-on time (Chapter 6 1),

-The physical model for the pulse-off time (Chapter 6 2)

The physical models of the discharge are completed through the modelling of the sputtering process and its time-scales by investigating the behaviour of the pre-sheath electric field through numerical simulations using a Monte Carlo simulation code based on single particle transport in the space and time-dependent electric field and space-dependent magnetic field of the magnetron discharge

The original algorithm that I have developed for charged particle transport and the Monte Carlo simulation algorithm and code as well as the obtained results are presented in Chapter (3 2) I have to emphasize here that the physical model used in the formulation of the MC simulation is entirely based on initial data that have been obtained experimentally in the opposed target magnetron

Although from the "historical" point of view I wrote first the trajectories code, the MC simulation has only been possible after the experimental data have set the framework for the problem For this reason, the chapter presenting the simulation makes repeated connections to the Chapter (5) presenting the experimental data

As the knowledge of the magnetic field is necessary for both the MC simulation and the understanding of the experimental set-up and analysis, the magnetic field values are calculated and presented in Chapter (3)

To allow for a certain classification of the presented work, the presentation involving numerical methods like the calculation of the magnetic field and the Monte Carlo simulation has been organized under Chapter (2) "Numerical Methods" and presented before the experimental chapters

CHAPTER 2

EQUIPMENT

In this Chapter are described the construction of the magnetron and the main characteristics and operating modes of the equipment used during the experiments the power supply, the IfU acousto-optic spectrometer and the HIDEN mass-energy analyser

2.1. CONSTRUCTION OF THE MAGNETRON

2.1.1 INTRODUCTION

The "Opposed Target Magnetron" built at DCU, School of Electronic Engineering, is a Penning –type magnetron [1, 2, 3] with rectangular targets.

The conventional magnetrons widely used in most applications are of planar type (Fig.2.1.1). Such planar magnetrons have the targets (backed by magnetic poles of opposed polarity) situated in the same plane and for magnetic confinement rely on the component of the magnetic field B parallel to the targets.

Penning-type magnetrons have opposed targets with a cylindrical geometry, as shown in Fig.2.1.2 and have been described first in 1939 by F.M. Penning (U.S Patent, 2,146,025, 7 Feb. 1939) [1]. In Penning-type magnetrons the targets (also backed by magnetic poles of opposed polarity) are facing each other, while the magnetic field B is mainly perpendicular to the targets (Fig.2.1.2).

The magnetic field distribution relative to the targets brings important advantages of the Penning geometry versus the conventional planar geometry. A detailed analysis of the magnetic field distribution will be provided in Chapter (3.1) while a short explanation of these effects is presented next.

At a boundary between two materials with different magnetic permeability, the magnetic induction (magnetic flux density) $\vec{B}$ components are continuous for the $\vec{B}$ component normal to the boundary and discontinuous for the $\vec{B}$ component parallel to it [10]. As only the parallel component is absorbed in the ferromagnetic material, the magnetic field B will be little affected in magnetron systems that have B lines normal to the targets, while systems that rely on the B component parallel to the targets will not be able to sustain a high magnetic field above the targets.

For planar magnetrons, any modification in the thickness of the targets will bring important changes in the strength of the magnetic field above the targets, leading to non-uniform target utilization, low sputtering rates, strong plasma perturbations and arcing.

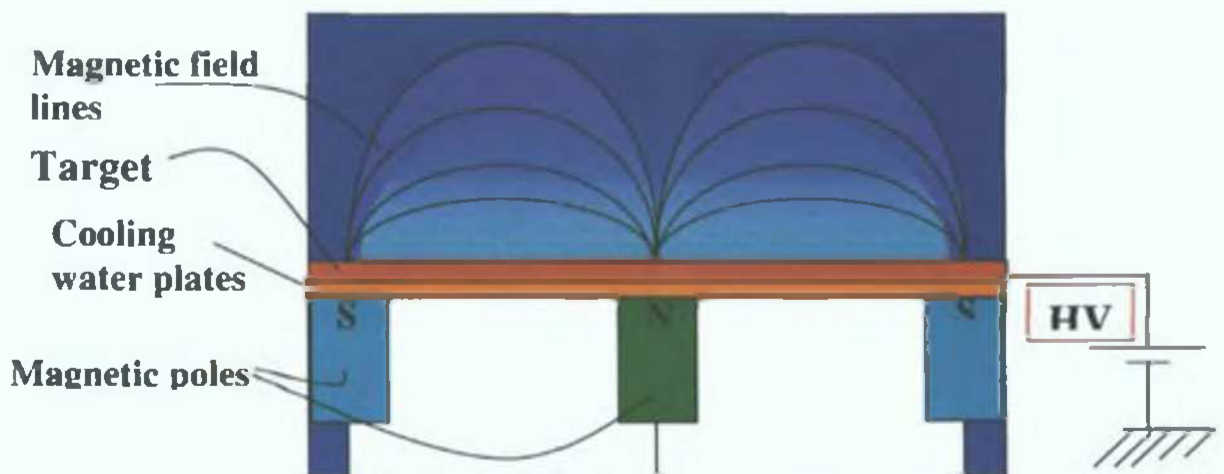

Fig.2.1.1. Magnetic field geometry and HV electrical connections for planar magnetrons.

For opposed target magnetrons, the facing targets as well as the orientation of the magnetic field relative to the targets provide important advantages:

- a very efficient confinement for charged particles;
- the possibility to use thick targets for both non-ferromagnetic and ferromagnetic target material with high sputtering rate.

The success and longevity of Penning – type magnetrons lies therefore in its effective sputtering of thick ferromagnetic targets.

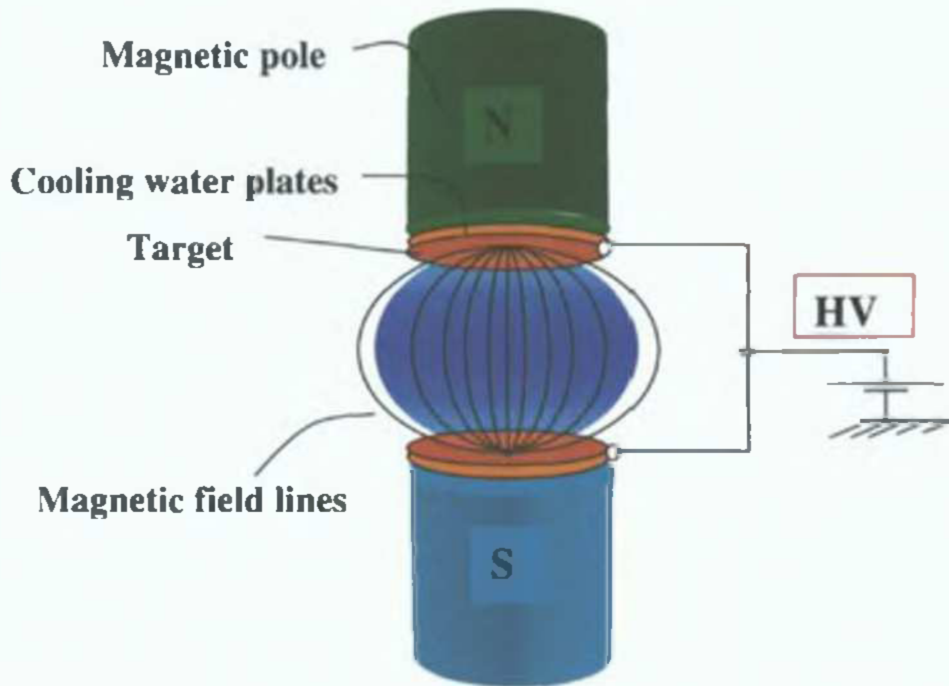

Fig.2.1.2. The geometry and High Voltage bias connections for the Penning-type magnetron.

As the cylindrical geometry proposed by Penning leads to a cylindrical spread of the sputtered material, this geometry is not suitable for in-line coating systems and large industrial applications.

A rectangular geometry was proposed as an improvement of the Penning type magnetron, through the use of rectangular magnetic poles and targets (Fig.2.1.3). This rectangular geometry has been designed, optimized and used for the construction of the opposed target magnetron that is studied throughout this thesis.

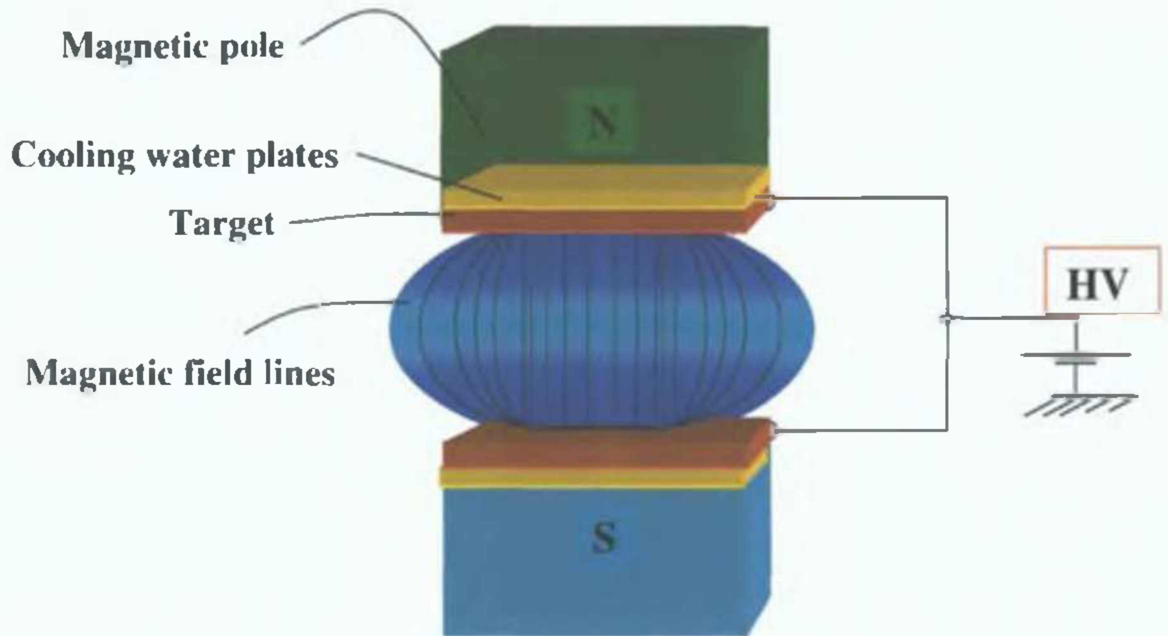

Fig.2.1.3. The geometry and High Voltage bias connections for opposed target (Penning –type) magnetrons with rectangular targets.

The magnetron with opposed rectangular targets (Fig.2.1.3) is provided with a specially designed magnetic field (designed as described in the Chapter 3 of the thesis) and it can be operated in both DC and pulsed DC modes using the power supply described in the next section.

My contribution to its design and construction consisted in choosing the magnetic pole structure, assembling the magnetic poles, targets and cooling water system and the design and assembling of anti-arcing shields. The operation of the magnetron under stable conditions of the discharge required special anti-arcing shields that I have designed for this application, which will be presented in Section 2.1.4.

2.1.2. THE MAGNETRON CONSTRUCTION

The geometry and electrical connections of the opposed target magnetron are presented in Fig.2.1.3. The overall schematics (view from the top) of the opposed targets system design, dimensions and electrical connections is presented in Fig.2.1.4. The components described in Fig.2.1.4 are the following:

1: Targets: a detailed drawing of the targets is presented in Fig.8a and Fig.8b.

Two configurations of the magnetron with for two types of target material have been used:

-Material: Cu. 99.995 % purity, target dimensions: 120x180x9mm;

-Material: Fe. 99.993 % purity, target dimensions: 120x180x11mm;

2: Cooling water plates;

3: Grounded electric shield (metal casing);

4: Magnetic poles' case;

5 Plastic insulators,

6 Plastic insulators and shield against sputtering A detailed presentation follows in the next section,

7 Holder bolt (and High Voltage connection),

8 Holder (steel),

9 Chambers' door (steel),

10 Insulated HV cable,

11 pass-through vacuum tight flange,

12 Shield (aluminium),

13 cooling water tubes

The targets (1) are in direct contact with the cooling water that circulates through the cooling water plates (2) underneath The cooling water pipes circuit ensures water circulation through the cooling plates, a separate cooling water circuit being provided for each target Vacuum tight flanges ensure the passage of the cooling water pipes inside the magnetron's chamber

The electrical connections are indicated in red for the High Voltage wires (10) and in blue for the ground connections The wires (10) are insulated with ceramic beads and covered in plastic tubing The targets are connected to the HV voltage through direct contact to the cooling water plates (2) and the magnetic poles casing (4), using a steel bolt (7) that also serves for holding the magnetic pole assembly to the holder (8) on the magnetron door (9)

As the steel holder (8) is in direct contact to the magnetron door and to the ground, a TEFLON insulator assembly (6) ensures the electrical insulation between the bolt (7) that is connected to HV and the grounded holder (8)

The magnetic pole casing in contact with the HV is insulated from the rest of the chamber by a metal shield case (3) that is connected to the ground, the electrical insulation between the magnetic pole casing and the shield case being achieved through the insulator assembly (5) Another shield in the shape of a flat panel (12) ensures protection against the deposition of sputtered material on the electric wire connections (10) and the cooling water pipes The cooling water pipes (13) are flexible plastic tubes that allow their passage in and out the magnetron chamber, through the vacuum tight flanges (14)

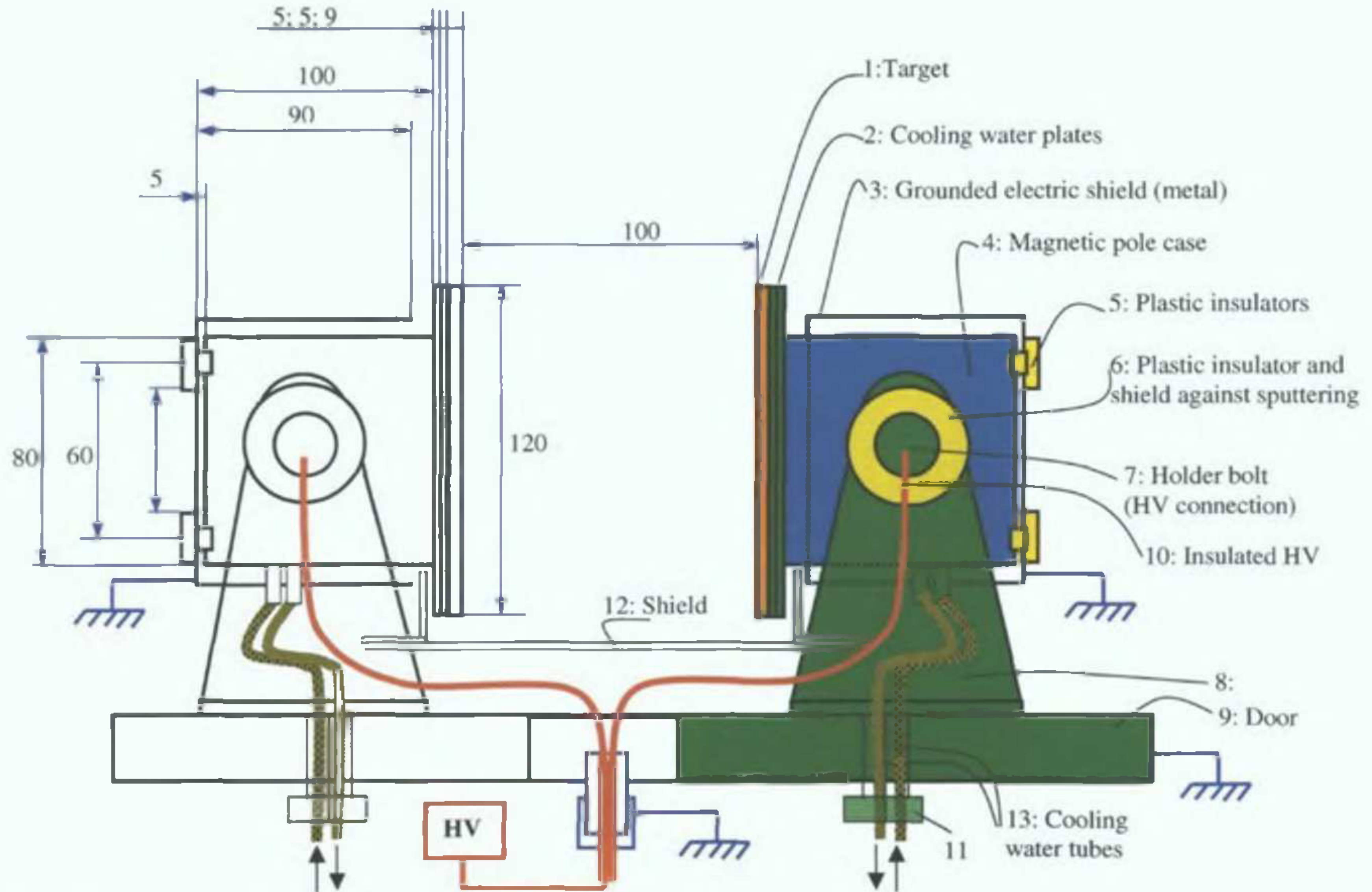

Fig.2.1.4. Overall construction of the magnetron with opposed rectangular targets used for the experiments.

2.1.3. THE DESIGN OF THE ANTI-ARCING SHIELDS

During the magnetron operation, the sputtered material is scattered in all directions, covering all surfaces inside the magnetron's chamber.

The design and mounting of the shields that prevent unwanted metal deposition, arcing, short-circuit paths and sputtering between the high voltage electrodes and the grounded components is therefore of high importance, as without these shields, the operation of the magnetron is not possible. These shields made possible a continuous long-term operation of the magnetron practically without any maintenance and allowed performing experiments with the designed magnetron.

The mounting of the anti-arcing shield assemblies is presented in Fig.2.1.5.

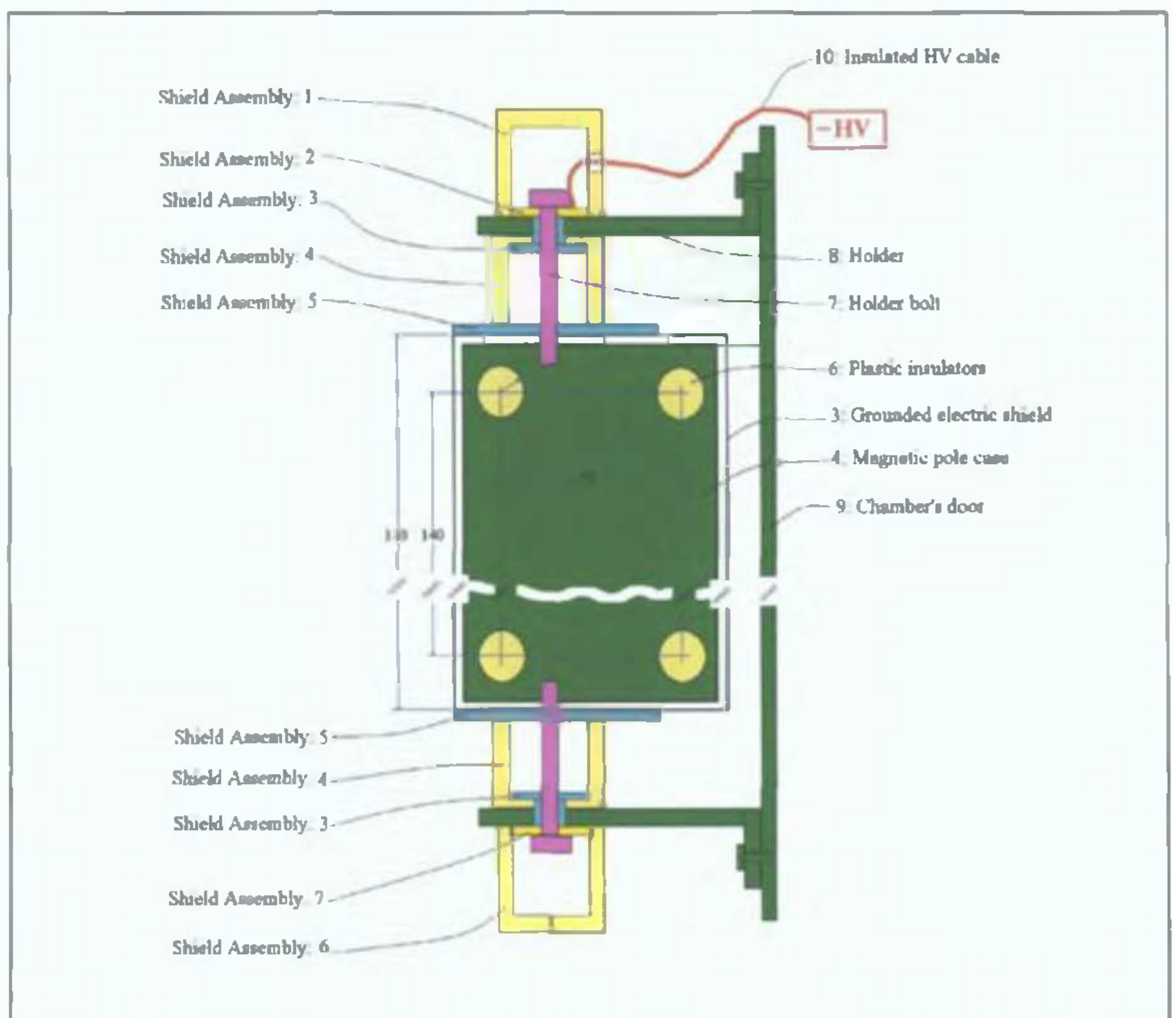

Fig.2.1.5. The target assembly showing the insulator shields designed to shield the hot electrode from the unwanted deposition and prevent arcing and sputtering on unwanted surfaces.

Detailed drawings of the anti –arching shield are presented in Fig.2.1.6 and Fig.2.1.7. Note that the insulators for the upper position are different from those for the lower position. A detailed drawing of the targets is presented in Fig.2.1.8 a, b.

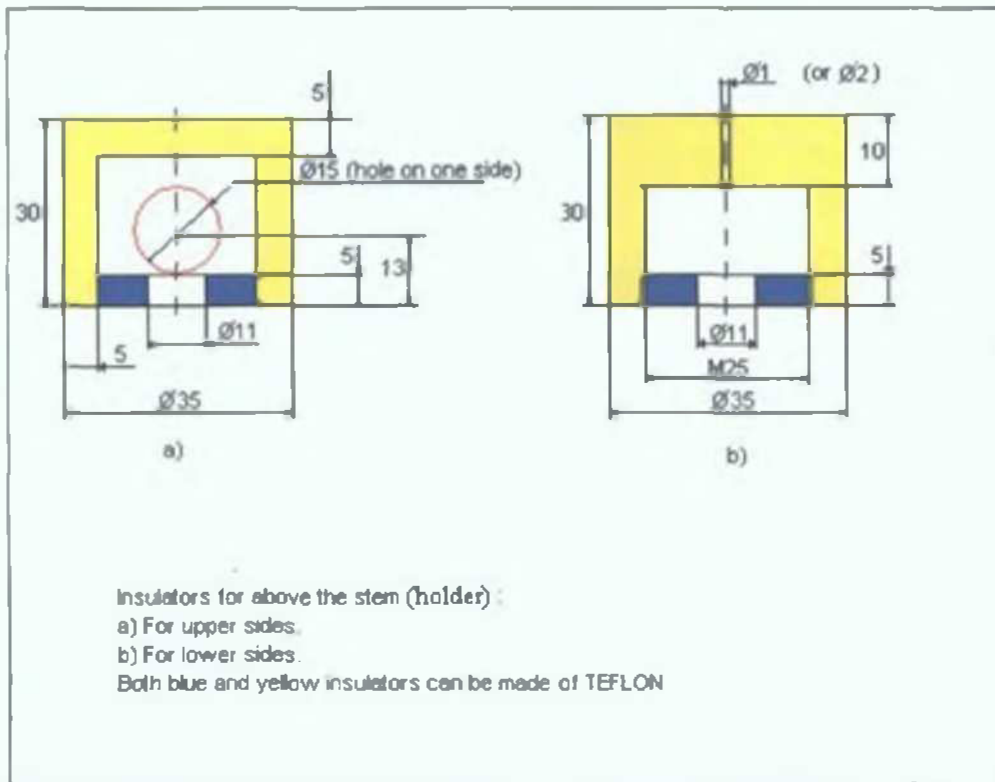

Fig.2.1.6: Insulators for above the stem (holder). The material used is TEFLON.

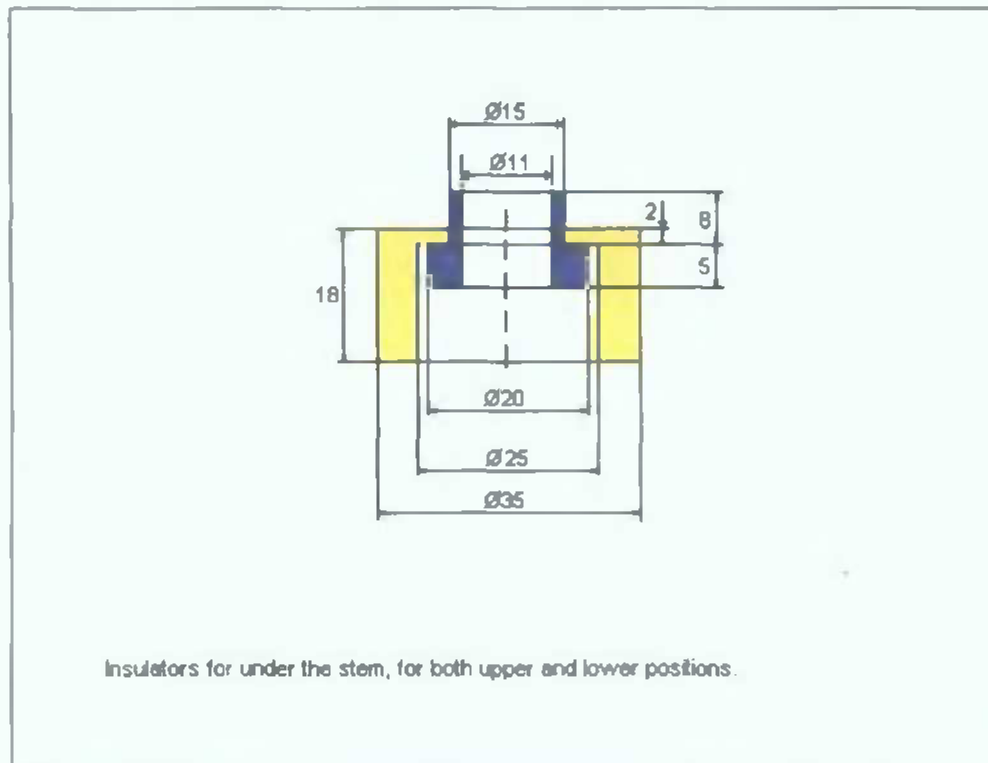

Fig.2.1.7: Insulators for below the stem (holder). The material used is TEFLON

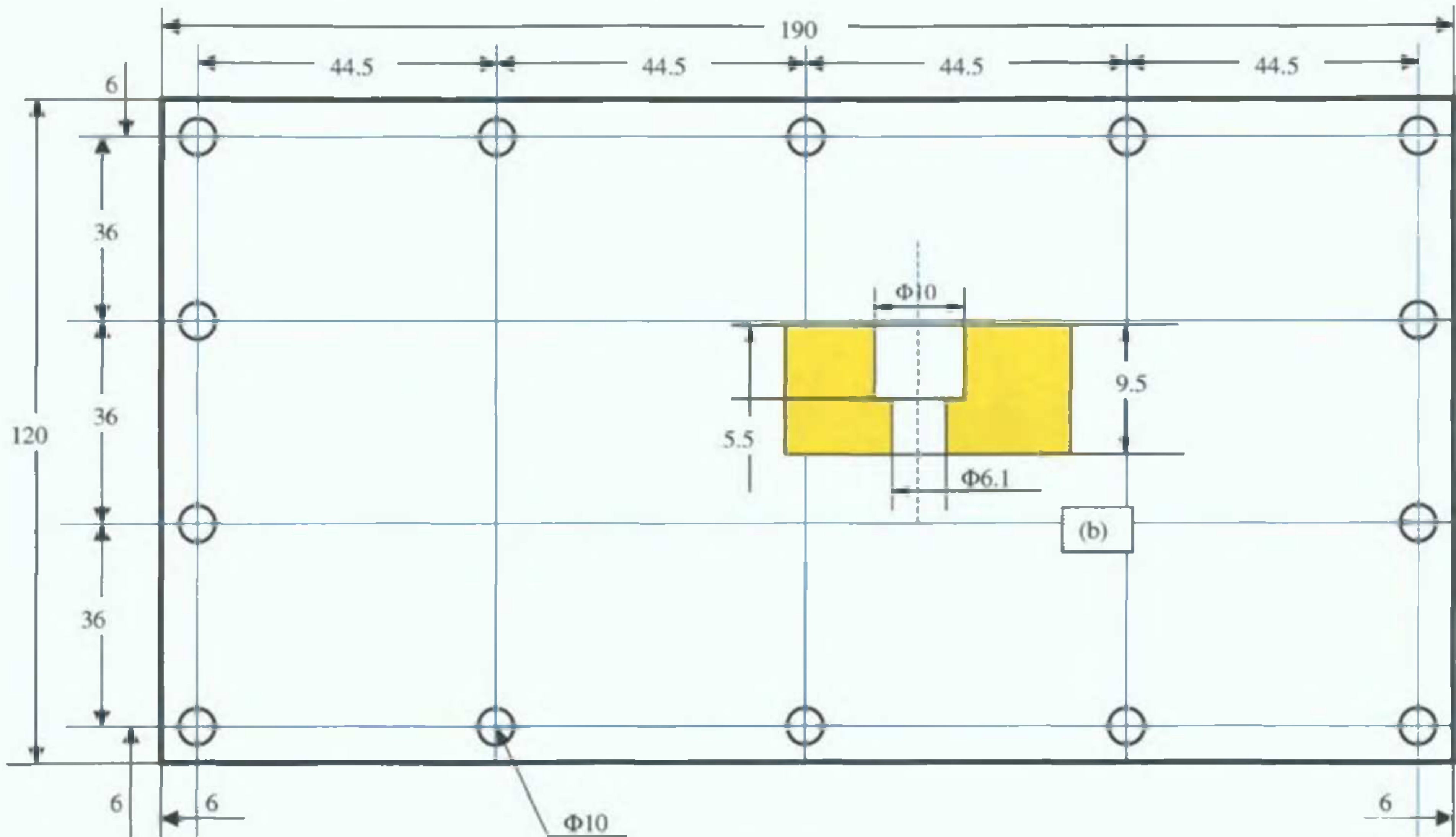

Fig.2.1.8 (a) TARGET, thickness=9.5mm (Cu target) and 11.0 mm (Fe target)
MATERIALS: Cu, Fe; 2 TARGETS OF EACH MATERIAL
Fig.2.1.8 (b) Countersink heads; h=5.5mm; M5.5, Φint=6.1 mm.

2 2 THE POWER SUPPLY AND PULSED DC BIAS

The power supply used to generate the High Voltage bias on the targets of the magnetron is an RPG-50 ENI Pulsed DC plasma generator Its main applications characteristics and operation modes and will be presented shortly next, having as reference the ENI Operation Manual [11]

Pulsed DC operation of magnetrons has opened wide possibilities for improvement in depositing all types of films, and especially dielectric films, a process that in conventional reactive DC plasma sputtering is hindered by arcing The arcing occurs as an insulating layer forms on the target and causes a build-up of electrical charges leading to the accumulation of high potentials producing arcs, through either dielectric breakdown of the dielectric material or between the target racetrack and the charged dielectric areas The ENI RPG eliminates these arcs by regularly pulsing a positive bias that allows plasma electrons to reach the targets and discharge the dielectric material

The RPG family of pulsed generators features Arc Detection allowing to estinguish arcs that cannot be prevented through the asymmetric bipolar, pulsed output, by checking for the low voltage values during arcing and setting a positive bias for 250μs to estinguish the arc

The RPG generator allows several modes of operation for DC and pulsed DC output, providing negative bias to the magnetron cathodes (targets) while acting as a constant current source

- Constant Run Mode enabling (or ramping) the output at the set-point,
- Run-time Mode allows the output to be energized for a specific period of time,
- Jules Mode allow the output to be energized until the required quantity of energy has been delivered to the load,
- Sequence Mode allows the user to define an output "waveform" of up to 10 segments

The Asymmetric Bipolar Pulsed DC Bias Mode with Constant Current Run Mode has been used throughout all experiments described in the following chapters as pulsed DC operation The constant current was set at a value in the range 0 2- 6A while the pulse frequency has been selected in the range 50kHz-250kHz (mainly at 50kHz) and the pulse –off time has been selected from values in the range 496ns- 8016ns

A schematics of the electrical connection used is presented in Fig 2 2 1 All blue connections are ground connections (the substrate, chamber and magnetic poles' shields) and the red connections (the targets) are connected to the High Voltage negative bias

The RPG is designed with a fully floating output This requires the user to supply both connections to the process chamber, thus avoiding multiple ground paths or loops The High Voltage connection cable recommended and used for this application was the RG 392U Silver-plated, double shield cable with Teflon Center Insulator

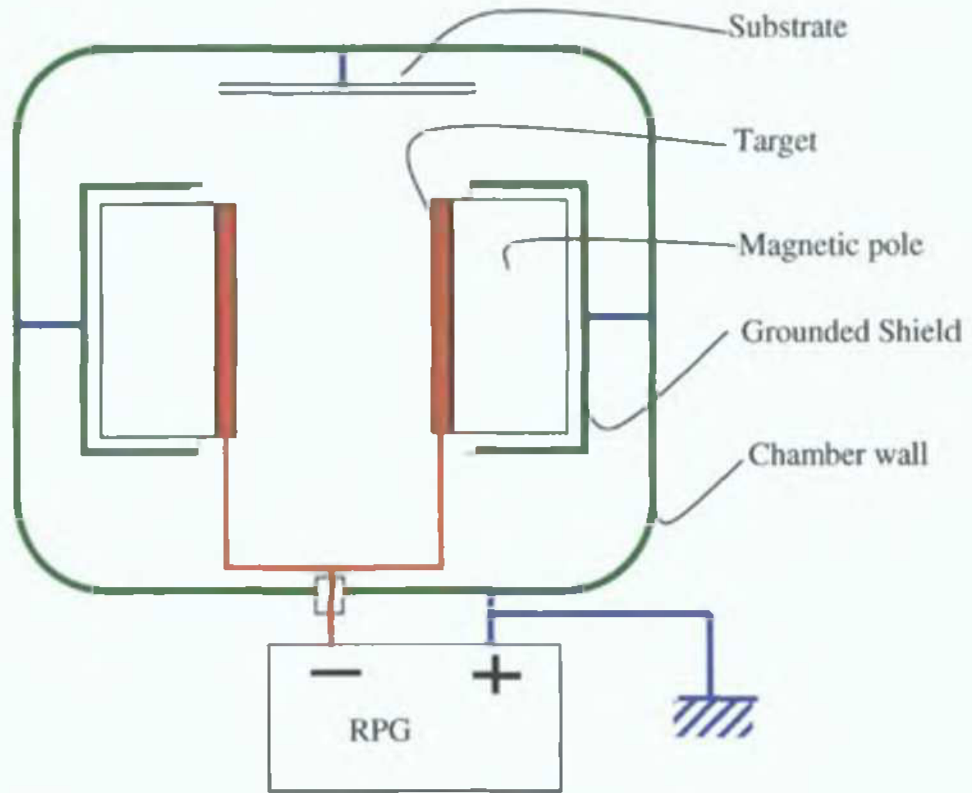

Fig.2.2.1. The RPG electrical connections to the discharge chamber.

2 3 THE ACOUSTO-OPTIC SPECTROMETER

The spectrometer used for Optical Emission Spectroscopy diagnostic in the work presented in this thesis is a Time-Resolving Acousto-optic UV/VIS Spectrometer (AOS 4-1 μchron 02) provided by IfU GmbH Privates Institut fur Umweltanalysen, Chemnitz, Germany [12]

The advantages of AOS to conventional (prism or grating) spectrometers are the following

- Do not require moving mechanical parts,
- Fast electronic wavelength selection,
- Bi-dimensional aperture,
- High resolution

The AOS-4 allows measuring small amounts of light in a narrow spectral band and fast random wavelength access (fast switching between free chosen wavelengths) A short description of the operation principle and its performances are presented next

2 3 1 THE OPERATING PRINCIPLE

In Acousto-optic spectrometers, the spectral dispersion of the broadband optical signal is performed by an Acousto-optic Tunable Filter (AOTF), that allows fast, tunable wavelength scanning and selection and a narrow band filtering

The selected wavelength is detected by a broadband photomultiplier PMT with a single cathode configuration and the electronic signal is fed to a computer, for analysis using the "Intellispec" software provided by IfU GmbH [12]

The AOTF is an electronically tuned optical filter that operates on the principle of acousto-optic diffraction in an anistropic medium This implies that no slit is required for wavelength selection as in conventional spectrometers and a bi-dimensional aperture can be used

The principle of the AOTF is based on the interaction between an acoustic wave and the optical beam inside the anisotropic crystal In the AOTF, an RF powered piezo-electric transducer bonded to a quartz (SiO_2) crystal generates sinusoidal acoustic compression waves that alter the refractive index of the birefringent crystal in a periodic pattern This creates a mobile diffraction grating with a constant equal to the acoustic frequency The principle of optical wavelength selection is based on the momentum matching condition (Fig 2 3 2)

$$\vec{K}_d = \vec{K}_i + \vec{k}_a, \qquad (2\ 3\ 1)$$

where $\vec{k}_a$ is the acoustic wave vector and $\vec{K}_i, \vec{K}_d$ are the incident and diffracted wave vectors

For collinear $\vec{K}_i$ and $\vec{k}_a$ (collinear acousto–optic interaction) the momentum matching (phase matching) condition becomes [2]

$$\lambda = \frac{v_a \Delta n}{f_a};\tag{2.3.2}$$

with λ the selected optical wavelength, v_a, f_a the acoustic velocity and respectively frequency, $\Delta n = |n_e - n_0|$ is the birefringence, n_0 and n_e are the refractive indices for the ordinarily and extraordinary polarized light.

The propagating acoustic wave generates a mobile phase grating in the volume of the crystal, which will diffract only a limited spectral band of the incident beam, that satisfies the phase-matching (momentum matching) condition (2.3.1). As diffraction occurs over an extended volume of the crystal, only a limited band of frequencies are affected, so AOTF performs more as a passband filter than as a diffraction grating. By changing the acoustic frequency it is thus possible to tune the passband of the filter over a wide spectral region. The selected wavelength is diffracted with maximum intensity in the first order beam (Bragg law). The resolving power of the spectral filter is given by [13]:

$$R = \frac{L\Delta n}{\lambda};\tag{2.3.3}$$

where L is the interaction length inside the crystal. For collinear AOTF the spectral resolution is maintained over a relatively large angular distribution of the incident light.

The periodicity and intensity of the refractive index modulation depends on the frequency and respectively on the amplitude (power) of the applied RF signal.

The time response of an AOTF is determined by the acoustic transit time across the optical beam, which is of the order of several µs [13].

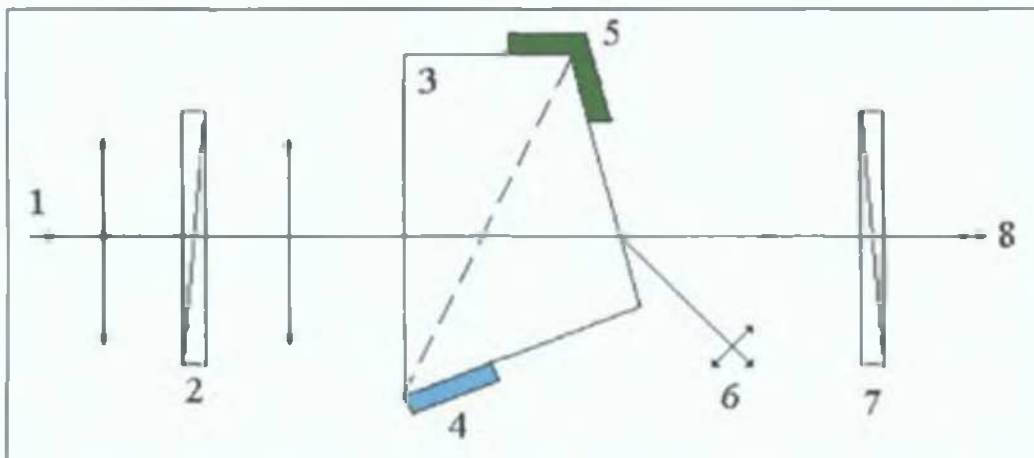

Fig.2.3.1. Schematics of the Acousto-optic system for quartz crystals: 1 - entrance non-polarized radiation; 2,7 - polarizers; 3 - anisotropic crystal; 4 - piezoelectric emitter of acoustic wave; 5 - absorber of acoustic wave; 6 – non-diffracted radiation with starting polarization; 8 - diffracted radiation polarized orthogonal to starting polarization.

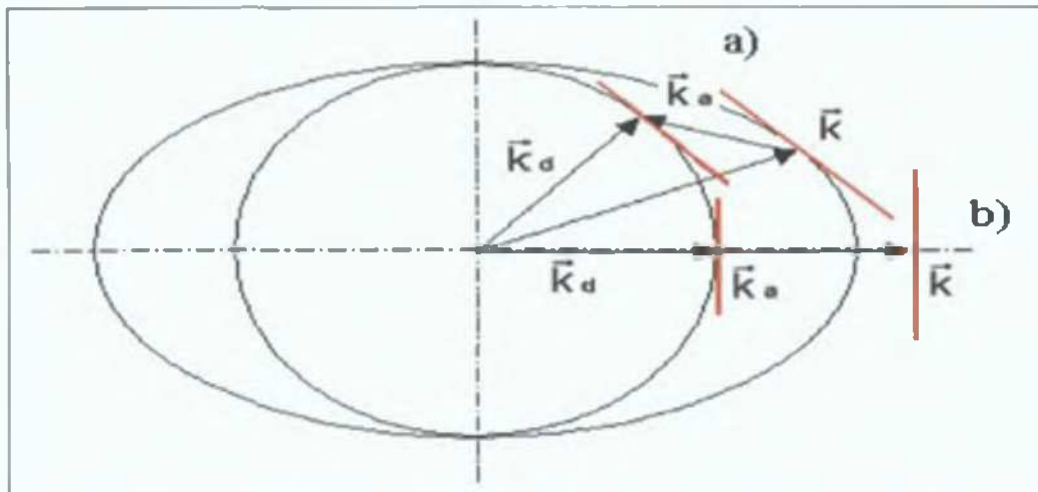

Fig.2.3.2. Vector diagram of the momentum match condition (2.3.1) for collinear and non-collinear acoustic and optical waves.

2.3.2. OPERATION MODES

a) The spectral scanning mode.

The spectrum of the optic signal can be scanned in the pre-defined range with data accumulation over a measuring time of 5,10,20,30,40,60 and 80 ms per spectral point depending on the settings.

b) Chronogram

Allows quasi-parallel observation of up to 20 wavelengths by fast switching between the wavelengths, with a wavelength access time of less than 1ms. The measurement per spectral point itself consists of signal and background integration time, leading to a total time resolution of 5ms.

c) Single Shot (Microchronogram)

The optical signal is sampled by a fast AD converter. The time resolution for this mode is 20ns. The measurement has to be triggered by an external trigger signal from the pulsed power supply.

2.3.3. PERFORMANCES

1. Wavelength range: 250-850nm;
2. The spectral resolution of a tunable filter is defined as the FWHM of the main peak of the selected optical output and is a function of both the wavelength and device configuration.

The AOS-4 resolution as given by the manufacturer is presented in Fig.2.3.3.

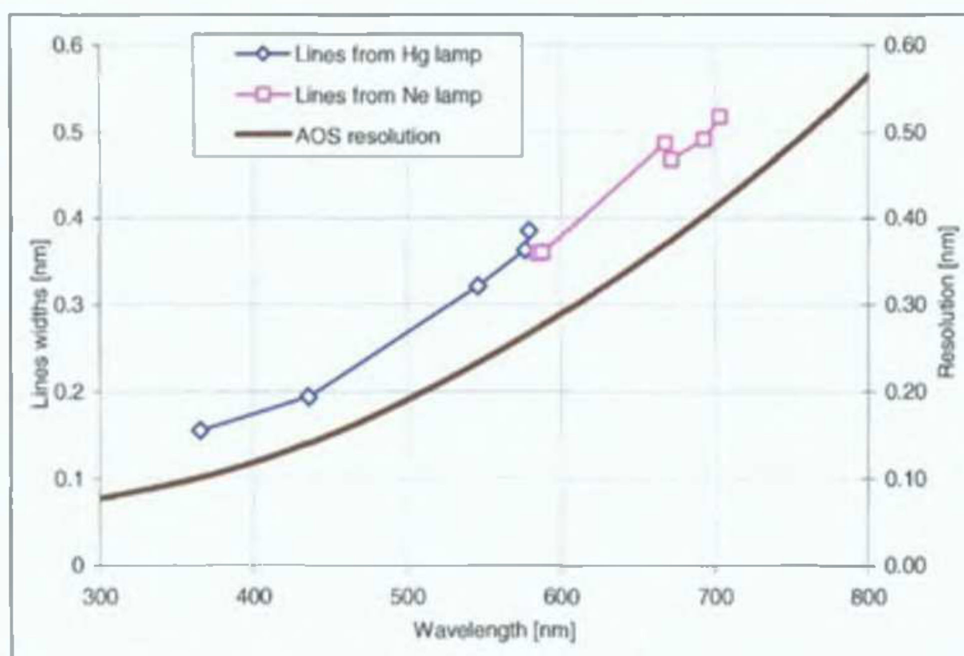

Fig.2.3.3. The passband and resolution for the AOS-4 .

3. Due to the combined filter action of the diffraction grating and the acousto-optic phase matching condition, the passband of the acousto-optic spectrometers - equivalent to the Instrumental Profile (IP) of conventional spectrometers -is very small. For quartz collinear AOS, the typical passband (bandwidth) is 1.5 Å. [13]. This is why, wavelength selection in AOS-4 can be made with a precision up to 0.1Å and the time-resolved measurements provide directly the intensity of the specified wavelength.

As the AOS-4 passband has not been defined by the manufacturer, it had to be determined using calibration lamps. The Ne and Hg (Phillips 93099) glow discharge calibration lamps have been used. These lamps have emission lines widths of the order of 0.01Å and are specifically designed for use in IP determination. The obtained IP, along with the AOS resolution are presented in Fig.2.3.3.

4. The Intensity Response IR of the AOS with wavelength is mainly determined by the acoustic power applied to the crystal, the crystal's optical transmission and the spectral response of the photomultiplier (PMT). The relative intensity of lines situated at close wavelengths is only affected by the spectral response of the PMT.

The accuracy in the determination of lines' intensities can be improved by performing a calibration of the intensity throughput of the system using a "blackbody" emission lamp. Nevertheless, the intensity response with wavelength is expected to be linear, mainly following the spectral response of the PMT and therefore, these corrections will not bring changes in the relative lines' intensities for lines situated at close wavelengths in the range 450-500nm.

2 3 4 FIBER OPTIC CABLES

The optical signal is fed to the optical port of the AOS-4 spectrometer through fiber optic cables with the following characteristics

- Cable A UVVIS,(200-850nm) fiber patchchord, 200μm aperture, 5m long, SMA 905 connectors, (953-579-T22T), manufacturer Thorlabs, USA,
- Cable B high powered UVVIS (200-900nm) fiber patchcord, 365/400μm aperture, 3mm OD jacketed, 5m long, SMA 905 connectors, (QMMJ-55-UVVIS-365/400) manufacturer OZ Optics Ltd Canada,
- Cable C high powered UVVIS (200-900nm) fiber patchcord, 365/400μm aperture, 3mm OD jacketed, 0 7m long, SMA 905 connectors, (QMMJ-55-UVVIS-365/400-3AS) manufacturer OZ Optics Ltd Canada

This is how they have been used during the experiments

- Cables A and B have a length of 5m, allowing the transport of the optical signal from the chamber port to the input of the spectrometer

- Cable A has been used only for readings with the probe in a fixed position, directly at the chamber's port

- Cables B and C (from the same manufacturer) have the same performances and have been used for space-resolved measurements that imply the use of two cables (inside and outside the chamber)

- Cable C has been used inside the discharge chamber and is provided with a metal outer jacket to prevent outgasing under vacuum

2.4 THE QUADRUPOLE MASS-ENERGY ANALYSER

An Electrostatic Quadrupole Plasma (EQP 300) mass-energy analyser provided by Hiden Analitical Ltd has been used for the measurements and analysis of Ion Energy Spectra at the substrate region in the opposed target magnetron discharge

A short description of the construction and operation of the HAL EQP analyser will be presented next, having as main reference the "EQP/EQS Analyser Manual" [14] provided by Hiden Analytical

The HAL EQP Analyser is a high-transmission 45° sector field ion energy analyser and quadrupole mass-spectrometer designed as a diagnostic tool for plasma or Secondary Ion Mass Spectrometer (SIMS) analysis Mass spectra of neutrals, ions and radicals, as well as energy spectra of ions in the energy range 0eV-100eV can be measured The standard system comprises a Plasma/SIMS Mass Spectrometer Interface Unit (MSIU), a Radio Frequency (RF) Head, and EQP probe installed within the vacuum system and the connection cables (Fig 2 4 1)

The EQP probe and analyser can be used to study plasma transients and afterglows and ion fluxes and the EQP probe has been used throughout all experiments described in this work

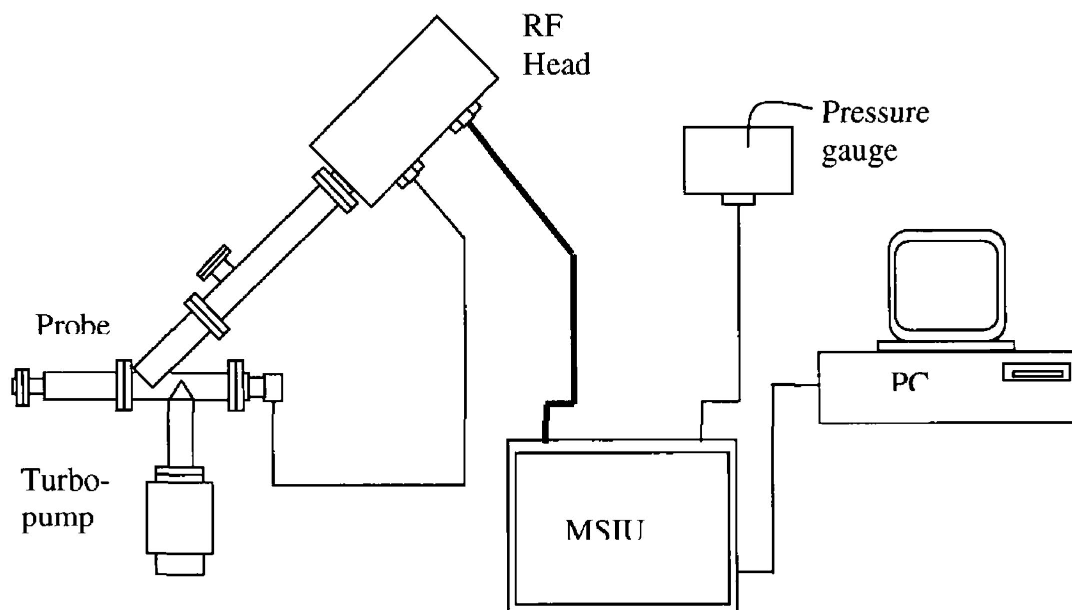

Fig 2 4 1 The standard HIDEN EQP 300 analyser system

The EQP probe is mounted in a compact differential pumping housing The EQP analyser is fitted with a twin filament electron-impact ion source for the analysis of neutral particles The RF Head contains signal-conditioning electronics and RF power supply for the quadrupole mass-filter and wiring to connect the MSIU generated signals and voltages to the probe

The instrument is operated via an IBM PC running the HAL MASsoft application under MS Windows The software (described in the HAL MASsoft User Manual) provides complete control over tuning the instrument, data acquisition, storage, recall and analysis

The EQP probe comprises the following items

- An Ion extraction system,
- A twin filament electron impact ion source for Residual Gas Analysis (RGA) of neutrals and radicals,
- A cover tube protects the ion extractor that is provided with a small sampling orifice (50μm diameter) connecting to the gas chamber for ion and gas inlet
- The EQP probe is pumped to operation pressures by its own turbo-molecular pump
- A 45° electrostatic field energy filter for energy analysis,
- A triple section quadrupole mass-filter for mass-to-charge ratio analysis,
- A detector an ion counting Secondary Electron Multiplier (SEM) which counts the number of ions striking it per second

The mass filter and detector are supported by a Conflat flange (DN-63-CF) located at the end of the energy filter

2 4 1 TUNING THE EQP ANALYSER

In order to perform the energy and mass analysis of ions, neutrals and radicals generated in the plasma, the EQP has a an array of about 20 electrostatic lenses (electrodes) that can be adjusted Both automatic and manual tuning can be performed For the measurements in the work further described, only the automatic tuning has been used The tuning is recommended in the following situations

-When the plasma energy has changed through changes in the gas pressure, power, etc

-Changing the mass of the neutral or ion to investigate,

-Changing the plasma gas,

-Changing the EQP orifice or detector,

-Changing the geometry of the system,

-If the Extractor, Lens 1 or ionisation source become coated,

-After the EQP probe cleaning

The automatic tuning is performed by running one of the tuning files provided for the application by the MASsoft software

-postune exp optimizes the ion extraction optics and sector field energy filter for positive ions,

-negtune exp optimizes the ion extraction optics and sector field energy filter for negative ions,

-rgatune exp optimizes the RGA operation using mass 18,

-master exp generates the Profile, Bar, MAP scans in the RGA mode

The RGA tuning is not necessary in most cases, the voltage settings being those from the factory

The tuning of the Secondary Ion Mass Spectrometer is necessary in order to adjust and optimize the analyser settings to the plasma energy, power, type of gas and its pressure, chamber's geometry, etc When setting – up the system, the critical values are the extraction electrodes, the energy and the mass More information on the structure and variables available to scan are presented in the MASsoft manual

The ion energy detected by the EQP probe is dictated by the electric field conditions inside the plasma at the probe region and the tuning process aim at adjusting the local plasma potential and the potential on the extractor lense, in order to provide a type of energy calibration for the system and accurately determine the actual ion energy More comments on the importance of the tuning for the EQP analyser will be discussed in Chapter (5 4) in connection to the space-resolved Ion Energy Spectra measured in the opposed target magnetron plasma

2.5. OVERALL VIEW OF THE EXPERIMENTAL SYSTEM

A drawing of the overall experimental system is presented in Fig. 2.5.4 and also several pictures of the magnetron (Fig. 2.5.1) the inside of the chamber (Fig.2.5.2) and the overall set-up picture (Fig.2.5.3).

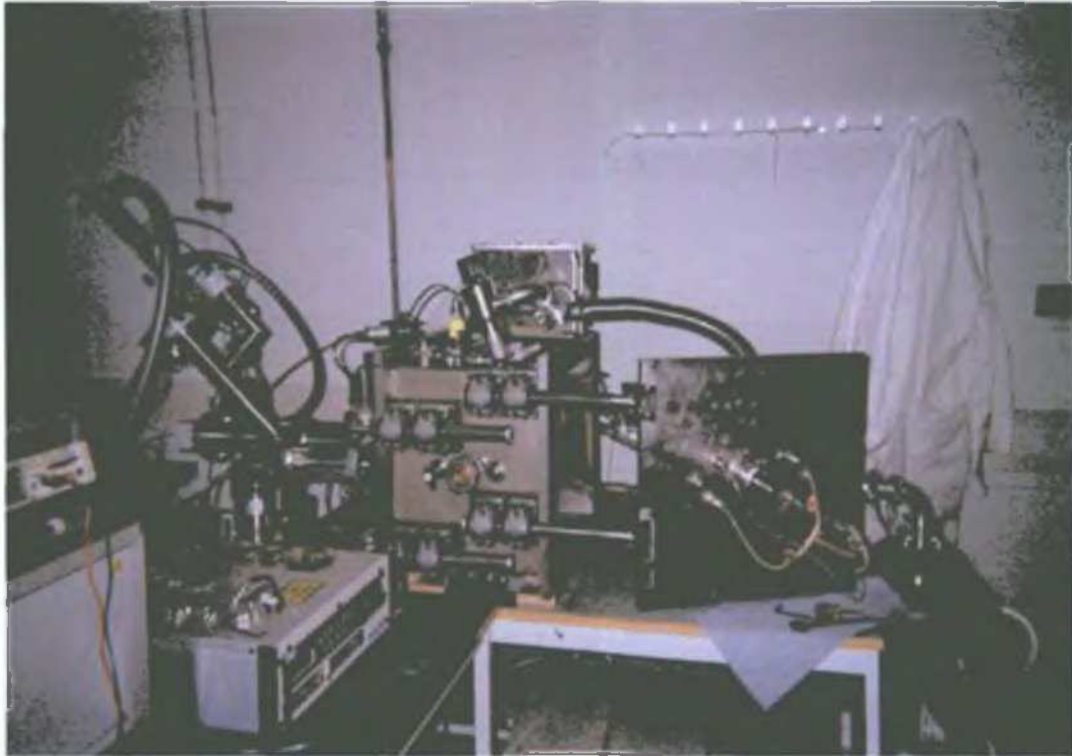

Fig.2.5.1. View of the magnetron.

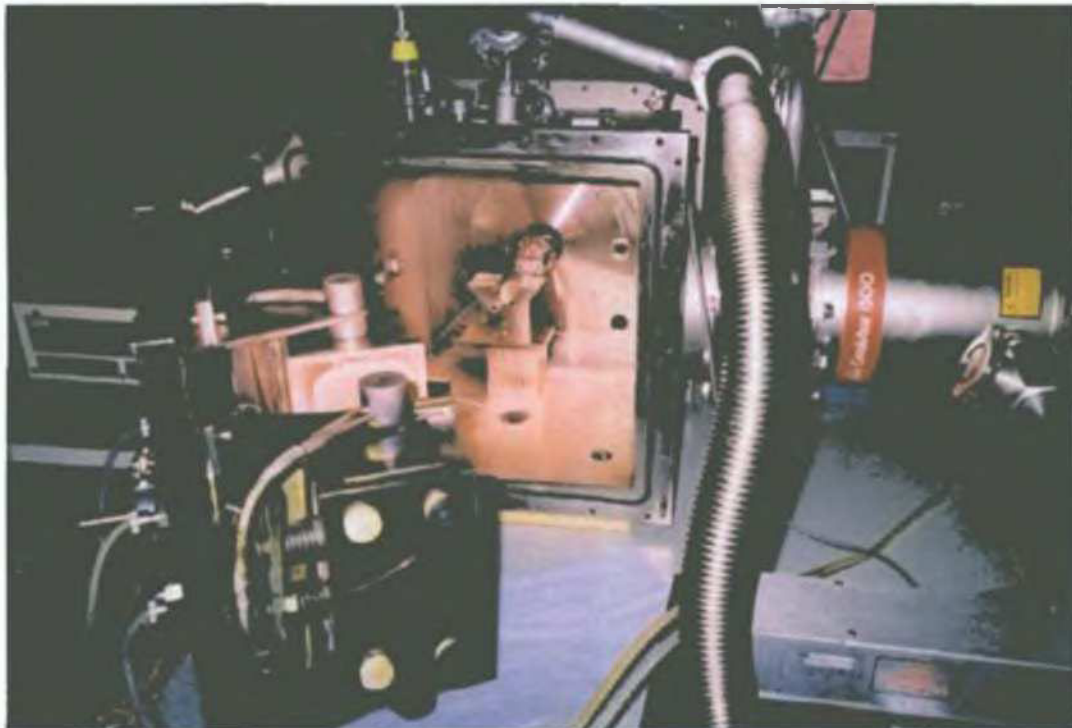

Fig.2.5.2. View inside the magnetron chamber.

Fig. 2.5.3. Overall view of the experimental set-up.

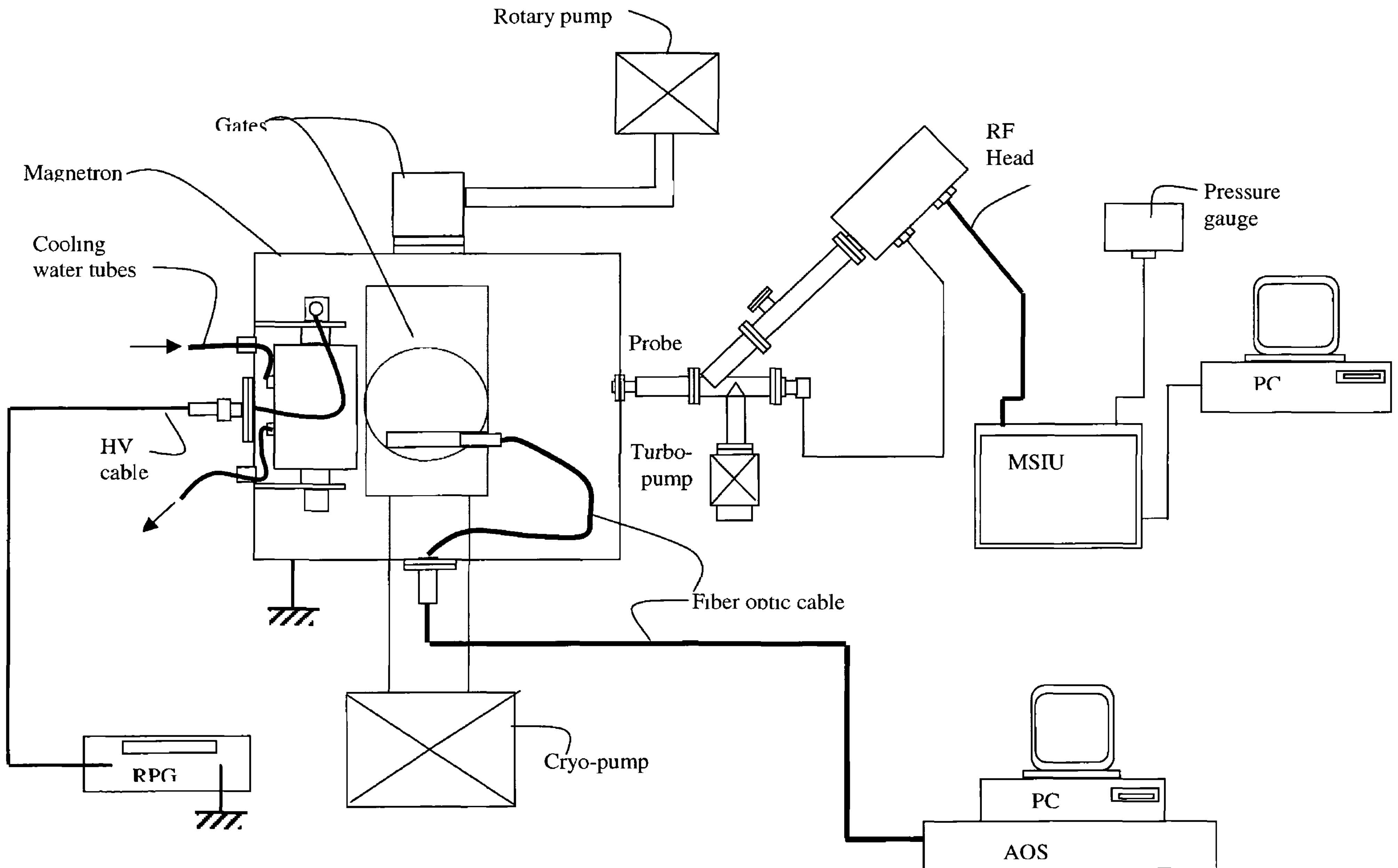

Fig 2 5 4 Overall schematic of the magnetron and experimental set-up

CHAPTER 3

NUMERICAL METHODS

Thıs chapter presents the numencal algonthms developed for the calculatıon of

-the magnetıc field,

-the 3D ıon trajectorıes ın electrıc and magnetıc fields,

-the Monte Carlo sımulatıon of ıon transport durıng pulsed DC sputterıng

The theoretıcal background, results, conclusıons and examples are provıded

3.1: CALCULATION OF THE MAGNETIC FIELD

3.1.1 THE CURRENT SHEET METHOD

The magnetic field produced by a magnetic dipole is equivalent to the magnetic field produced in the cross-section of two parallel wires with opposed current density [15], while for a 3D magnet, the magnetic field is equivalent to that produced by two parallel current sheets of equal current density and opposed direction (Fig.3.1.1).

The magnetic field can be calculated [15] starting from the magnetic vector potential $\vec{A}$ generated by a linear current density, deduced from the Ampere's Law:

$$\vec{A}(\vec{r}) = \int \frac{\mu \vec{I}(\vec{r})dl'}{4\pi |\vec{r} - \vec{r}'|}; \qquad (3.1.1)$$

If the current $I(\vec{r})$ is in fact a current density per unit area in a volume V, the magnetic vector potential $\vec{A}(\vec{r})$ becomes:

$$\vec{A}(\vec{r}) = \int_V \frac{\mu \vec{I}(\vec{r})dV}{4\pi |\vec{r} - \vec{r}'|}; \qquad (3.1.2)$$

which for a 3D rectangular distribution (Fig.3.1.1) can be written as:

$$\vec{A}(\vec{r}) = \int_0^h \int_0^w \int_0^L \frac{\mu \vec{I}(\vec{r})dzdxdy}{4\pi |\vec{r} - \vec{r}'|}; \qquad (3.1.3)$$

and

$$\vec{B}(\vec{r}) = \nabla \times \vec{A}(\vec{r}); \qquad (3.1.4)$$

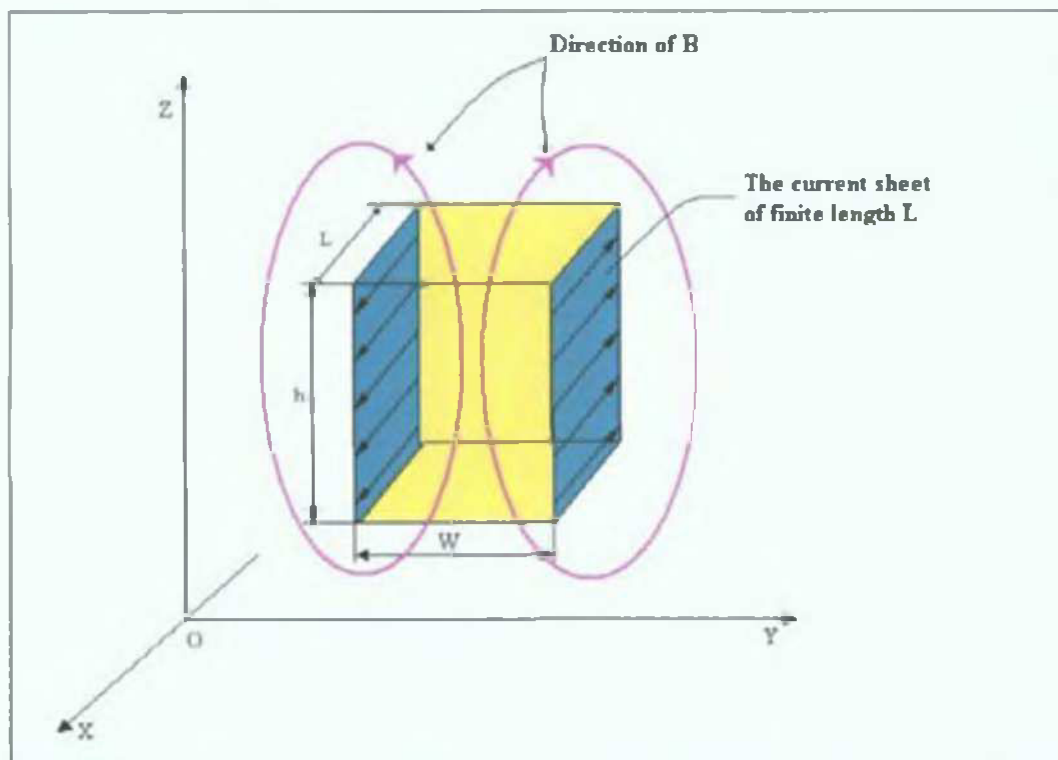

Fig.3.1.1: The current sheets producing a magnetic field equivalent to a rectangular magnet.

To evaluate the magnetic in the XOZ cross-section of a long magnetron, only the field given by 2D rectangular magnets has to be found, while $\vec{A} = (0, A_y, 0)$ Considering only 2D rectangular magnets the integral over W is no longer necessary

To evaluate the integral over L, the magnetic vector potential A_y can be derived [15] as the magnetic vector potential given by two current wires of length L situated at the distance W from each other in the plane XOZ

$$A_y = \frac{2\mu}{4\pi}\left[\int_0^L \frac{Idy'}{\sqrt{(x-x_1)^2+(y'-y_1)^2+(z-z_1)^2}} - \int_0^L \frac{Idy''}{\sqrt{(x-x_2)^2+(y''-y_2)^2+(z-z_2)^2}}\right], \quad (3\ 1\ 5)$$

where x_1, x_2, y_1, y_2, and z_1, z_2 are the coordinates of the wires in a 3D geometry, $W = \sqrt{(x_1 - x_2)^2 + (y_1 - y_2)^2 + (z_1 - z_2)^2}$ is the distance between the wires and I is the current density

The evaluation of the integrals leads to

$$A_y = \frac{I\mu}{2\pi}\{\ln[y'+\sqrt{(x-x_1)^2+(y'-y_1)^2+(z-z_1)^2}] - \ln[y''+\sqrt{(x-x_2)^2+(y''-y_2)^2+(z-z_2)^2}]\}_0^L, \quad (3\ 1\ 6)$$

For a long magnetron, the contribution to A_y given by each current element along the length of the wire L can be then evaluated allowing L to approach infinity, leading to

$$A_y = \frac{I\mu}{4\pi}\ln\left[\frac{(x-x_2)^2+(z-z_2)^2}{(x-x_1)^2+(z-z_1)^2}\right] \quad (3\ 1\ 7)$$

Finally, the magnetic vector potential produced by a 2D rectangular magnetic layer (of dimensions W x h) can be derived by integrating the expression of the magnetic vector potential (3 1 7) over the height h of the current sheets (situated at the distance W from each other)

$$A_y = \int_0^h \frac{I\mu}{4\pi}\ln\left[\frac{(x-x_2)^2+(z-z_2)^2}{(x-x_1)^2+(z-z_1)^2}\right]dh, \quad (3\ 1\ 8)$$

The magnetic flux density components Bx and Bz can be derived from Eq 3 1 4 giving

$$B_X = -\frac{\partial A_y}{\partial z} = \int_0^h \frac{\mu I}{2\pi}\left[\frac{z-z_1}{(x-x_1)^2+(z-z_1)^2} - \frac{z-z_2}{(x-x_2)^2+(z-z_2)^2}\right]dh, \quad (3\ 1\ 9)$$

$$B_Z = \frac{\partial A_y}{\partial x} = \int_0^h \frac{\mu I}{2\pi}\left[\frac{x-x_2}{(x-x_2)^2+(z-z_2)^2} - \frac{x-x_1}{(x-x_1)^2+(z-z_1)^2}\right]dh, \quad (3\ 1\ 10)$$

The current sheet with a normal $\vec{n}$ to the surface and a current intensity I are related to the magnetization Br of the magnetic material through the relation

$$\vec{I} = \frac{1}{\mu_0}\vec{B}_r \times \vec{n}, \quad (3\ 1\ 11)$$

Considering a large magnet being composed of smaller magnets forming an array of $m \times n$ magnet elements, the field generated by the large magnet is a summation of the fields generated by each element in the array

$$B_X = \sum_{1}^{m\times n} \int_{0}^{h} \frac{\mu I}{2\pi}\left[\frac{z-z_1}{(x-x_1)^2+(z-z_1)^2} - \frac{z-z_2}{(x-x_2)^2+(z-z_2)^2}\right]dh, \qquad (3\ 1\ 12)$$

$$B_Z = \sum_{1}^{m\times n} \int_{0}^{h} \frac{\mu I}{2\pi}\left[\frac{x-x_2}{(x-x_2)^2+(z-z_2)^2} - \frac{x-x_1}{(x-x_1)^2+(z-z_1)^2}\right]dh, \qquad (3\ 1\ 13)$$

where x and z are the coordinates in the plane XOZ of the point where the field components are calculated and x_1, x_2 and z_1, z_2 are the coordinates of the magnet elements forming the array

In the case of the opposed target magnetron the two magnet arrays are identical and with opposed polarities having the same direction of the individual components of the magnetic field (B1x, B2x and respectively B1z, B2z) and the total components of magnetic field Bx and Bz in the region between the targets are given by

Bx=B1x + B2x,

Bz=B1z + B2z, (3 1 14)

where B1x, B1z are the components of the magnetic field produced by one magnet and B2x, B2z are the magnetic field components produced by the second (opposed magnet) The above formulas apply when the targets are made of a non-ferromagnetic material

When using Fe targets, the magnetic field components parallel to the targets are absorbed by the ferromagnetic material of the target due to the discontinuity in this component at the boundary between two materials with different magnetic permeability [10]

$$\vec{B}\times\vec{n} = \frac{\mu}{\mu_0}\vec{B}_0\times\vec{n}, \qquad (3\ 1\ 15)$$

where $\vec{n}$ is the normal to the boundary (the target surface), μ_0, $\vec{B}_0$ are the permeability and field values in air, while μ, $\vec{B}$ are the values in the ferromagnetic material As the permeability of iron is at least 100 times higher than that of air, the tangential component of the magnetic field can be approximated as

Bx=(B1x + B2x)/100, while the normal component Bz, stays the same

Bz=B1z + B2z, (3 1 16)

Calculations of the magnetic flux density B distribution in the space region between the targets are presented next, for both non-ferromagnetic (Cu) and ferromagnetic (Fe) targets

The above formulas (3 1 14 and 3 1 16) were used to calculate the magnetic field distribution produced by the magnetic poles in the opposed target magnetron

3 1 2 THE C PROGRAM STRUCTURE

Based on the above considerations I have written a computer program in the C language to calculate the magnetic field in the XOZ cross-section of the magnetron A diagram of the program is shown in Fig 3 1 2

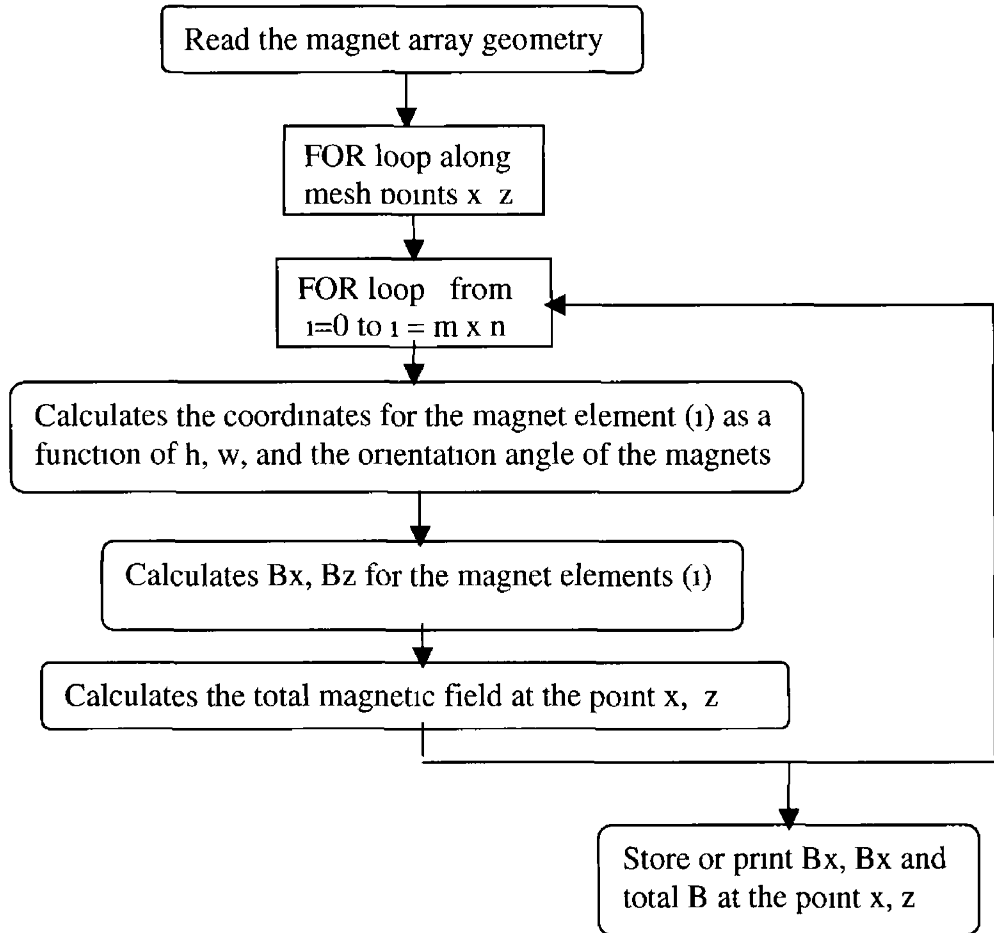

Fig 3 1 2 Diagram of the algorithm for the calculation of the magnetic field

3 1 3 THE MAGNETIC POLE CONFIGURATION

The configuration of the magnetic poles has been chosen in such a way that the magnetic field flux density is uniform in front of each target The structure of the chosen geometry for the magnetic pole is shown in Fig 3 1 3

Due to the necessity to pass the cooling water tubes for the targets situated in front of the magnetic poles (on top of the structure presented in Fig 3 1 3), the magnetic pole has a complex structure with gaps It is mainly composed out of 2 blocks separated on the OY axis by a 30mm gap The blue colour represents the magnet material and the yellow colour the plastic material used to separate the magnets and form a gap The space between the 2 blocks is empty (to allow the passage of cooling water tubes) the separation being provided by the outer casing of the magnetic pole

Due to the large gaps in the structure of the magnetic pole, the magnetic field is not constant in different cross-sections along the OY axis. In order to avoid the magnetic field non-uniformities along the OY axis, for all the experiments, the XOZ cross-section considered for observing different plasma parameters, especially for the optical emission observations is considered at 30mm from the edge of the magnetic pole, where the magnetic field distribution along OY is not perturbed.

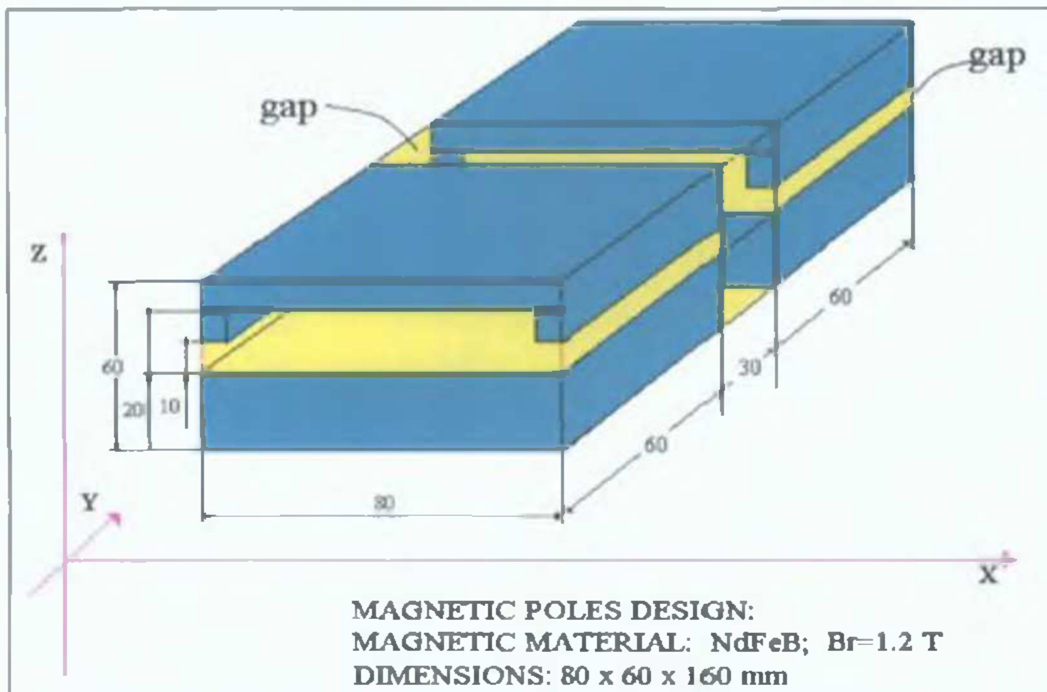

Fig.3.1.3: 3D view of one magnet pole in the opposed target magnetron.

Each magnetic pole (Fig. 3.1.3) is provided with gaps (yellow) in the XOZ and XOY cross-sections to allow the passage of cooling water tubes. The opposed pole has a symmetrical structure, with opposed polarity of the magnetic field.

For the purpose of calculation, the magnetic regions are divided into an array of magnets, with elements having the following dimensions: h=5mm, w=10mm, l=30mm. The resulting magnet array in the XOZ cross-section can be seen in Fig.3.1.4.

3.1.4 THE MAGNETIC FIELD DISTRIBUTION

The magnetic flux density B distribution for the opposed target magnetron with Cu targets is shown in Fig.3.1.4, Fig.3.1.5, Fig.3.1.6, Fig.3.1.7 and Fig.3.1.8. The image in Fig.3.1.4 has been obtained with a Matlab code for calculating magnetic fields provided by Prof. D.C. Cameron.

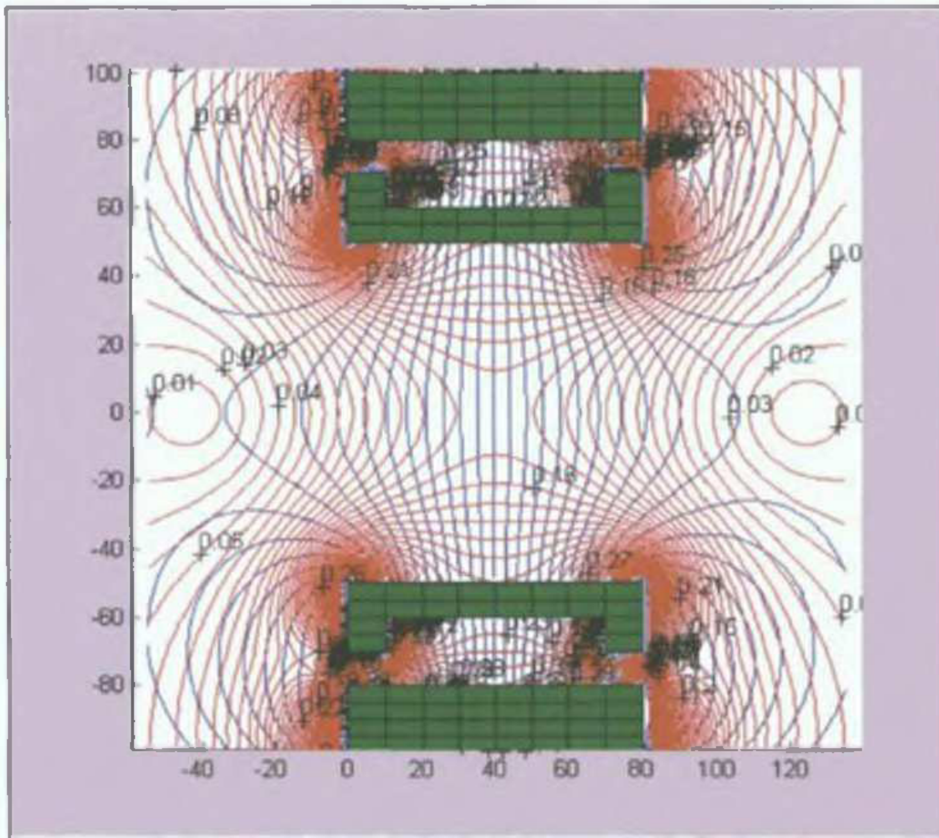

Fig.3.1.4: The magnetic flux density B[T] distribution in the plane XOZ with the actual magnet arrays. The blue lines represent the magnetic vector potential while the red lines represent the magnetic flux density.

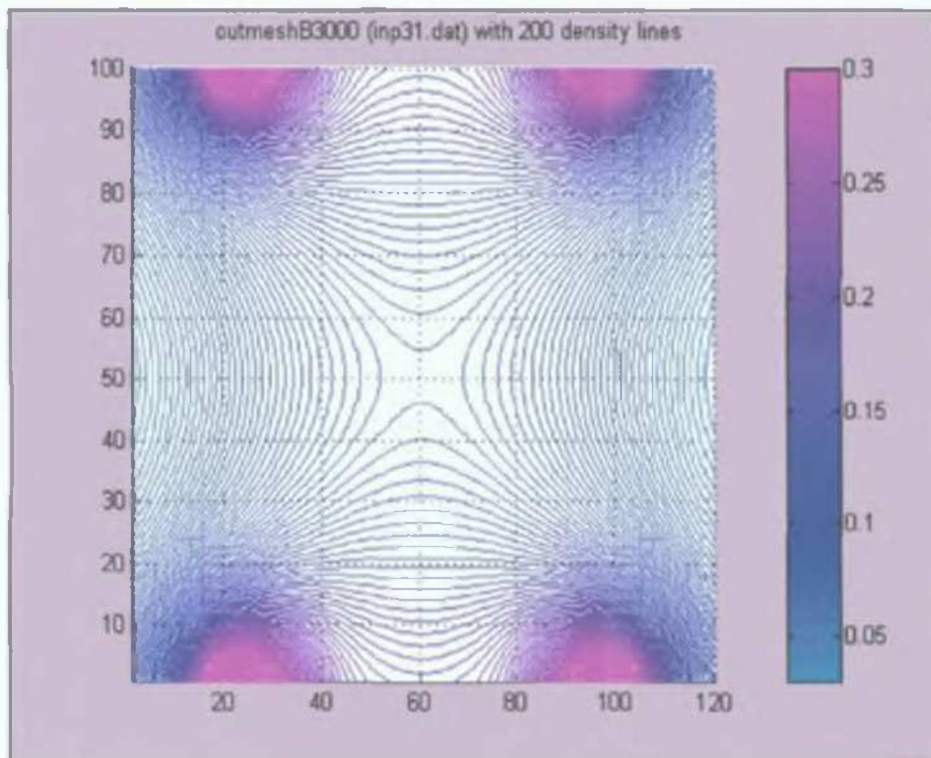

Fig.3.1.5: The magnetic field flux density B[T] distribution for the opposed target magnetron in the plane XOZ. The targets are situated at top and bottom edges of the figure.

In Fig.3.1.4 and Fig.3.1.5, the B field contour lines are parallel to the Ox axis near the target, indicating a constant magnetic flux density in these regions. This is a result of a special design of the magnet array. The magnet arrays are situated at the top and bottom of the figure.

The image in Fig.3.1.5 and the following have been obtained using the C code described in the previous section and a Matlab viewer.

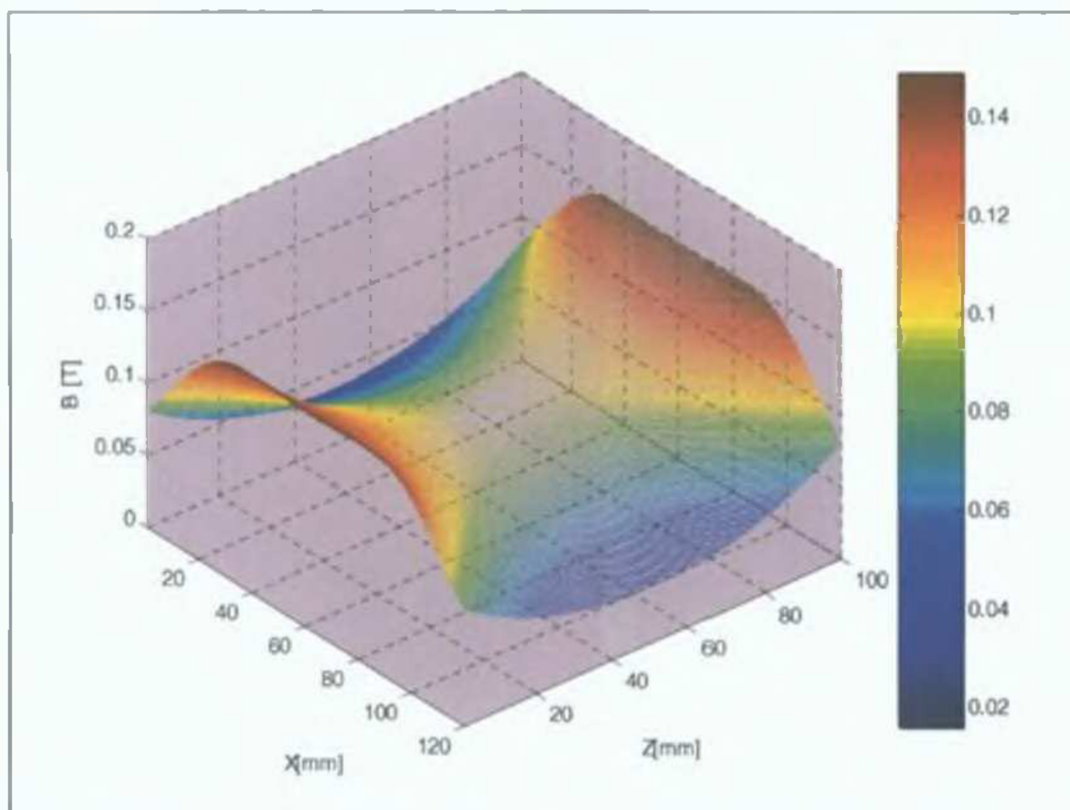

Fig.3.1.6: 3D view of the magnetic flux density B contour lines in the region between the targets, for the configuration with Cu targets.

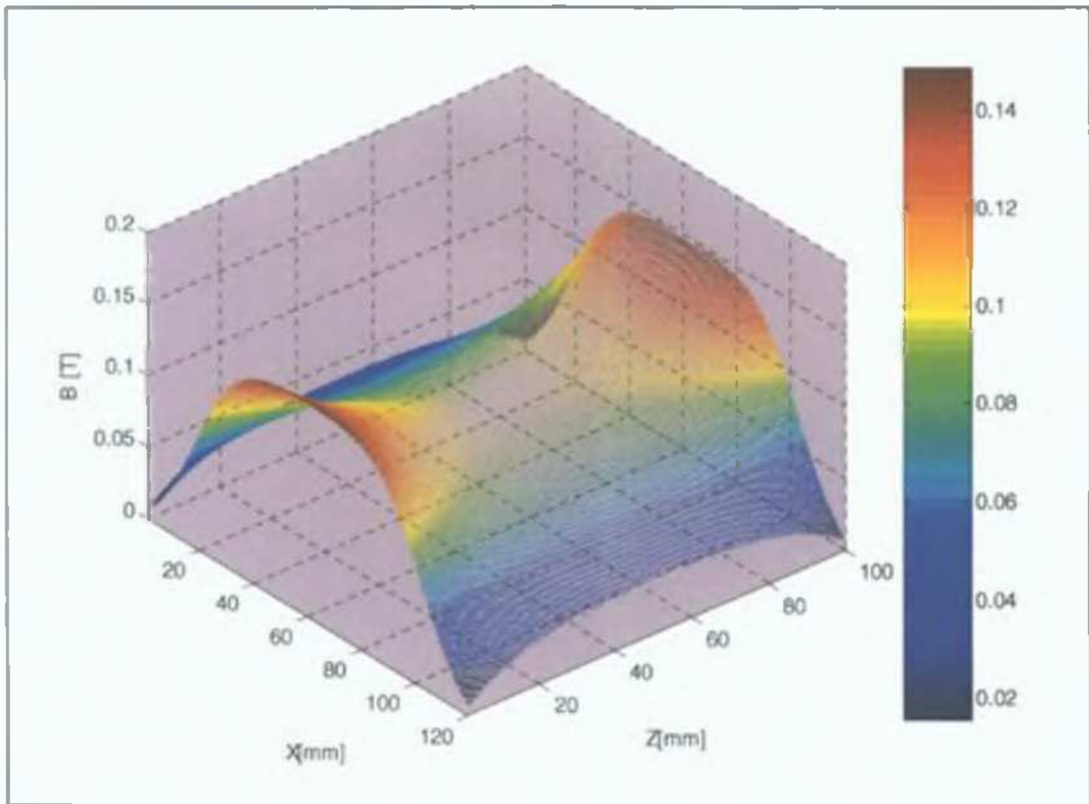

Fig.3.1.7: 3D view of the magnetic flux density B contour lines in the region between the targets, for the configuration with Fe targets.

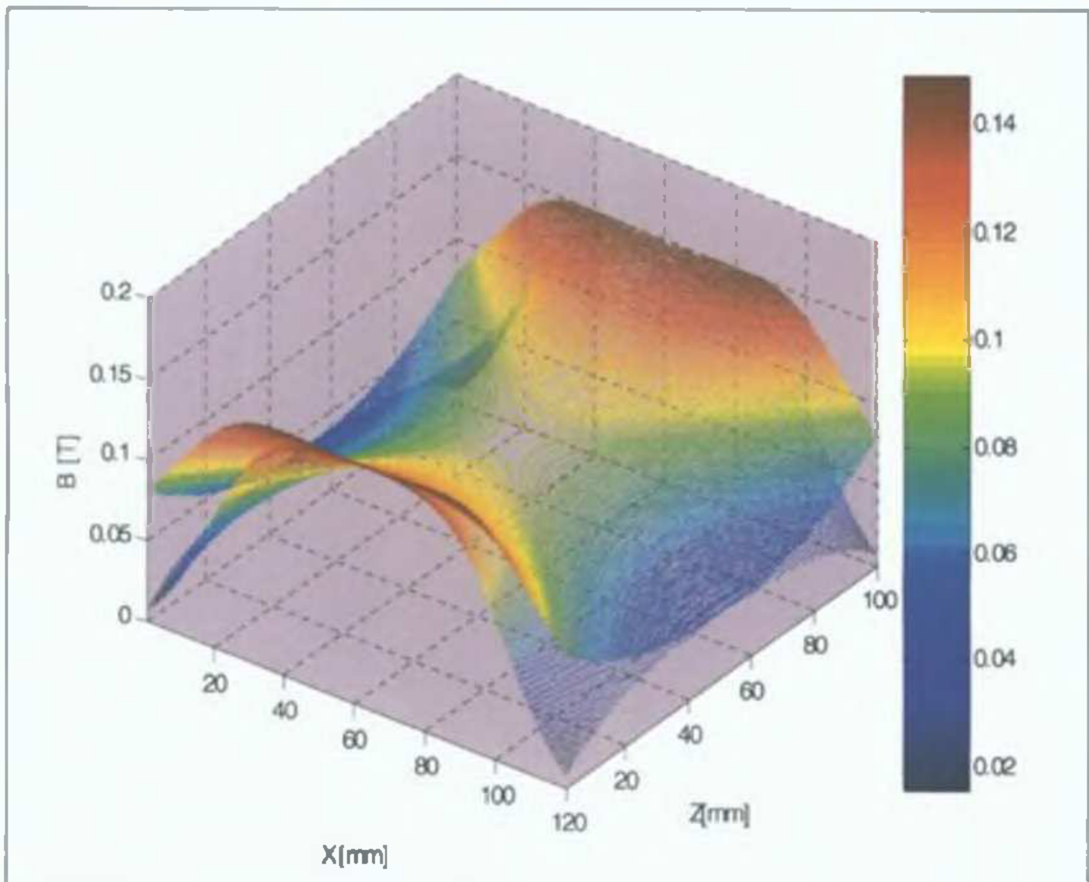

Fig.3.1.8: 3D comparative view of the magnetic flux density B contour lines for the two configurations (Cu targets, respectively Fe targets). The configuration with Cu targets has higher values. Z[mm] is the distance between the targets.

3 1 5 DISCUSSION AND CONCLUSIONS

In this chapter, the structure of the magnetic poles has been presented along with the algorithm for calculating the distribution of the magnetic flux density based on a calculation of the magnetic vector potential generated by the equivalent current densities of the magnetic regions

I have written the computer program in C language that allows the calculation of the magnetic field flux density for any cross-section in a complex magnet structure according the presented algorithm The magnetic field can be calculated for any 2D array composed of magnet elements of different intensities and gaps of various sizes situated at different locations

The original side of this program is the calculation of the magnet elements coordinates that allow reading complex magnet array geometries including gaps

The program will be used to calculate the magnetic field mesh or values at each point for use in calculating the charged particle trajectory for Monte Carlo simulations as presented in the next section The advantage in using the C language to calculate the magnetic field is that the code can perform the calculations much faster than using the Matlab routine, allowing its use during a computer simulation of particles trajectories in magnetic and electric fields

The calculated distribution of the magnetic flux density has been presented as 2D and 3D images for the configuration with Cu and with Fe targets

In the case of Fe targets, the magnetic field is strongly affected by the presence of the ferromagnetic material, leading to a less uniform field in front of the targets, the magnetic flux density being concentrated in the centre of the target cross-section

3 2 3D CHARGED PARTICLES TRAJECTORIES IN TIME-DEPENDENT ELECTRIC AND MAGNETIC FIELDS

3 2 1 INTRODUCTION

In general, the dynamics of magnetized plasmas can be described by solving the equation of motion for each individual particle The electric and magnetic fields generated by the particles distribution and movement have to be included in each equation, along with the external electric and magnetic fields This leads to an ensemble of coupled equations that have to be solved simultaneously leading to a solution that is difficult to obtain and has little information about the collective behaviour of the plasma particles

Therefore, there are several types of approximations that lead to different approaches in studying the behaviour and properties of magnetized plasmas

1 The single particle motion description it describes the motion of a particle under the influence of external electric and magnetic fields, neglecting the collective behaviour of the plasma This approach is useful for studying low-density plasmas and can be used for Monte Carlo simulations of particle transport in magnetized plasmas To ensure a good statistics, a large number of particles trajectories should be studied, along with their interactions history Typical results can provide information on time and space-dependent particles' energy and density, number of interactions and density of ionised and exited atoms, particles' transit times, etc

2 The magnetohydrodynamic approach treats plasma as a conducting fluid immersed in a magnetic field, able to maintain local equilibria This fluid is described by macroscopic variables average density, velocity, temperature This approach is useful when studying low frequency wave phenomena

3 The multi-fluid approach applies the magnetohydrodynamic theory to different particle species electrons, protons, heavier ions, assuming that each species behaves like a separate fluid This approach accounts for charge separation fields and can be used for studying high-frequency wave propagation in the plasma

4 The kinetic theory is the most advanced plasma theory, adopting a statistical approach Instead of solving the equation of motion for each individual particle, it observes the evolution of the distribution function of the system of particles under different conditions and simplifying assumptions

The single particle motion description will be developed in the following chapters

3 2 2 SINGLE PARTICLE MOTION

In a situation where the charged particles do not interact directly with each other and their movement is not coupled to influence the total magnetic field significantly, the motion of each particle can be treated independently This approach is valid only for very rarefied plasmas

where collective effects are negligible and the magnetic field produced by the current generated by the charged particle's motion is much smaller than the external magnetic field

The single particle motion in magnetized plasmas can be applied only for collisionless (ν<<Ω) magnetized plasmas, where the gyroradius r is much smaller than the typical variation length-scale of the external E and B fields, and the gyroperiod Ω^{-1} is much less than the typical time scale τ on which these fields can change This type of collisionless, magnetized plasmas are encountered in magnetic fusion and space plasma physics as well as in certain types of magnetrons, where the above conditions apply

3 2 3 MOTION IN UNIFORM FIELDS

The motion of charged particles in electromagnetic fields is often treated as a set of two separate motions parallel and perpendicular to the magnetic field direction each of them including several types of drifts

In the following presentation, to keep all equations and variables consistent with each other and make them suitable for numerical computation in the frame of a C language program, this separation will be applied, but the governing equation for the total particle velocity will contain all possible motions, being derived from the second law of dynamics

The equation of motion of a charged particle in a constant, static, electric and magnetic fields is described by the following equation of motion

$$m\frac{d\vec{v}}{dt}=e(\vec{E}+\vec{v}\times\vec{B}) \qquad (3\ 2\ 1)$$

The change in the total velocity d$\vec{V}$ for each time interval dt can be written as

$$d\vec{V}=q(\vec{E}+\vec{v}\times\vec{B})dt=q[(\vec{E}_p+\vec{E}_n)+(\vec{v}_p+\vec{v}_n)\times\vec{B}\ ]dt \qquad (3\ 2\ 2)$$

where the indexes p and n indicate the components of the electric field $\vec{E}$ or total velocity $\vec{V}$ parallel, respectively normal to the direction of the magnetic field $\vec{B}$ and $q=e/m$ is the specific charge of the particle

The particles' velocity can be decomposed into two components, parallel and normal to the direction of the magnetic field $\vec{B}$

$$d\vec{v}_p=q[\vec{E}_p+\vec{v}_p\times\vec{B}\ ]dt=q\vec{E}_p dt \qquad (3\ 2\ 3)$$

$$d\vec{v}_n=q[\vec{E}_n+\vec{v}_n\times\vec{B}]dt \qquad (3\ 2\ 4)$$

Taking into account the initial velocities, the total velocity of a charged particle after each time interval dt is

$$\vec{v}=\vec{v}_p+q\vec{E}_p dt+\vec{v}_n+q[\vec{E}_n+\vec{v}_n\times\vec{B}\ ]dt \quad \text{, or}$$

$$\vec{v}=\vec{v}_0+q\vec{E}_p dt+q\left[\vec{E}_n+\vec{v}_n\times\vec{B}\right]dt\ , \qquad (3\ 2\ 5)$$

where $\vec{v}_0 = \vec{v}_p + \vec{v}_n$ represents the initial total velocity at the moment $t=t_0$ and $\vec{v}$ is the total velocity at the moment $t=t_0+dt$ The equation indicates that the particle has a translation motion along the $\vec{B}$ field combined with a circular motion in a plane normal to $\vec{B}$

The circular motion is sustained by the Lorentz force $F_{\perp} = q(\vec{v}x\vec{B})dt$ and the force $\vec{F}_N$ given by $\vec{E}_n$, the electric field component normal to the magnetic field $\vec{B}$ As at every moment *dt*, the force $\vec{F}_N$ can provide a mechanical work and increase the particle's energy only along the direction of $\vec{v}_n$ which changes in *dt* by an angle α_i, the actual $\vec{F}_N$ is

$$\vec{F}_N = q\,\vec{E}_n \cos(\alpha_i) \quad (3\ 2\ 6)$$

So the general equation for the total velocity vector evolution in time is

$$\vec{v} = \vec{v}_p + q\,\vec{E}_p \mathrm{d}t + \vec{v}_n + q\,\vec{E}_n dt\, cos(\alpha_i) + q(\,\vec{v}_n \mathrm{x}\ \vec{B}\,)dt, \text{ or} \quad (3\ 2\ 7)$$

$$\vec{v} = \vec{v}_0 + q\,\vec{E}_p \mathrm{d}t + q\,\vec{E}_n dt\, cos(\alpha_i) + q(\,\vec{v}_n \mathrm{x}\ \vec{B}\,)dt, \quad (3\ 2\ 8)$$

The parallel and normal components of the velocity and the electric field can be expressed as a function of the magnetic field direction and magnitude by using the scalar and vector product

$$\vec{v}_p = \frac{\vec{v}\ \vec{B}}{B}, \quad \vec{v}_n = \vec{B}\times(\vec{v}\times\vec{B})/B^2, \quad (3\ 2\ 9)$$

$$\vec{E}_p = \frac{\vec{E}\ \vec{B}}{B}, \quad \vec{E}_n = \vec{B}\times(\vec{E}\times\vec{B})/B^2, \quad (3\ 2\ 10)$$

The gyrofrequency of the rotation around the gyrocentre is $\Omega=q$B and the gyroradius is defined by

$$r = \frac{v_n}{qB}, \quad (3\ 2\ 11)$$

where $v_n = |\,\vec{v}_n\,|$ is the magnitude of the vector $\vec{v}_n$

The sense of a particle's gyromotion relative to the magnetic field direction depends on the particle's charge, positive charges gyrating in a clockwise sense and negative charges like electrons gyrating in an anti-clockwise sense Considering the current and magnetic field associated with charged particles moving about the external magnetic field, it can be proven that these fields are anti-parallel to the external (background) field, in a plasma the particles having a diamagnetic behaviour [16]

As the particle's motion can be described at any moment as a superposition of a translation of the gyrocentre and a rotation around the gyrocentre, the particle's coordinates at any time *t* can be described as

$$\vec{R} = \vec{R}_0 + \vec{R}_T + \vec{R}_R, \quad (3\ 2\ 12)$$

where $\vec{R}_T$ is the coordinate vector indicating the coordinate changes due to the translation motion and $\vec{R}_R$ is the coordinate vector indicating the coordinate changes due to the rotation, while $\vec{R}_0$ gives the initial coordinates of the particle at time t_0

The $\vec{R}_R$ coordinates can be calculated by performing a 3D rotation of the initial $\vec{R}_R$ coordinates around the vector $\vec{B}=$ (Bx, By, Bz), taking into account its director angles α_x=atan(By/Bx), α_y=atan(Bx/Bz) and α_z=atan(By/Bx)

The 3D rotation can be described as three rotations, each about one coordinate axis, by an angle α_x, α_y and α_z respectively The coordinates after the 3D rotation can be written as a function of the initial coordinates $[X^0_R, Y^0_R, Z^0_R]$ and the displacements dx, dy, dz in the rotated coordinate system

$$[X_R - X^0_R,\ Y_R - Y^0_R,\ Z_R - Z^0_R] = [dx, dy, dz]\ R(z)\ R(y)\ R(x), \qquad (3\ 2\ 13)$$

where the rotation matrixes R(z), R(y) and R(x) are

$$R(x)=\begin{pmatrix}1 & 0 & 0\\ 0 & \cos a_x & -\sin a_x\\ 0 & \sin a_x & \cos a_x\end{pmatrix}, R(y)=\begin{pmatrix}\cos a_y & 0 & \sin a_y\\ 0 & 1 & 0\\ -\sin a_y & 0 & \cos a_y\end{pmatrix}, R(z)=\begin{pmatrix}\cos a_z & -\sin a_z & 0\\ \sin a_z & \cos a_z & 0\\ 0 & 0 & 1\end{pmatrix}$$

(3 2 14)

Taking into account that in the initial coordinate system (where the gyration takes place) with α_i the gyration angle at the moment t and α_{i0} the gyration angle at the moment t_0 and R the gyroradius, dx=R($\sin\alpha_i$-$\sin\alpha_{i0}$), dy= R($\cos\alpha_i$ –$\cos\alpha_{i0}$) and dz=0, the new rotation coordinates can be written as

$X_R-X^0_R = dx\,(\cos\alpha_y\cos\alpha_z) + dy(\cos\alpha_y\sin\alpha_z) - dz(\sin\alpha_y)$

$Y_R-Y^0_R = dx(-\sin\alpha_z\cos\alpha_x+\sin\alpha_y\cos\alpha_z\sin\alpha_x)+ dy(\cos\alpha_x\cos\alpha_z+\sin\alpha_x\sin\alpha_y\sin\alpha_z)+ dz(\sin\alpha_x\cos\alpha_y)$,

$Z_R-Z^0_R=dx(\sin\alpha_x\sin\alpha_z+ \cos\alpha_z\sin\alpha_y\cos\alpha_x) +dy(-\sin\alpha_x\cos\alpha_z + \cos\alpha x\sin\alpha_y\sin\alpha_z)+dz(\cos\alpha_x\cos\alpha_y)$,

(3 2 15)

and finally as

$X_R = X^0_R + R(\sin\alpha_i-\sin\alpha_{i0})(\cos\alpha_y\cos\alpha_z) + dy(\cos\alpha_y\sin\alpha_z)$

$Y_R =Y^0_R+ R(\sin\alpha_i-\sin\alpha_{i0})(-\sin\alpha_z\cos\alpha_x+\sin\alpha_y\cos\alpha_z\sin\alpha_x)+R(\cos\alpha_i-\cos\alpha_{i0})(\cos\alpha_x\cos\alpha_z +$
$\sin\alpha_x\sin\alpha_y\sin\alpha_z)$,

$Z_R=Z^0_R+R(\sin\alpha_i-\sin\alpha_{i0})(\sin\alpha_x\sin\alpha_z+\cos\alpha_z\sin\alpha_y\cos\alpha_x)+R(\cos\alpha_i-\cos\alpha_{i0})(-$
$\sin\alpha_x\cos\alpha_z+\cos\alpha x\sin\alpha_y\sin\alpha_z)$,

(3 2 16)

For a 2D magnetostatic field where By=0, leading to α_x=0 and α_z=0 and the rotation coordinates can be written as

$X_R = X^0_R + R(\sin\alpha_i - \sin\alpha_{i0})\cos\alpha_y$;

$Y_R = Y^0_R + R(\cos\alpha_i - \cos\alpha_{i0})$; (3.2.17)

$Z_R = Z^0_R + R(\sin\alpha_i - \sin\alpha_{i0})\sin\alpha_y$;

The traslation coordinates can be calculated as the space formula for a linear accelerated motion:

$X_T = X^0_T + (V_xP + V_xD + V_xB)dt + qE_{xp}dt^2/2$;

$Y_T = Y^0_T + (V_yP + V_yD + V_yB)dt + qE_{yp}dt^2/2$; (3.2.18)

$Z_T = Z^0_T + (V_zP + V_zD + V_zB)dt + qE_{zp}dt^2/2$;

where VxP, VyP and VzP are the parallel velocity componets, VxD, VyD and VzD are the electric drift velocity components and VxB, VyB and VzB are the magnetic drift velocity components. The drift velocities are presented in the following chapters.

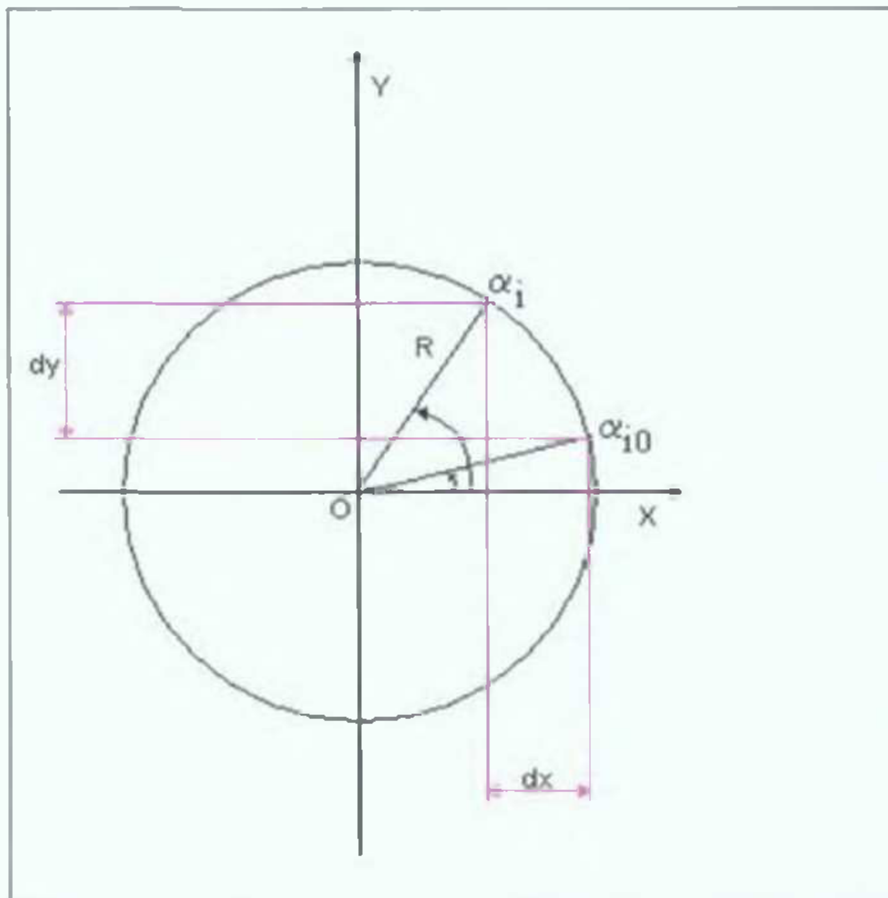

Fig.3.2.1. The displacements dx and dy in the initial (un-rotated) coordinate system where the gyration takes place around OZ axis.

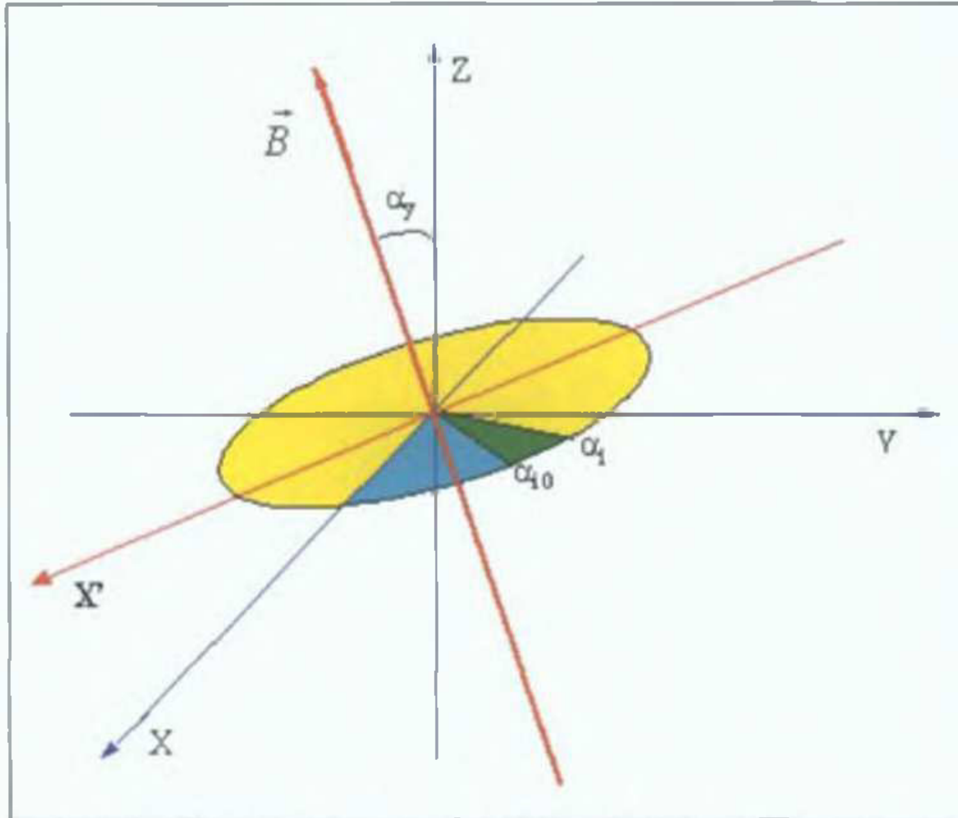

Fig.3.2.2.The 3D rotation plane, magnetic field and initial and final gyration angles.

3.2.4. ELECTRIC DRIFTS

Considering particles moving in time-invariant and homogenous plasma subject to a magnetic field $\vec{B}$ and other forces $\vec{F}$ (electric or/and gravitational forces), the parallel and normal motions to the direction of the magnetic field can be split into:

$$m\frac{d\vec{v}_p}{dt} = \vec{F}_p ; \quad (3.2.19)$$

and

$$m\frac{d\vec{v}_n}{dt} = \vec{F}_n + e\vec{v}_n \times \vec{B} ; \quad (3.2.20)$$

For the perpendicular motion we assume that $v_n = v_D + v_G$. Substituting in (3.2.20) and rearranging gives:

$$m\frac{dv_D}{dt} + m\frac{dv_G}{dt} = (\vec{F}_n + e\vec{v}_D \times \vec{B}) + e\vec{v}_G \times \vec{B} ; \quad (3.2.21)$$

As for the usual gyromotion the gyration velocity is $\vec{v}_n$, it means that the term in the brackets has to be zero, so:

$$\vec{F}_n = - e\vec{v}_D \times \vec{B} ; \quad (3.2.22)$$

Performing a vector product by $\vec{B}$ to the right on the above equation, we obtain:

$$\vec{F}_n \times \vec{B} = = - (e\vec{v}_D \times \vec{B}) \times \vec{B} ;$$

leading to

$$\vec{v}_D = \frac{1}{e}\frac{\vec{F}\times\vec{B}}{B^2}, \qquad (3\ 2\ 23)$$

So particles subjected to a force with a component perpendicular to the magnetic field will undergo a drift with the constant velocity $\vec{v}_D$, which is perpendicular to both the force $\vec{F}$ and the magnetic filed $\vec{B}$ When the force is due to an electric field, this is called the $\vec{E}\times\vec{B}$ drift and it is independent of the particle charge or mass This means that the plasma may undergo bulk motion due to an $\vec{E}\times\vec{B}$ drift without any charge separation or buid-up of electric fields

Other drift motions [16] and corrections to the main $\vec{E}\times\vec{B}$ drift can be obtained by applying the vector product of $\frac{\vec{B}}{B^2}$ to the right on both sides of the equation of motion

$$\vec{v} - \frac{\vec{B}(\vec{v}\ \vec{B})}{B^2} = \frac{\vec{E}\times\vec{B}}{B^2} - \frac{1}{q}\frac{d\vec{v}}{dt}\times\frac{\vec{B}}{B^2}, \qquad (3\ 2\ 24)$$

As the left-hand side is the component of the velocity vector normal to $\vec{B}$, we obtain

$$\vec{v}_n = \vec{v}_D - \frac{1}{q}\frac{d\vec{v}}{dt}\times\frac{\vec{B}}{B^2}, \qquad (3\ 2\ 25)$$

Averaging over the gyroperiod in order to neglect the changes due to the gyromotion, the left-hand side of the equation becomes the total drift velocity, leading to

$$\vec{v}_E = \vec{v}_D - \frac{1}{qB^2}\frac{d}{dt}(\vec{v}\times\vec{B}), \qquad (3\ 2\ 26)$$

As from Eq 3 2 22, for a perpendicular force given only by the electric field the vector product $\vec{v}\times\vec{B} = -E_n$ the above equation becomes

$$\vec{v}_E = \vec{v}_D + \frac{1}{qB^2}\frac{dE_n}{dt}, \qquad (3\ 2\ 27)$$

and

$$\vec{v}_{POL} = \frac{1}{qB^2}\frac{dE_n}{dt}, \qquad (3\ 2\ 28)$$

is the polarization drift velocity

The polarization drift increases with the mass of particles and it is directed along the electric field with a different sense for electrons and positive ions In a plasma this creates a current which carries in opposite directions the electrons and the ions leading to a polarized plasma

$$J_P = n_e e(\vec{v}_{POL\ ions} - \vec{v}_{POL\ electrons}) = \frac{n_e(m_{ion} + m_{electron})}{B^2}\frac{dE_n}{dt}, \qquad (3\ 2\ 29)$$

Since $m_{ion} >> m_{electron}$, the polarization current is mainly carried by the ions

A more complete expression for the electric drift can be derived for situations when the electric field changes over space and has a considerable change over a gyroradius leading to a correction as a second order effect in r (the gyroradius) known as the Finite Larmour radius effect [16]

$$v_E = (1+\frac{1}{4}r^2\nabla^2)\frac{\vec{E}\times\vec{B}}{B^2}, \qquad (3\ 2\ 30)$$

The second spatial derivative takes into account the spatial variation of the electric field averaged over a gyration orbit Finite Larmour radius effects can be neglected in macroscopic applications of particles motion but become important in the vicinity of plasma boundaries and small-scale structures in a plasma

3 2 5 MAGNETIC DRIFTS

Static magnetic fields encountered in magnetrons have strong gradients and magnetic fields lines are curved These non-homogenities in the magnetic field lead to a magnetic drift [16] of the charged particles and provide a means for plasma confinement

A) THE GRADIENT DRIFT

Assuming that the scale length of a magnetic field gradient is much larger than the particle's gyroradius, the magnetic field can be expanded in Taylor series about the guiding centre of the particle

$$\vec{B} = \vec{B}_0 + (\vec{R}\ \ \nabla)\vec{B}_0, \qquad (3\ 2\ 31)$$

where $\vec{B}_0$ is measured at the guiding center and $\vec{R}$ is the distance from the guiding centre

From the general equation of motion with the above Taylor expansion of the field, we obtain

$$\mathrm{m}\frac{d\vec{v}}{dt} = \mathrm{e}\,\vec{v}\ \mathrm{x}\ \vec{B}_0 + \mathrm{e}[\vec{v}\times(\vec{R}\ \ \nabla)\vec{B}_0], \qquad (3\ 2\ 32)$$

The velocity can be expressed as a gyration and a drift motion as $\vec{v} = \vec{v}_G + \vec{v}_\nabla$ and observing that $\vec{v}_\nabla << \vec{v}_G$, from the above equation results

$$\mathrm{m}\frac{d\vec{v}_\nabla}{dt} = \mathrm{e}\,\vec{v}_\nabla\ \mathrm{x}\ \vec{B}_0 + \mathrm{e}[\vec{v}_G\times(\vec{R}\ \ \nabla)\vec{B}_0], \qquad (3\ 2\ 33)$$

When averaging over one gyration the left term vanishes and applying a vector product to the left by $\frac{\vec{B}_0}{B_0^2}$ we obtain

$$\vec{v}_\nabla = \frac{1}{B_0^2}\left\langle \vec{B}_0\times(\vec{v}_G\times(\vec{R}\times\nabla)\vec{B}_0)\right\rangle, \qquad (3\ 234)$$

where the angle brackets indicate the averaging

The above expression can be developed [16] and after averaging over a gyroperiod it becomes

$$\vec{v}_\nabla = \frac{mv_n^2}{2eB^3}(\vec{B}\times\nabla\vec{B}), \qquad (3\,2\,35)$$

The magnetic field gradient leads to a drift perpendicular to both the magnetic field and its gradient and depends on the particle's charge and its perpendicular energy $W_\perp = mv_n^2/2$

As for the case of the polarization drift, the opposed directions of motion for electrons and positive ions lead to a transverse current This magnetic gradient drift current has the form

$$J_\nabla = \frac{n_e(\mu_i + \mu_e)}{B^2}\vec{B}\times\nabla\vec{B}, \qquad (3\,2\,36)$$

B) THE CURVATURE DRIFT

It appears when the magnetic field lines are curved The particles experience a centrifugal force due to their parallel velocity

$$\vec{F}_R = mv_p^2\frac{\vec{R}_c}{R_c^2}, \qquad (3\,2\,37)$$

where $\vec{R}_c$ is the local radius of curvature Using the expression for the general force drift (Eq 23) we obtain the expression for the curvature drift

$$\vec{v}_R = \frac{v_p^2}{q}\frac{\vec{R}_c\times\vec{B}}{R_c^2B^2}, \qquad (3\,2\,38)$$

The curvature drift is proportional to the parallel particle energy and perpendicular to the magnetic field and its curvature Since positive ions and electrons have opposed drift directions they create a curvature drift current

$$\vec{J}_R = n_e e(\vec{v}_{Rion} - \vec{v}_{Relectron}) = \frac{2n_e(W_{p(ion)} + W_{p(electron)})}{R_C^2B^2}(\vec{R}_C\times\vec{B}), \qquad (3\,2\,39)$$

C) THE TOTAL MAGNETIC DRIFT

The total Magnetic Drift is given by the sum of the gradient and curvature drifts and takes the form

$$\vec{v}_B = \vec{v}_R + \vec{v}_\nabla = (v_p^2 + \frac{1}{2}v_n^2)\frac{\vec{B}\times\nabla\vec{B}}{\Omega B^2}, \qquad (3\,2\,40)$$

3 2 6 ADIABATIC INVARIANTS

Adiabatic invariants represent a quantity characteristic for each particle and can be treated as constants even if they are not absolute constants like the total energy or momentum of the particle For periodic motions the theory of mechanics shows that quantities called actions can remain constant for slow changes in the system An action I can be defined in terms of generalized coordinates q_{gen} and conjugate momenta p_{gen} by

$$I=\oint p_{gen}dq_{gen}\,, \qquad (3\ 2\ 41)$$

where the integral is over one period of the motion

For periodic motions and slow changes in the system, the action integral is a constant of the motion and it describes an Adiabatic Invariant Defining q_{gen} to be the gyration angle then the angular mometum $p_{gen}=L=mv_nr$ is the conjugate momentum Inserting these in the above equation and integrating leads to

$$I=2\pi\, mv_n/(eB)=4\pi\mu/e, \qquad (3\ 2\ 42)$$

The quantity

$$\mu=\frac{mv_n^2}{2B} \qquad (3\ 2\ 43)$$

is known as the first adiabatic invariant of a plasma particle This implies that a particle's perpendicular energy is proportional to **B** if μ is constant

Adiabatic invariants are associated with each type of motion a particle can perform The magnetic moment μ is associated with the gyration about the magnetic field, the longitudinal invariant J with the motion along the magnetic field and another invariant Φ can be associated with the perpendicular drift

A) MAGNETIC MIRRORS

Considering the magnetic moment

$$\mu=\frac{mv_n^2}{2B}=\frac{mv^2\sin^2\alpha}{2B}, \qquad (3\ 2\ 44)$$

we observe that since μ is a constant of the motion, as B changes, the pitch angle $\alpha=\mathrm{atan}(v_n/v_p)$ has to change So, pitch angles at different locations are related to the magnetic field induction **B** at those locations according to

$$\frac{\sin\alpha_1}{\sin\alpha_2}=\sqrt{\frac{B_1}{B_2}}, \qquad (3\ 2\ 45)$$

In a converging magnetic field geometry, a particle moving towards regions with stronger fields will have its perpendicular energy $W_\perp$ increased at the expense of its parallel energy $W_\parallel$

For a point where the pitch angle α= 90° the particle will have all its energy into perpendicular energy and no parallel energy so the particle will be reflected back by the gradient force $F = -\mu\nabla B$ In order to model the magnetic mirror effect in a computer simulation, the condition that has to be checked is

$$\sin^2(\tan^{-1}(\frac{v_n(0)}{v_p(0)}) \geq \frac{B(0)}{B}, \quad (3\,2\,46)$$

with the obvious notation for the quantities at the particle's entrance point in the increasing field If the above condition is satisfied, the particle's parallel velocity changes the sign, being "bounced back" The particles which do not satisfy this inequality will not be trapped by the magnetic field and can escape along magnetic field lines

B) ADIABATIC HEATING

The mirror effect takes place when a particle is moving **along** the $\vec{B}$ lines towards increasing values of **B** When the particle moves **across** the $\vec{B}$ lines towards increasing values of B, since the magnetic moment is conserved

$$\frac{W_{\perp 2}}{W_{\perp 1}} = \frac{B_2}{B_1}, \quad (3\,2\,47)$$

meaning that B2>B1 leads to $W_{\perp 2} > W_{\perp 1}$, so the particle's perpendicular energy will increase

In this case the particle will not bounce back as its parallel energy will not be affected This is a type of particle energization called adiabatic heating and it resembles betatron acceleration since the energy to increase the particle energy is taken from the electric drift motion that transports the particle into the stronger field

Both magnetic mirror effect and adiabatic heating are consequences of the magnetic moment conservation and they are directly provided by the total velocity decomposition in magnetic fields as parallel and perpendicular velocities

3 2 7 THE TRAJECTORIES PROGRAM STRUCTURE

The program I have designed in the C language to calculate 3D trajectories in a 3D electric field and a 2D magnetic field is presented in the following schematics (Fig 3 2 3) The number inside each flow segment represents the number of the equation used as presented in the previous sections

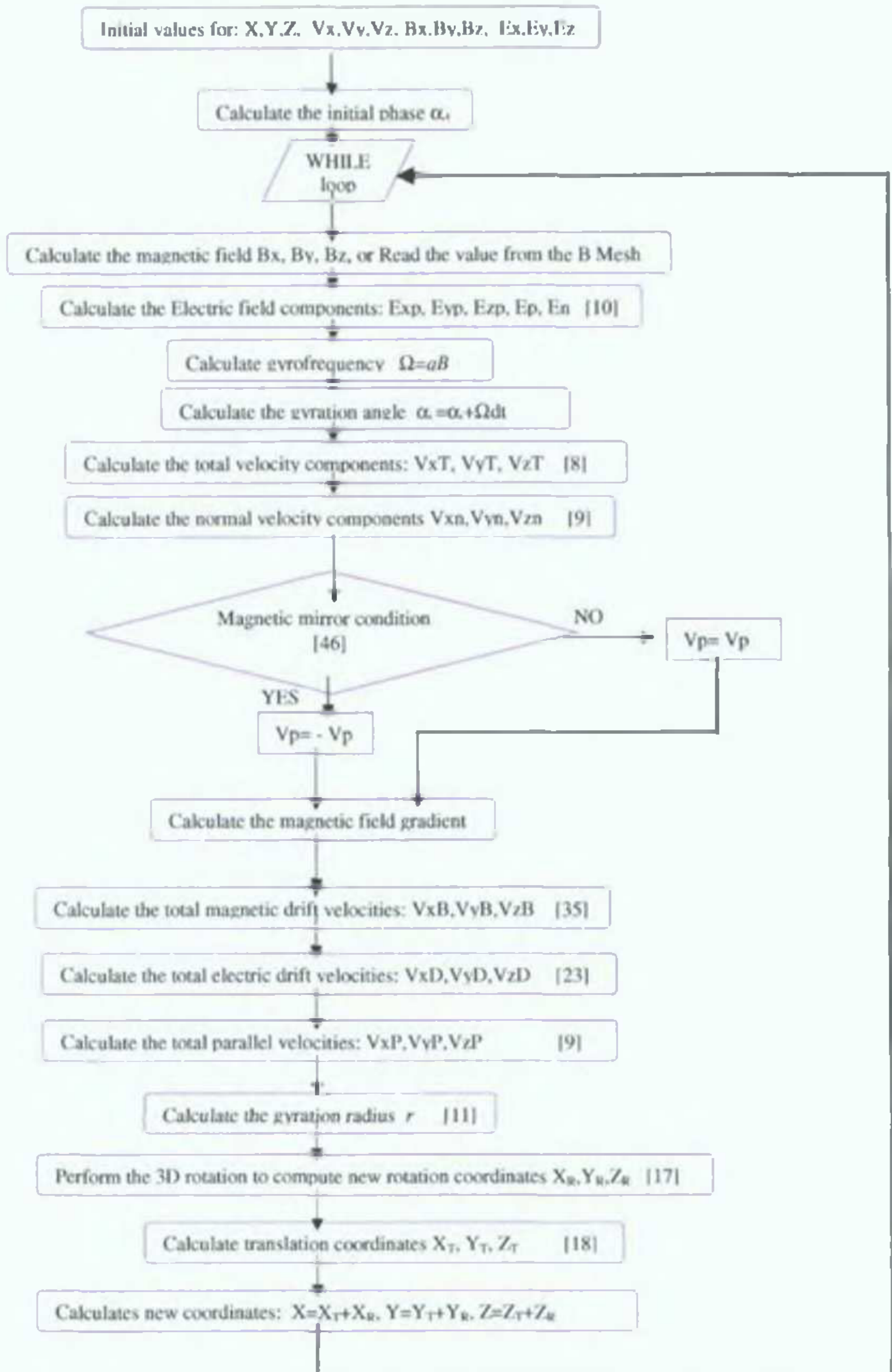

Fig. 3.2.3: Flow diagram of the trajectories program.

3 2 8 DISCUSSION AND CONCLUSIONS

Writing a computer program to describe a charged particle's motion in electric and magnetic fields seems to be a simple task, as one can simply use the equation of motion to write the coordinates, the velocity and acceleration at each time interval *dt* and use a loop to go forward in time

$$\vec{a} = \vec{a}_0 + q(\vec{E} + \vec{v} \times \vec{B}),$$

$$\vec{v} = \vec{v}_0 + \vec{a}dt,$$

$$\vec{r} = \vec{r}_0 + \vec{v}\,dt + \vec{a}\frac{dt^2}{2},$$

Why this approach simply cannot work? It presumes that the particle's motion during the time interval *dt* is a straight line segment, while, in fact, this motion follows a segment of a circle The resulting trajectory in constant *B* and for *E=0*, due to the continuously increasing radius, will be a spiral instead of a circle

The "leap-frog" method [17] was developed to counter balance the propagated errors induced by the assumption the particle moves on straight line segments by considering the velocities at time t-dt/2 and coordinates at time t+dt/2 This method is well-known and actually uses finite-difference equations for the integration

$$m\frac{v_{new} - v_{old}}{dt} = F_{old},$$

$$\frac{x_{new} - x_{old}}{dt} = v_{new},$$

For the leap-frog method, the error in the phase advance at one step is given by

$$\omega\Delta t + \frac{1}{24}(\omega\Delta r)^3 + \ldots + \text{higher order error terms},$$

The error terms dictate a choice of the $\omega\Delta t \leq 0\ 3$ in order to observe oscillations or waves for tens of cycles with acceptable accuracy The error in the phase step induces an error in the amplitude of the oscillator So, the leap-frog method keeps the accumulated error small, but only for a limited period of time

Another method for integrating the equation of motion is to use a numerical integration method for differential equations like the Runge-Kutta method This method is reasonably simple and robust and is a good general candidate for numerical solutions of differential equations when combined with an intelligent adaptive step-size routine The fourth-order (most used) routine is

$k_1 = h\,f(x_n, y_n)$,

$k_2 = h\,f(x_n + h/2,\ y_n + k_1/2)$,

$k_3 = h\,f(x_n + h/2,\ y_n + k_2/2)$,

$k_4 = h\,f(x_n + h\ \ y_n + k_3)$

$$y_{n+1} = y_n + \frac{1}{6}k_1 + \frac{1}{3}k_2 + \frac{1}{3}k_3 + \frac{1}{6}k_4 + O(h^5),$$

As we can see, there is a propagated error depending on the size of the step h

The approach that I have used for calculating 3D trajectories in electric and magnetic fields does not use any of the above methods It simply follows the particle's trajectory by taking into account all possible types of motion and most important, by considering the particle motion during the time step dt as an arch of a circle This provides an exceptionally accurate result there is no phase error and no propagated error[1]

In constant electric and magnetic fields the gyroradius is constant and the particle's coordinates and velocities at any moment can be calculated with the same accuracy, regardless of the time step interval The time step interval has to be adjusted only in accordance to the scale-length variations of the external electric and magnetic field

A drawback of this method may be the complicated development required to design the accurate 3D movement of the particle by taking into account all possible motions, drifts, velocity decompositions in the magnetic field and performing the 3D rotation of coordinates Nevertheless, the length of the algorithm is easily compensated by the speed of the new computers

The magnetic field can be calculated before the simulation and used as a mesh, or the magnetic field can be calculated at each step The calculation of the magnetic field at each step will extend the calculation time but this does not lead to a significant slowing down of the simulation, especially when fast computers are available

The original sides, advantages and refinements of this code are

1 Writing a general Newton-Lorentz equation for the total velocity which allows the construction of the total velocity from the actual parallel and normal components of the total velocity found at the previous step,
2 The calculation of the parallel and normal components for the total velocity and the electric field using the scalar and vector product,
3 Considering the movement of the particle to take place on an arch of a circle,
4 Calculating the number of rotations that take place in the step interval dt and the actual position on the trajectory at any time, regardless of the time step interval (according to the gyration speed),
5 No phase error and no propagated error, constant gyration radius,
6 The calculated position is accurate at every moment even if the time step interval is much larger the gyration period

The inaccuracies in calculation can occur only due to the use of too large mesh elements for the magnetic field In fact a very small element mesh is not appropriate either, as it requires a very large memory space and it might require a special routine to access it

The use of a mesh introduces large errors as the magnetic field can have very large, discontinuous variations from one mesh element to the other. The calculation of the magnetic field at each step is preferred and used later in my Monte Carlo simulation code.

In Fig.3 to Fig.15 some examples of trajectories are shown for simple constant fields, non-constant virtual fields and the actual combination of E and B fields encountered in the opposed target magnetron.

3.2.10 EXAMPLES OF TRAJECTORIES

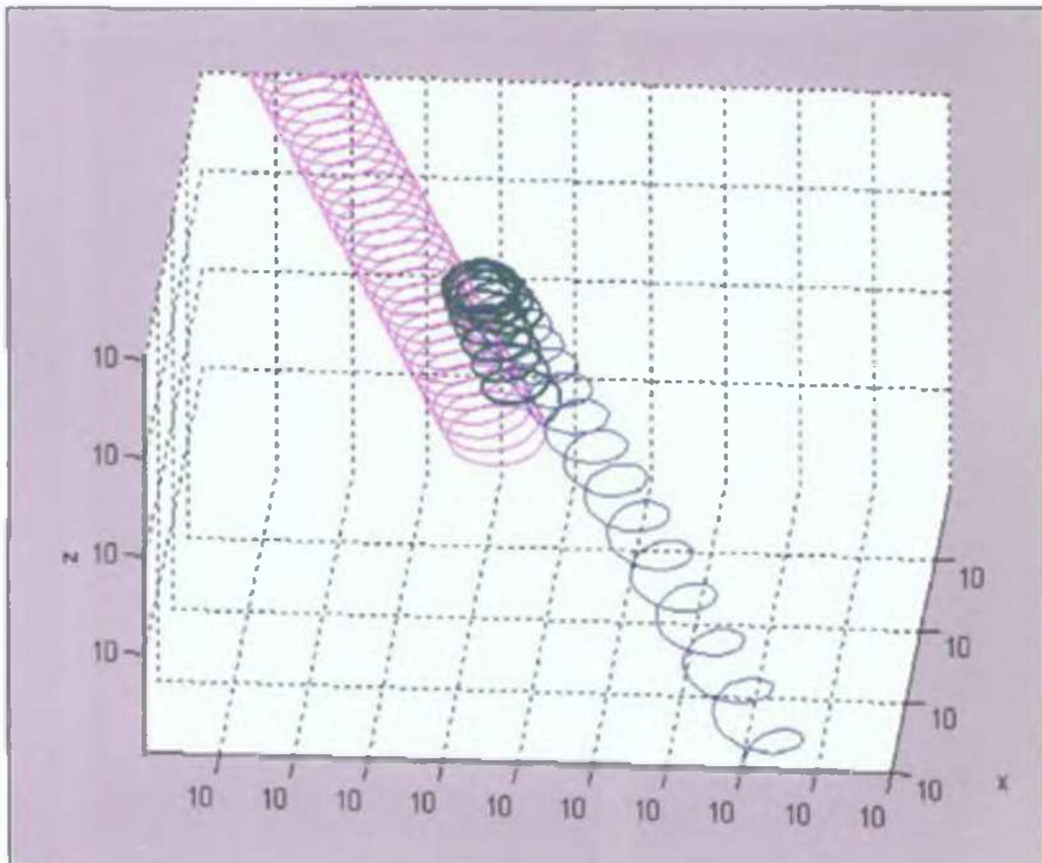

Fig.3.2.4. Trajectories (blue) with starting velocities along and opposed to the direction of an electric field E=1V/m with Bx=Bz=1 T. The trajectory for E=0 V/m (pink) has a perfect stable radius, indicating conservation of energy.

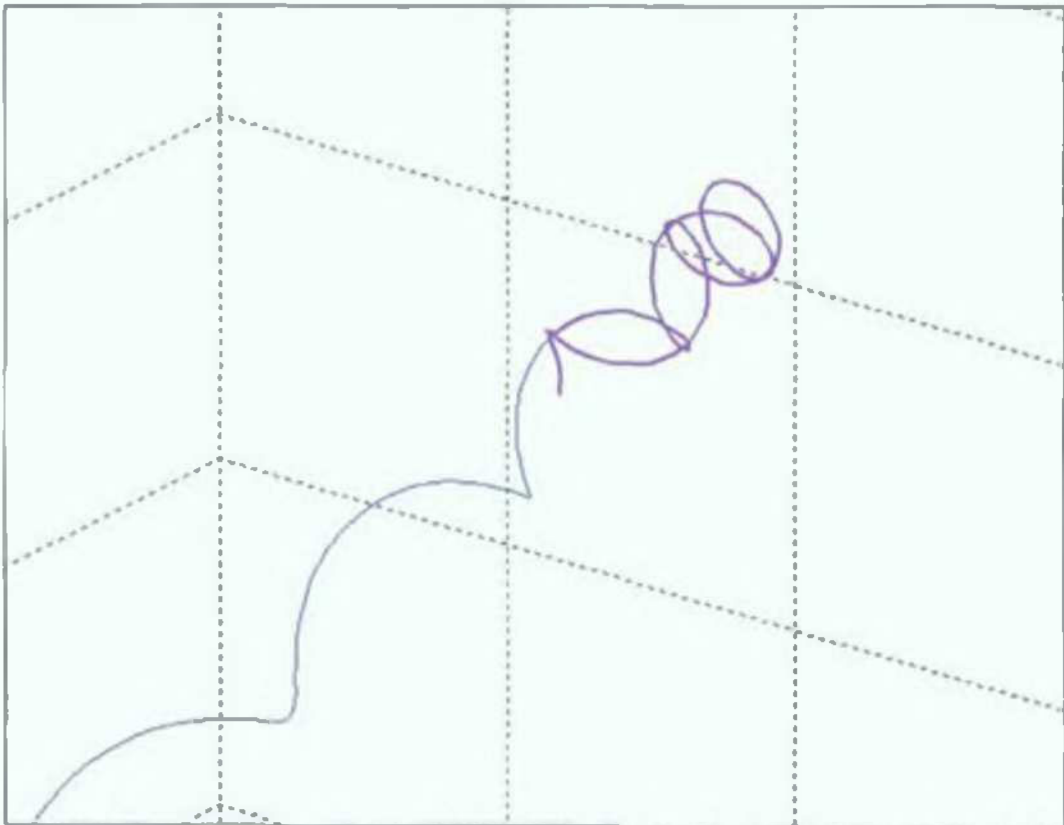

Fig.3.2.5. Trajectory in an electric field E=1 V/m for Bx=Bz=1 T and Vx=10000m/s. It can be noticed how the trajectory "turns back" due to the electric field.

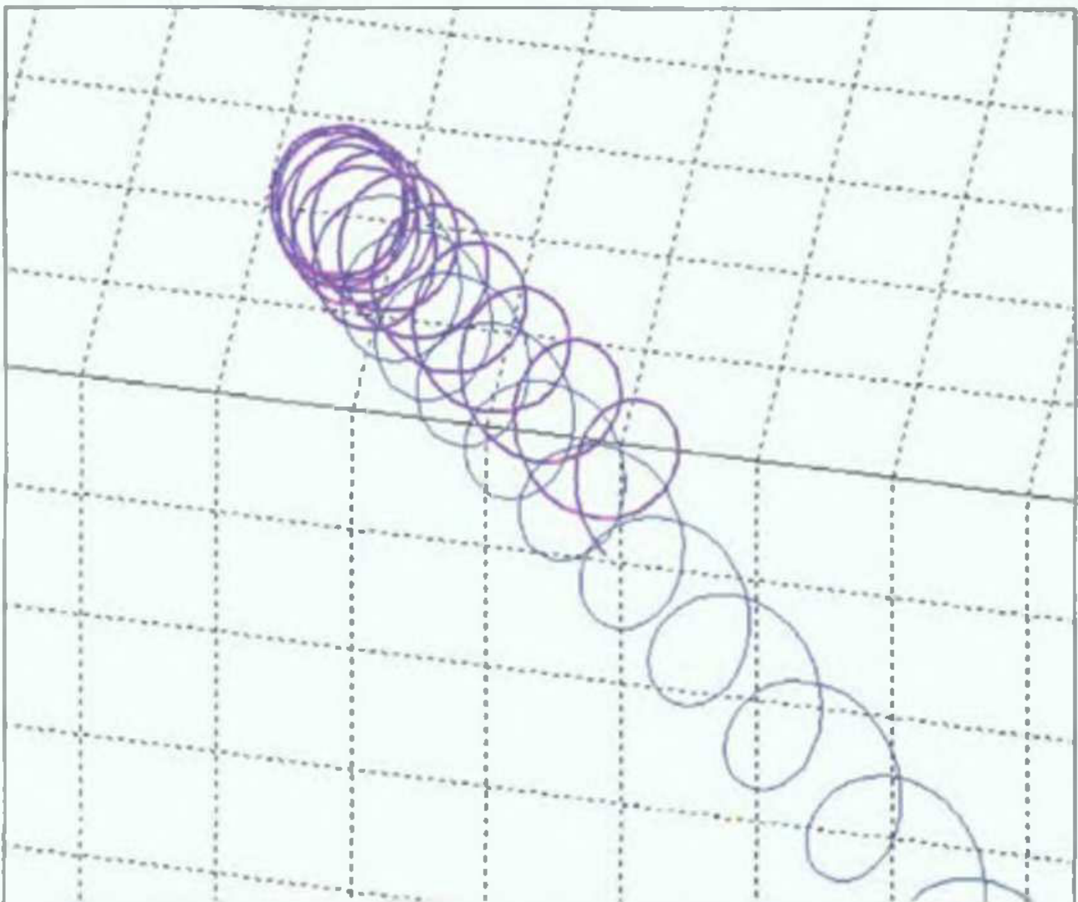

Fig.3.2.6. Trajectory in Bx=Bz=1 T and Ez=1V/m. The perfect resulting cycloid after the parallel velocity becomes zero due to the opposed electric field, can be noticed (blue colour).

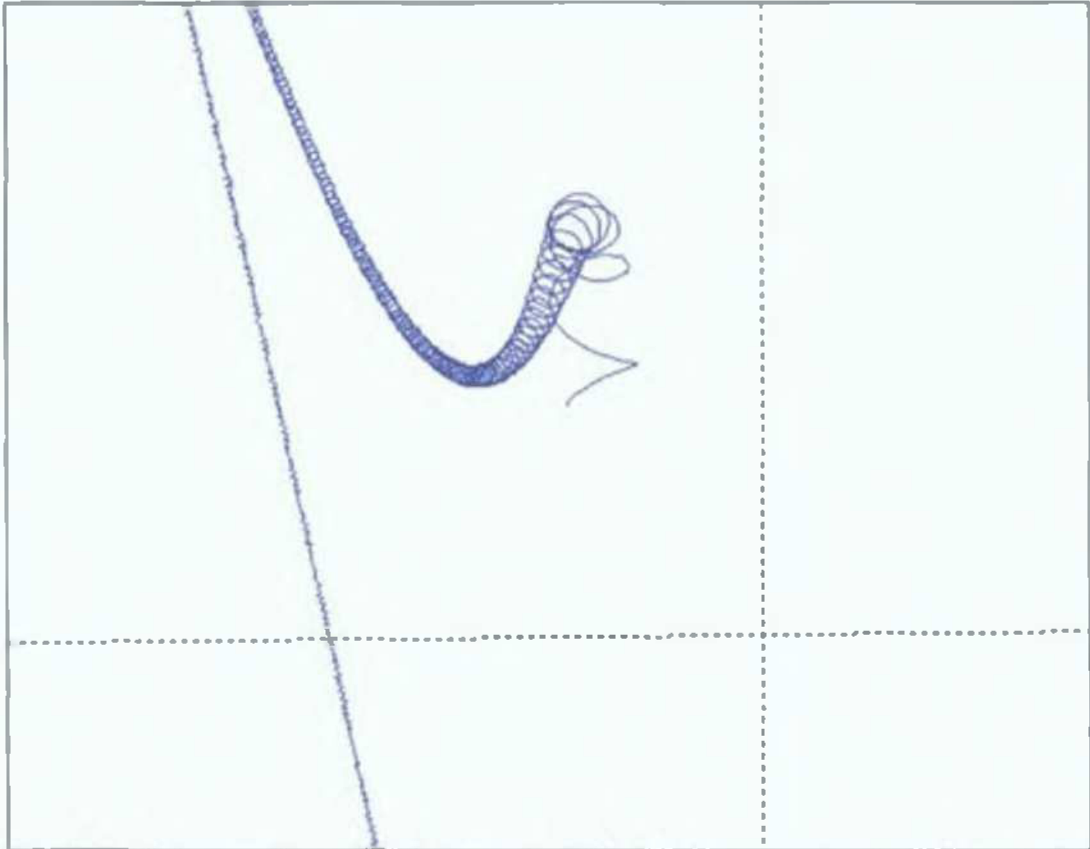

Fig.3.2.7. Trajectory in a virtual magnetic field that increases continuously regardless of position: Bx=Bx+0.001T, Bz=0.1T;

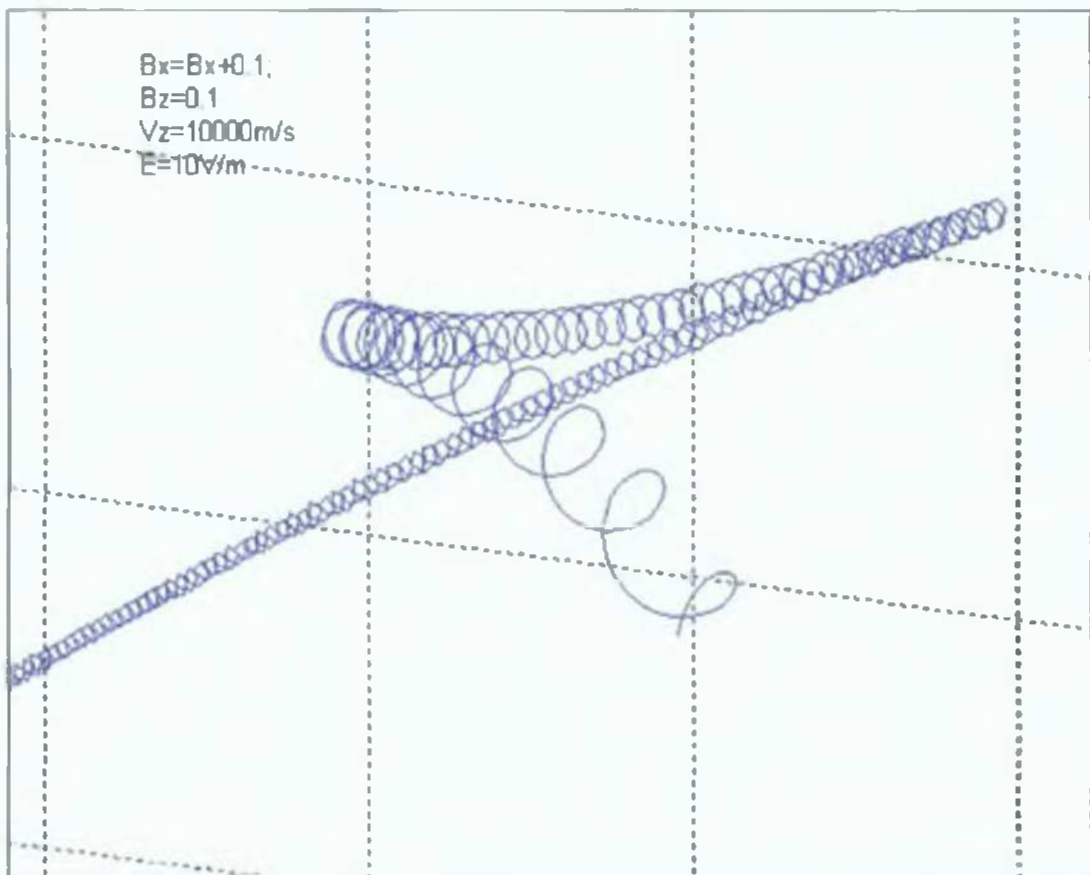

Fig.3.2.8. Trajectory in a virtual field. One mirror effect can be noticed. The second mirror effect is can not be encountered for real fields. In this case the Electric field is higher.

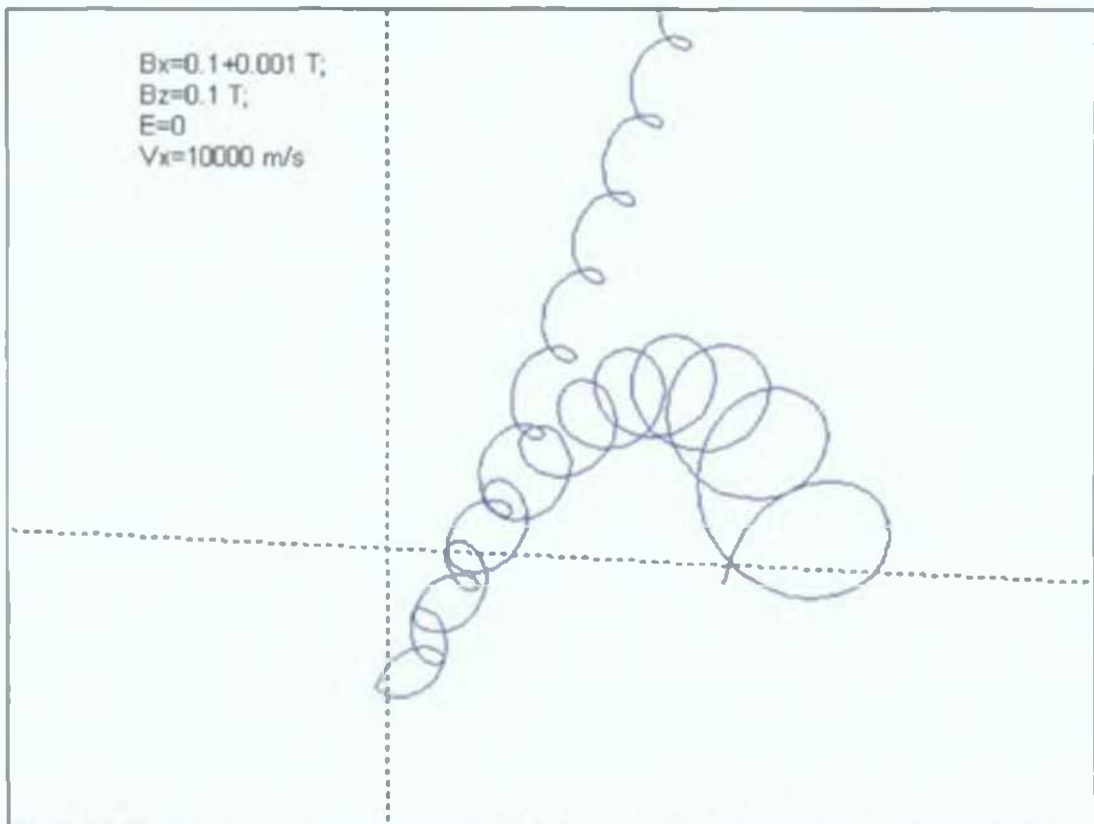

Fig.3.2.9. Trajectory in a virtual magnetic field as indicated in the figure. The parallel velocity is increased while the normal velocity is diminished for a particle going across the field lines in a magnetic field when there is no electric field.

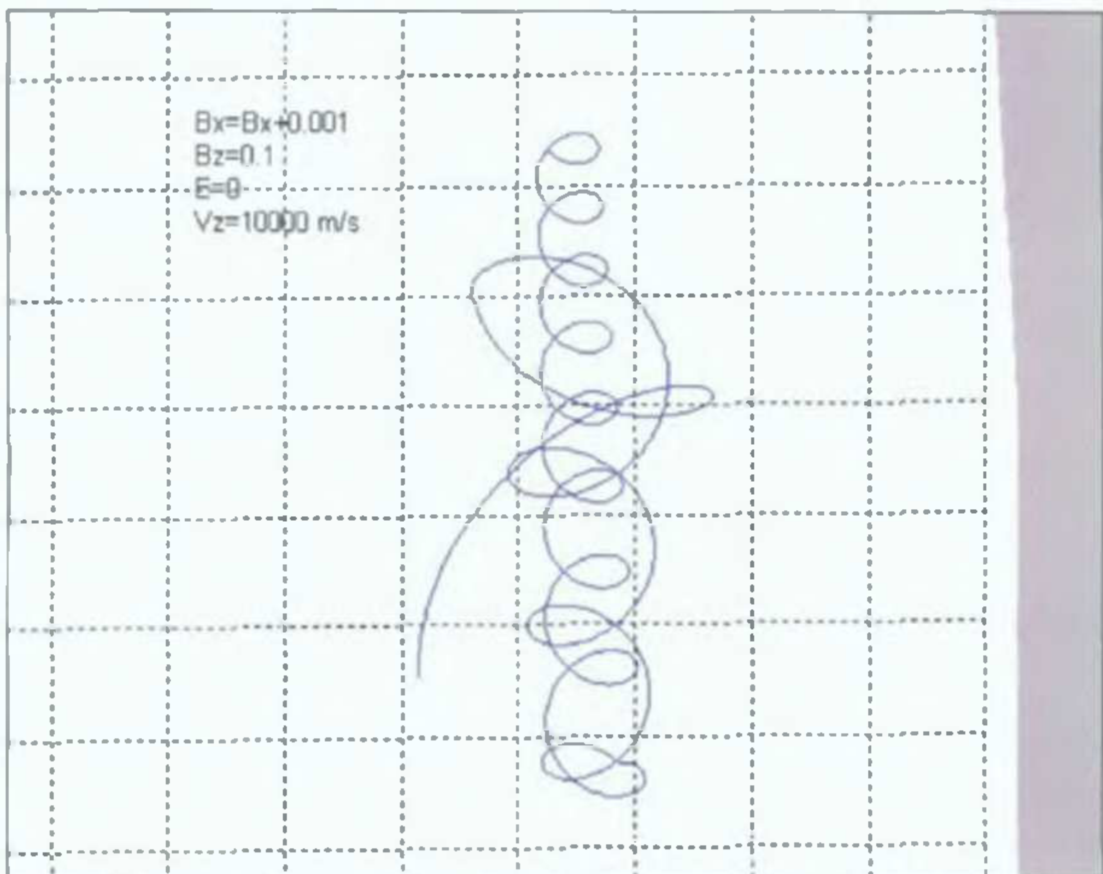

Fig.3.2.10. Trajectory for a particle moving along the field lines in a virtual field. Two "mirror" events can be noticed.

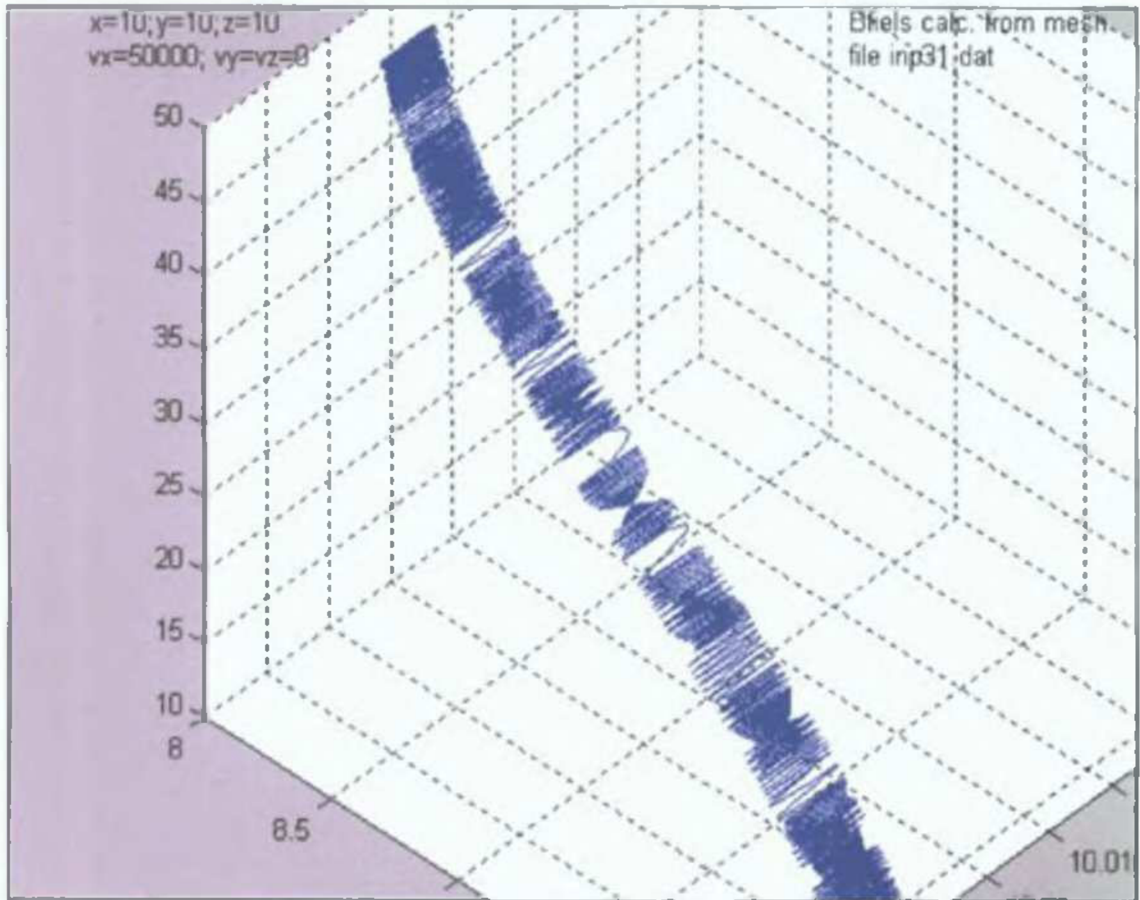

Fig.3.2.11. Real trajectory in the magnetron magnetic field given by the calculated mesh. The electric field is Ez=1V/m. The electron starts from the point (10,10,10) with Vx=Vy=Vz=10000 m/s. The sudden changes in the magnetic field between different mesh intervals are observed as the gyroradius changes suddenly.

3 3 MONTE CARLO SIMULATION OF IONS DURING PULSED DC MAGNETRON OPERATION

3 3 1 MONTE CARLO SIMULATIONS WHY

In opposed targets magnetron plasmas, Langmuir probe measurements are perturbed by the highly ionized and magnetized plasma or they can interfere with the magnetic and electric fields inside the bulk, therefore, such a diagnostic method cannot be used

While planar magnetrons have been investigated using Langmuir probes that provide a good evaluation for the plasma potential and the electric field distribution across the plasma, such measurements are difficult to perform for opposed target magnetrons, especially under pulsed DC operation

Whenever experimental measurements are difficult or impossible to perform, Monte Carlo (MC) simulations of the plasma behaviour can provide an insight into the phenomena that take place in the discharge, beyond the possibilities offered by experimental diagnostic methods The average values obtained from the simulation provide a good estimation of the real variables if the simulation is based on an accurate enough model of the plasma under study

At present, state-of-the art MC simulations using Particle in Cell (PIC) methods can simulate the sputtering process in detail [18] Classical MC simulations of ion behaviour in planar magnetrons have been performed by Goeckner et al [19] providing important information for the understanding of magnetron operation ion energy, density and transit times The model for the pre-sheath electric field was based on Langmuir probe measurements and ion density profiles and velocities obtained from Laser Induced Fluorescence (LIF) emission measurements [20]

A large number of papers have been dedicated to the computational study of magnetrons and glow discharges using Monte Carlo simulations in order to assess the behaviour of the discharge and the various phenomena given by ion interactions sputtered/reflected atom and ion thermalization at their energies at substrate [21], the gas heating and rarefaction due to sputtered atoms and ions [22], the sputtering and self-sputtering efficiency [23] All these studies start from simple and well-defined models of the discharge, where all initial data are determined by experimental methods the electric field in the cathode sheath and pre-sheath are known and constant in time and space, and the start locations of the ions are either calculated or determined experimentally

The behaviour of the plasma pre-sheath in pulsed DC discharges is difficult to predict theoretically and the complex time and space dependent phenomena make experimental measurements difficult The existence and intensity of the pre-sheath electric field can influence the time-scale of the sputtering and self-sputtering processes, important with pulsed DC magnetron operation

The plasma pre-sheath has therefore a tremendous importance for magnetron sputtering as its magnitude determines the ion transit times, the amount of ions that reach the targets and the sputtering rate.

Theoretical and experimental work to predict the evolution of the sheath [9, 24, 25, 26] and pre-sheath for sudden changes in the cathode potential has been devoted to Plasma Immersion Ion Implantation (PIII) applications, showing that the pre-sheath expansion appears only for slow evolving sheaths and appears to be delayed, as if the information about the changes in the potential on the cathodes travels with the ion acoustic velocity [27]. The ion acoustic velocity (the Bohm velocity) is a characteristic of the electric field intensity in the pre-sheath, respectively of the plasma potential values and electron temperature.

The temporal evolution of the pre-sheath observed experimentally [26] and by PIC/MC simulations [27] indicates that the pre-sheath forms after the expansion speed of the sheath falls below the ion acoustic velocity, the pre-sheath continuing to expand slowly for more than 10μs after the sheath has collapsed.

Using the above model for pulsed DC discharges indicates that after the voltage waveform has reached the maximum value the pre-sheath is formed and its extent and field values can be considered quasi-constant. Considering the plasma potential values constant during the "on" phase of a pulsed DC discharge (as shown by Langmuir probe measurements performed by Bradley et. al. [7]) the value of the pre-sheath electric field intensity will be constant and can be estimated by analysing the behaviour of the gas ions that have to return to the targets in order to maintain the discharge and produce sputtering.

In this chapter, the intensity of the pre-sheath electric field in the opposed target magnetron pulsed DC discharge is investigated through Monte Carlo calculations of the travel time to targets of Ar gas ions. The calculated values of the travel time to targets obtained from the MC simulation are then compared to the experimental value, estimated from the delay between the time-resolved OES Ar ion peak and the applied power peak.

As presented in the previous chapter, I have developed a computer code that simulates 3D ion trajectories in 3D electric and magnetic fields. This code has been used to simulate Ar ion trajectories in a 50kHz, 2016ns pulsed DC discharge at 2A constant current run and 0.4Pa Ar gas pressure.

Starting from a model of the discharge based on experimental data from space-resolved and time-resolved OES and the values of the I and V waveforms during the pulse, Monte Carlo simulations of Ar ion trajectories in the pulsed DC opposed target magnetron discharge are performed in order to observe the influence of the pre-sheath electric field on the return time to target of Ar ions. Once the intensity and space variation of the pre-sheath electric field has been estimated, the discharge model is complete and MC simulations of sputtered ions transit time can be performed in order to evaluate the time-scale for self-sputtering.

3 3 2 THE PRINCIPLE OF MONTE CARLO SIMULATIONS

Monte Carlo methods are largely and efficiently used to solve many physical and mathematical problems, in particular those involving multiple independent variables, where conventional analytical or numerical methods are not applicable

In Monte Carlo simulation for particle transport problems, the history (path) of a particle is followed as a random sequence of free paths, each ending with a scattering event, changing the energy and velocity direction of the particle The MC simulation of an experiment consists in the numerical generation of a large number of such particle histories For radiation or particle transport, the MC method yields the same information as the solution of the Boltzmann transport equation but it is easier to implement for finite and complex geometries

The Monte Carlo method relies on the laws of statistics and its results are affected by statistical uncertainties given by the random nature of the modelled phenomena

The foundation of the MC method is the Central Limit Theorem stating that for a given distribution of independent random variables with non-zero mean μ and standard deviation σ, sampling the distribution of the mean approaches a Normal (Gaussian) distribution with mean μ and standard deviation $\sigma / \sqrt{N}$, as the sample size N increases

According to the Strong Law of Large Numbers, if the true mean *M(x)* of a distribution is finite, the average value $\bar{x}$ of a number N of history results tends to the true mean when N tends to infinity Therefore, averaging the results over a large number of histories leads to the true mean within the confidence intervals given for the Normal function

$$\bar{x} - \frac{\sigma}{\sqrt{N}} < M(x) < \bar{x} + \frac{\sigma}{\sqrt{N}} \text{ , at 68\% of the time, and} \quad (3\ 3\ 1)$$

$$\bar{x} - 2\frac{\sigma}{\sqrt{N}} < M(x) < \bar{x} + 2\frac{\sigma}{\sqrt{N}} \text{, at 95\% of the time} \quad (3\ 3\ 2)$$

Every random variable has a probability distribution, assigning to the interval [*a*, *b*] the probability $\Pr[a \leq X \leq b]$, i e the probability that the variable x will take a value in the interval [*a*, *b*] The probability distribution function can be a discrete, or a continuous function normalized to unity

$$p(x) \geq 0 \text{ and } \int_a^b p(x)dx = 1 , \quad (3\ 3\ 3)$$

The statistical process modelled in the presented simulation is the mean free path or time between collisions, which is best modelled by an exponential (Poisson) distribution function

$$p(l) = \frac{1}{\lambda}\exp(-l / \lambda) , \quad (3\ 3\ 4)$$

where *l* is the path length and λ is the mean free path between interactions

Knowing the mean free path from interaction cross-sections, the random values of l are generated from

$$l = -\lambda Ln(\xi), \qquad (3\ 3\ 5)$$

where ξ is a random number

So, the occurrence of each random event is modelled using random number generators A large variety of functions and routines have been developed to generate random numbers with repetition sequences much larger than 10^9 In this work I have used the function "drand48" given by the GNU (C) library This function generates pseudo-random numbers uniformly distributed in the interval [0, 1] based on the linear congruential algorithm and 48-bit integer arithmetic

$$X_{n+1} = (aX_n + c)\,\mathrm{mod}(m) \qquad (3\ 3\ 6)$$

The parameter $m=2^{48}$ The sequence is repeating after $\sim 10^{14}$ numbers

There is an important observation to be made on the difference between the Accuracy and the Precision of a MC simulation result The Precision is the uncertainty in $\bar{x}$ given by the statistical fluctuations of x and this can be improved by variance reduction techniques and by increasing the number of particles run The Accuracy is a measure of how close the expected value of $\bar{x}$ is to the true physical value to be estimated, therefore it indicates the systematic error given by the code and the designed physical model Getting a good accuracy for a MC simulation involves modelling nature faithfully

As perfect physical models are practically impossible to obtain, there is always a trade back between the complexity of the problem and the sought solution, trade back that can only be solved by using as much experimental data in the model as possible and by always checking the MC results against relevant experiments

The MC code that I have developed here is an analog MC code that samples the events according to their natural physical probabilities and no variance reduction techniques have been used

3 3 3 INTEGRATING 3D TRAJECTORIES IN ELECTRIC AND MAGNETIC FIELDS

The trajectories were calculated using the algorithm presented in Chapter (3 2)

The algorithm follows the motion of the charged particles on their rotation in a plane perpendicular to the direction of the local magnetic field The velocity values are advanced at each step in the local electric and magnetic field using the equation of motion, then decomposed in the magnetic field to find the new rotation radius and the advancement velocity along the direction of magnetic field lines The electric drift and magnetic mirror effects as well as the drift due the magnetic field gradient and curvature are taken into account

The coordinates' changes due to rotation calculated in the rotation plane are then projected (by performing a 3D rotation of coordinates) on the real axes The coordinates changes due to translation are calculated in the real coordinates system

As this method of calculating the trajectories does not involve Runge-Kutta type integration, the truncation errors related to Taylor expansion of derivatives will be avoided, as well as the problems related to the corrections necessary at each step to provide energy conservation

The errors in Runge–Kutta routines are related not only to the method of integration, but also to the fact that the trajectory between two steps is considered a straight line segment Considering in our routine the particles' motion along a circular path, the trajectory between two steps is actually an arch of a circle, thus eliminating all errors related to approximating a circle by straight-line segments

The error levels in the Rungge-Kutta routines are directly dependent on the advancement time step and smaller time steps provide a better accuracy The choice of adaptive time steps in Runge-Kutta routines is thus of crucial importance and the required small time steps will involve longer computation times

In the routine used here, the trajectories are stable without the need for energy conservation corrections and the time step choice is only related to the scale length variations of the electric and magnetic field and the particle's specific charge For ion trajectories, time steps of 10^{7} s provide a good accuracy for the magnetic field gradients existent in our magnetron discharge As the cathode sheath thickness is calculated from the current waveform that was measured with a time resolution of 0 02μs, we consider this as the value of the time step for regions outside the cathode sheath This choice of the time step allows for a small computation time during the MC computation The time step in the sheath is taken to be 10^{5} times smaller 0 2ps

A concise diagram of the Monte Carlo simulation is presented in Fig 3 3 1, with the following notations

-**B**(x,z) The magnetic flux density vector,

-**E**(z,t) The electric field vector with its projections normal (E_N) and parallel (E_P) to B,

-E_i ions' energy at step (i),

-$\mathbf{V}_i$, $\mathbf{V}_N$, $\mathbf{V}_P$ The total velocity vector at each step (i) and its projections normal (V_N) and respectively parallel (V_P) to the direction of the magnetic field B,

-$\mathbf{F}_i$ The total force vector acting upon the particle,

-$\mathbf{X}^*_{R(i)}$ coordinates vector due to rotation in the rotation plane at step (i),

-$\mathbf{X}_{R(i)}$ coordinates vector due to rotation in the real coordinate axes at step (i),

-$\mathbf{X}_{T(i)}$ coordinates vector for translation at step (i),

-$\mathbf{X}_{(i)}$ total (rotation plus translation) coordinates vector at step (i),

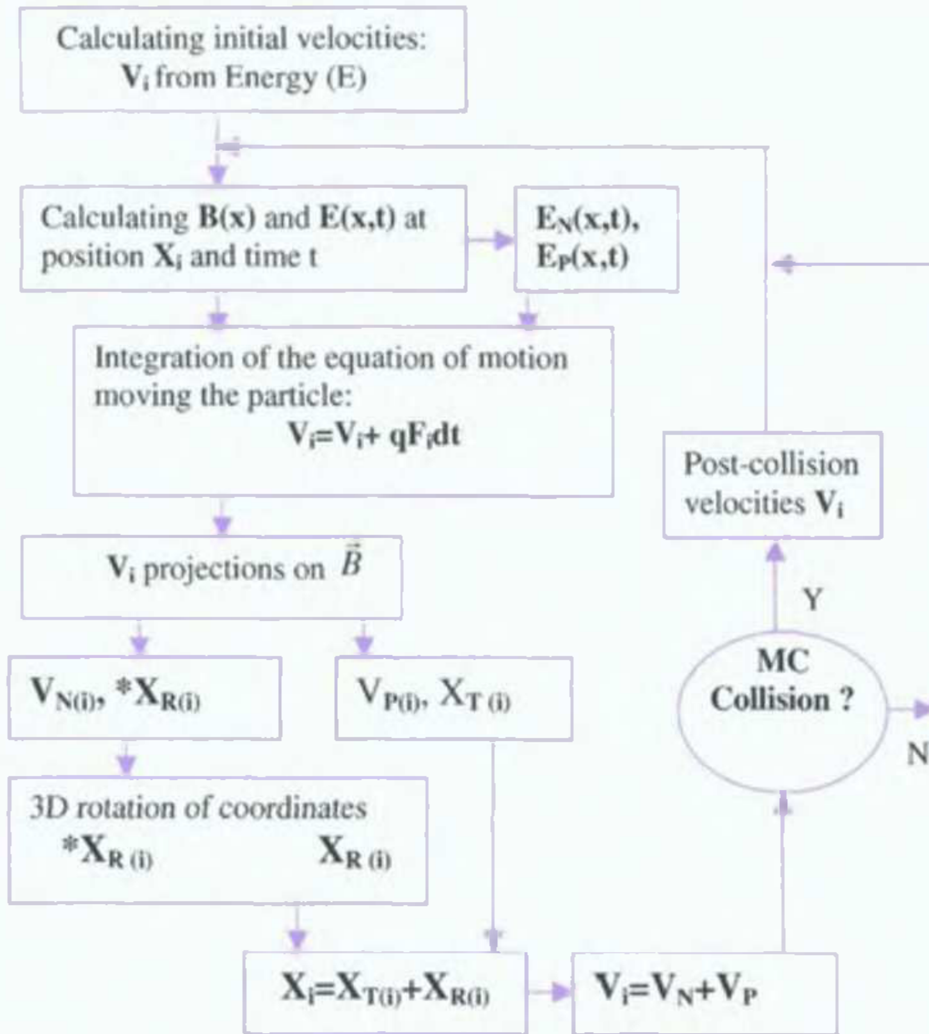

Fig.3.3.1. Concise diagram of the Monte Carlo simulation. All bold symbols are vectors.

3.3.4 THE TRANSPORT PROCESS

The ion trajectories are simulated including collisions with the Ar gas atoms and ions. Collisions with gas atoms and ions are random processes described by a Poisson (exponential) distribution [21, 22]. The collision frequency is randomly chosen from the Poisson distribution:

$$\nu = -\nu_0 Ln(R)\,; \qquad (3.3.7)$$

where R is a random number between 0 and 1 and ν_0 is the collision frequency of the particles involved, at the given temperature and pressure.

The collision frequency with gas atoms at a certain temperature and pressure is given by:

$$\nu_0 = V n_g \sigma\,; \qquad (3.3.8)$$

where V is the relative velocity of the colliding atoms before collision, n_g is the gas density and σ is the total (elastic and charge-exchange) interaction cross-section:

$$\sigma = \sigma_{el} + \sigma_{ch-ex}, \quad (3\,3\,9)$$

The elastic scattering cross-section in SI units is calculated at each step as a function of the ion's velocity **V** from [18, 28]

$$\sigma_{el} = [c + d \ln(V)]^f \text{ [m}^2\text{]}, \quad (3\,3\,10)$$

where c=-2 27x10^36, d=3 08x10^35 and f=-0 52, the coefficients being obtained from a fit to Cramer's [28] experimental measurements of the cross-section for $V \geq 3800$m/s, below this value the cross-section being considered constant

The charge-exchange cross-section was calculated from the formula given by S Sakabe and Y Yzawa [29] and gives values closer to the experimental values than the older formulas given by Rapp and Francis [30] and Popescu-Iovitsu and Ionescu -Pallas [31]

$$\sigma_{ch-ex} = (A - B\log_{10}V)(I/I_0)^{-1\,5} \text{ [cm}^2\text{]}, \quad (3\,3\,11)$$

where A=1 81x10^14, B=2 12x10^15, I_0 = 13 6eV is the ionization potential of Hydrogen, I=15 7eV is the ionization potential of Argon and V [cm/s]

The charge-exchange cross-section formula is accounted as reliable to a degree of 15-20% by the authors [14] and matches the experimental data closer than the Rapp and Francis formula especially for the low velocity range The formula given by Ionescu–Pallas et al [31] has a similar trend as the one given by Shuji et al but with higher values in the low energy range below 10eV The actual values for the charge-exchange cross-section are about one order of magnitude higher than those obtained from the Rapp and Francis formula (Fig 3 3 2)

The obtained Collision Frequency (Fig 3 3 3) and Mean Free Path (Fig 3 3 4) obtained for elastic collisions are in good agreement to those deducted from the molecular theory of gases

The mean free paths in Fig 3 3 4 are calculated from $\lambda = 1/n\sigma$, where n is the gas density and σ the respective interaction cross-section and can be also expressed as a function of the gas temperature T and pressure p

$$\lambda = kT/p\sigma, \quad (3\,3\,12)$$

with $E=3kT/2$ the average kinetic energy of gas atoms at temperature T, leading to

$$\lambda = 2E/3p\sigma, \quad (3\,3\,13)$$

The hard-sphere model is considered for both the elastic and charge – exchange collisions

The resonant symmetric charge-exchange collisions (Ar+, Ar) mechanism requires an overlapping of the electron wave-functions of the two participants in the collision, involving a close interaction, allowing to be considered as a hard – sphere model collision, especially at low energies [29]

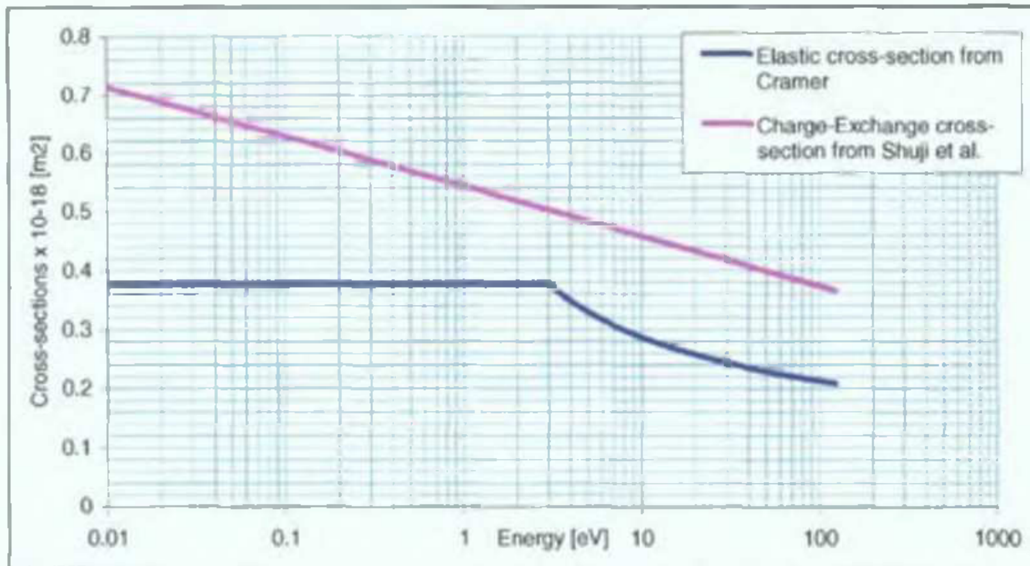

Fig.3.3.2. Elastic and charge-exchange cross-sections for Ar at 3mtorr (0.4Pa).

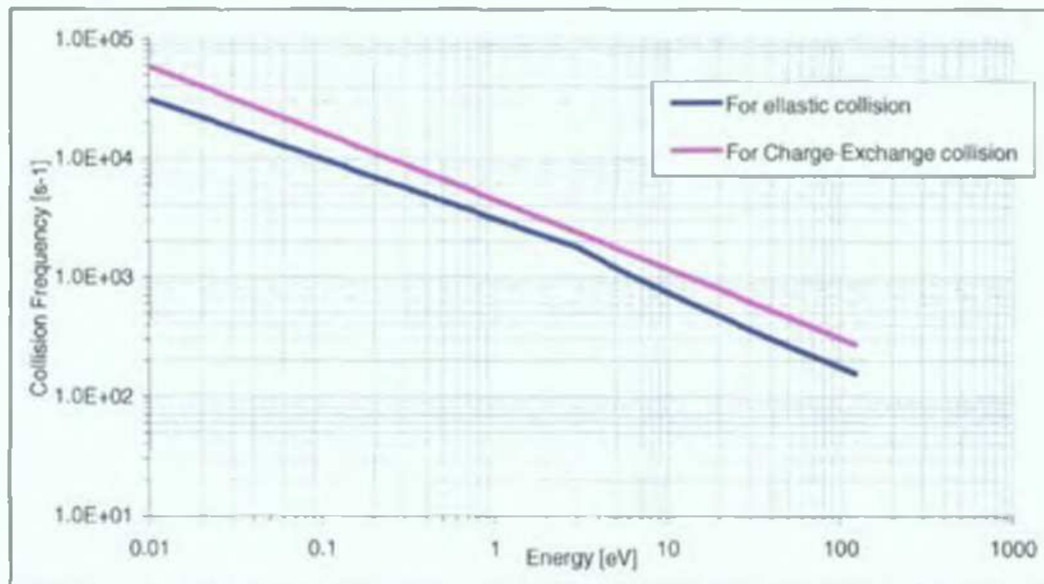

Fig.3.3.3. The Collision frequency as a function of energy for Ar at 3 mtorr (0.4Pa).

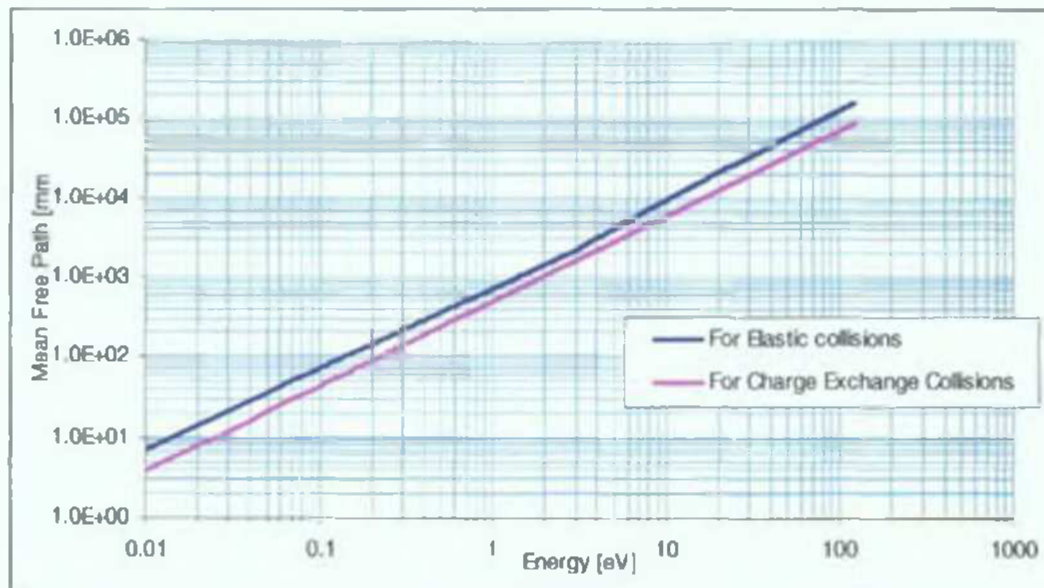

Fig.3.3.4. Mean Free Path as a function of energy for Ar at 3mtorr (0.4Pa).

The 3D scattering process between two particles is described by Yamamura and Gryzinski [21, 32] where the velocities after collision are determined by the scattering angle in the orbital plane and the relative velocity before collision In my code I have used a different approach, using the kinetics in the Centre of Mass Frame According to classical mechanics and using the kinematics in the Centre of Mass Frame [33] the final velocities of two particles with masses M_1 and M_2 after a 3D collision can also be written as

$$\vec{V}_{1f} = \vec{V}_{1i} - \frac{M_2 C}{M_1 + M_2}(1+e)\vec{n}, \qquad (3\,3\,14)$$

$$\vec{V}_{2f} = \vec{V}_{2i} + \frac{M_1 C}{M_1 + M_2}(1+e)\vec{n}, \qquad (3\,3\,15)$$

where $C = \vec{n}\ (\vec{V}_{1i} - \vec{V}_{2i})$ has the role of a "collision parameter" for the direction of collision, e is the coefficient of restitution ($e = 1$ for elastic collisions) and $\vec{n}$ is the normal unit vector from particle 1 to particle 2

The director cosines of normal unit vector $\vec{n} = (\cos a, \cos b, \cos c)$ are randomly generated for each collision as random numbers uniformly distributed between 0 and 1, therefore generating the direction of encounter in the reference frame

The initial velocities of the background gas atom (ion) are randomly generated and normalized to the average gas energy (temperature) as

$$V_{2,x} = \pm R_x E_{gas} / \sqrt{R_x^2 + R_y^2 + R_z^2}, \qquad (3\,3\,16)$$

$$V_{2,x} = \pm R_y E_{gas} / \sqrt{R_x^2 + R_y^2 + R_z^2}, \qquad (3\,3\,17)$$

$$V_{2\,x} = \pm R_z E_{gas} / \sqrt{R_x^2 + R_y^2 + R_z^2}, \qquad (3\,3\,18)$$

where Rx, Ry and Rz are independent random numbers in the interval [0, 1] and the plus or minus signs are also randomly chosen

3 3 5 THE DISCHARGE MODEL

For MC calculations, both the model and the start data have to be carefully determined and designed Using a model based on experimental data increases the accuracy in designing the model thus improving the expected accuracy of the results

The data used for building the magnetron discharge model consist of the following

a) The magnetron geometry presented in Fig 3 3 5,

b) The magnetic field flux density values B, calculated according to the method and algorithm presented in Chapter (3 1) The distribution of the intensity of the magnetic field flux density in the discharge cross-section XOZ is shown in Fig 3 3 6,

c) The electric field in the cathode sheath is calculated from the current and voltage waveforms values and the extent of the cathode sheath is presented in Fig.3.3.8;

d) The electric field in the pre-sheath is calculated from two types of functions presented in Fig.3.3.10.

a) The Magnetron Geometry

The opposed target magnetron geometry is presented in Fig.3.3.5. and consists of two opposed rectangular targets (120mmx180mmx9mm), with a distance between the targets of 100mm, and the corresponding magnetic poles arrays at the back of each target.

The coordinate axes considered in the MC simulation geometry are represented in Fig.3.3.5. in red, as well as the start planes for the ion simulation. As it will be shown next, the Ar and respectively Cu ion relative densities are determined through OES at the level of these planes.

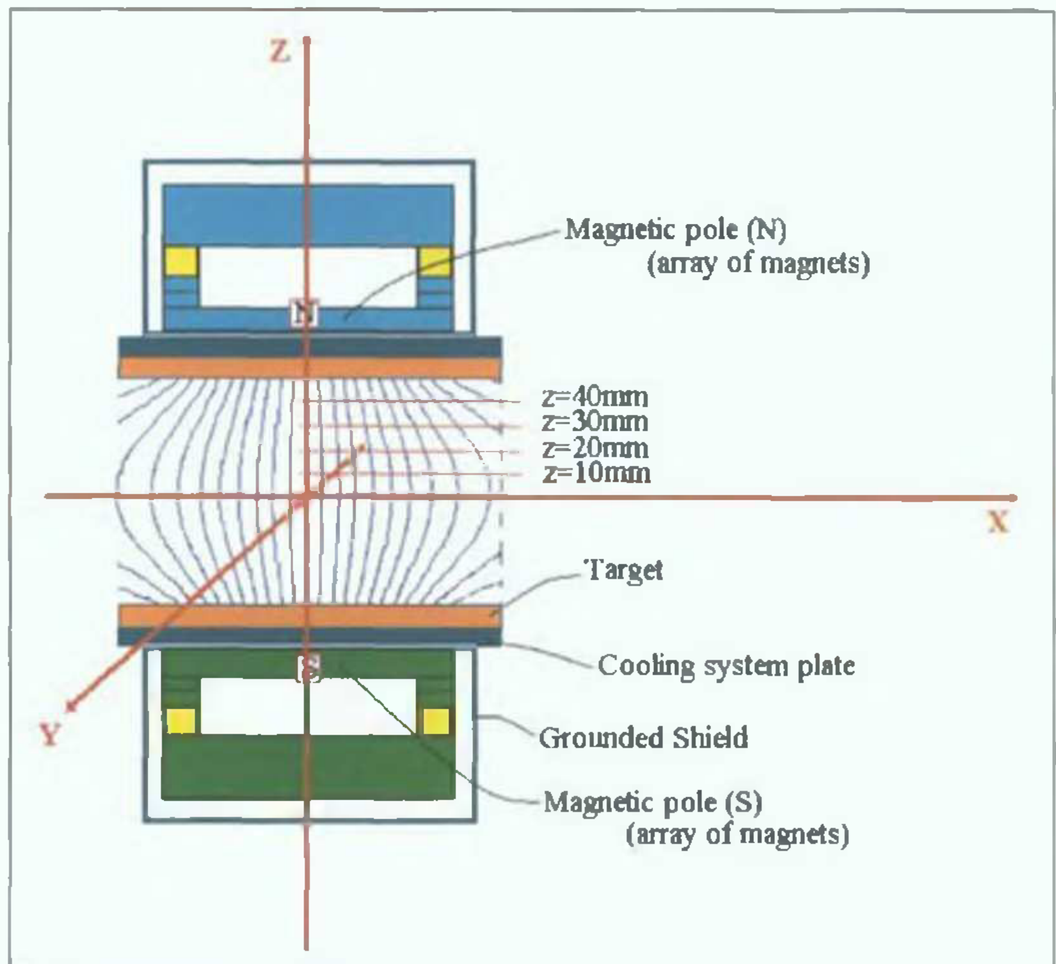

Fig.3.3.5: The geometry set-up for the MC simulation. The direction of the magnetic filed lines between the targets is shown in blue lines.

b) The Magnetic field

The magnetic field flux density values and direction are calculated as described in Chapter (3.1). The direction of magnetic field lines between the targets is shown in Fig.3.3.5. The magnetic field flux density B has intensity contour lines parallel to the targets, a maximum of 0.2T being achieved at the targets surface (Fig.3.3.6). The magnetic flux density values are calculated at each time step during the simulation.

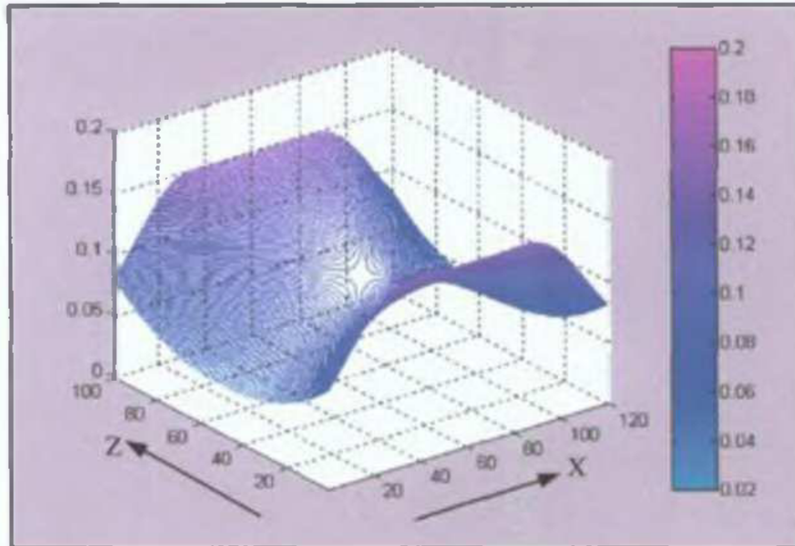

Fig.3.3.6. Contour lines of the total magnetic flux density between the targets, where Z is the distance between the targets and the targets are situated along OX axis at Z=0 and Z=100mm

c) The Electric field in the cathode sheath

An ENI pulse generator has been used to provide the pulsed DC bias of the targets at 50kHz and pulse off time 2016ns. The operation mode was set for a constant current run at 2A.

The I-V waveforms have been measured as shown in Chapter (5.1) and the values that have been used in the calculation of the cathode sheath and the electric field intensity in the sheath are presented in Fig.3.3.7.

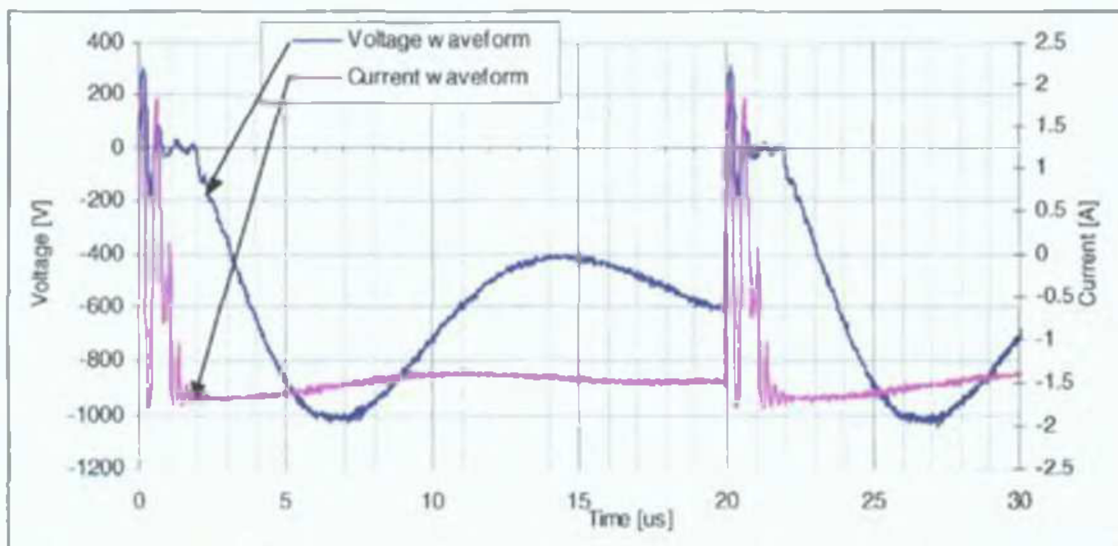

Fig.3.3.7. Typical Current and Voltage waveforms on the cathodes during a 50kHz, 2016ns pulse-off time pulsed DC operation at a set current run of 2A.

The formation of a matrix sheath and then of a Child–Langmuir sheath at the on-set of the negative voltage on the cathodes is well understood and described in many reference books as the one by M A Lieberman, A J Lichtenberg [4] The formation of a time-dependent sheath in pulsed DC discharges has been studied both though modelling and experiments for PIII applications [9, 20] The models assume that the transient sheath obeys the Child-Langmuir law at each instant during the propagation of the sheath and are in good agreement with the electron density temporal evolution in the sheath from Langmuir probe measurements [21]

For opposed target magnetrons where the magnetic field is perpendicular to the targets, the sheath thickness is not influenced by the magnetic field and the Child-Langmuir law can be applied directly, as for the case of un-magnetized discharges [34] The ions uncovered by the expansion of the sheath and those arriving at the sheath edge from the plasma bulk will be accelerated towards the targets, generating a space-charge limited current at the targets The space-charge limited current J_i in a plane diode given by the Child-Langmuir law [4] is

$$J_i = \frac{4}{9}\varepsilon_0 \sqrt{\frac{2e}{M}} \frac{V_c^{\frac{3}{2}}}{s^2}, \qquad (3\,3\,19)$$

where ε_0 is the permittivity of the free space, e the particle charge, M the ion mass, V_C the cathode voltage and s the plasma sheath thickness

From equation (33 19), the value of the cathode sheath thickness s can be calculated when the ion current J_i is known The discharge current consists of ions and secondary electrons

$$J_d = J_i + J_e, \text{ and } J_e = \gamma J_i, \qquad (3\,3\,20)$$

where J_e is the electron current density, γ the secondary emission coefficient and J_i the ion current density

The knowledge of the secondary electron emission coefficient is required in order to obtain information on the extent of the plasma sheath s when the cathode voltage V_C and discharge current density J_d are known The secondary electron emission coefficient γ values calculated from ion beam measurements for Ar ions on Cu targets, for clean surfaces (as those during sputtering) are from 0 08 to 0 1 at ion energies from 500V to 2000V [35] As most of the voltage values are above 600V for our pulsed discharge, a constant value of γ=0 1 and a total targets area of 256cm^2 (2x 8cmx16cm) have been used in the simulation

The variation of the cathode sheath thickness s during the pulse is presented in Fig 3 3 8 The values are in good agreement with those measured at 3mtorr (Ar) in a planar DC magnetron by Rossnagel [36] The calculation assumes that the time-dependent sheath obeys the Child-Langmuir law at each instant during the pulse, an assumption also used by Scheuer [24] in describing the propagation of a transient sheath during a pulse of high negative voltage applied in PIII

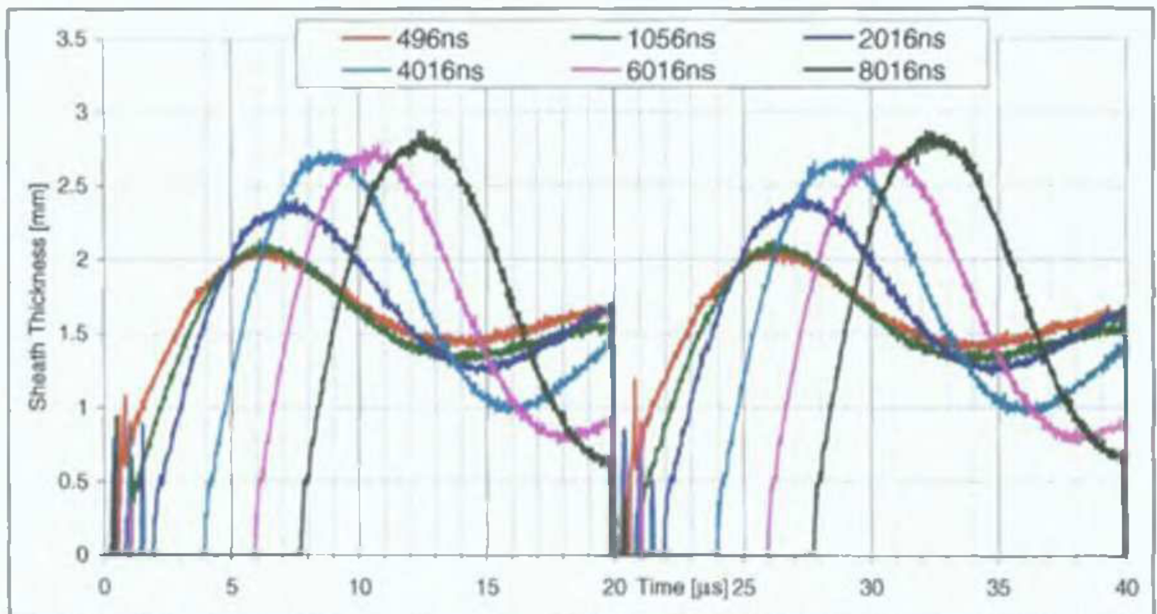

Fig.3.3.8. The sheath thickness for pulse-off times from 496ns to 8016ns, 50kHz, I=2A, p=3mtorr, calculated from the Child-Langmuir law and the I-V waveforms.

The resulting cathode sheath thicknesses for several values of the pulse-off time, at 50kHz, 2A current run and 3mtorr Ar pressure are presented in Fig.3.3.8. The time dependent sheath thickness calculated using the Child-Langmuir formula has a strong variation of its extent during the pulse.

The electric field E in the cathode sheath is given by [4]:

$$E = \frac{4}{3}\frac{V_c}{s}\left(\frac{z}{s}\right)^{1/3}; \tag{3.3.21}$$

where s is the sheath thickness, V_c the cathode potential and z the distance to the cathode.

The secondary electrons generated during the sputtering process are accelerated in the cathodes sheath at high voltages and produce ionizations in the plasma bulk. The magnetic confinement will dictate their path and confinement time as well as the resulting ion density distribution in the bulk.

Once ionized, the gas ions have to travel towards the targets in order to continue the sputtering process.

d) The Electric Field in the Plasma Pre-Sheath

The plasma pre-sheath is a transition layer between the neutral plasma and the cathode sheath that maintains the continuity of the electric field at the plasma-sheath boundary, thus giving rise to an electric field across the transition region due to a positive plasma potential V_p.

This electric field in the transition layer ensures the ion drift towards the cathodes with at least the Bohm velocity and allows the continuity of the ion flux. The requirement for a certain electric field that allows ions from the plasma bulk to reach the targets, ensuring a constant ion flow towards the targets [4] leads to the concept of Bohm velocity u_B, as the minimum velocity

the ions should acquire in the pre-sheath in order to reach the targets:

$$u \geq u_B = \sqrt{\frac{kT_e}{M}} \; ; \qquad (3.3.22)$$

The Bohm velocity has as a low limit given by the thermal average velocity of the gas atoms:

$$u_B \geq \sqrt{\frac{kT_g}{M}} \text{ : where } T_g \text{ is the gas average temperature.} \qquad (3.3.23)$$

This means that the velocity acquired by the ions in the pre-sheath has to be at least the Bohm velocity, which has to be higher than the ions' velocity at the average gas temperature.

The consequences of these simple requirements will be clearly shown in the results of the simulations presented in this paper, as the ions located at regions with low pre-sheath electric field reach the targets with low probability, their motion being random and dictated mainly by their temperature.

According to the considered gas temperature, the electric field in the pre-sheath has to overcome the initial (thermal) ion energy in order to bring them to the targets. The higher this initial ion energy, the higher has to be the required value for the electric field in the pre-sheath.

A schematic of the plasma discharge bulk is presented in Fig.3.3.9, indicating the expected behaviour of the electric field, given by the formation of the cathodes' sheath and the plasma pre-sheath covering the centre of the bulk.

Models for the formation of a pre-sheath in pulsed discharges have been mainly developed for Plasma Immersion Ion Implantation (PIII) applications. Here, in some models, the pre-sheath develops only if the expansion speed of the sheath edge is slower than the ion acoustic speed [24], while other models assume that the pre-sheath exists independent of the propagation speed of the sheath [37]. The results from measurement [25] and simulations [26] demonstrate that in the case of PIII discharges (for sudden electrode voltage jumps) the pre-sheath develops with a delay given by the time the information about the changes at the electrode travels with the ion acoustic speed.

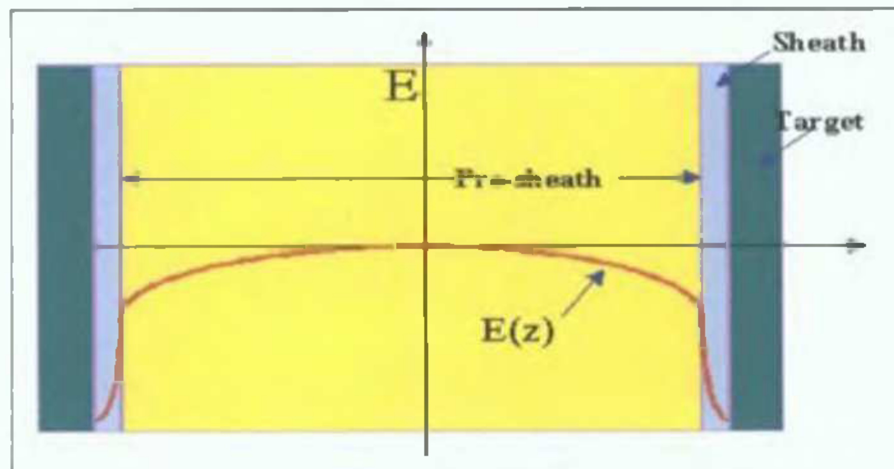

Fig.3.3.9.Sheath and pre-sheath models for the electric field behaviour (schematics).

The evolution of the pre-sheath observed experimentally [25] and by PIC/MC simulations [26] indicates a slow expansion that continues for more than 10μs after the sheath collapsed.

For pulsed DC discharges, after the voltage waveform has reached the maximum value, the pre-sheath is formed, its evolution is slow and its extent can be considered quasi-constant. Space and time-resolved Langmuir probe measurements [7] in a 100kHz pulsed rectangular magnetron system show that the plasma potential has positive constant values (~ few volts) during the pulse-on phase, in a planar magnetron. The constant plasma potential during the pulse-on time supports the idea of a pre-sheath field independent of the voltage oscillations on the cathodes.

Therefore, the present model assumes that once formed, the pre-sheath has a quasi-constant extent and a constant value of the electric field. The pre-sheath considered in this model extends from the sheath edge towards the centre of the discharge, with an electric field independent of time.

Several functions of distance for the electric field in the pre-sheath will be used in the present MC simulation in order to evaluate the function of distance and the intensity range of the pre-sheath electric field necessary to give the observed value of ions' travel time to targets.

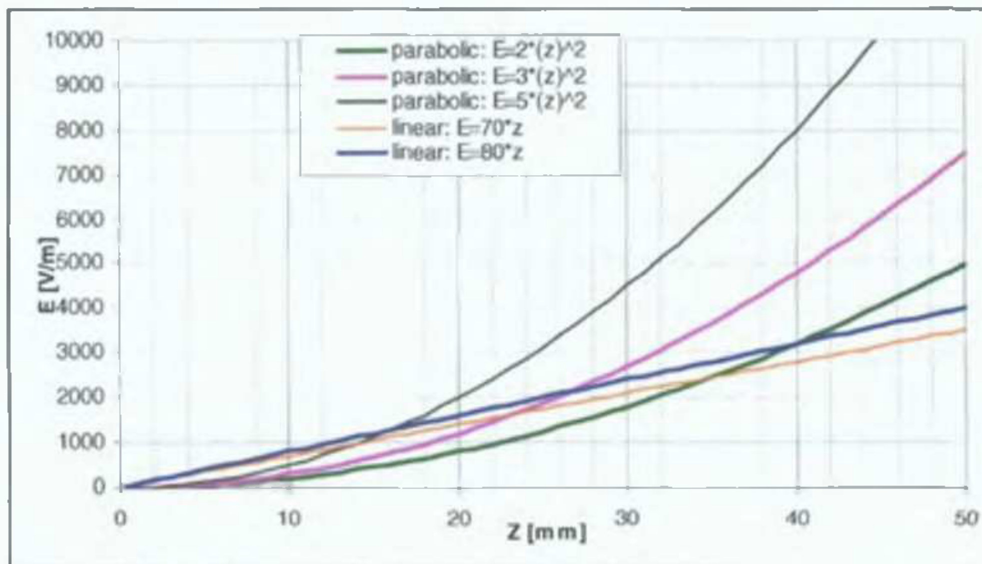

Fig.3.3.10. Several types of pre-sheath electric field functions.

The pre-sheath electric field has been chosen from several linear and parabolic functions represented in Fig.3.3.10.

For the MC analysis, two functions have been selected for use in the model in order to assess their suitability for describing the pre-sheath electric field:

- a linear function of the distance z from the discharge centre to the targets:

$E(z)=80*z$ [V/m], where z is expressed in [mm]; (3.3.24)

- a parabolic function of z: $E(z)=3*z^2$ [V/m] where z is expressed in [mm]. (3.3.25)

3 4 THE MONTE CARLO SIMULATION FOR Ar IONS

3 4 1 THE START DATA

The start data necessary for the input of the MC simulation that have to be determined experimentally, in order to keep an accurate discharge model consist of the following

a) The value for the Ar ion transit (travel) time to targets determined experimentally,

b) The relative ion density distributions,

c) The start moment during the pulse

Other start data are included in the initial model, as the ions' start energy and the gas pressure

The Ar ion initial energy considered here is the kinetic thermal energy at a temperature of 300°K, E=0 0387eV and the Ar gas pressure is 3mtorr (0 4Pa)

The initial ion density at the start location and moment in the discharge is determined from the relative intensities of the time and space resolved Optical Emission Spectroscopy (OES) data for Ar ion lines as it will be shown next The time-resolved OES measurements were performed with the optical probe placed in the centre of the discharge, while for the space and time-resolved OES measurements the probe was placed parallel to the targets surfaces, at a distance of 20mm from the targets edge, viewing points between the targets (at z=10mm, 20mm, 30mm and 40mm from the target surface) corresponding to the planes indicated in Fig 3 3 5 For the MC simulation, the ions start planes will be considered at the same distances in order to match the relative intensity of Ar ion emission lines (and their relative density) to the weight in the averaging of results over the bulk volume

The travel time to targets of Ar ions is determined experimentally from time-resolved OES data as will be explained next and it will be used for comparison with the results of the MC computation of Ar ion travel time to targets to evaluate the best fit to the electric field in the pre-sheath

a) The Ion Transit Time –Experimental Values

The time-resolved OES provides information on the intensity of the Ar ion emission lines during pulse and on the ion transit time to the targets For the OES analysis, the Acousto-Optic Spectroscopy Analyser (IfU) AOS-4 presented in Chapter (2 3) has been used

The evolution of the most intense Ar ion line (488nm) in the OES line spectrum was observed A typical example is presented in Fig 3 4 1, along with the power waveform We can observe the delay between the applied power peak and the Ar ion line intensity peak This 2 5μs delay is attributed to the average time needed by the Ar ions to return to the targets and produce (through sputtering) the secondary electrons that will maintain the discharge The considerations leading to this conclusion are largely presented in Chapter (5 2) and a recent published paper [38]

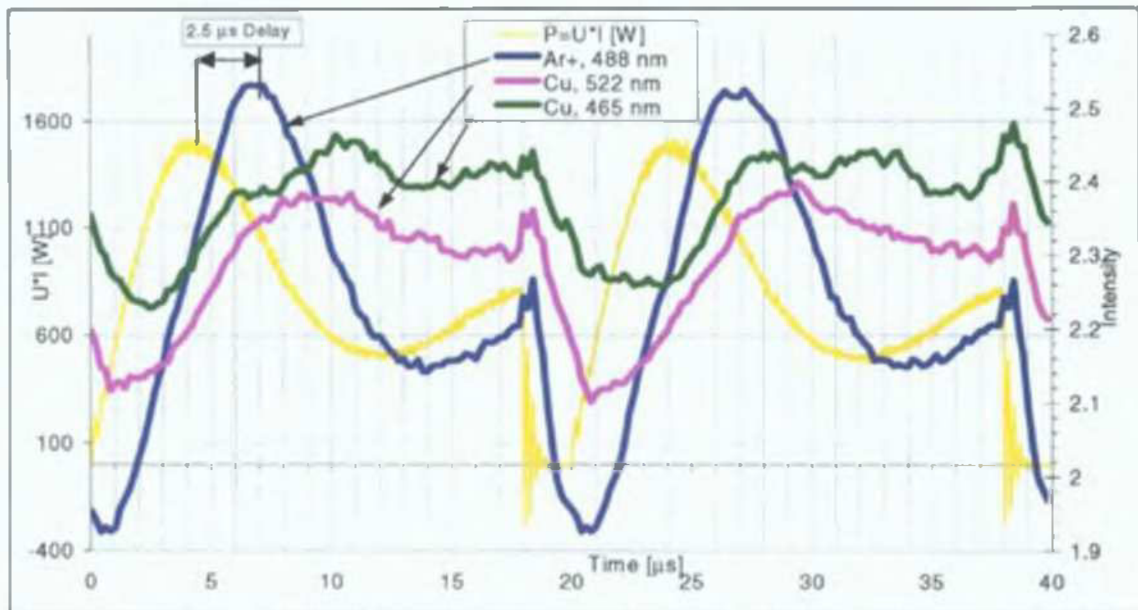

Fig.3.4.1.Time-resolved OES and the power waveform for a 50Khz, pulse off time 2016ns, I=2A pulsed DC discharge at 3mtorr (0.4Pa) Argon pressure.

The Ar ions created in the plasma bulk at the moment when the power peak has a maximum (t=4.5µs, Fig.3.4.1) travel back to the targets and produce more secondary electrons which generate the maximum Ar ion peak at t=7µs. This travel time of the Ar ions to the targets generates the delay between the power peak and the Ar ion peak.

The shape of the Ar ion peak follows closely the one of the applied power peak indicating that ionization is mainly due to direct electron impact processes - which is expected at the low pressures and high electron energies in this type of discharge.

As observed in Chapter (5.2) the ~2.5 µs delay between the Ar ion emission peak and the power peak has almost constant values with the pulse-off time, showing that this is a characteristic of the magnetron discharge at a certain pressure and it is due to the time the Ar ions need to travel from the location where they were produced, to the targets. This value will be later compared with the results from the MC simulation of Ar ion transit time to targets for each considered pre-sheath electric field.

b) The relative ion density distributions

The space and time-resolved OES analysis provides information on the relative distribution of Ar ion density (ionization density) in the bulk discharge. Fig.3.4.2 shows the relative intensity distribution of the 488nm Ar ion emission line over a cross-section of the bulk discharge during the pulsed DC operation at 50kHz, 2016ns pulse-off time and 2A constant current run. The ions are distributed mainly in the centre of the bulk with a strong increase in the ion density in a region situated at 30mm to 40mm from the targets. (10mm to 20mm from the discharge centre).

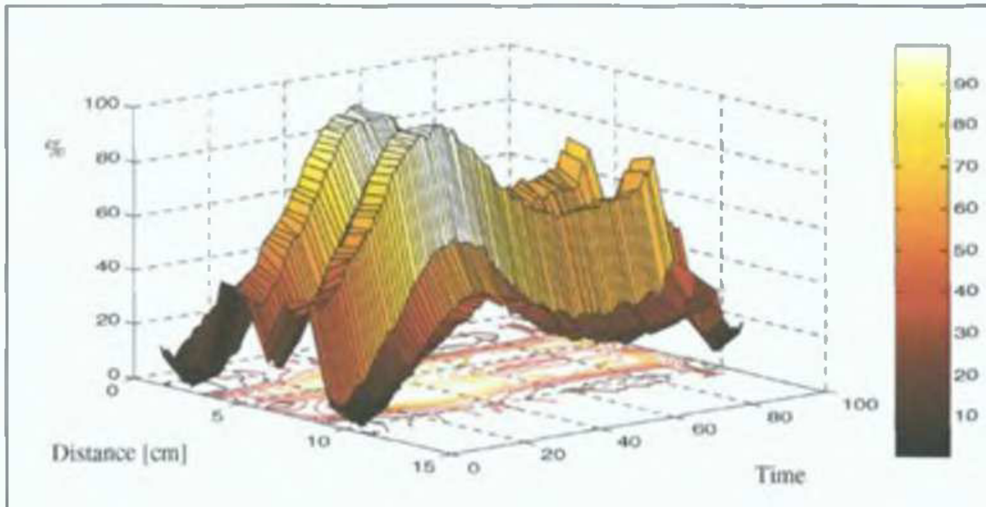

Fig.3.4.2: 3D relative Ar ion emission lines intensity in the bulk from time and space –resolved OES. Time intervals: 0.2 μs.

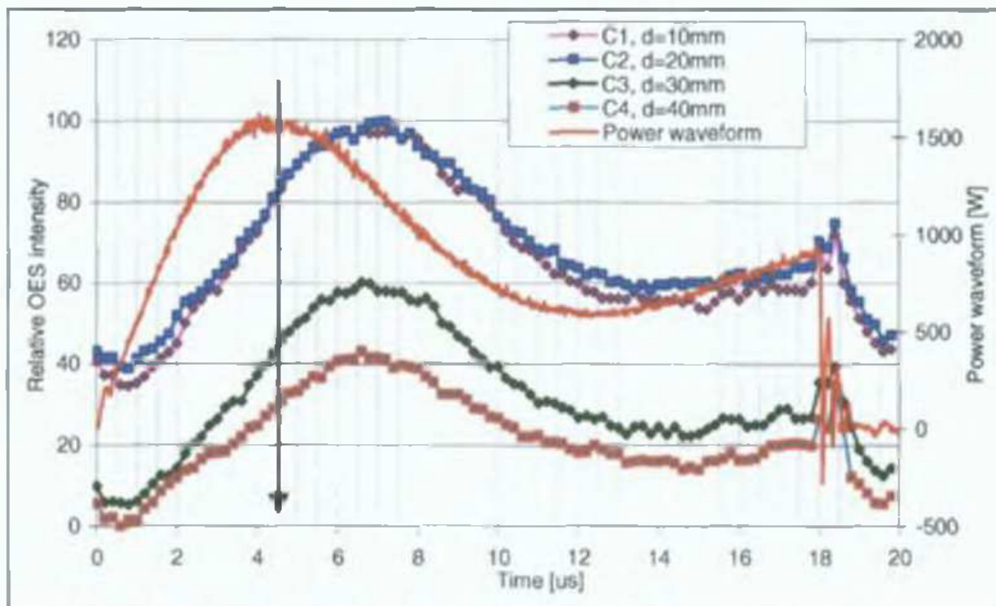

Fig.3.4.3: The relative Ar ion emission lines intensity from time and space–resolved OES at 50Khz, 2016ns, 2A and the Power waveform on the cathodes. Time resolution: 0.2μs. The arrow indicates the start moment in the simulation, coinciding with the maximum power peak.

The space-resolved Ar ion density distribution in the bulk will be used in the MC simulation to establish the start position and time for the Ar ions as well as their relative density at the start moment and location in the discharge. The statistical weights will be taken from the ions relative density (OES intensity) at the start moment (indicated by an arrow in Fig.3.4.3).

c) The start moment during the pulse.

The start moment for the ion simulation can be chosen at any moment of the pulse situated at or after the voltage peak, when the pre-sheath extent and electric field can be considered constant. In the considered model, the start moment of the simulation was taken as the moment when the voltage reaches the maximum value (t=4.5μs).

3.4.2 THE SIMULATION FOR Ar IONS

A short review of the simulation parameters for Ar ions is presented next.

The MC simulation follows Ar ions on 3D trajectories in a pulsed DC magnetron discharge during the pulse-on time of a pulsed DC operation (50kHz, pulse off time 2016ns and 2A constant current run) at an Ar gas pressure of 0.4Pa. The magnetic field values are calculated at each time step of 0.02μs using the current sheet method.

The extent of the plasma sheath *s* is calculated at each time step from the Child–Langmuir formula, where the ion current density is obtained from the measured discharge current waveform, assuming a constant secondary emission coefficient of γ=0.1.

The ions' start positions are chosen on several planes situated at distances *z* of 10mm, 20mm, 30mm, 40mm from the targets and x positions in the XZ cross-section situated 5mm apart: x=0mm, 5mm, 10mm, 15mm, 20mm, 25mm, 30mm, 35mm and 40mm, thus covering a quarter of the plasma volume between the targets (Fig 3.3.5). The chosen start positions for the ions correspond to the positions (planes) where the relative ion density is known in our experiment from the space and time-resolved OES data.

The moment in time from the start of the pulse when ion's trajectories are started corresponds to the maximum peak of the space and time-resolved OES (or just time-resolved OES), at 4.5μs from the start of the pulse, as most of the ions are created around that moment during the pulse.

The ions start energy is 0.0387eV, corresponding to a gas temperature of ~300°K and their initial velocities have randomly distributed directions.

The ions trajectories are followed until they reach the targets or they leave the discharge, at a limit of 100mm on the Y direction (along the targets length) and 60mm on the X direction (on the targets width).

Both elastic and charge-exchange collisions with the neutral gas atoms having random velocities and an energy corresponding to the gas temperature (0.0387eV) were taken into account. The collisions with the sputtered metal atoms and ions are not taken into account. The collision cross-sections and the type of interaction are also calculated at each time step.

The precision of the MC simulation is influenced by random and statistical error. The statistical error is related to the simulation procedure and the considered model. The random error can be maintained low by running a large number of particles. We have chosen to run 1000 ions from each start location, which brings the total ion number run from each considered plane (layer) of the plasma bulk to 9000 and the overall total to 36000. All final values are presented as weighted averages (to the relative ion density at the starting point) and normalized to the number of particles run.

3.4.3. RESULTS FOR Ar IONS

a) Ar ions mean transit times

A histogram representation of the transit time for Ar ions from their start location to the targets (or until the end of the pulse-off time) is presented in Fig.3.4.4 and Fig.3.4.5.

The considered time bin size is 0.2µs. Results are normalized to the total number of particles run from each layer (9000). Each time bin contains the relative number of ions that ended their transit in the respective time bin. This representation indicates directly the most probable time needed by ions from each start layer to reach the targets. The last bin (situated at t=13.5µs) indicates the percentage of ions that have not reached the targets and are left in the bulk at the end of the pulse-on time.

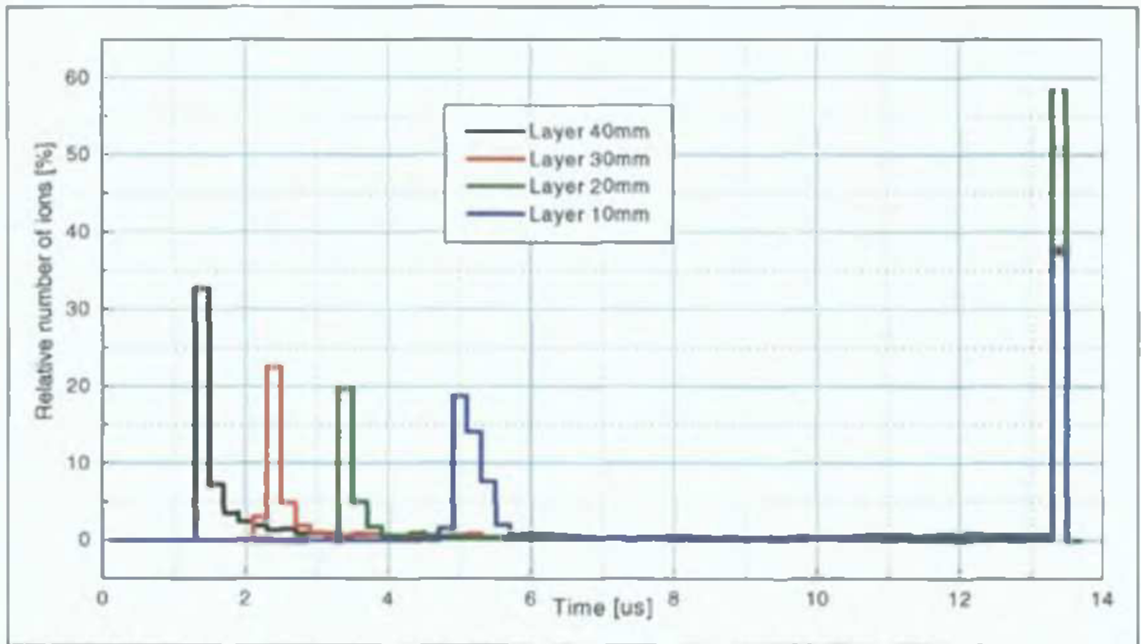

Fig.3.4.4. Ar ion transit times statistics for the linear pre-sheath field: E(z)=80*z.

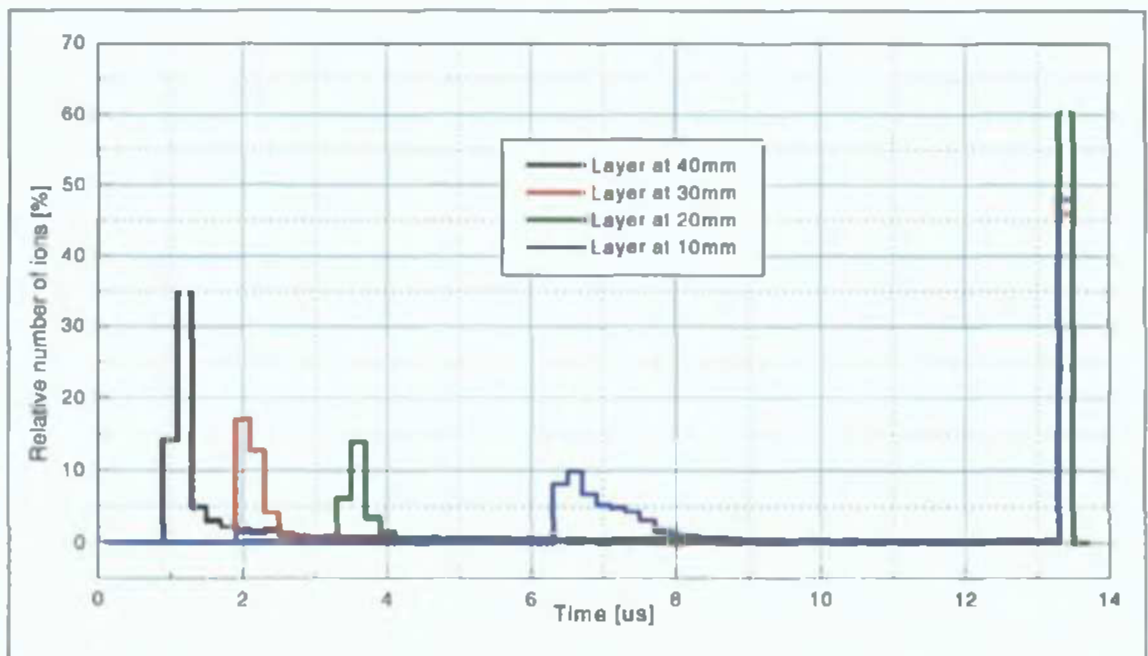

Fig. 3.4.5. Ar ion transit time statistics for the parabolic pre-sheath field: $E(z)=3*z^2$.

The most probable value for the return time to targets of Ar ions is given by the statistical charts (Fig.3.4.4 and Fig.3.4.5), where the average travel (transit) time to targets (TT) can be calculated using a weighted average of the most probable transit times of ions starting in each layer:

$$[TT] = \frac{\sum_i w_i p_i (TT)_i}{\sum_i w_i p_i}; \quad (3.4.26)$$

where:

- $(TT)_i$ =the most probable transit time for the layer (i);
- W_i =the initial Ar ion density in layer (i);
- P_i =relative number of ions reaching the target for layer (i).

The initial Ar ion density W_i is taken from Fig.3.4.3, as the relative OES intensity at the moment t=4.5µs when the simulation starts (at maximum power peak).

The obtained values for the travel time to targets of Ar ions starting in the layer situated at z=10mm from the discharge centre indicate that these ions arrive at the targets much later (at t=5 µs and 6.5µs from the ions' start) than the ions starting from layers situated closer from the targets and will not be responsible for the intense sputtering that generates the Ar ion peak maximum at 7µs (2.5µs after the power peak). Therefore, the transit time of ions starting in layer z=10mm should not be included in the weighted average.

The average travel time to targets of Ar ions calculated for each type of pre-sheath field, for the first 3 layers (z=40mm, z=30mm and z=20mm) and respectively including the fourth layer (z=10mm, highlighted results) are presented in Table 3.4.1.

Function E(z); [V/m]	Layer z[mm]	W_i [%]	P_i [%]	$(TT)_i$ [µs]	[TT] [µs]
linear: $E(z)=80*z$; z[mm]	40	30	33	1.4	2.57
	30	43	23	2.4	3.26
	20	80	20	3.4	
	10	80	18	5	
parabolic: $E(z)=3*z^2$; z[mm]	40	30	35	1.3	2.42
	30	43	17	2.1	3.3
	20	80	14	3.7	
	10	80	10	6.5	

Table 3.4.1. Values of the travel time to targets for Ar ions.

Values of ~2.5µs are obtained when performing the weighted average for the first 3 layers. Including in the average the layer z=10mm, the average transit time increases to ~3.3µs.

As the OES Ar ion emission has a flat peak centred at t=2.5µs from the power peak maximum and extending up to t=3µs after the power peak maximum, the values obtained for the Ar ion transit time are in good agreement with the experimental observations, therefore, the chosen pre-sheath electric fields are a good approximation for the sought fields.

The considered pre-sheath functions provide the required value for the average travel time to targets for the Ar ions.

b) Energy distributions for Ar ions

An analysis of the ions' energy at the end of their path (or the end of the simulation) provides more information on the influence of the considered pre-sheath fields on the sputtering process.

The distribution of translation energies for Ar ions reaching the targets has a wider spread and higher energies for the parabolic pre-sheath field than for the linear pre-sheath field Fig.3.4.6, Fig. 3.4.7).

According to their start layer, the ions are accelerated over different distances, leading to a different energy distribution at the cathode sheath edge. These energy distributions are generated by:

- The random initial distribution of Ar ion velocities;

- The variations in the magnetic field direction and intensity that can change ions' direction through magnetic mirror effects;

- The distance from the cathode where the ions simulation starts;

- The moment during the pulse when the ions reach the cathode sheath edge and the value of the electric field in the cathode sheath at that moment.

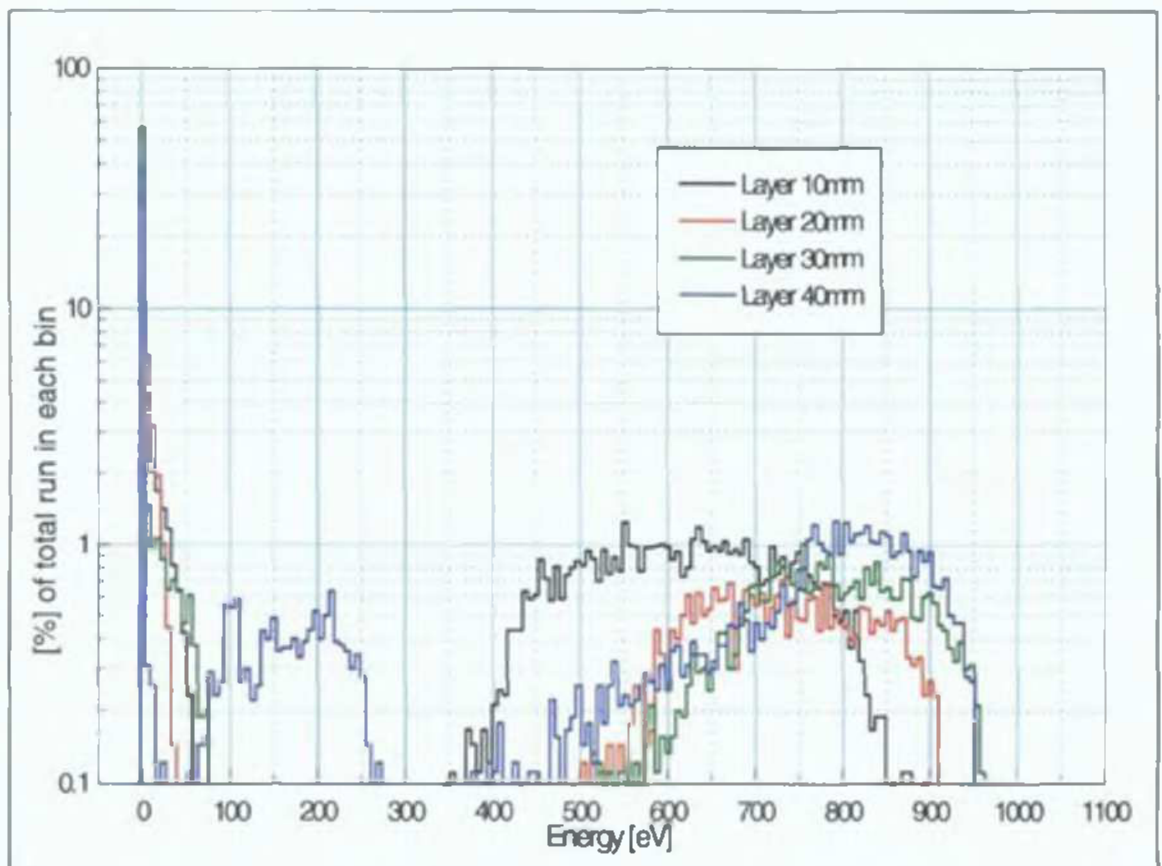

Fig.3.4.6. Ar ion translation energy distribution for linear pre-sheath field. The ions start from several layers. Energy bin: 10eV.

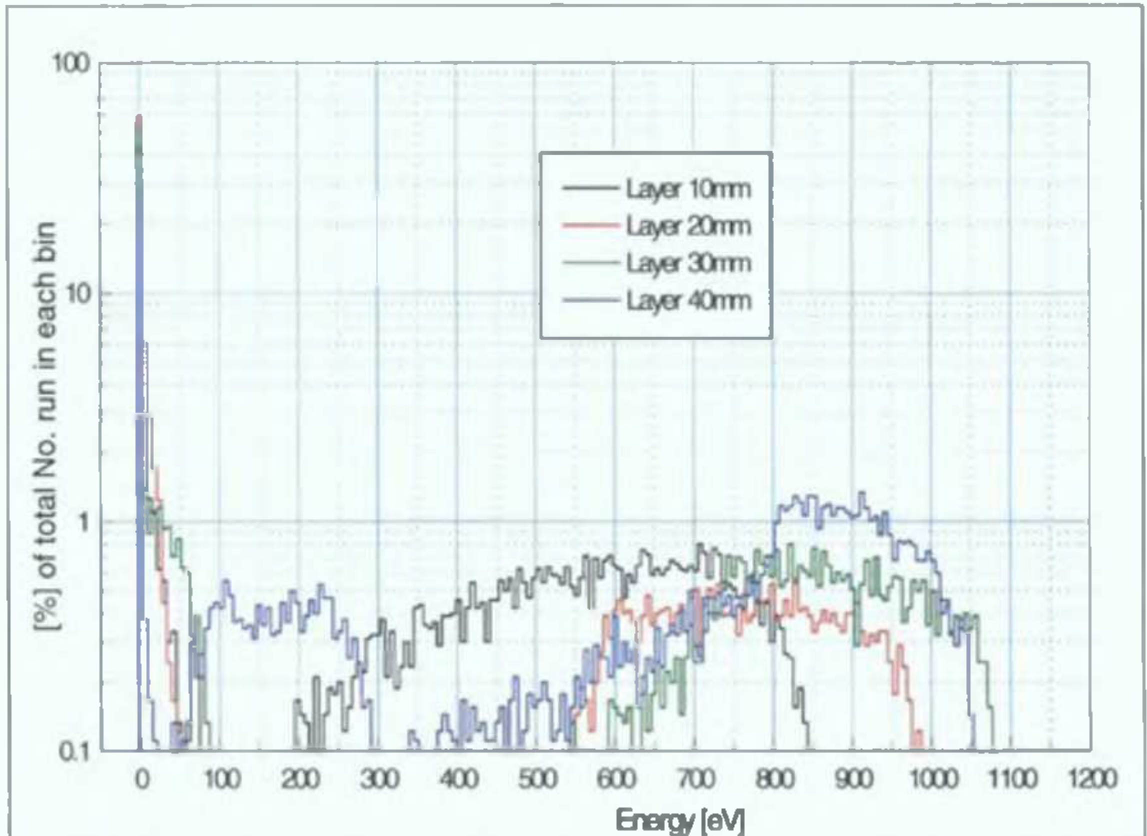

Fig.3.4.7. Ar ion translation energy distribution for parabolic pre-sheath field. The ions start from several layers. Energy bin: 10eV.

The distribution of gyration energy is similar for both types of fields, with very small percentage of ions with gyration energy in the high-energy bin. In the case of gyration energy, as can be seen from Fig.3.4.8 and Fig.3.4.9 most ions (up to 70% of all ions) have gyration energies in the lowest energy bin (0-10eV).

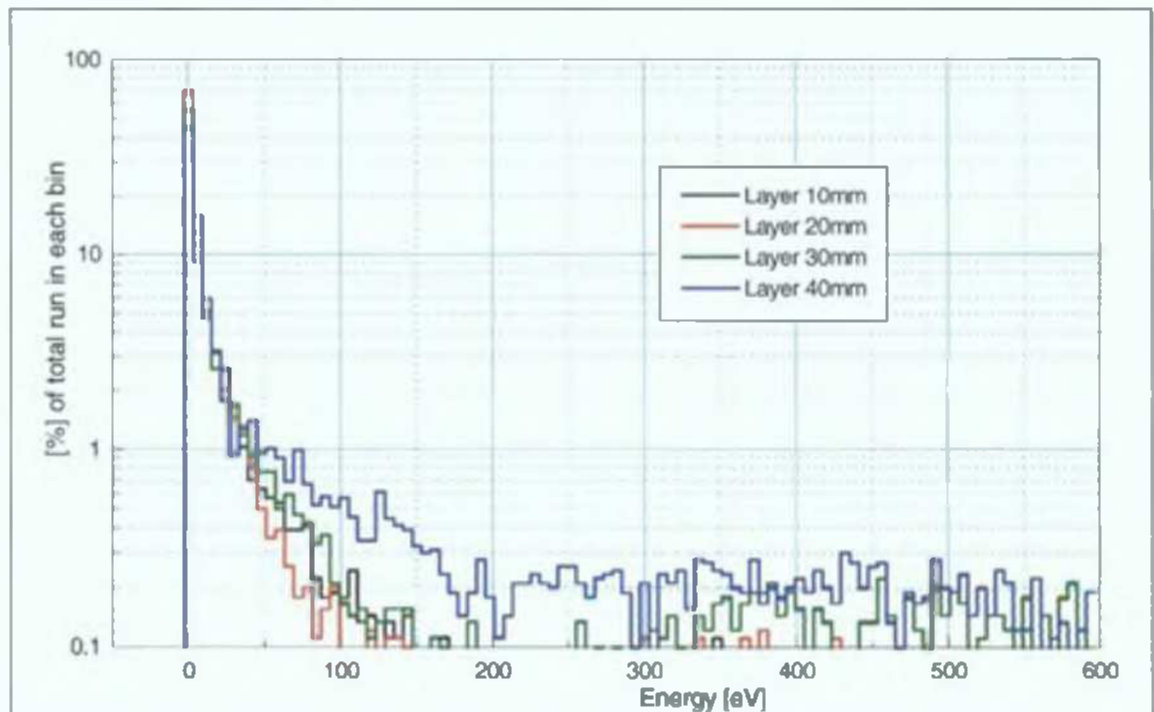

Fig.3.4.8. Ar ion gyration energy distribution for linear pre-sheath field. Energy bin: 10eV.

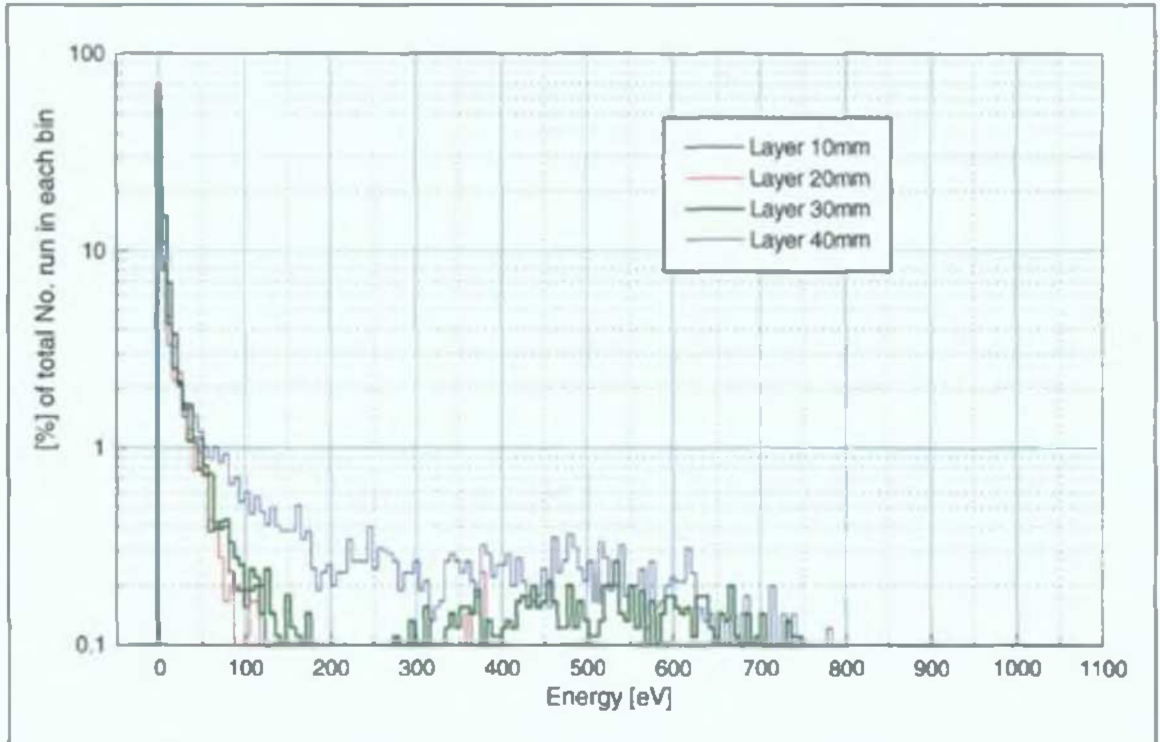

Fig.3.4.9. Ar ion gyration energy distribution for parabolic pre-sheath field. Energy bin: 10eV.

From the energy distribution of translational energies, (Fig.3.4.10 and Fig.3.4.11) we can notice that 45% to 63% (for a linear pre-sheath field) and 42% to 73% (for a parabolic pre-sheath field) of the Ar ions actually reach the targets during the pulse-on time, according to their start layer.

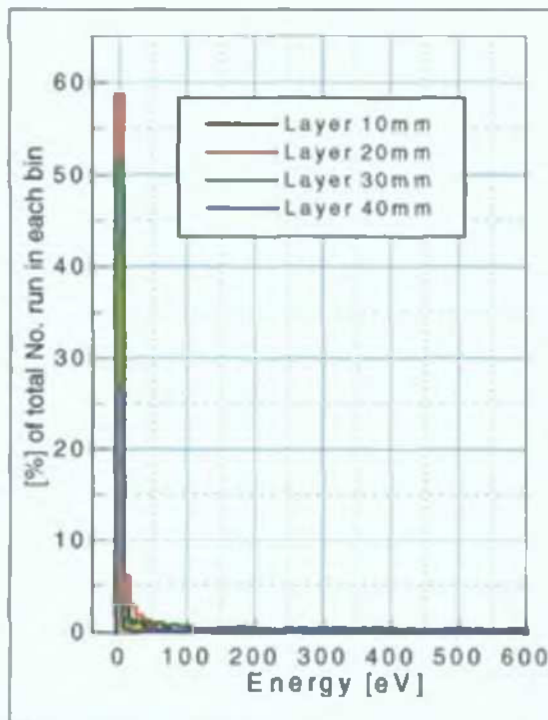

Fig.3.4.10. Total energy distribution for gyration energy of Ar ions in linear pre-sheath field.

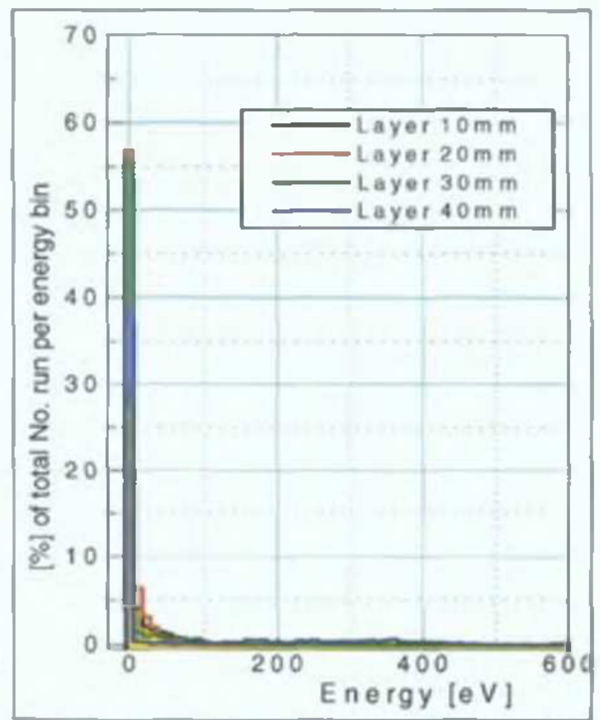

Fig.3.4.11. Total energy distribution for translation energy of Ar ions in linear pre-sheath field.

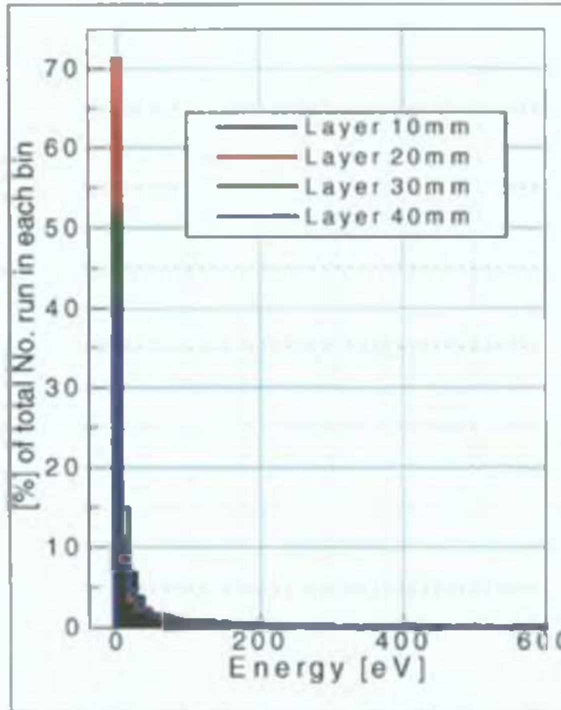

Fig.3.4.12. Total energy distribution for gyration energy of Ar ions in parabolic pre-sheath field. Ion simulation starts in different layers.

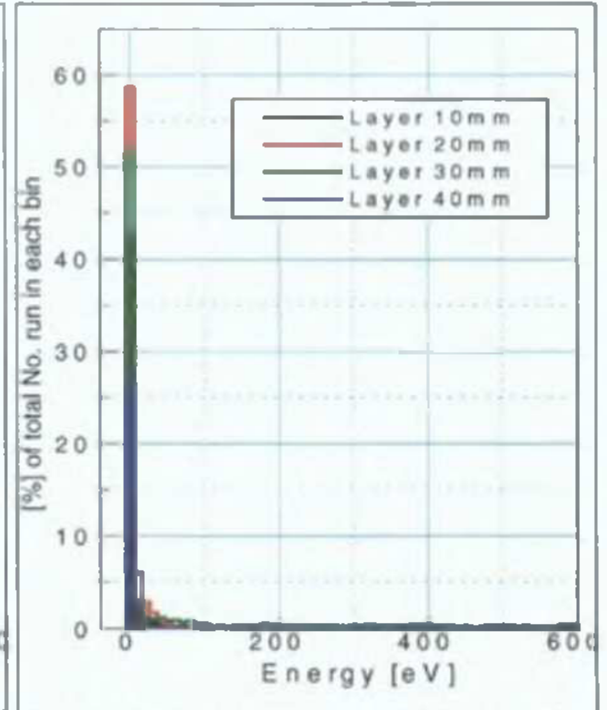

Fig.3.4.13. Total energy distribution for translation energy of Ar ions in parabolic pre-sheath field. Ion simulation starts in different layer.

This is due to the random distribution of the initial direction of the Ar ion velocity and to the fact that the initial Ar ion energy is not considered zero, but a value corresponding to a temperature of 300° K (0.0387 eV). Most of the Ar ions that don't reach the targets are moving back and forth between the targets while they change direction due to magnetic mirror effects, gaining and loosing energy against the pre-sheath electric field. The mean energy of the Ar ions that don't reach the targets is thus around the value of their start (thermal) energy, most of these ions having energies situated in the first 10eV energy bin.

In conclusion, the pre-sheath electric field behaviour in opposed target magnetrons can be investigated through MC calculations coupled to experimental data from space and time-resolved OES.

Two functions that match closely the experimental value for the return time to target for Ar ions have been determined:

-A linear function: $E(z)=80*z$ [V/m] , where z[mm];

-A parabolic function: $E(z)=3*z^2$ [V/m], where z[mm].

Although the parabolic field brings more ions to the targets, as its values are generally higher, there is a higher dispersion in the most probable Ar ion travel time to targets and also in their energies.

3.5. THE MONTE CARLO SIMULATION FOR Cu IONS

3.5.1. THE SELF-SPUTTERING TIME-SCALE

Time-resolved O. E. S. of Ar ions and Cu sputtered atoms in a pulsed DC magnetron discharge shows that the intensities of the exited Cu lines are maintained at almost constant levels for several μs after the Ar ion lines intensity has decayed. This effect can be attributed to Cu self-sputtering.

To assess the amount of self-sputtering and the time scale of this effect relative to the operating duty-cycle in a pulsed DC magnetron, the return time to the targets of the sputtered metal ions have been evaluated through Monte Carlo calculations.

The pulse-on time of a pulsed DC magnetron plasma at 50kHz, pulse-off time 2016ns, 2A constant current run and 0.4Pa Ar gas pressure has been modelled for a magnetron with opposed rectangular copper targets. The same computer code that simulates 3D charged particles trajectories in 3D electric and magnetic fields described in Chapter (3.1) has been used to simulate Cu ion trajectories in the plasma bulk.

The return time to target for Cu ions has been evaluated and compared to the time-resolved OES measurements. The consequences of the self-sputtering and its time-scales are discussed in connection to the starting energy of Cu ions and the operating duty cycle of the magnetron.

3.5.2. THE SIMULATION FOR Cu IONS

A short review of the simulation parameters for Cu ions is presented next.

The MC simulation follows Cu ions on 3D trajectories in a pulsed DC magnetron discharge during the pulse-on time of a pulsed DC operation (50kHz, pulse off time 2016ns and 2A constant current run) at an Ar gas pressure of 0.4Pa. The same MC simulation code and model assumptions as for the Ar ions have been used, with start data specific for the Cu ions. The same two functions for the pre-sheath electric field as shown in Chapter (3.3) have been considered:

- Linear pre-sheath field: $E(z)=80*z$ [V/m];
- Parabolic pre-sheath field: $E(z)=3*z^2$ [V/m];

The start positions for the Cu ions are chosen on several planes situated at distances z of 10mm, 20mm, 30mm, 40mm from the discharge centre and x positions in the XZ cross-section situated 5mm apart: x=0mm, 5mm, 10mm, 15mm, 20mm, 25mm, 30mm, 35mm and 40mm, covering a quarter of the plasma volume between the targets (Fig.3.3.5).

The chosen start positions for the ions correspond to the positions (planes) where the relative ion density is known in our experiment from the space and time-resolved OES data (Fig.3.5.1).

The moment in time from the start of the pulse when Cu ion's trajectories are started corresponds to the moment when the maximum number of Ar ions should have reached the targets: at 10μs from the start of the pulse. At this moment, the density of sputtered Cu atoms has a maximum.

The Cu ions start energy is 0.5eV, corresponding to the most probable energy of Cu atoms from Ar-Cu sputtering, as determined from ACAT calculations [4] and the initial velocities have randomly distributed directions. Cu ions with higher energies will have lower transit times, but their density is much lower, so their contribution can be neglected. The Cu ions are followed until they reach the targets or they leave the discharge, at a limit of 100mm on the Y direction (along the targets length) and 60mm on the X direction (on the targets width).

Both elastic and charge-exchange collisions with the neutral Ar gas atoms having random velocities and an energy corresponding to the gas temperature (0.0387eV) were taken into account. The collisions between Cu ions and Ar ions, or other Cu sputtered metal atoms (ions) are not taken into account. The collision cross-sections and the type of interaction are also calculated at each time step (0.02μs) according the procedure described for the Ar ion simulation.

The number of particles run from each start location is 1000, with 9000 ions run from each considered plane (layer) of the plasma bulk and 36000 in total. All final values are presented as weighted averages (to the relative ion density at the starting point) and normalized to the number of particles run.

3.5.3. THE START DATA:

As in the case for Ar ions, the start data that have to be determined experimentally are:

a) The relative density of Cu ions: from relative OES intensity;

b) The start moment during the pulse.

a) The Space and Time-resolved OES

The time and space-resolved OES for Cu I emission lines indicates a quasi-constant intensity for both 465nm and 522nm Cu I lines. As explained in Chapter (5.2.4) this effect can be related to self-sputtering.

The relative density of Cu ions at different distances from the targets can be estimated directly from the intensity of Cu ion emission lines, when these can be observed, which was not the case for the described discharge.

As detailed in Chapter (5.2) the 465nm Cu I line has an upper level (7.737eV situated above the ionization potential of Cu I) and populated by Cu ion recombination. Assuming at least PLTE, where ionization (excitation) processes are balanced by the recombination (de-excitation), the intensity of the 465nm line is a good indicator of the Cu ion density.

The time and space-resolved OES for the 465nm Cu I line is presented in Fig.3.5.1. The arrow indicates the start moment of the simulation, chosen at t=10μs. The relative density of ions at the start moment is considered in the weighted average to calculate the average return time to targets of the Cu ions.

b) The start moment during the pulse

The start moment during the pulse has been chosen at t=10μs (Fig.3.5.1) when the 465nm OES intensity line has a maximum. At this moment during the pulse, the pre-sheath electric field can be considered quasi-constant and described by the functions considered for the Ar ion transport.

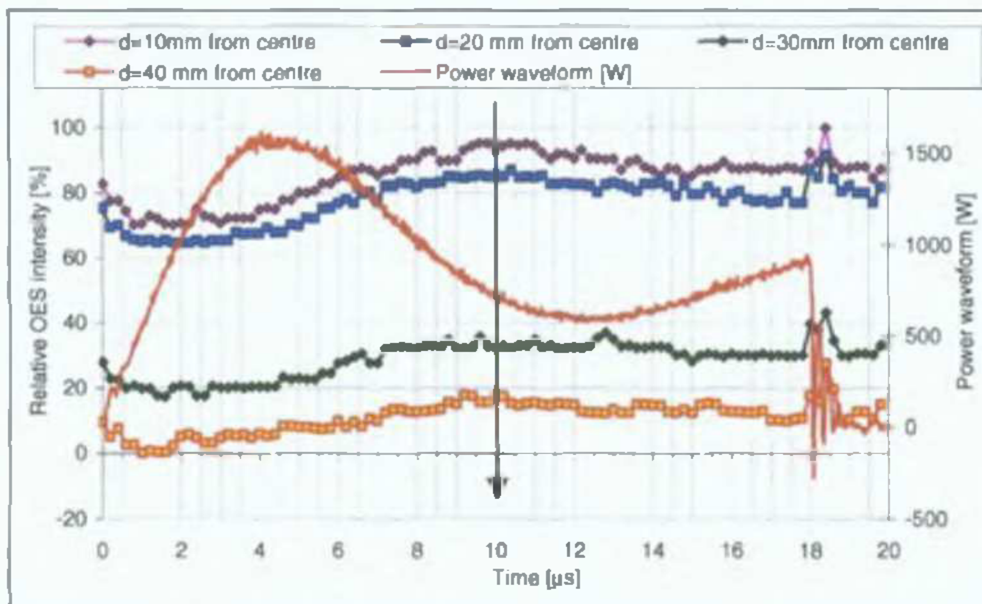

Fig.3.5.1. The relative (normalized) OES intensity for Cu I, 465nm line during the pulse. The arrow indicates the start moment for the simulation.

3.5.4. RESULTS FOR Cu IONS

a) Cu ions mean transit times

A histogram representation of the transit time for Cu ions from their start location to the targets (or until the end of the pulse-off time) is presented in Fig.3.5.2. and Fig.3.5.3.

The bin size is 0.2μs. Results are normalized to the total number of particles run from each layer (9000). Each time bin contains the relative number of Cu ions that have ended their transit during the respective time bin. This representation indicates directly the most probable time needed by Cu ions from each start layer to reach the targets. The last bin (situated at t=8μs from the start moment in the simulation) indicates the percentage of Cu ions that have not reached the targets and are left in the bulk at the end of the pulse-on time.

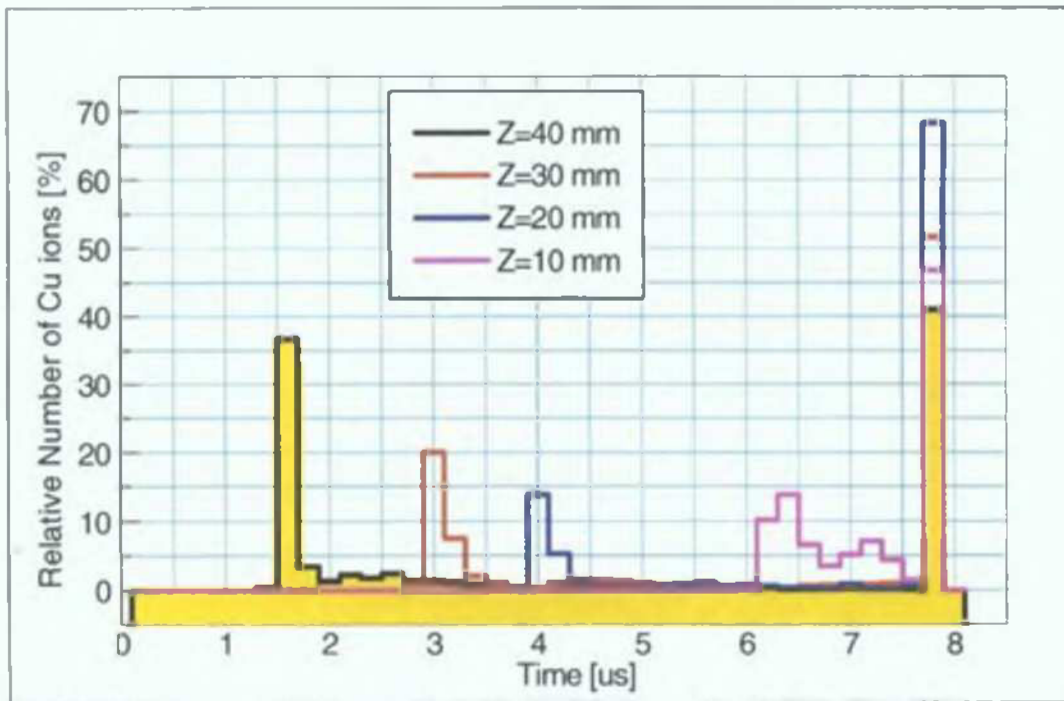

Fig.3.5.2. Cu ions transit times statistics for the linear pre-sheath field: E(z)=80*z.

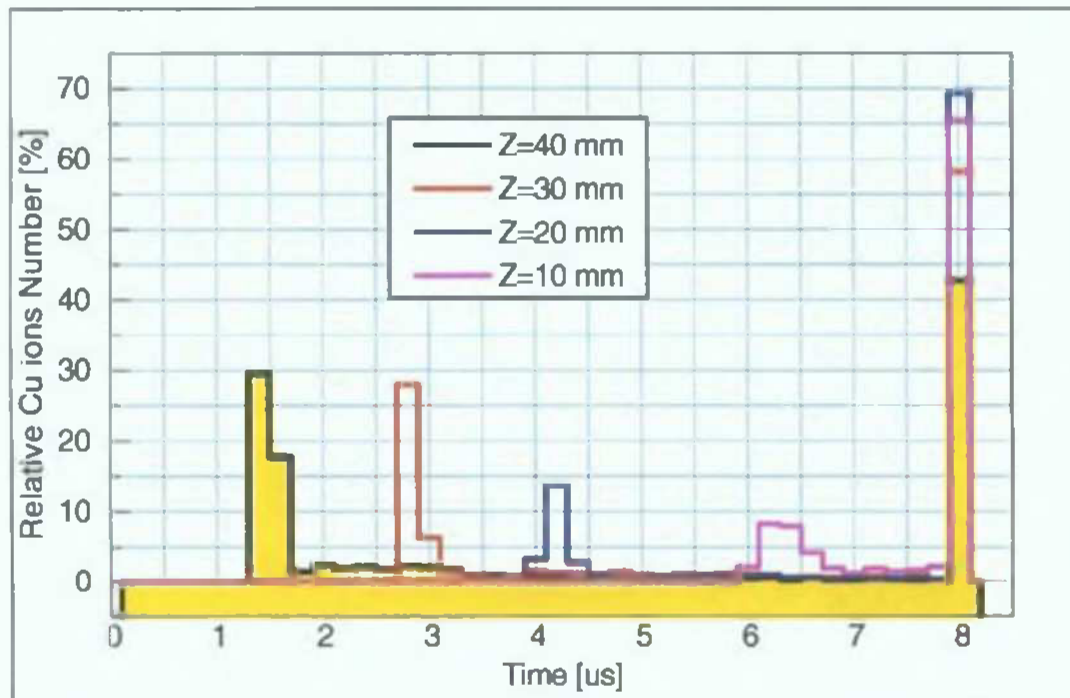

Fig.3.5.3. Cu ions transit time statistics for the parabolic pre-sheath field: $E(z)=3*z^2$.

The most probable value for the return time to targets of Cu ions is given by the statistical charts (Fig.3.5.2 and Fig.3.5.3), where the average return (transit) time to targets (RT) can be calculated using a weighted average of the most probable transit times of ions starting in each layer:

$$[RT] = \frac{\sum_i w_i p_i (RT)_i}{\sum_i w_i p_i}; \qquad (3.5.1)$$

Where:

- $(RT)_i$ =the most probable transit time for ions stating in the layer (i);
- W_i =the initial Cu ion density in layer (i);
- P_i =relative number of Cu ions reaching the target for layer (i).

Function E(z); [V/m]	Layer z[mm]	W_i [%]	P_i [%]	$(TT)_i$ [μs]	[TT] [μs]
linear: $E(z)=80*z$; z[mm]	40	18	37	1.7	3.3
	30	32	22	3.2	4.4
	20	85	14	4.2	
	10	95	14	6.6	
parabolic: $E(z)=3*z^2$; z[mm]	40	18	30	1.5	3.3
	30	32	28	3.0	4.0
	20	85	14	4.3	
	10	95	8	6.5	

Table 3.5.1. Values of the travel time to targets for Cu ions.

The results of the weighted average for both types of pre-sheath electric fields are presented in Table 3.5.1. The weighted average is strongly influenced by the initial ion density in each layer, and therefore by the moment considered as a start for the simulation. Nevertheless, the transit times obtained for the Cu ions indicate that self-sputtering can occur during the pulse-on time and has a time-scale of 3.3 – 4.4μs for Cu ions of 0.5eV.

As the Cu ions have an energy distribution similar to that of sputtered Cu atoms, a better understanding of the self-sputtering time-scale can be obtained by performing a more rigorous study over the entire energy range of the Cu ions.

The results obtained here reflect only the main trend of the self-sputtering time-scale, indicating that self-sputtering can occur for pulse-on times longer than 10μs and can have a significant effect for pulse-on times durations above 14μs.

b) Energy distribution for Cu ions

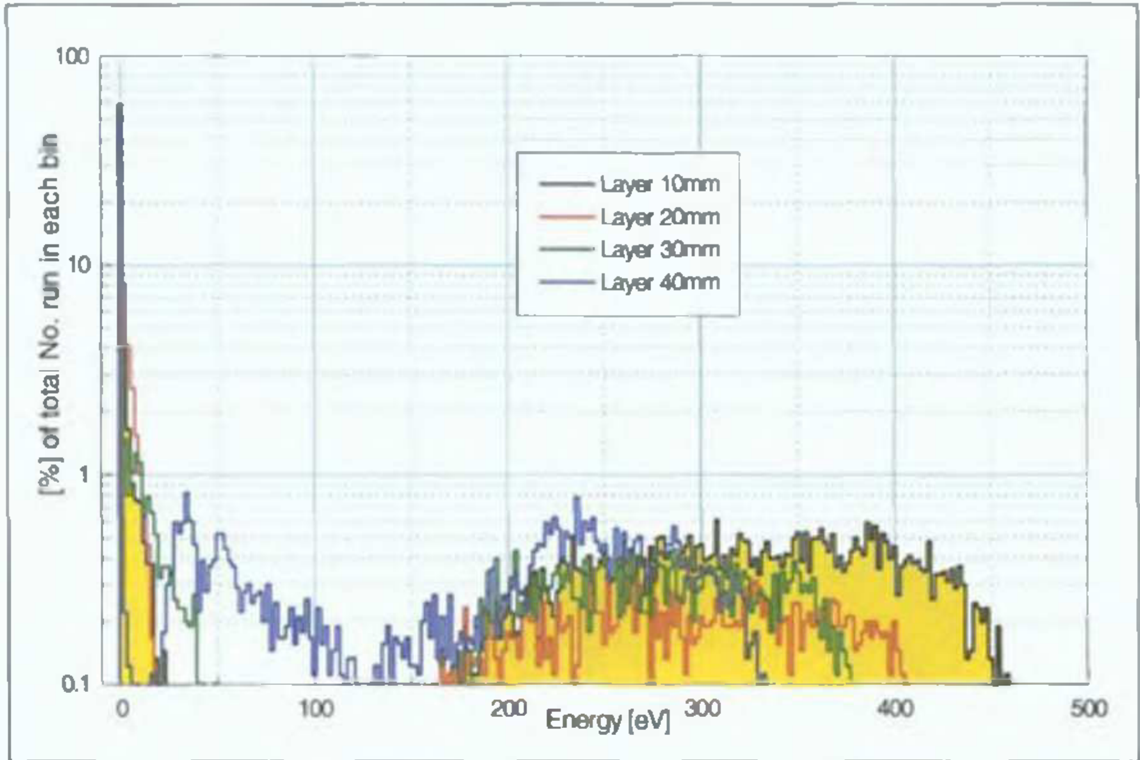

Fig.3.5.4. Cu ion translation energy distribution for linear pre-sheath field. The ions start from several layers. Energy bin: 10eV.

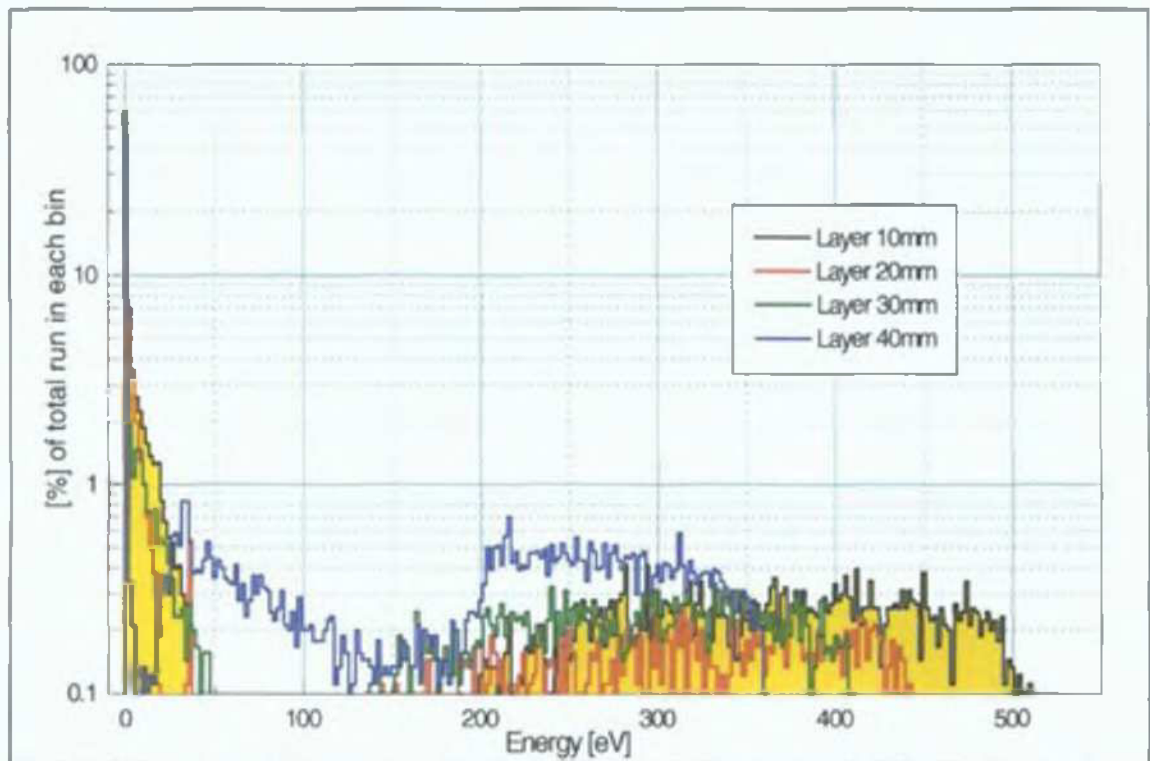

Fig.3.5.5. Cu ion translation energy distribution for parabolic pre-sheath field. The ions start from several layers. Energy bin: 10eV.

The translation energy (impact energy on the targets) for Cu ions has a wider distribution than that for Ar ions and with a lower percentage of particles in each energy bin (Fig.3.5.4, Fig.3.5.5).

The large energy dispersion is due mostly to the initial Cu ion energy of 0.5eV and the random directional distribution of the total velocity. This leads to a large spread in the final energies as well as in a lower percentage of Cu ions reaching the targets (compared to similar data for Ar).

As the start moment for Cu ion formation is considered at t=10μs, there is less time for the Cu ions to travel to the targets until the end of the pulse-on time. A larger percentage of Cu ions than Ar ions will be trapped in the bulk at the end of the pulse on time. The ions starting in layer z=10mm, can reach the highest energies, as they are accelerated over a larger distance, entering the cathode sheath at higher energy.

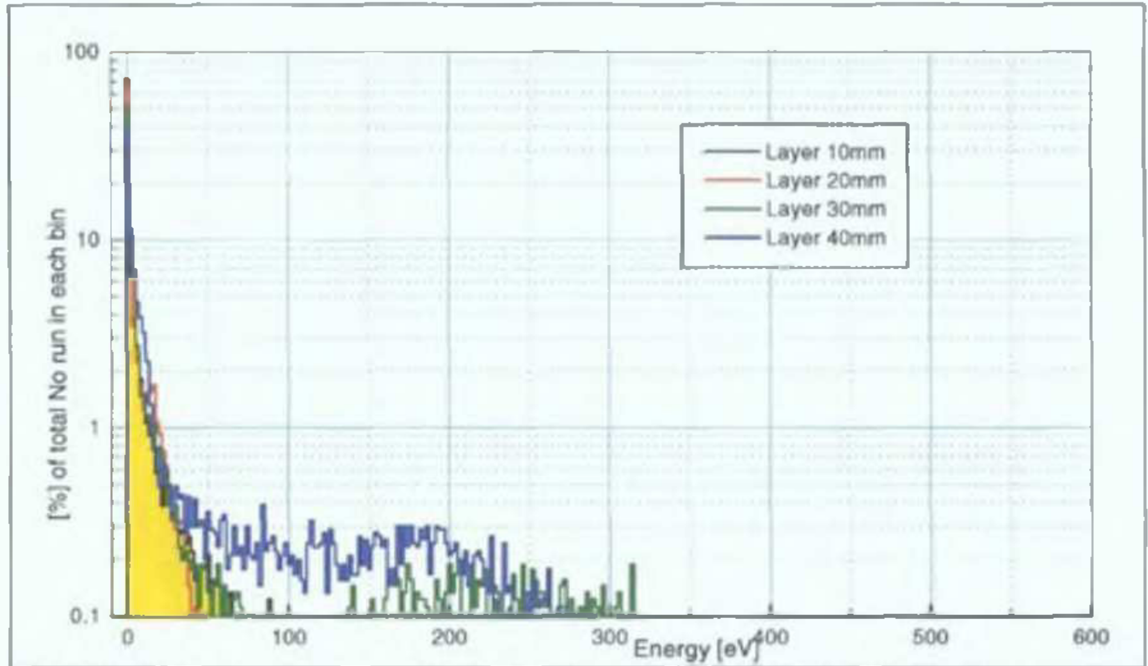

Fig.3.5.6. Cu ion gyration energy distribution for parabolic pre-sheath field. The ions start from several layers. Energy bin: 10eV.

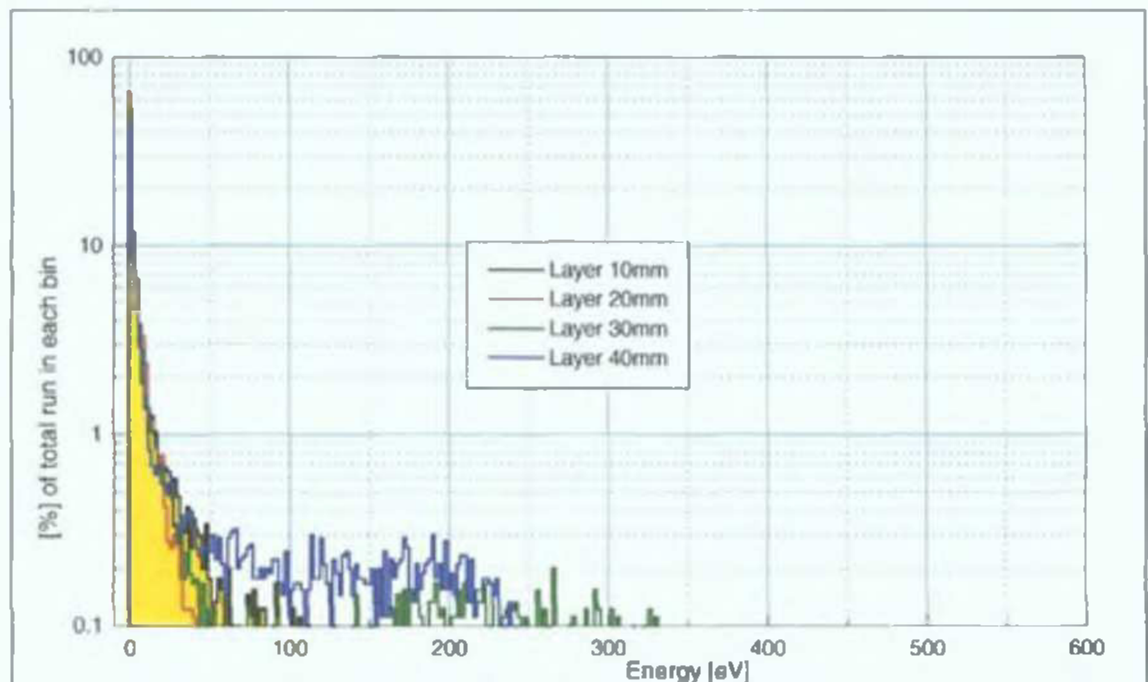

Fig.3.5.7. Cu ion gyration energy distribution for linear pre-sheath field. The ions start from several layers. Energy bin: 10eV.

The distribution of energy due to gyration is much wider and presents an exponential decrease with energy (Fig.3.5.6 and Fig.3.5.7). Only ions starting from layer 40mm have significant increase in the gyration energy. Again, this is due to the initial Cu ion energy of 0.5eV and its random directional distribution.

The gyration energy component has also a large distribution over the energy values, with insignificant percentages in the high-energy bins. The Cu ions starting in the layer 40mm have larger gyration energy values, again, due to their random distribution of the start velocity direction.

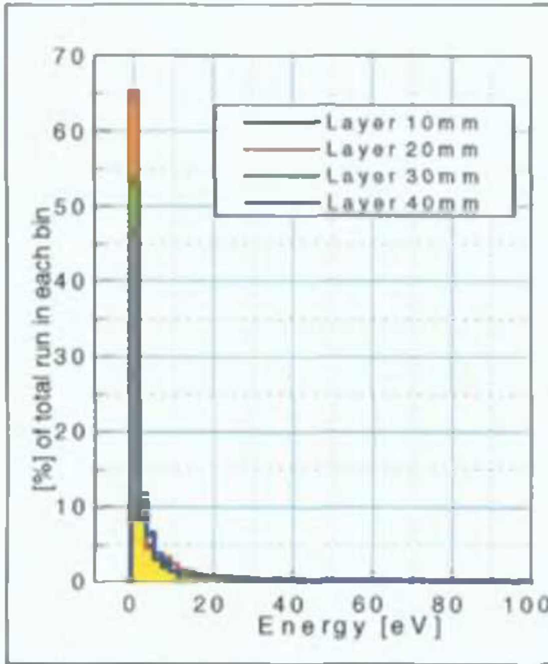

Fig.3.5.8. Total energy distribution for gyration energy of Cu ions in linear pre-sheath field.

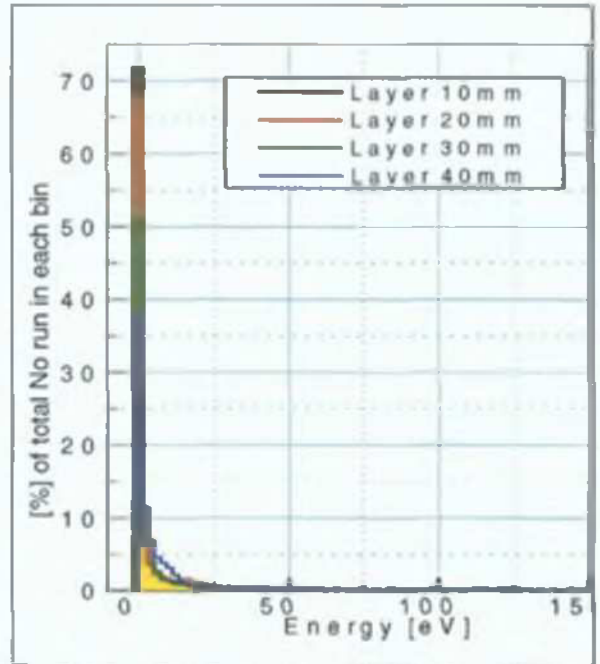

Fig.3.5.9. Total energy distribution for gyration energy of Cu ions in parabolic pre-sheath field.

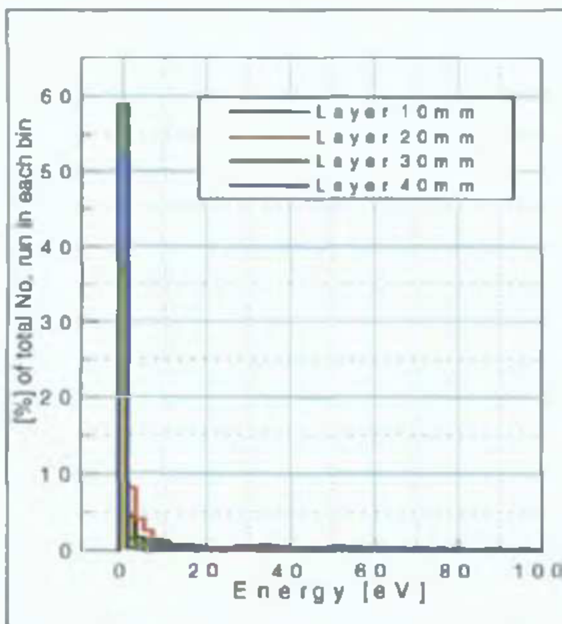

Fig.3.5.10. Total energy distribution for translation energy of Cu ions in linear pre-sheath field.

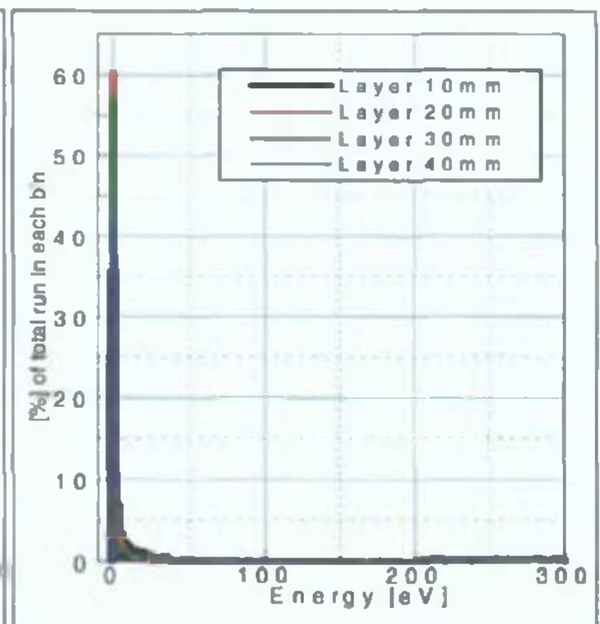

Fig.3.5.11.Total energy distribution for translation energy of Cu ions in parabolic pre-sheath field.

The total energy distribution reveals (as in the case of Ar ions) that a large percentage of Cu ions are trapped in the discharge and do not reach the targets until the end of the pulse off time. Most of these ions (from 38% to 70% of the total number of ions run, Fig.3.5.8-3.5.11) have low energies, in the energy bin 0-10eV.

3.6 CONCLUSIONS ON THE SIMULATION RESULTS

Although both the linear and the parabolic pre-sheath fields bring ions to the targets in average times that are in good agreement to the experimental observations from the OES and I-V waveforms data for Ar ions, a large number of ions cannot reach the targets, mainly due to magnetic mirror effects.

The actual values and behaviour of the pre-sheath electric field are only roughly estimated from this study. An accurate determination (possible only through experimental methods) of the pre-sheath electric field is extremely important for a good knowledge of the efficiency of the sputtering process, given by the number and energy of ions brought to the targets from different layers (distances from the targets).

As observed from the ion transit times, the intensity of the pre-sheath electric field plays a major role in the discharge development and sputtering process, especially in pulsed DC discharges. Too small values of the pre-sheath electric field lead to long ion transit times and a low percentage of ions reaching the targets during the pulse-on time duration. The pre-sheath electric field has to provide to the ions at least the Bohm velocity, in order to ensure ion transport to the cathodes. In most cases, the low limit ion velocity value (the Bohm velocity) is largely over-passed by the actual ion velocities in the pre-sheath electric field.

The knowledge of the intensity and space distribution of the electric field in the pre-sheath has an essential contribution to the percentage of ions brought to the targets, their transit times and their energies, and all MC modelling should take these data with great care, as these values have a tremendous influence on the simulation results.

The study presented here has limited validity as it is based on a pre-sheath model with electric field values that are constant in time. A more accurate study can e performed for pre-sheath electric fields given by functions that are position and time dependent: $E(z, t)$.

CHAPTER 4:

THEORETICAL BASIS FOR PLASMA DIAGNOSTICS

In this chapter are presented the main theoretical considerations regarding the equilibrium conditions in plasmas and the main equations derived from statistics of plasma systems under equilibrium and non-equilibrium conditions, with comments on their applicability for plasma diagnostic and modelling of either the pulse-on or the pulse-off time conditions.

The information presented here is based on several monographic books on plasma physics [4, 39, 40, 41].

4.1. EQUILIBRIUM RELATIONS IN PLASMAS

4.1.1. THERMODINAMIC EQUILBRIUM

The most used "in situ" plasma diagnostic methods - Langmuir probe measurements and Optical Emission Spectroscopy - rely heavily on the concept and conditions of plasma Thermodynamic Equilibrium (TE).

Plasma diagnostic methods provide information over the complex processes of interaction taking place in the plasma and the measured values are averages over a large statistical group of interactions and particles. The experimental data can be related to macroscopic physical quantities and to simple physical models only if:

- the measured values are true averages over the observed processes; and
- the statistical averaging can be performed in order to derive their dependence on the main macroscopic quantities: plasma temperature and density.

To ensure that the measured values are true averages, several corrections should be applied to take into account the "noise signal" induced by the diagnostic method, for example:

- for Optical Emission Spectroscopy: background and continuum levels, superposition of lines and absorption;
- for Langmuir probes: the method and algorithm for calculating the plasma parameters have to be adapted to the conditions of measurement and type of plasma.

Defining averages over large statistical groups of particles and relating them to macroscopic quantities requires the use of statistical averages under the assumption of thermodynamic equilibrium, as statistical averaging relies on the statement of constant number of particles and constant total energy of the system.

Complete Thermodynamic Equilibrium (CTE) can only occur in isolated systems or in very large thermodynamic systems like those in the stellar atmospheres, or related to a "blackbody". Unless thermodynamic equilibrium holds, the equilibrium models for species' distributions cannot be applied and the information provided by diagnostic methods can no longer be related to the above statistics. A definition of thermodynamic equilibrium and the criteria that ensure its existence are therefore necessary and will be briefly presented next, as stated by Fridman et al. [39].

In laboratory plasmas, only Local or Partial Thermodynamic Equilibrium can occur (LTE or PLTE). The LTE allows the use of thermal equilibrium equations for level populations and particle velocity distributions, although the radiation field is much weaker than the blackbody intensity at the given electron temperature. LTE can occur only at high electron densities, such that collisional rates exceed radiative rates by at least one order of magnitude.

As observed by H. R. Griem [40] in order to ensure LTE in the presence of rapid time variations and steep spatial gradients the collisional–radiative relaxation times for level populations must be significantly shorter than the time-scale for the variations in electron temperature and density.

In the case of strong spatial gradients, these relaxation times should be compared to the time required for the diffusion across certain gradient of macroscopic plasma parameters.

4.1.2. CONCEPTS OF COMPLETE THERMODINAMIC EQUILIBRIUM (CTE)

Complete Thermodynamic Equilibrium (CTE) is related to a uniform, homogenous plasma, in which chemical equilibrium and all plasma properties are unambiguous functions of temperature [39]. This temperature is supposed to be homogenous and the same for all degrees of freedom, all plasma components and all their possible reactions. Under these conditions the following equilibrium statistical distributions should take place:

-The Maxwell –Boltzmann velocity or translational energy distribution for all neutral and charged species that exist in the plasma;

-The Boltzmann distribution for the population of excited states for all neutral and excited species that exist in the plasma;

-The Saha equation for the ionization equilibrium to relate the number densities of electrons, ions and neutral species;

-The Boltzmann equilibrium for dissociation, or, more generally, the thermodynamic relations for chemical equilibrium;

-The Plank distribution for the spectral density of electromagnetic radiation.

CTE plasmas are ideal systems: large volumes of homogenous plasma, isolated from the boundaries. In this case, the radiation of the plasma can be considered as blackbody radiation with temperature.

Actual plasmas obtained in laboratory conditions are far from these ideal conditions. Most plasmas are optically thin over a wide range of wavelengths and the plasma radiation is much less than that of a blackbody. Also, plasma non-uniformity and exchange of particles and energy at its boundaries leads to irreversible losses related to conduction, convection and diffusion, disturbing the CTE. In the LTE approach, a thermal plasma is considered optically thin and thus radiation is not required to be in equilibrium. Only the collisional (not the radiative) processes are required to be locally in equilibrium similar to that described for CTE, but the temperature can vary from point to point, in space and time.

The above-mentioned equilibrium distributions, the equations derived from these and the concept of optically thin plasmas will be explained in the following sections.

4.1.3. EQUILIBRIUM RELATIONS

The main equations describing equilibrium plasmas are presented next. The main reference texts used for this theoretical background are the review book by A. Fridman and A.L. Kennedy [39] and the monograph on gas discharges by M.A. Liebermann and A. J. Lichtenberg [4].

The Poisson equation.

The Poisson equation can be derived from the macroscopic form of the Maxwell equations in vacuum:

$$\nabla \times \vec{E} = -\mu_0 \frac{\partial \vec{H}}{\partial t}; \quad (4.1)$$

$$\nabla \times \vec{H} = \varepsilon_0 \frac{\partial \vec{E}}{\partial t} + \vec{J}; \quad (4.2)$$

$$\varepsilon_0 \nabla \cdot \vec{E} = \rho; \quad (4.3)$$

$$\mu_0 \nabla \cdot \vec{H} = 0; \quad (4.4)$$

where $\vec{E}(\vec{r},t)$ and $\vec{H}(\vec{r},t)$ are the electric and magnetic field vectors, $\mu_0 = 4\pi \times 10^{-7}$ [H/m] and $\varepsilon_0 = 8.854 \times 10^{-12}$ [F/m] are the permeability and permittivity of the free space.

The charge continuity relation relates the charge density $\rho(\vec{r},t)$ and the current density $\vec{J}(\vec{r},t)$:

$$\frac{\partial \rho}{\partial t} + \nabla \cdot \vec{J} = 0; \quad (4.5)$$

As in DC and pulsed magnetron discharges the magnetic field intensity is constant over time, then $\nabla \times \vec{E} = 0$ and the electric field can be derived from the gradient of a scalar potential: $\vec{E} = -\nabla \Phi$. Substituting into the third equation we obtain the Poisson equation:

$$\nabla^2 \Phi = -\frac{\rho}{\varepsilon_0}; \quad (4.6)$$

The Poisson equation is a fundamental equation that characterizes the plasma, as it indicates how the plasma potential depends on the charge density. A quasi-neutral plasma is characterized by small plasma potential values corresponding to small deviations from charge neutrality.

The Boltzmann distribution

Considering the laws of statistics for plasmas in thermodynamic equilibrium, the statistical distribution of particles over different states can be inferred. For an isolated system at a constant energy E, consisting of a large number of particles N_i in the state i with the energy E_i, (relative to the ground state) the distribution function of particles over states can be found without details of probability transitions between states. This is the Boltzmann distribution and has the general form:

$$\bar{n}_i = C \exp(-\frac{E_i}{T}); \quad (4.7)$$

If the states are degenerated, the statistical weights g_i are taken into account to show the number of states with a given quantum number, the equation becomes:

$$\bar{n}_i = C g_i \exp(-\frac{E_i}{T}); \quad (4.8)$$

which can be expressed in terms of number densities N_i and N_o of the particles in state i and the ground state (0):

$$N_i = N_0 \frac{g_i}{g_0} \exp(-\frac{E_i}{T}); \qquad (4.9)$$

The general Boltzmann distribution can be applied to derive specific equilibrium distribution functions over different states, the most famous being:

- the Maxwell or Botzmann-Maxwell Electron Distribution function over translational velocities; and
- the Saha equation.

The Maxwell equation is the analytical form of the electron distribution function over velocities obtained using the Boltzmann distribution considering the density of states in the "velocity space" $4\pi v^2$:

$$f(v) = 4\pi v^2 (\frac{m}{2\pi kT})^{3/2} \exp(-\frac{mv^2}{2kT}); \qquad (4.10)$$

(a detailed derivation of the electron distribution function is presented by Liebermann, Lichtenberg [4]).

The Saha equation:

Extending the Boltzmann distribution to population ratios of two bound states m and n of an atom or ion at LTE conditions gives:

$$\frac{N_n}{N_m} = \frac{g_n}{g_m} \exp(-\frac{E_n - E_m}{kT}); \qquad (4.11)$$

Generalizing the above equation to continuum states [39, 40], an equilibrium equation linking the atom and ion densities N and N_i, is obtained, known as the Saha equation:

$$\frac{N_e N_i}{N_m} = \frac{2g_i}{g_m a_0^3} (\frac{kT}{4\pi E_H})^{3/2} \exp(-\frac{E_{mi}}{kT}); \qquad (4.12)$$

where E_H =13.598 eV is the ionization potential of Hydrogen, and a_0=0.529.10^{-10} m is the Bohr atomic radius.

4.2. NON-EQUILIBRIUM STATISTICS OF PLASMAS

The description of non-equilibrium plasmas requires the application of detailed kinetic models. Application of statistical models for these systems can lead to large deviations from reality, but yet statistical models can be successful in thermal plasmas where the electron temperature is not too far from that of heavy particles, in which case a two-temperature statistics can be developed [39]. These models suppose that partition functions depend either on electron temperature or the temperature of heavy particles. The electron temperature determines the partition function related to ionization processes, while the temperature of chemical processes is determined by the temperature of heavy particles.

Numerous papers have reported experimental observation of a two-temperature plasma behaviour in glow and magnetron discharges [7, 42, 43, 44]. A short presentation of the main equations derived from such kinetic models is presented next, based on the text from ref. [39].

4.2.1. BOLTZMANN AND FOCKKER-PLANK KINETIC EQUATIONS

Kinetic equations allow the description of time and space evolution of different distribution functions, taking into account the energy exchange and particle generation and loss.

The distribution function of particles over position, velocities and time $f(\vec{r},\vec{v},t)$ can be considered as a function in the six-dimensional phase space $(\vec{r},\vec{v})$ of particle positions and velocities. In the absence of collisions between particles:

$$\frac{df}{dt}=\frac{f(\vec{r}+d\vec{r},\vec{v}+d\vec{v},t+dt)-f(\vec{r},\vec{v},t)}{dt}; \tag{4.13}$$

Taking into account that in the collisionless case, the number of particles in a given state is fixed: $\frac{df}{dt}=0$; $\frac{d\vec{v}}{dt}=\frac{\vec{F}}{m}$; and $\frac{d\vec{r}}{dt}=\vec{v}$, where m is the particle mass and $\vec{F}$ is the external force, (using a Taylor series expansion up to the first order), the equation can be re-written as:

$$\frac{df}{dt}=\frac{\partial f}{\partial t}+\vec{v}\frac{\partial f}{\partial \vec{r}}+\frac{\vec{F}}{m}\frac{\partial f}{\partial \vec{v}}=0; \tag{4.14}$$

and becomes the well-known form of the **collisionless Boltzmann or Vlasov Equation:**

$$\frac{\partial f}{\partial t}+\vec{v}\bullet\nabla_r f+\frac{\vec{F}}{m}\bullet\nabla_v f=0; \tag{4.15}$$

Taking into account collisions, the distribution function can be described by adding the collisions integral $I_{col}(f)$ (equal to the total change in the particle number in unit volume per unit time) leading to the **Boltzmann kinetic equation**:

$$\frac{\partial f}{\partial t}+\vec{v}\bullet\nabla_r f+\frac{\vec{F}}{m}\bullet\nabla_v f=I_{col}(f); \tag{4.16}$$

4.2.1.1. MACROSCOPIC EQUATIONS DEDUCED FROM THE KINETIC BOLTZMANN EQUATION

The Continuity Equation

Integrating the kinetic Boltzmann equation over particle velocities leads <u>to *the first moment of the Boltzmann equation*</u>. The collisions integral $I_{col}(f)$ over velocities is equal to the total change in the particle number in unit volume per unit time and can be written as the generation rate G minus the loss rate L. Integrating the kinetic Boltzmann equation over particle velocities leads to:

$$\int d\vec{v}\frac{\partial f}{\partial t}+\int d\vec{v}*(\vec{v}\frac{\partial f}{\partial \vec{r}})+\frac{\vec{F}}{m}\int\frac{\partial f}{\partial \vec{v}}d\vec{v}=G-L; \tag{4.17}$$

The distribution function is normalized here to the number of particles, then $\int f d\vec{v} = n$, where n is the number density of particles. The particle flux is defined as $\int \vec{v} f d\vec{v} = n\vec{u}$, where $\vec{u}$ is the particle mean velocity (the drift velocity). The third term is zero as the distribution function is zero at infinite velocities. The above equation, re-written as below reflects particle conservation and is known as *the continuity equation*.:

$$\frac{\partial n}{\partial t} + \nabla_r (n\vec{u}) = G - L; \quad (4.18)$$

If there are no processes of particle generation and loss, the right-hand side of the equation is zero.

The momentum conservation equation can be obtained multiplying by $\vec{v}$ and integrating over velocity. The resulting equation when considering only the neutral species at rest and neglecting the inertial force; becomes a form of *the momentum conservation equation*:

$$m\frac{\partial \vec{u}}{\partial t} = q\vec{E} - \frac{1}{n}\nabla p - m\nu_m \vec{u}; \quad (4.19)$$

The energy conservation equation for electron and ion fluids can be derived by multiplying the kinetic Boltzmann equation by $mv^2/2$ and integrating over velocity. A simplified form of the equation is used to write the energy balance for steady-state discharges:

$$\nabla * \frac{3}{2}(p\vec{u}) = \frac{\partial}{\partial t}(\frac{3}{2}p)_{col}; \quad (4.20)$$

This equation balances the macroscopic energy flux with the rate of energy change due to collisional processes.

The Boltzmann relation

The density of electrons in thermal equilibrium at varying positions in plasma under the action of a spatially varying potential can be obtained from the momentum conservation relation, in the absence of drifts ($\vec{u} = 0$):

$$en_e\vec{E} + \nabla p_e = 0; \quad (4.21)$$

with $\vec{E} = -\nabla\Phi$ and assuming that a thermodynamic equation of state can be attributed to the pressure: $p_e = n_e kT_e$; equation (4.21) becomes:

$\nabla(e\Phi - kT_e \ln n_e) = 0$; and integrating gives: $e\Phi - kT_e \ln n_e = const.$; or :

$$n_e(\vec{r}) = n_0 e^{e\Phi(\vec{r})/kT_e}; \quad (4.22)$$

The above is the Boltzmann relation for electrons, showing that electrons are attracted to regions of positive potential. Although the same relation should apply for ions which should be repelled by a positive potential, this never occurs, as the ions in low pressure discharges have large drift velocities, leading to inertial or frictional forces that are comparable to the electric field or pressure gradient forces [4].

4.3. THEORETICAL BASIS FOR THE DIAGNOSTIC OF PULSE-ON TIME PLASMA

Knowledge of electron kinetics in magnetron plasmas is an important factor in understanding the formation and equilibrium conditions of such magnetized plasmas.

The sputtering process taking place during the pulse-on time is directly determined by the electron kinetics, respectively by the evolution of electron temperature and density. During pulsed DC magnetron operation the electrons move in strong magnetic field gradients and variable electric fields, leading to a complex space and temporal distribution of electron temperature and density, with a direct influence on the evolution of the sputtering process.

The measurement of electron temperature and density throughout the space and temporal evolution of the magnetron plasma poses serious problems from both theoretical and experimental point of view. Theoretical problems in the assessment of electron temperature and density in magnetron plasmas relate to the assumptions of plasma Local Thermodynamic Equilibrium (LTE) or Partial LTE (PLTE) conditions and an expected Maxwellian electron energy distribution function. The main diagnostic methods for experimental determination of electron temperature and density during the pulse-on time are the Langmuir probes method and the Optical Emission Spectroscopy (OES), both having certain limitations.

The Langmuir probe method requires the use of probes that do not perturb the plasma and are not interfering with plasma magnetic and electric fields. Therefore their use is limited to regions outside the "plasma bulk region"* and less relevant for the actual plasma behaviour. The covering of the probe with sputtered material also leads to limitations of its applications to regions outside the bulk [44] or for magnetron operation levels that are well below the usual magnetron operation regime [43]. Due to strong magnetic and electric interferences, Langmuir probes cannot be used in the opposed target magnetron configuration.

Although still relying on the occurrence of LTE or PLTE conditions, Optical Emission Spectroscopy (OES) provides a non-invasive method for the evaluation of T_e inside the plasma bulk, at normal operating conditions of the opposed target magnetron.

In the following considerations, the main atomic processes taking place in the plasma during the pulse-on time will be presented, along with the theoretical basis for understanding the formation, measurement and interpretation of emission spectra and OES data for electron temperature estimations.

* The "plasma bulk" region will be considered throughout this work as the plasma region inside the magnetic confinement.

4.3.1. ATOMIC SPECTROSCOPY BASICS

The main references for the theoretical background presented in this section are H. R. Griem [40] and D. Salzmann [41]. The notations used in the following theoretical presentation are those used by D. Salzmann [41] as these give a complete description of the processes involved through transitions.

4.3.1.1. ATOMIC PROCESSES IN PLASMAS

The atomic processes in plasma are due to interactions of its constituents: atoms, ions, and electrons through their electromagnetic fields or by direct impact collisions.

The interactions that provide the most important information on plasma temperature and its evolution are those in which the excitation state of an atom or ion is changed through interaction with an electron.

The classification of the most important processes as presented by D. Salzmann [41] is shown in Table 4.1 and Table 4.2.

	REACTION	DIRECT PROCESS	INVERSE PROCESS
1	$A_{m'}^{\zeta+} \Leftrightarrow A_m^{\zeta+} + h\nu$	Spontaneous Decay	Resonant Photoabsorption
2	$A_m^{+\zeta} + e \Leftrightarrow A_m^{+\zeta+1} + e + e$	Electron Impact Ionization	Three-body Recombination
3	$A_m^{+\zeta} + e \Leftrightarrow A_{m'}^{+\zeta} + e$	Electron Impact Excitation	Electron Impact De-excitation
4	$A_m^{+\zeta} + h\nu \Leftrightarrow A_m^{+\zeta+1} + e$	Photoionization	Radiative Recombination
5	$A_{mm'}^{+\zeta} \Leftrightarrow A_0^{+\zeta+1} + e$	Autoionization	Dielectronic recombination
6	$A_m^{+\zeta} + e \Leftrightarrow A_m^{+\zeta} + h\nu + e$	Bremstrasslung	Inverse Bremstrasslung

Table 4.1: List of atomic processes in plasmas.

The above transitions are explained in Table 4.2, where the term ion refers to either an atom (ion with charge $\zeta=0$) or an ion ($\zeta>0$). Multiple interactions like many body interactions and double excitations and ionizations are less encountered in low-pressure plasmas.

The probability of occurrence for the above processes depends on plasma density as the three particle processes require high-density plasmas, while single particle process are independent of plasma density, but they will be dominant in low-density plasmas.

Ion-ion interactions can also lead to excitation, ionization, de-excitation and de-ionization of the interacting ions, the processes being identical to those between ions and electrons described above.

A process different from the above is the ***charge-exchange*** between ions, in which an electron jumps from one ion to the other in the encounter. This process has the effect of charge re-distribution and it is of little importance in steady–state plasmas.

	DIRECT PROCESS	REVERSE PROCESS
1	***Spontaneous Decay***: An ion decays into a lower state by emitting a photon whose energy equals the energy difference between the two levels.	***Resonant Photoabsorption***: a photon having the energy equal to the energy difference between two ionic states is absorbed from the radiation field, inducing a transition of the ion to the higher state.
2	***Electron Impact Ionization***: a free electron hits an ion, knocking out a bound electron into the continuum.	***Three-body Recombination***: two free electrons enter at the same time into the volume of an ion. One electron is captured into an ionic state while the extra electron carries away the extra energy.
3	***Electron Impact Excitation***: a free electron that moves close to an ion loses energy by inducing a transition of a bound electron from a lower state to a higher state.	***Electron Impact De-excitation***: an electron moving near an excited ion induces a downward transition from an upper to a lower ionic state.
4	***Photoionization***: A photon is absorbed from the radiation field while a bound electron is moved into the continuum.	***Radiative Recombination***: an electron is captured into one of the ionic states with the emission of a photon taking the extra energy.
5	***Autoionization*** (in double excited ions). One of the electrons decays to a lower state (ground) while the other takes its energy and moves into the continuum. It occurs only when the sum of the energies of the two excited states is higher than the ionization energy of the ion.	***Di-Electronic Recombination***: a free electron is captured into an ionic excited state and the excess energy is absorbed by one of the ground states electrons that moves into a higher state.
6	***Bremstrasslung***: an electron that moves close to an ion is deccelerated by the Coulomb field of the ion and emits a photon.	***Inverse Bremstrasslung:*** an electron that moves near an ion absorbs a photon from the radiation field.

Table 4.2: The atomic processes, explained.

4.3.1.2. ELECTRON IMPACT EXCITATION AND DE-EXCITATION

In the process of electron impact excitation and de-excitation the ions' charge stays the same, only its state of excitation changes.

$$A_m^{+\zeta} + e \Leftrightarrow A_{m'}^{+\zeta} + e ; \qquad (4.23)$$

the direct process having a rate coefficient $\mathcal{E}(\zeta,u\rightarrow\zeta,u;T_e)$ and the inverse process a rate coefficient $\mathcal{D}(\zeta,u\rightarrow\zeta,u;T_e)$, related through the detailed balance principle:

$$\frac{\mathcal{D}(\zeta,u\rightarrow\zeta,l;T_e)}{\mathcal{E}(\zeta,u\rightarrow\zeta,u;T_e)}=\frac{g_{\zeta,l}}{g_{\zeta,u}}\exp(-\frac{\Delta E}{T_e}); \qquad (4.24)$$

Lists of references of published formulas for calculating the electron impact excitation rate coefficient are given by Salzmann [4].

The behaviour of electron impact excitation rate coefficient described by Salzmann [4] indicates that the rate coefficient is small when the electron temperature is much smaller than the transition energy $T_e \ll \Delta E$, it increases sharply to a maximum around $T_e \approx \Delta E$, and decreases slowly at higher temperatures. At temperatures higher than a few times the transition energy, the energy of most of the electrons is too high for excitation into a discrete state and the ionization of the electron into the continuum becomes the more probable process.

4.3.1.3. ELECTRON IMPACT IONIZATION AND THREE-BODY RECOMBINATION

Electron impact ionization is probably the most important process in hot plasmas, particularly in optically thin ones. Its inverse process, the three-body recombination is only important in high-density plasmas.

$$A_m^{+\zeta}+e\Leftrightarrow A_m^{+\zeta+1}+e+e; \qquad (4.25)$$

The direct process occurs when a free electron hits an ion and knocks out one bound electron into the continuum. In most cases, the knocked out electron belongs to the outermost populated ground state shell. In this cases, the ion is left in its ground state, m'=0. If ionizations of inner electrons occur, the ion is left in an excited state. There-body recombination occurs when two free electrons enter at the same time into the volume of one ion and one of the two is captured in a bound state, while the other takes up the extra energy.

The ratio of rate coefficients between these processes is given by the detailed balance principle:

$$\frac{I(\zeta,m\rightarrow\zeta+1,m';T_e)}{R^{(3)}(\zeta+1,m'\rightarrow\zeta,m;T_e)}=2(\frac{mc^2T_e}{2\pi(\hbar c)^2})^{3/2}\frac{g(\zeta+1,m')}{g(\zeta,m)}\exp(-\frac{E_{\zeta+1,m'}-E_{\zeta,m}}{T_e}); \qquad (4.26)$$

Many formulas have been proposed for the calculation of the electron impact ionization rate coefficient (McWhirter (1965), Drawin (1968), Lotz (1968), Sampson and Golden (1978), Younger (1980), etc. Complete references are given by Salzmann [41].

The behaviour of the ionization rate coefficient is similar to that of the excitation rate coefficient. The rate coefficient increases sharply at low temperatures and attains its maximum when the temperature is a few times the binding energy. At higher temperatures the rate coefficient decreases slowly. Such behaviour is common to all ionizing states, of every charged ion. Highly excited states undergo rapid ionization and recombination processes as both processes probabilities have maximum probability for the uppermost states.

4.3.1.4. THE PROBABILITY FOR DIRECT ELECTRON IMPACT IONIZATION

The direct electron impact ionization takes place when the energy transferred between the electron and the ion (atom) exceeds the ionization potential (I).

Thomson [4] has obtained the probability for direct electron impact ionization using the Rutherford formula for the differential scattering cross-section of an electron with energy E on the valence electron (assumed at rest) with energy transfer dE, integrated over dE for dE>I, gives:

$$\sigma_i = 4\pi a_0^2 (\frac{E_H}{E})^2 (\frac{E}{I} - 1); \qquad (4.26)$$

where E_H =13.598 eV is the ionization potential of Hydrogen, and $a_0=0.529.10^{-10}$ m is the Bohr atomic radius. The above is called "the Thomson formula". The Thomson cross-section reaches a maximum value for E=2I.

4.3.2. THE EMISSION SPECTRUM

The radiation emitted from plasma is an important diagnostic tool as it carries information about the local and instantaneous plasma temperature and density, providing a reliable means of observation and evaluation of plasma parameters and their temporal evolution.

The emission spectrum has two components:

1. The continuous spectrum;
2. The line spectrum with intensity and spectral distribution characteristic to the plasma temperature and density and the emission mechanism.

1. The continuous spectrum is generated in two kinds of processes [41]:

- The bremsstrahlung radiation given by free electrons movement in the Coulomb field of an ion. In high-Z plasmas at low-temperatures, the main emission mechanism is line emission, relative to which bremstrasslung provides a low continuous background radiation.
- The recombination radiation, emitted during the recombination of a free electron with an ion. The radiation is emitted only above sharp "edges" which correspond to the binding energies of the bound states of ions. The recombination into the ground state has the highest probability, as it depends on the main quantum number (n_P) of the ion as $1/n_P$.

2. The line emission spectrum is the most important process in intermediate and high Z plasmas in which ions are not fully stripped of electrons. The emission rate of a spectral line is given by [41]:

$$P_{\zeta,m'\to\zeta,m} = N_{\zeta,m'} \hbar\omega_{\zeta,m'\to\zeta,m} A(\zeta,m'\to\zeta,m) \; ; \qquad [eV/(cm^3.s] \qquad (4.27)$$

where N is the density of ions in the upper initial ionic state and $\hbar\omega_{m'\to m} = E_{\zeta,m'} - E_{\zeta,m}$ is the transition energy, which is also the energy of the emitted photon and $A(\zeta,m'\to\zeta,m)$ is the Einstein coefficient for the transition.

The spectra of H and He like ions are well known and understood. The spectral lines of H-like atoms have energies given by the Bohr formula:

$$\hbar\omega_{u\to l} = \frac{Z^2 e^3}{2a_0}\left(\frac{1}{n_l^2} - \frac{1}{n_u^2}\right); \qquad (4.28)$$

where n_u and n_l are the principal quantum numbers of the lower and respectively the upper states of the transition. The states are degenerate with respect with to the quantum number *l*, so the levels within the same shell have the same energy.

All transition lines that end on the same ionic state form a "series of lines". The spectrum corresponding to a given series is located slightly below the recombination edge corresponding to the lower state.

4.3.2.1. LINE BROADENING

The spectral lines' width is an important parameter in plasma diagnostic as it provides information about the local plasma parameters (electron temperature and electron density).

The shape of a spectral line is conveniently described by means of the line profile function $L(\omega)$ [s^{-1}] that is normalized to unity [40, 41]:

$$\int L(\omega)d\omega = 1 ; \qquad (4.29)$$

and defined such that: $I(\omega)d\omega = I_0 L(\omega)d\omega$ is the number of photons emitted in the range of frequencies [ω, ω+dω] and I_0 is the number of photons emitted in the line.

The shapes $L(\omega)$ are in general a Lorentzian distribution:

$$L(\omega) = \frac{\Gamma}{2\pi}\frac{1}{(\omega-\omega_0)^2 + (\Gamma/2)^2}; \qquad (4.30)$$

or a Gaussian distribution:

$$L(\omega) = \frac{1}{\sqrt{2\pi}\sigma}\exp\left[-\frac{1}{2}\left(\frac{\omega-\omega_0}{\sigma}\right)^2\right]; \qquad (4.31)$$

There are several mechanisms the lead to lines broadening:

1. The natural line broadening due to the finite life-time of ionic excited states.
2. Doppler broadening due to the thermal velocity distribution of the emitting ions;
3. Electron impact broadening, due to electron collisions.;
4. Quasi-static Stark broadening due to local electrostatic fields generated by nearby ions, that split and shift the energy levels of the radiating ions.

Each emission line is a convolution of all the above effects, although in general, depending on the local plasma parameters, only one of them dominates.

A convolution of the two types of broadenings, Lorentzian and Gaussian gives a Voigt type profile. This type of a profile follows the Gaussian distribution in the centre of the line and Lorentzian distribution in the wings region far from the centre line.

The following considerations on emission lines' broadening have been presented by Salzmann [4] and are summarized here.

1. Natural line broadening.

An atomic excited state decays spontaneously to one of the lower states within a time period that is characterised by the Einstein coefficient $A_{u \to l}$, where u and l are the quantum numbers of the upper, respectively, lower state, so excited states of an atom have a finite lifetime: $\tau \sim A_{ul}^{-1}$. Thus, according to the quantum mechanical uncertainty principle, the energy level E_u has a characteristic width of $\Delta E \sim \hbar / \tau \approx \hbar A_{ul}$.

The spectral line related to this transition has a specific width $\Delta\omega \approx A_{ul}$, which is independent of external conditions and called the "*Natural Spectral Line Width*". Typically, $\Delta\omega \approx 10^8\ \text{sec}^{-1} << \omega_{ul} \approx 10^{15}\ \text{sec}^{-1}$; where $\omega_{ul} = 2\pi\nu_{ul}$ is the emission frequency.

The amplitude of the photon emission has a damped oscillatory time dependence as it characterizes the photon emission probability and describes the attenuation of the electromagnetic wave because of the finite life-time of atomic states:

$A(t) \propto e^{i\omega t} e^{-\Gamma t/2}$, where $\omega = (E_u - E_l)/\hbar$ is the transition energy.

The photon distribution function and the natural profile of a spectral line related to finite lifetime of excited states is:

$$F(\omega) = \frac{\nu}{\pi} \frac{1}{\nu^2 + (\omega - \omega_{nk}^2)^2} \qquad (4.32)$$

and has a Lorentzian shape. The spectral line width of a Lorentzian profile can be estimated as:

$\Delta\lambda = \dfrac{e^2}{3\varepsilon_0 mc^2} = 1.2 \cdot 10^{-5}\ nm$; where m is the electron mass.

The natural broadening is the minimum width possible for a spectral line, much smaller than other types of broadenings and seldom measurable.

2. Doppler broadening.

Due to the motion of emitting ions, the frequency of the detected photon in the laboratory frame ω, differs from the emitted frequency in the frame of the moving ion ω_0 by an amount equal to:

$$\Delta\omega = \omega - \omega_0 = \omega_0 \frac{v_x}{c}; \qquad (4.33)$$

where v_x is the component of the velocity of the emitter along the line of sight to the detector.

The resulting profile has a Gaussian distribution:

$$L(\omega) = \frac{1}{\sqrt{\pi}\,\omega_D} \exp[-(\frac{\Delta\omega}{\omega_D})^2]; \qquad (4.34)$$

where ω_D is the Doppler broadening parameter. The FWHM of the line is equal to ω_D multiplied by 2ln2:

$$FWHM = \omega_0 \sqrt{\frac{kT \ln 16}{Mc^2}}; \qquad (4.35)$$

The width of the Doppler broadening depends therefore on plasma temperature only.

3. Electron impact broadening

Collisions with the rapidly moving free electrons lead to perturbations in the atomic levels of the ion (radiator) that modify the emission frequency, the resulting shape of the line being Lorentzian.

In terms of the Half Width at Half Maximum (HWHM) w and shift d of the line the Lorentzian shape of the is described by:

$$L(\omega)=\frac{w/\pi}{w^2+(\Delta\omega-d)^2}; \qquad (4.36)$$

It has been demonstrated [4] that the electron impact broadening is proportional to the electron density and inversely proportional to the electron temperature:

$$w\propto\frac{n_e}{\sqrt{T_e}}; \qquad (4.37)$$

The rather complicated formula for the electron impact broadening does not make the object of this presentation. A method to deduce the formula is presented by Salzmann [41] and important corrections to the formula have been proposed by Griem [40].

4. Quasi-static Stark broadening

The mechanism of the Stark broadening is the electrostatic field generated by the perturber on the radiator, which for weak electrostatic fields is proportional to the square of the field intensity. This mechanism applies when the interaction time is longer than the time between two collisions and it is produced by interactions with the slow moving neighbouring ions. The detailed analysis for the Stark broadening is presented by Salzmann [41].

In general, the different types of collision broadening can be considered to be statistically independent processes and the resulting line profiles are a convolution of profiles given by each type of broadening.

4.3.2.2. CONTINUOUS SPECTRA

Atoms and incompletely stripped ions generate along with the line spectrum a continuous spectrum. The continuous spectrum is important not only as a background for the line spectrum, but also because continuum intensities scan provide relatively direct measures of electron density and temperature. The most significant processes leading to emission of a continuum spectrum are the electron-ion recombination and the bremsstrahlung.

The recombination emission is due to radiative electron-ion recombination during which a free electron with kinetic energy $\frac{mv_e^2}{2}$ is trapped in a bound atomic state with a discrete energy E_n. This is a free-bound transition leading to emission of a quantum of energy:

$$\hbar\omega=|E_n|+\frac{mv_e^2}{2}; \qquad (4.38)$$

The recombination cross-section depends on the electron energy ε and density n [39].

The bremsstrahlung emission is an energy loss process (a free-free transition) due to electron slowing down in the Coulomb field of an atom or ion and its cross-section depends on the cross-section of electron-heavy particle collisions.

4.3.2.3. SPECTROSCOPIC TEMPERATURE MEASUREMENTS

Most spectroscopic temperature measurements provide an evaluation of electron temperatures T_e. The most used methods are based on relative lines intensities of either the same atom or ion, neighbouring ionization stages, on relative continuum intensities, ratios of line to continuum intensities.

Relative intensities of lines of the same atom or ion

Integrating line intensities requires a measurement process that includes the contribution of extended line wings and takes into account of the necessary continuum corrections and blends with neighbouring lines. As evaluated by Griem [40], the above corrections as well as relative intensity calibrations lead to large errors in the ratio, generally larger than 10%.

The main conditions to relate the intensities of two lines to their statistical distribution on energy levels given by the Boltzmann formula (4.10) are that the LTE (or at least PLTE) conditions apply and the plasma is optically thin, therefore the absorption processes are negligible.

In optically thin plasmas of length l, along the line of sight, the spectrally integrated emission line intensities (radiances) are given by:

$$i_{nm} = \int I_{nm}(\omega)d\omega = \frac{h\omega_{nm}}{4\pi}A_{nm}\int_0^l N_m dx \; ; \qquad (4.39)$$

and assuming homogenous plasma:

$$i_{nm} = \frac{\hbar\omega_{nm}}{4\pi}A_{nm}N_m l; \qquad (4.40)$$

Under PLTE conditions, the ratio of radiances from two lines of the same atom or ion (using the Boltzmann formula for the populations of the two levels m_1 and m_2) becomes:

$$R = \frac{i_{n1m1}}{i_{n2m2}} = \frac{\omega_{m1n1}A_{n1m1}g_{m1}}{\omega_{m2n2}A_{n2m2}g_{m2}}\exp\left(-\frac{E_{m1}-E_{m2}}{kT}\right); \qquad (4.41)$$

So, the temperature corresponding to the above line ratio is:

$$kT = \frac{E_{m2}-E_{m1}}{\ln\dfrac{\omega_{m2n2}g_{m2}A_{n2m2}R}{\omega_{m1n1}g_{m1}A_{n1m1}}}; \qquad (4.42)$$

The relative error in the determination of the temperature is related to any error in the determination of the quantity X under the logarithm as:

$$\left|\frac{\Delta T}{T}\right| = \frac{kT}{E_{m2}-E_{m1}}\left|\frac{\Delta X}{X}\right|;$$

As errors in $\Delta X / X$ are rarely below 0.1, the relative errors in the determination of kT are rarely smaller than 10% [40].

Other means to estimate electron temperatures are by using the ratio of emission lines of different charge states (which requires the knowledge of the electron density and the Saha equation) or by using several lines from the same series and drawing the logarithm of lines' intensities as a function of energy, which should result in a straight line, its slope giving T_e. More information on these diagnostic methods and related ones can be found in refs. [40, 41].

4.3.2.4. TIME-RESOLVED SPECTRA

The measurement of time-resolved OES raises the question of the relationship between the plasma life-time and the temporal resolution of the spectrometer [41].

The emission spectra of plasmas with life-times longer than 10^{-8}s can be measured by photosensitive devices like photodiodes and photomultipliers. As the speed of the electronic circuits used in the detection of the signal is of the order of 10^{-9} s, such devices are fast enough to provide a time-resolved evolution of the plasma. For short-lived plasmas (life times of the order of nanoseconds) framing cameras or CCD cameras can be used [41]. In most applications, the photosensitive detector is placed on the focal plane of the spectrometer.

From the ratios of temporal shape of the pulse heights in the detector the temporal evolution of electron temperature can be determined. The above applies for ordinary spectrometers that observe the plasma through a "slit". These types of spectrometers provide directly the radiances of the observed lines, with some drawbacks related to the particularities of the observation method.

Using more advanced spectrometers that allows the observation of the plasma through a two-dimensional aperture (lenses) situated directly in the discharge chamber - like the acousto-optic spectrometers - has certain advantages and particularities that are described in Chapter (2.3) dedicated to the measurement equipment performances.

The use of an acousto-optic spectrometer with an optical probe situated inside the discharge chamber is the method of choice for the OES measurements presented in this thesis. The acousto-optic spectrometer allows time-resolved OES measurements and also space – resolved readings according to the position of the probe inside the chamber.

4.4. THEORETICAL BASIS FOR THE DIAGNOSTIC OF PULSE-OFF TIME PLASMA

4.4.1. CHARGE–LOSS PHENOMENA IN PLASMAS

Magnetron discharges are Low Temperature Glow Discharges, therefore, essentially non-thermal and non-equilibrium discharges due to the marked discrepancy between electron and ion temperatures. Nevertheless, the existence of a stable discharge is only possible under at least PLTE (equilibrium) conditions; therefore, equilibrium relations in plasma should apply at any time.

During the pulse-on time, charge equilibrium is established at the plasma bulk, in the presence of a magnetic field plus external and internal (self-consistent) plasma electric fields, while the creation of charges has to be balanced by charge – loss phenomena. In magnetron glow discharges, the magnetic field is added in order to achieve confinement of charges, thus to improve the balance between creation and loss of charges. The stability and existence of the discharge is maintained for as long as the charge balance in the discharge is stable. Accumulation of charges of either sign can lead to arcing, these strong perturbations of the discharge affecting the sputtering process and the quality of the deposited films.

The pulsed DC operation mode has been developed in order to allow a cyclic release of accumulated space-charge gradients and thus a cyclic restoration of charge neutrality at all regions inside the discharge.

During the pulse-off time, the power input stops and the external electric field changes direction, allowing the accumulated charges to dissipate through charge–loss phenomena: drift to the anodes, free diffusion, ambipolar flows (drift and diffusion in the polarization electric fields generated by existing charge density gradients) and recombination. As charge generation stops, the pulse-off time is dominated by charge-loss phenomena. These effects lead to a new quasi-equilibrium: overall plasma neutrality at a lower plasma density, achieved through loss of charges to the walls, anodes or through recombination.

A short presentation of the main theoretical approaches and formulas that describe charge-loss phenomena in plasmas follows. More information on these aspects can be found in refs. [4, 39].

4.4.2. DIFFUSION AND TRANSPORT

The steady-state macroscopic force equation in a uniform density plasma can be written as:

$$m\frac{\partial \vec{u}}{\partial t} = q\vec{E} - \frac{1}{n}\nabla p - m\nu_m \vec{u}\,; \qquad (4.43)$$

where $m\nu_m \vec{u}$ is a friction term arising from collisions with the background species. These collisions lead to diffusion.

Assuming that the background species are at rest and the momentum transfer frequency ν_m is constant, independent of the drift velocity $\vec{u}$; and considering an isothermal plasma such that $\nabla p = kn\nabla T$ we obtain:

$$\vec{u} = \frac{q\vec{E}}{m\nu_m} - \frac{kT}{m\nu_m}\frac{\nabla n}{n}; \qquad (4.44)$$

which can be written as:

$$\vec{\Gamma} = \pm\mu n\vec{E} - D\nabla n; \qquad (4.45)$$

where $\vec{\Gamma} = n\vec{u}$ is the particle flux and $\mu = \frac{|q|}{m\nu_m}$ [m²/V.s] and $D = \frac{kT}{m\nu_m}$ [m²/s] are the macroscopic mobility and diffusion constants that can be calculated separately for both species.

Using the mean speed $\bar{v} = (8kT/\pi m)^{1/2}$ and the mean free path for scattering $\lambda = \bar{v}/\nu_m$, D becomes: $D = \frac{\pi}{8}\lambda^2\nu_m$; having the basic structure of a diffusion process dependent on the square of the step length and on the time between steps [4].

4.4.3. FREE DIFFUSION

From the particle flux formula, in the absence of an electric field we can obtain the diffusion law relating the flux to the density gradient, which is called the *Fick's law*.:

$$\Gamma = -D\nabla n;$$

Using the continuity relation and choosing the source and sink terms to be zero, we obtain:

$$\frac{\partial n}{\partial t} + \nabla\cdot\Gamma = 0;$$

If D is independent of position, we obtain the ***diffusion equation for single species:***

$$\frac{\partial n}{\partial t} - D\nabla^2 n = 0; \qquad (4.46)$$

4.4.4. FREE DIFFUSON OF ELECTRONS AND IONS

If electron and ion densities are low, their diffusion in plasma can be considered independent and described by the continuity equation (4.18). The total flux of charged particles includes in this case the actual drift in the electric field and diffusion following Fick's law:

$$\Gamma_{e,i} = \pm n_{e,i}\mu_{e,i}\vec{E} - D_{e,i}\frac{\partial n_{e,i}}{\partial \vec{r}}; \qquad (4.47)$$

The signs + and – correspond to the charge of the particles. The continuity equation can be re-written as:

$$\frac{\partial n_{e,i}}{\partial t} + \frac{\partial}{\partial \vec{r}}(\pm n_{e,i}\mu_{e,i}\vec{E} - D_{e,i}\frac{\partial n_{e,i}}{\partial \vec{r}}) = G - L; \qquad (4.48)$$

In the case of Maxwellian energy distribution function, a relationship, valid for different particles occurs between the diffusion and mobility coefficients, known as the *Einstein relation:*

$$\frac{D}{\mu}=\frac{kT}{e}; \qquad (4.49)$$

The Einstein relations are used for calculating the diffusion coefficients of charged particles, based on experimental measurements of their mobility.

4.4.5. AMBIPOLAR FLOWS

The term "ambipolar flow" used here replaces the misnomer "ambipolar diffusion", a necessary adjustment to the term, proposed and demonstrated by Franklin [45]. When the ionization degree is high, the electron and ion movement cannot be considered free and independent. The electrons are moving faster than the ions and form a charge separation zone with a polarization field that adjusts the electron and ion fluxes. This electric polarization field accelerates ions and slows down electrons, making all of them to move together. This phenomenon is known as "ambipolar flow".

If the separation of charges is small, the electron and positive ion densities are approximately equal: $n_e \approx n_i$ and also their fluxes. Equating their fluxes and eliminating the electric field, the general equation for the electron and ion fluxes can be obtained:

$$\Gamma_{e,i}=-\frac{D_i\mu_e+D_e\mu_i}{\mu_e+\mu_i}\frac{\partial n_{e,i}}{\partial \vec{r}}; \qquad (4.50)$$

where the coefficient is the coefficient of ambipolar flow ("diffusion"):

$$D_a=\frac{D_i\mu_e+D_e\mu_i}{\mu_e+\mu_i}; \qquad (4.51)$$

Taking into account the Einstein relation, D_a becomes: $D_a = D_i(1+\frac{T_e}{T_i})$; so the ambipolar flow coefficient depends on the diffusion coefficient of the ions and on the ratio of electron and ion temperatures.

If Te>>Ti (during the pulse-on time plasma) both ions and electrons leave the plasma at a rate that exceeds the ion diffusion coefficient, while during the pulse-off time, the electron temperatures become close to ion temperatures and the ambipolar flow is dominated by the diffusion coefficient of the ions [4]. For non-equilibrium plasmas with Te>>Ti, the ambipolar flow coefficient $D_a=\frac{\mu_i}{e}T_e$ corresponds to the temperature of the fast electrons and mobility of the slow ions [4]. Franklin [45] has demonstrated that for large differences between electron and ion temperatures (as those encountered in magnetron plasmas) the actual diffusion process is far from being dominant; the dominant process is the motion under the electric field.

Comparing the mobility and diffusive component of electrons and respectively ions flux ($\Gamma_{ed}, \Gamma_{em}; \Gamma_{id}, \Gamma_{im}$) to the total ambipolar flux Γ, in two temperature plasmas where (usually) $T_e \sim 100T_i$ and $\mu_e \sim 1000\,\mu_i$, the following expressions are found:

$$\frac{\Gamma_{id}}{\Gamma} = \frac{D_i(\mu_i + \mu_e)}{\mu_i D_e + \mu_e D_i} = \frac{T_i(\mu_i + \mu_e)}{\mu_e(T_e + T_i)} \sim \frac{T_i}{T_e}; \qquad (4.52)$$

$$\frac{\Gamma_{im}}{\Gamma} = \frac{\mu_i(D_e - D_i)}{\mu_i D_e + \mu_e D_i} = \frac{T_e\mu_e - T_i\mu_i}{\mu_e(T_e + T_i)} \sim 1; \qquad (4.53)$$

From similar considerations, for electrons: $\frac{\Gamma_{ed}}{\Gamma} \sim \frac{\mu_e}{\mu_i}$ and $\frac{\Gamma_{em}}{\Gamma} \sim -\frac{\mu_e}{\mu_i}$; (4.54)

Therefore, the ion movement is determined by the mobility flux, while the electron flux is equally diffusive and mobility dominated.

4.4.7. CONDITIONS OF AMBIPOLAR FLOW: THE DEBYE RADIUS

To determine the conditions of ambipolar flow with respect to free diffusion of electrons and ions, the absolute value of the polarization field has to be estimated [39]:

$$E = \frac{D_e}{\mu_e}\frac{1}{n_e}\frac{\partial n_e}{\partial r} = \frac{kT_e}{e}\frac{\partial \ln n_e}{\partial r} \propto \frac{kT_e}{eR};$$

where R is the characteristic length of change in the electron concentration.

The difference between the ion and electron concentration $\Delta n = n_i - n_e$ characterizing the space charge is related to the electric field by the Maxwell equation:

$$\frac{\partial \vec{E}}{\partial \vec{r}} = \frac{e\Delta n}{\varepsilon_0}$$

Using the above two equations, the relative deviation from quasi-neutrality can be obtained:

$$\frac{\Delta n}{n_e} \approx \frac{kT_e}{e^2 n_e}\frac{1}{R^2} = (\frac{r_D}{R})^2 \text{ and } r_D = \sqrt{\frac{kT_e\varepsilon_0}{e^2 n_e}}; \qquad (4.56)$$

where r_D is the Debye radius.

The Debye length (radius) characterises the plasma quasi-neutrality, the charge separation and plasma polarization. If the electron density is high and Debye radius is small, $r_D \ll R$, the deviation from plasma neutrality is small, the electrons and ions move as a group and the flow can be considered ambipolar. If the electron concentration is relatively low and the Debye radius is large, $r_D \geq R$, then the plasma is not quasi-neutral, the electrons and ions move separately and their diffusion can be considered free.

The Debye length gives the characteristic plasma size necessary to screen or to suppress the electric field, and also indicates the scale of the plasma non-neutrality.

4.4.9. PLASMA DIFFUSION ACROSS MAGNETIC FIELD LINES

This effect is of great importance for plasma confinement by magnetic fields. Calculation of the diffusion coefficients for electrons and ions from a two-fluid magneto-hydrodynamic model describing the electron and ion diffusion in a direction perpendicular to the magnetic field lines gives [4]:

$$D_{\perp,e} = \frac{D_e}{1+\left(\frac{\omega_{B,e}}{\nu_e}\right)^2} \ ; \text{ and } \ D_{\perp,i} = \frac{D_i}{1+\left(\frac{\omega_{B,i}}{\nu_i}\right)^2} \qquad (4.57)$$

where D_e and D_i are the coefficients for the free diffusion of electrons and ions without magnetic field, ν_e and ν_i are the collision frequencies of electrons and ions; $\omega_{B,e}$ and $\omega_{B,i}$ are the electron and ion cyclotron frequencies: $\omega_{B,e}=\frac{eB}{m}$; $\omega_{B,i}=\frac{eB}{M}$; (with B the magnetic flux density and m and M the mass of electrons, respectively ions).

If diffusion is ambipolar (becomes an ambipolar flow), which applies for highly ionized plasma under consideration, then equation (4.57) can still be applied to find D_a in a magnetic field where the free diffusion coefficients have to be replaced by those in the magnetic field (above). The regular electron and ion mobilities in eq. (4.52) have also to be replaced by those corresponding to the drift perpendicular to the magnetic field.

The coefficient of ambipolar flow perpendicular to the magnetic field becomes:

$$D_\perp = \frac{D_a}{1+\frac{\omega_{B,i}^2}{\nu_i^2}+\frac{\mu_i}{\mu_e}\left(1+\frac{\omega_{B,e}^2}{\nu_e^2}\right)}; \qquad (4.58)$$

where D_a is the regular coefficient of ambipolar flow in a plasma without magnetic field.

If the electrons are magnetized ($\omega_{B,e}/\nu_e >> 1$) and ions are not ($\omega_{B,i}/\nu_i << 1$) the equation becomes:

$$D_\perp = \frac{D_a}{1+\frac{\mu_i}{\mu_e}\frac{\omega_{B,e}^2}{\nu_e^2}}; \qquad (4.59)$$

Equation (4.59) can be further simplified in strong magnetic fields, where $\frac{\mu_i}{\mu_e}\frac{\omega_{B,e}^2}{\nu_e^2} >> 1$, leading to:

$$D_\perp = D_a\frac{\mu_e}{\mu_i}\frac{\nu_e^2}{\omega_{B,e}^2} \approx D_e\frac{\nu_e^2}{(e/M)^2}\frac{1}{B^2}; \qquad (4.60)$$

Franklin [13] comments also on electron mobility across magnetic field lines in plasmas where the electrons are magnetized and the ions are not:

$$\mu_{em} = \frac{\mu_e}{1 + (\frac{\omega_{B,e}}{\nu_e})^2}; \qquad (4.61)$$

It follows that the electron mobility is reduced to a value comparable to the ion mobility across magnetic field lines.

Formulae (4.60 – 4.61) do not mean that discharges with magnetic confinement will never allow an ambipolar flow on a direction perpendicular to the magnetic field lines. The ambipolar flow is major process that ensures the charge balance in the discharge at all times and thus the stability of low temperature discharges against "over-heating" and turning into arcs.

The formula (4.60) shows the dependence of the ambipolar flow coefficient across $\vec{B}$ lines to be inversely proportional to B^2, so as B decreases, the diffusion across $\vec{B}$ lines will increase quickly.

Large B values (encountered close to the targets) will not allow charges to leave the respective region of the discharge, thus maintaining a high plasma density near the targets.

Low B values at the boundaries of the magnetic confinement (especially on the centre line between the magnets) will allow a flow of electrons outside the bulk, thus preventing the accumulation of large charge density gradients and arcing.

Another charge-loss effect dependent on the values of $\vec{B}$ can occur when a charge density gradient generates an electric field perpendicular to $\vec{B}$. This will lead to the $\vec{E} \times \vec{B}$ drift that will guide charged particles outside the bulk on a direction perpendicular to both $\vec{E}$ and $\vec{B}$.

Discharges that cannot allow for any charge–loss effects will generally become unstable.

CHAPTER 5:

TIME-RESOLVED PLASMA DIAGNOSTIC METHODS

In this chapter are presented the time-resolved diagnostic methods used for deriving the physical models for the pulse-on and pulse-off time plasma in the opposed target magnetron with non-ferromagnetic (Cu) and ferromagnetic (Fe) targets.

The experiments performed, the data analysis and interpretation of results provided by the following diagnostic methods are presented:

-the measurement of I-V characteristics and the Current (I) and Voltage (V) waveforms;

-the time and space resolved excited atom and ion distribution: Ar, Ar+, Cu, Fe from optical emission spectroscopy data;

-the evaluation of time and space resolved of electron temperature, and T_e charts for the Cu and Fe targets;

- the method for obtaining time-resolved information from the ion energy distributions obtained using the HIDEN mass-energy analyser.

5.1 THE *I-V* CHARACTERISTICS AND THE *I* AND *V* WAVEFORMS

5.1.1. THE I-V CHARACTERISTICS

5.1.1.1. INTRODUCTION

The measurement of "static" IV characteristics is the oldest and most basic means for studying the behaviour of all types of discharges, providing information on:

- the limits of "existence" and stability of the discharge (pressure range, current or power range);
- the optimum amount of power that has to be delivered to the discharge in order to obtain the desired operating regime (glow discharge, arc, self-sustained discharge, electron avalanche processes, sputtering rate, etc);
- the operating conditions where the "breakdown" of the discharge or its stable operation is achieved;
- the way the ionization density depends on the input current and/or voltage.

The I-V characteristics for sputtering magnetrons have been studied by Rossnagel [36, 46, 47, 48] for conventional planar magnetrons and by Ehiasarian et al.[49] for high power density pulsed magnetrons. The I-V characteristics for planar magnetrons follow a law of the form $I=kV^n$ [50], where the constant *k* and the exponent *n* depend on the gas-target combination, design of the magnetron, the magnetic field and other experimental parameters.

Rossnagel et al. [44] has demonstrated that at gas pressures above 10 mtorr the gas rarefaction effect leads to an increase in the plasma impedance and a consequent increase of discharge voltage with current. A high exponent *n* occurs for combinations of gas-target material where the atomic mass of gas atoms is low and that of metal is high, leading to almost constant voltage for large changes in the discharge current. Such discharges have a very low sputtering rate and are not efficient. The low values n values are reached for very low pressures or for very low magnetic fields.

Turner et al. [22], has confirmed by Monte Carlo calculations the mechanism for gas rarefaction in magnetron sputtering discharges. Monte Carlo simulation of thermalization for sputtered and reflected atoms in magnetron discharges performed by Y. Yamamura [21] evaluate the contribution of sputtered and respectively reflected atoms to the gas rarefaction effects.

For high power densities pulsed magnetrons at low pressure (3mtorr) [49] the discharge exhibits two slopes, depending on the discharge current: at current densities < $600 mA/cm^2$, n=7 indicating normal magnetron operation, while at higher currents n=1 (the increase in voltage is not accompanied by a change in current).

For opposed target magnetrons in cylindrical geometry (Penning Type) the I-V characteristics have been studied by Window et al. [2, 3] for magnetic fields from 5mT to 42mT and obtained a similar $I=kV^n$ law, with n=6.

The I-V characteristics for the opposed target magnetron with rectangular geometry studied in this thesis work are presented and are discussed here.

5.1.1.2. THE EXPERIMENTAL SET-UP

The ENI power supply has been used to power the opposed target magnetron. The operation mode of the power supply used for all experiments described in this thesis is "set current run" for both DC and pulsed DC modes.

For this type of operation, the power supply provides a fixed current that can be set by the user, while the voltage in the circuit is mainly given by the loads' impedance [51].

The measurement of the I-V characteristics has been done by direct readings of the set current and resulted voltage as given by the power supply's meters. For pulsed operation, the voltage and current readings are average (RMS) values.

5.1.1.3. TYPICAL I-V CHARACTERISTICS

A study of the I-V characteristics evolution for DC and pulsed DC operation at different Ar pressures (from 1 mtorr to 5mtorr) different frequencies (50kHz to 250kHz) and pulse-off times (from 496ns to 4016ns) has been performed for the Cu targets magnetron configuration. To enable comparison, some I-V characteristics have been also measured for the Fe targets configuration.

The results are presented in figures: Fig.5.1.1 – Fig.5.1.6 as graphs of Voltage as a function of Current: V=f(I), instead of the classical I=f(V), as this representation provides a better view for the I-V evolution.

The I-V characteristics have a shape very similar to that of glow discharges, for certain situations displaying a region with negative resistance. The negative resistance of the I-V characteristics connected to the on-set of a self-sputtering process (and sustained self-sputtering) was also observed in Very High Target Power Density Magnetron sputtering [52, 53, 54].

The negative resistance region of the I-V characteristics is a result of the significant decrease in the discharges' impedance as the current increases. This process is similar to the "breakdown" processes usually encountered in low-pressure glow discharges and indicates that starting with a certain level of ionization (induced by a certain current level) the discharge is stable and practically independent of the current input. The presence of the negative resistance region is more pronounced in the situations where the ionization density is achieved at a low rate and the charge loss rate from the discharge is also low:

- At low pressures;
- For DC discharges or short pulse-off times.

Under such operating conditions, a build-up of charge that stays in the plasma bulk even though the pulse-off time occurs, starting at a certain current value and leading to a decrease of the discharge impedance and voltage.

At higher Ar gas pressures (above 2mtorr) and higher pulse-off times the negative resistance region of the I-V characteristic disappears, as the ionization density is higher and the charge losses from the discharge are also high due to the longer duration of the pulse-off time. Under such conditions the discharge becomes stable and independent of the input current based only on the direct ionization processes taking place during each pulse, as the charge built-up has less chances to occur.

With the increase in pulse frequency and/or pulse-off time, the charge losses in the discharge slowly increase with current and the discharge impedance also increases (Fig.5.1.3). As it can be seen from the presented I-V characteristics, the discharge is stable for currents starting with 1.0 A; and maintains almost constant values of voltage up to 6A. The voltage on the cathodes gives the average electron kinetic energy, which is proportional to the average electron temperature [5].

The fact that the voltage is practically independent of current for these discharges indicates that also the average electron temperature (excitation temperature) is independent of current, a property that will be used (Chapter 5.2) in studying the conditions for "optically thin" plasmas that allow optical emission spectroscopy diagnostic methods for such plasmas.

As we can see, the discharge voltage is strongly affected by the gas pressure and therefore, the expected plasma temperature (electron temperature) will be affected in the same way.

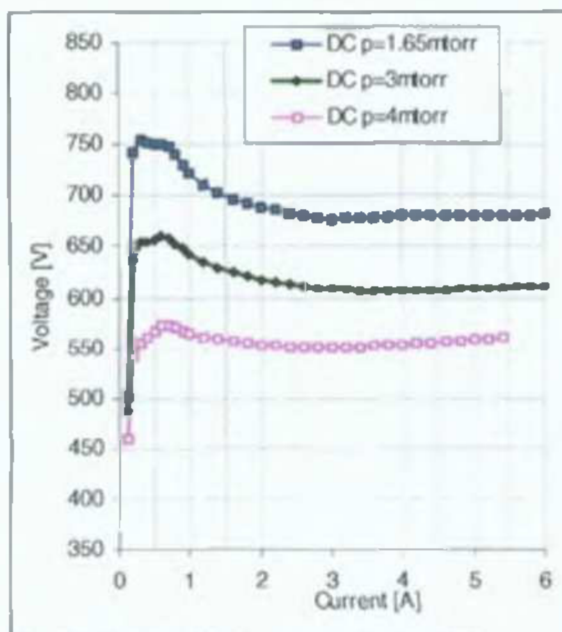

Fig.5.1.1: The IV characteristics for DC operation at different pressures.

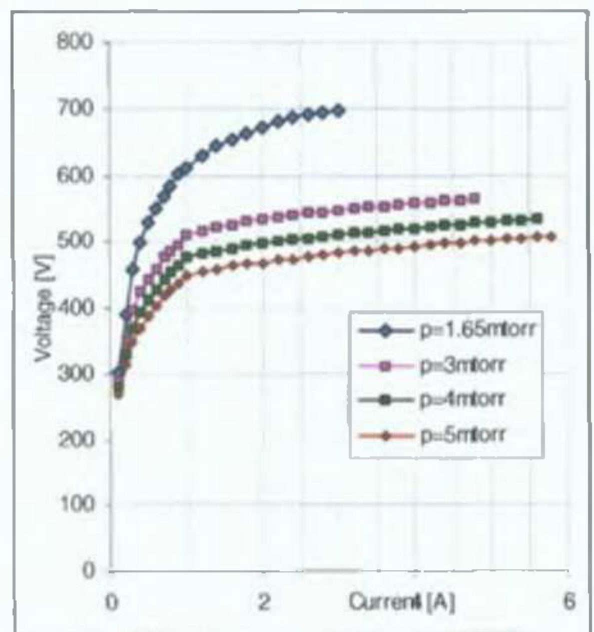

Fig.5.1.2. The IV characteristics at f=50kHz, w=4016ns for different pressures.

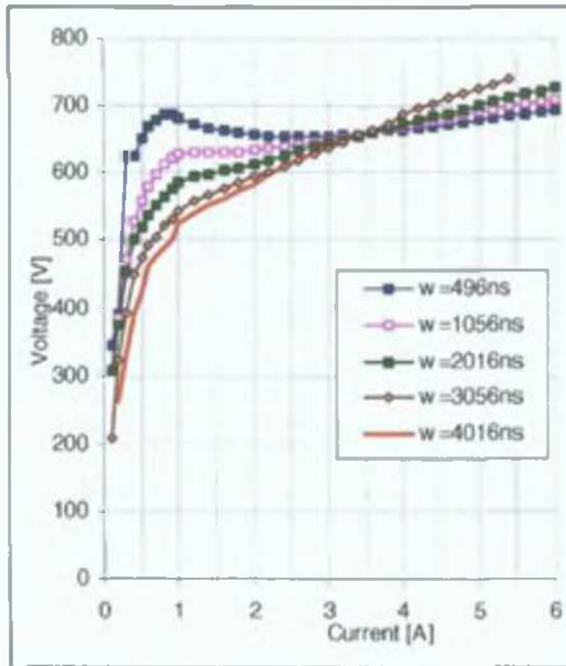

Fig.5.1.3. The IV characteristics at p=3mtorr and f=100kHz for different values of the pulse-off time w.

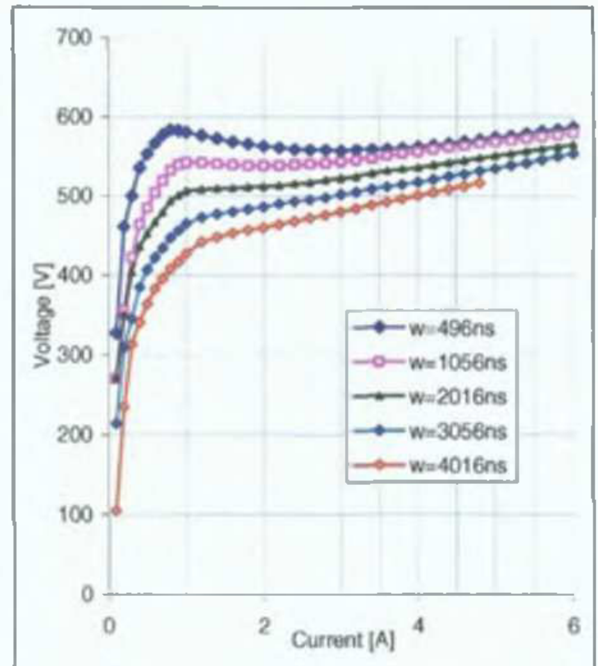

Fig.5.1.4. The IV characteristics at p=5mtorr and f=100kHz for different values of the pulse-off time w.

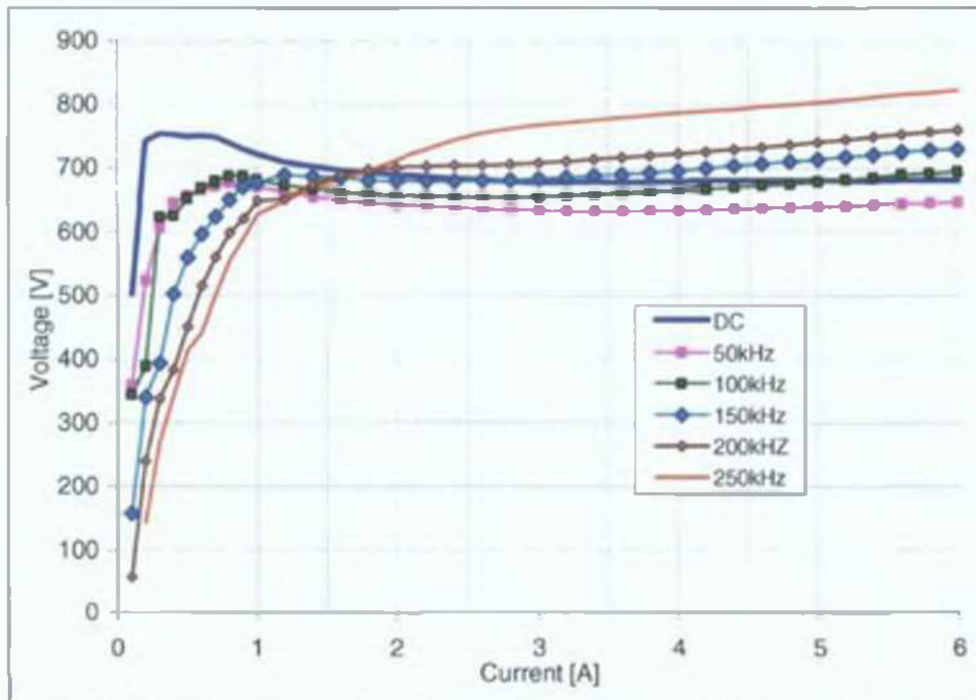

Fig.5.1.5. The IV characteristics at p=3mtorr and pulse-off time w=496ns, for different values of the pulse frequency.

5.1.1.4. DISCUSSION ON THE I-V CHARACTERISTICS

While planar magnetrons display I-V characteristics following a power law:

$$I = kV^{n};\qquad (5.1.1)$$

where n~5-15 and k is a constant, the I-V characteristics for this rectangular, opposed target magnetron follow a law of the type: $V = m + kLn(I)$; where V is the negative voltage on the cathodes measured in Volts, I is the discharge current measured in Amps and the coefficients

values are: m~-600 V and k~-100. The function is represented along with the I-V characteristics for the Fe targets in Fig.6. This function is following closely the obtained I-V characteristics (Fig.5, Fig.6) and can also be written as:

$$I = \exp[\frac{V-m}{k}]; \qquad (5.1.2)$$

indicating an exponential increase of the Current with Voltage for voltages lower than a "breakdown voltage" V=*m*; and almost constant values for |V|>|m|.

The above indicates an avalanche type ionization process followed by "breakdown" due to the high magnetic and electric confinement provided by the opposed target configuration.

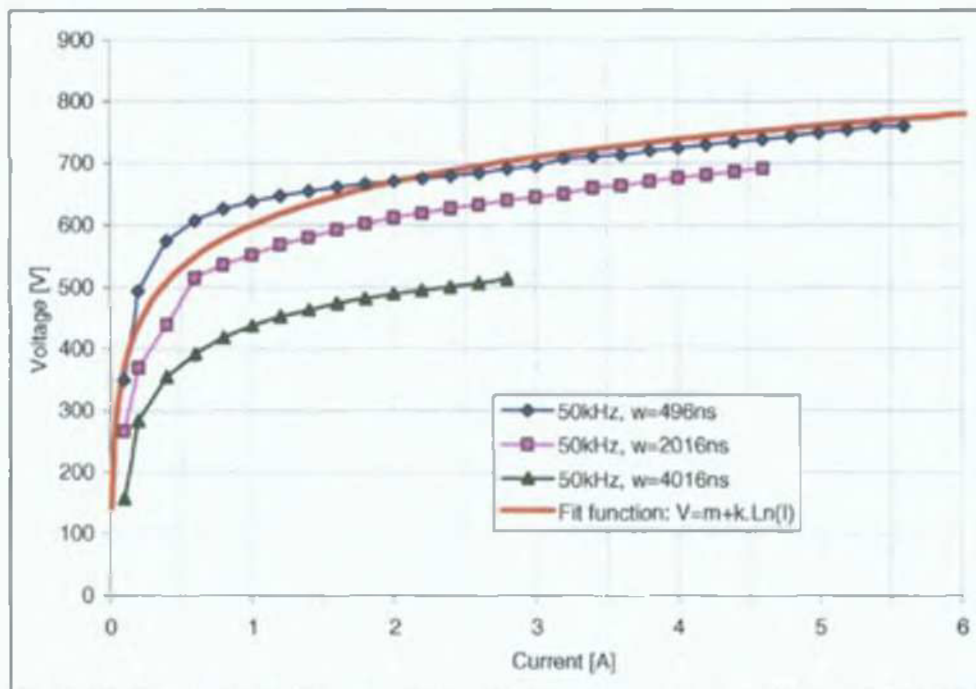

Fig.5.1.6 Typical I-V Characteristics for Fe targets during DC and pulsed DC at p=2mtorr, 50kHz and different pulse-off times (w).

5.1.1.5. CONCLUSIONS ON THE I-V CHARACTERISTICS

The behaviour of the I-V characteristics for non-ferromagnetic and ferromagnetic targets indicate that this type of rectangular, opposed target geometry allows magnetron operation at high currents without an increase in the applied voltage, ensuring a stable discharge for currents from 1A up to 6A and working gas (Ar) at pressures from 1mtorr up to 5mtorr.

It is interesting to notice here that the shapes (and even voltage potentials) of the IV characteristics obtained for the opposed target magnetron with rectangular targets are very similar to those obtained in Very High Target Power Density Magnetron sputtering for power density levels in the range 30 W/cm^2-240 W/cm^2 [52, 53, 54], although in the opposed target magnetron, the target power density is only in the range 1.5 W/cm^2 – 10 W/cm^2.

This effect is probably due to the opposed target geometry that allows good confinement and high ionization density as well as ionization of sputtered material leading to self-sputtering.

The voltage values are highly dependent on the gas pressure, while constant voltage with current can be obtained for higher pressures.

Considering the above behaviour for the discharge, the best conditions for performing and developing new methods for time-resolved plasma diagnostic are those that allow a stable discharge and a constant average plasma temperature (constant voltage with current). Therefore, the chosen discharge operating conditions used throughout this work are the following:

-Ar gas pressure: 3 mtorr (2 mtorr for Fe targets);

-Set current run: 2A (1.5A for Fe targets).

As pointed – out in this chapter, the study of the I-V characteristics provides information on the discharge behaviour and stability regions and indicates the parameter responsible for the increase of ion density at constant plasma temperature, information that will be used in the next chapters.

5.1.2. THE I AND V WAVEFORMS

5.1.2.1. INTRODUCTION

The time – resolved measurement of the Current (I) and Voltage (V) waveforms at the cathodes during pulsed DC operation provides important information on the evolution of the time-resolved voltage and power at every moment during the pulse-on, respectively pulse-off time, that correlated to other diagnostic methods leads to the development of various physical models of the discharge, as it will be shown in the next chapters.

Although presented in many papers [7, 55, 56], the current and voltage waveforms at the cathodes have not yet been used for plasma diagnostic in pulsed DC discharges. Links between the pulse-off time plasma potential values and the voltage waveform oscillations have been observed by several authors [56, 57, 58].

As will be shown next, for the opposed targets magnetron discharge, the Voltage waveforms are strongly influenced by the working gas pressure as well as by the variations in the discharge's impedance during the pulse.

The waveforms during the pulse-off time are initiated by the power supply that behaves like an inductor [51] leading to large oscillations of the voltage and current on the cathodes. The voltage and current oscillations at the targets ensure that the excess electron density in the plasma bulk is lost during the pulse-off time as a result of resistive losses in the targets - power supply circuit, thus enabling the plasma to reach quasi-equilibrium before the next pulse-on time. This process is one of the purposes of using the pulsed DC operation, as it allows the dissipation of charge density gradients that otherwise can lead to arcing and unstable discharges and finally to defaults in the thin films structure.

The voltage oscillations at the cathodes leading to oscillations of the plasma potential at the substrate region have a strong influence on the ion flux and energy incident on the substrate as it will be shown in the Chapter on "Pulse –off time physical model of the discharge".

The I and V waveforms will be correlated to the time-resolved optical spectroscopy data and to time and energy-resolved mass spectrometry results in order to analyse the waveform effects on the plasma behaviour.

5.1.2.2. THE EXPERIMENTAL SET-UP

The experimental set-up is presented in Fig.5.1.7. The Current is measured using a Hall current probe (5) connected to a Tektronix AM503B Current Probe Amplifier (8) while the Voltage is measured directly on the oscilloscope using a Voltage Probe (6). The oscilloscope readings are saved in the computer as ASCII files using the software WAVESTAR.

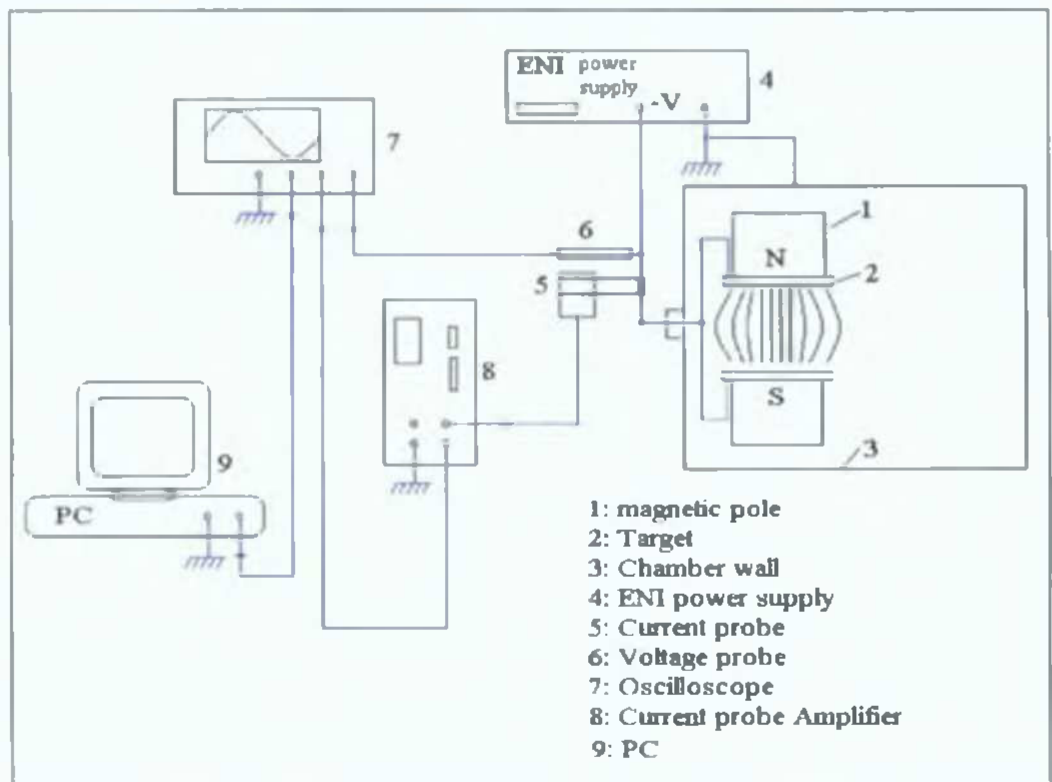

Fig.5.1.7: The experimental set-up for measuring the Current and Voltage waveforms.

The voltage and current waveforms for a range of frequencies between 50kHz up to 250kHz and pulse-off times between 496ns and 4016ns at Ar pressures of 1mtorr, 2mtorr and 3 mtorr have been measured. These waveforms display a high frequency oscillation with a high current or voltage peak during the pulse-off time.

The influence of the pressure on the amplitude of the pulse-off time oscillation, as well as during the "on" time can be noticed. A global, macroscopic plasma parameter as the pressure has a strong influence on the power delivered to the system.

5.1.2.3. VOLTAGE WAVEFORMS FOR Cu TARGETS

Typical voltage waveforms are presented in Fig.5.1.8-Fig.5.1.15. The typical evolutions of voltage waveforms with current at constant pressure (Fig.5.1.8) and respectively with pressure at constant current (Fig.5.1.9) are presented.

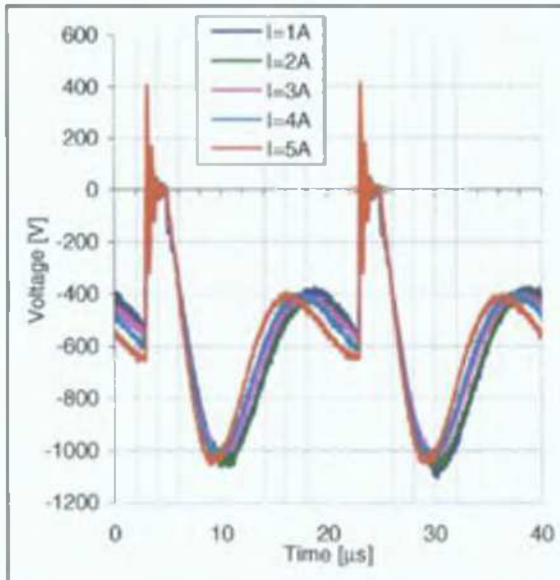

Fig.5.1.8. Voltage waveforms for different currents at p=3mtorr, 50kHz.

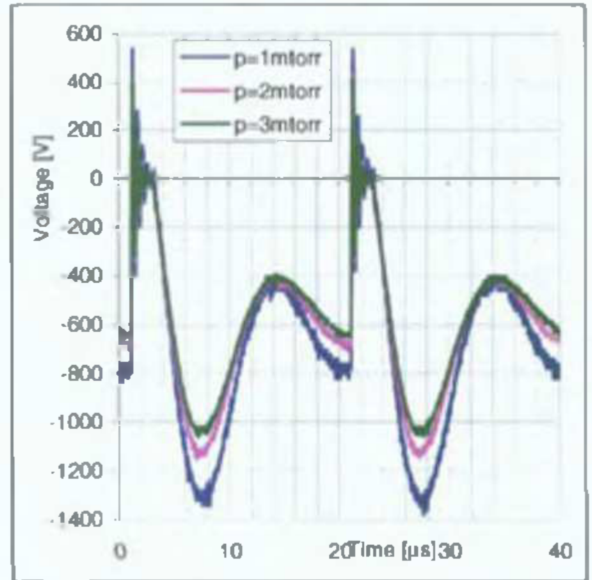

Fig.5.1.9. Voltage waveforms at different Ar gas pressures for 50kHZ, I=1A.

The voltage waveforms have the same shape and extreme values, independent of the current run at the same pressure; while the changes in pressure affect strongly the peak voltage values (Fig.5.1.8, and respectively Fig.5.1.9 and Fig.5.1.10). This behaviour is similar to the one observed for the I-V characteristics: the discharge voltage is not affected by changes in the current run, but by changes in pressure.

As the electron temperature (given by their average kinetic energy) is proportional to the cathode voltage [5], the above described behaviour indicates that changes in pressure strongly affect the electron temperature, while changes in current will allow an almost identical electron temperature evolution. Both the peak values and the temporal evolution of the voltage waveforms are strongly influenced by the duration of the pulse-off time Fig.5.1.11.

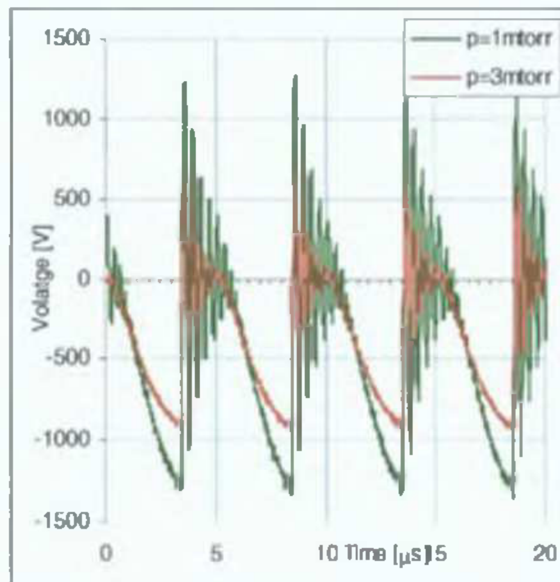

Fig.5.1.10. Voltage waveforms with pressure at 200kHz and I=1A., w=2016ns.

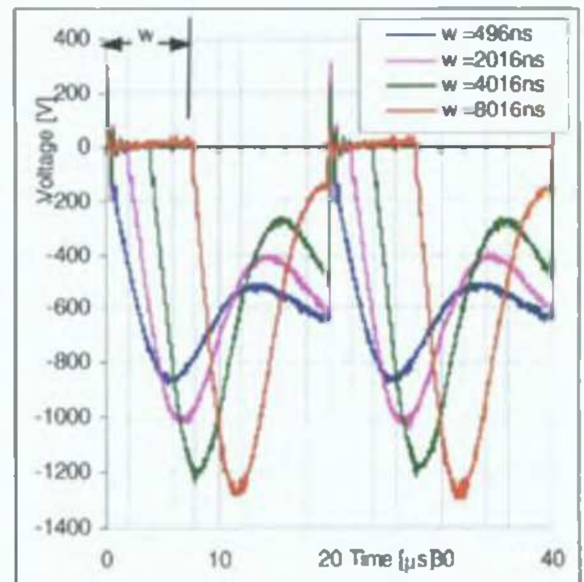

Fig.5.1.11. Voltage waveforms with pulse-off time at 50kHz, p=3mtorr, I=2A.

5.1.2.4. CURRENT WAVEFORMS FOR Cu TARGETS

The measured current waveforms are a summation of the direct electron current provided into the discharge by the power supply, the ion current into the cathodes (targets) and the secondary electrons generated through sputtering.

As seen from Fig.5.1.12 and Fig.5.1.13, the current waveforms change with the set current run, but not with the working gas pressure. As expected, the current waveforms temporal behaviour depends strongly on the pulse-off time duration (Fig.5.1.14.). A typical set of voltage and current waveforms at 50kHz, I=2A, and 3mtorr Ar gas pressure is presented in Fig.5.1.15.

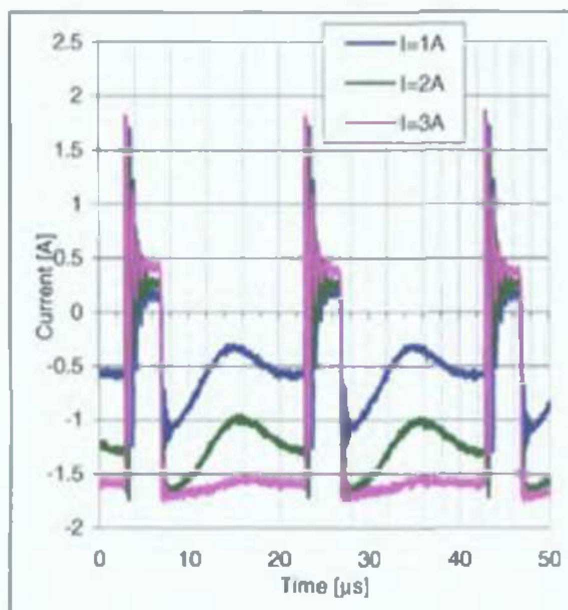

Fig.5.1.12. Current waveforms for several values of the set current run at 50kHz, p=3mtorr and w=4016ns.

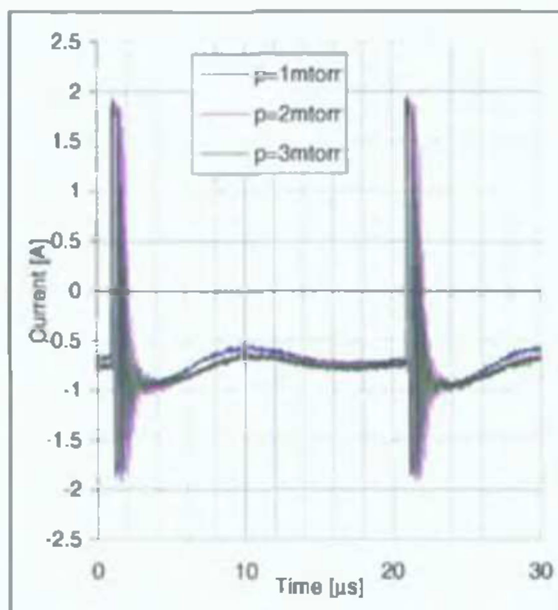

Fig.5.1.13.Current waveforms with pressure at 50kHz, w=496ns, I=1A

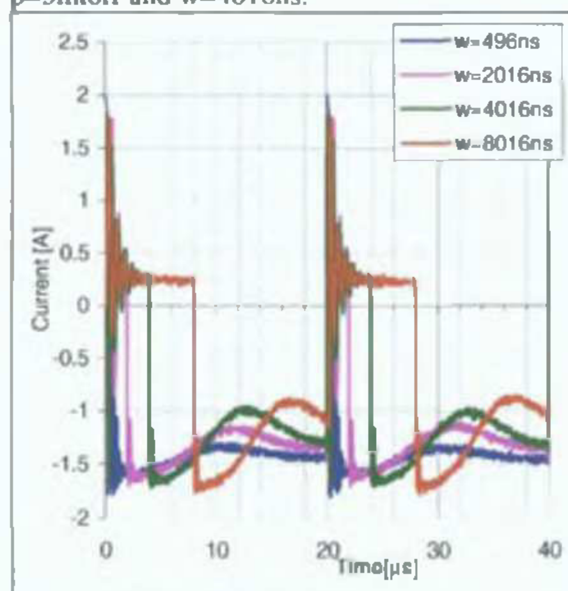

Fig.5.1.14. Current waveforms at Ar pressure p=3mtorr, f=50kHz, I=2A and different pulse widths.

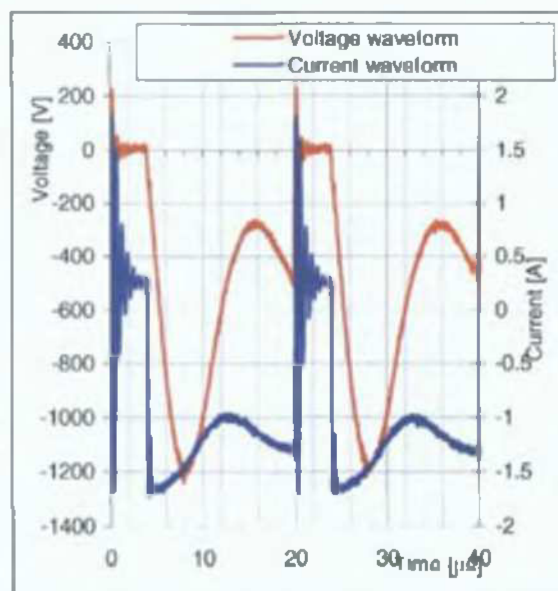

Fig.5.1.15. Current and Voltage waveforms at 50kHz, w=4016ns, p=3mtorr I=2 A.

5.1.2.5. TYPICAL WAVEFORMS FOR THE Fe TARGETS.

The voltage and current waveforms for the Fe targets display the same behaviour with regard to pressure and current changes:

- the voltage waveforms are strongly affected by changes of the Ar gas pressure while they are not affected by changes in the current run (Fig.5.1.16 and Fig.5.1.17).
- the current waveforms are not affected by changes of the Ar gas pressure and they depend on the set current run (Fig.5.1.18 and Fig.5.1.19).

Typical waveforms for the Fe targets are presented next.

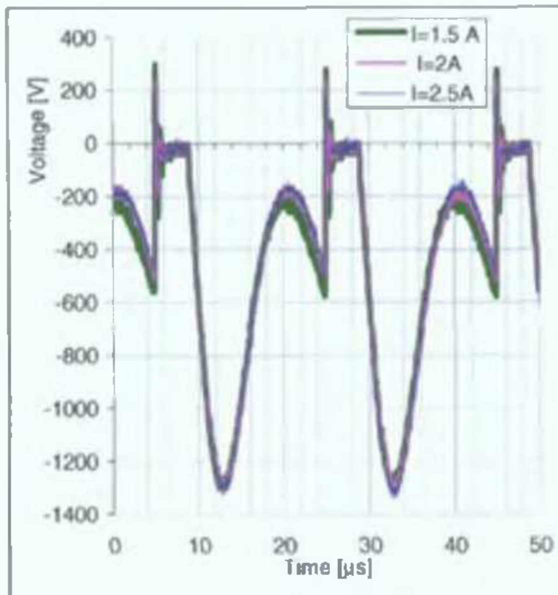

Fig.5.1.16: Voltage waveforms for Fe targets at 2mtorr, 50kHz, 4016ns.

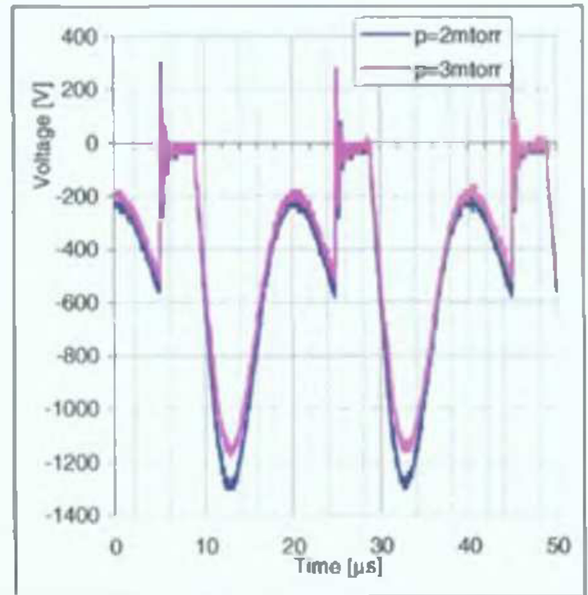

Fig.5.1.17: Voltage waveforms with pressure at I=1.5A, 50kHz, 4016ns.

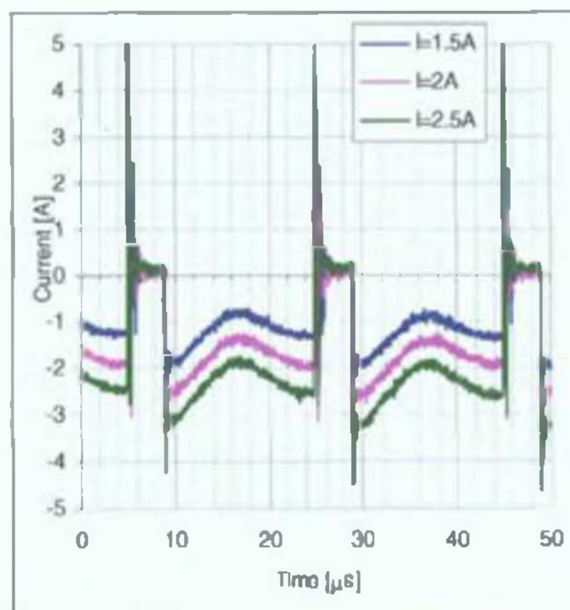

Fig.5.1.18. Current waveforms at 2mtorr, 50kHz, w=4016ns for different set current run.

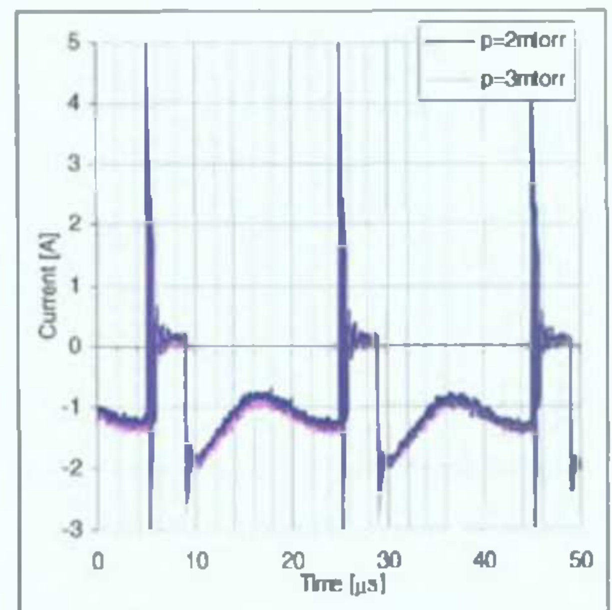

Fig.5.1.19. Current waveforms at two pressures for Fe targets, 50kHz, w=4016ns, I=1.5A.

From Fig.5.1.20 and Fig.5.1.21 we can see that the voltage and current waveforms for the Fe targets are affected by the pulse-off time in a similar manner as those for the Cu targets configuration. The current oscillations during the pulse-off time for Fe targets reaching 6A are much higher than those for the Cu targets (2A).

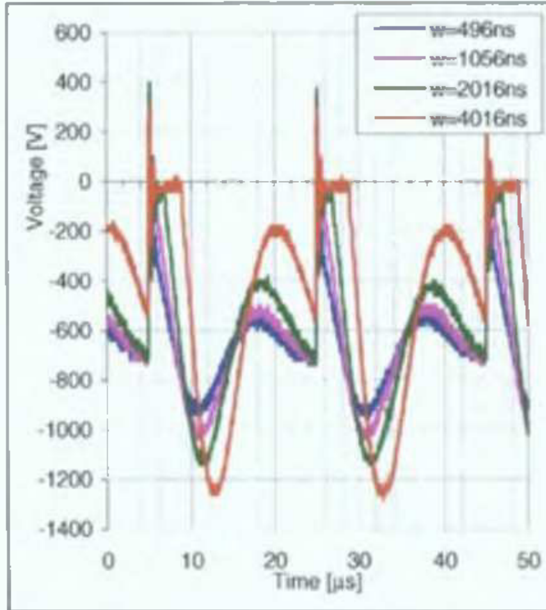

Fig.5.1.20. Voltage waveforms for Fe targets for different pulse-off times at 50kHz, I=1.5A, p=2mtorr.

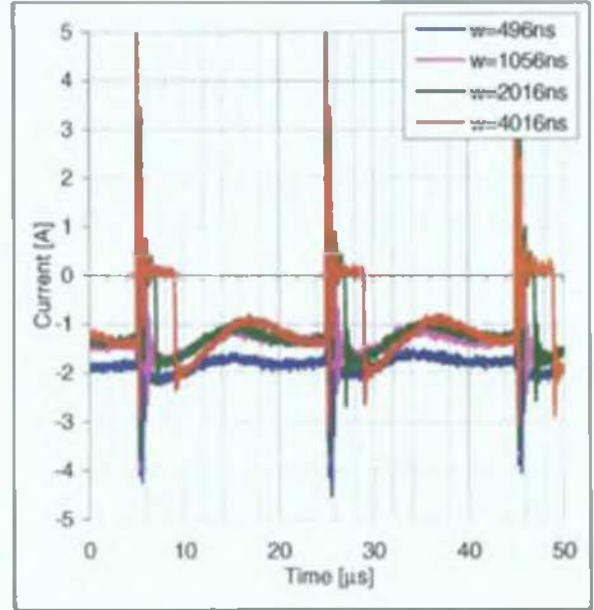

Fig.5.1.21. Current waveform for Fe targets for different pulse-off times at 50kHz, I=1.5A, p=2mtorr.

5.1.3. CONCLUSIONS

The I-V characteristics and Current and Voltage waveforms have almost identical trends for the Cu and Fe targets.

Both the I-V characteristics and Voltage waveforms display the same behaviour: they are strongly affected by changes in the gas pressure, but practically independent of the current run.

The Current waveforms are independent of gas pressure. Both Current and Voltage waveforms are strongly affected by the duration of pulse-off time. For the Fe targets, the current oscillations during the pulse-off time have higher intensity.

These similarities between the discharge behaviour for the Cu and Fe targets configurations indicate that the ionization density levels as well as sputtering rates are similar, although there are significant differences in the intensity and distribution of the magnetic field for non-ferromagnetic and ferromagnetic discharges.

The current and voltage waveforms are equivalent to a time-resolved measurement of the IV characteristics and provide the temporal evolution of Voltage and Current at the targets, indicating:

- the moment of "breakdown" during each pulse (maximum of the voltage waveform, when the discharge conduction level turns from that of an insulator to that of a conductor);

- the moment when the plasma density has the highest level (minimum in the voltage waveform);
- the pulse-off time oscillations of the voltage give an estimation of the temporal evolution of the plasma potential during the off time.

The Current and Voltage waveforms are an important indicator of the temporal evolution of the power delivered to the discharge as well as of phenomena taking place in the plasma during the pulse-on and pulse-off time.

Therefore, this time-resolved diagnostic method -although under-estimated- is extremely useful on its own and in connection to other time-resolved diagnostic methods as a base for building physical models of pulsed sputtering discharges.

Some of the results discussed in this section have already published [54] and presented as poster by the author of this thesis at the 9th Conference on Plasma Surface Engineering, Garmisch-Partenkirchen, Germany, Sept. 12-17, 2004.

5.2. OPTICAL EMISSION SPECTROSCOPY

5.2.1. INTRODUCTION

Optical Emission Spectroscopy (OES) has always been a powerful tool for plasma diagnostic and it is currently used for monitoring the magnetron plasmas discharge evolution through the observation of excited species densities.

For plasma processing, OES provides information on rate processes for active species and it is in most cases a non-invasive technique, thus, an invaluable method of diagnostic. Approaches of different complexity include the analysis of line spectra and their relative intensities, the time-resolved, or the space and time-resolved observation of several significant lines.

Using the OES line spectra, the population of different energy levels can be estimated, allowing conclusions on the mechanisms for the excitation/ionization processes and the electron kinetics. Several authors have analysed line spectra in planar magnetrons and metal vapour arc plasma sources as a function of discharge parameters (current, power, working gas pressure and composition) [59-64]. The evolution of the sputtering process can be observed by calculating atom density ratios from line OES data when some knowledge of the kinetic model of the discharge is assumed [59].

The time-resolved OES gives direct information on the temporal evolution of the various processes in the discharge [65]. The space – resolved OES observations provide information on the distribution of ionized/excited species, allowing the development of a physical model of the discharge and sputtering process as a function of various parameters, including the magnetic field distribution [66-68].

The experimental studies are complemented by analytical approaches through simulations of emission spectra of Ar-Cu glow discharges based on physical models that include all significant excitation/ionization and recombination processes generated by electron or atom/ion impact in the discharge [69]. Such simulations allow for a reliable generation of the lines' intensities and a further analysis of the influence of the discharge parameters on the observed spectrum.

Time and space –resolved OES provides complete information on the bulk plasma properties, location, density and life-times of different species as well as recombination rates and the conditions of Thermal Equilibrium and several studies can be found in literature related to pulsed glow discharges [70, 71].

The observation of relative line intensities can be used under appropriate LTE conditions to calculate the electron temperatures, while time and space –resolved mapping of electron temperatures provides direct information on electron kinetics and the development of relevant processes in the discharge [70-75].

5.2.2. EXPERIMENTAL SET-UP

All optical spectroscopy experiments have been performed using an Acousto-optic spectrometer described in Chapter (2). The OES line spectra and the time and space-resolved OES data were recorded by an optical probe situated inside the discharge chamber.

The observation of the spectrum has been done for two types of positioning for the optical probe in the geometry of the discharge:

A) Viewing the centre of the discharge on a diagonal direction across the YOZ plane;

B) Viewing the space between the targets at 5 positions, from the centre of the discharge at z=5 cm from the targets (d=0 cm from the discharge axis) to z=1cm from the targets (d=4cm from the discharge axis) situated in the plane ZOX, situated at Y=4 cm from the targets' lower edge.

The first type of positioning allows gathering general information about global behaviour of the discharge while the second allows the observation of space-resolved OES data in the region between the targets.

A schematic of each experimental set-up is presented in Fig.5.2.1 and respectively Fig.5.2.2. The probe is placed inside a collimator tube (15cm long, 0.8cm interior diameter) equipped with a transparent window in front of the probes' lenses. The window's transparency has been checked using a UV-VIS transmission spectrometer and it is constant in the wavelength range from 300nm to 800nm. The tube provides shielding from light coming from other regions of the discharge as well as against covering of the probe with sputtered material.

The probe's position and alignment parallel to the targets has been verified using the projection of a laser beam propagated through the optic system (cable and lenses) into the chamber.

For each position, the beams' projection into the chamber was checked against a semi-transparent grid placed on the area between the targets and aligned to the targets edge. The region where this projection fell on the grid was the region observed by the AOS probe during the measurement.

Only 8 measurements were performed for each window, in order to keep low the covering of the window with sputtered material.

For the time–resolved OES measurements, the accumulation was set to 30000 for each wavelength in order to provide maximum signal intensity.

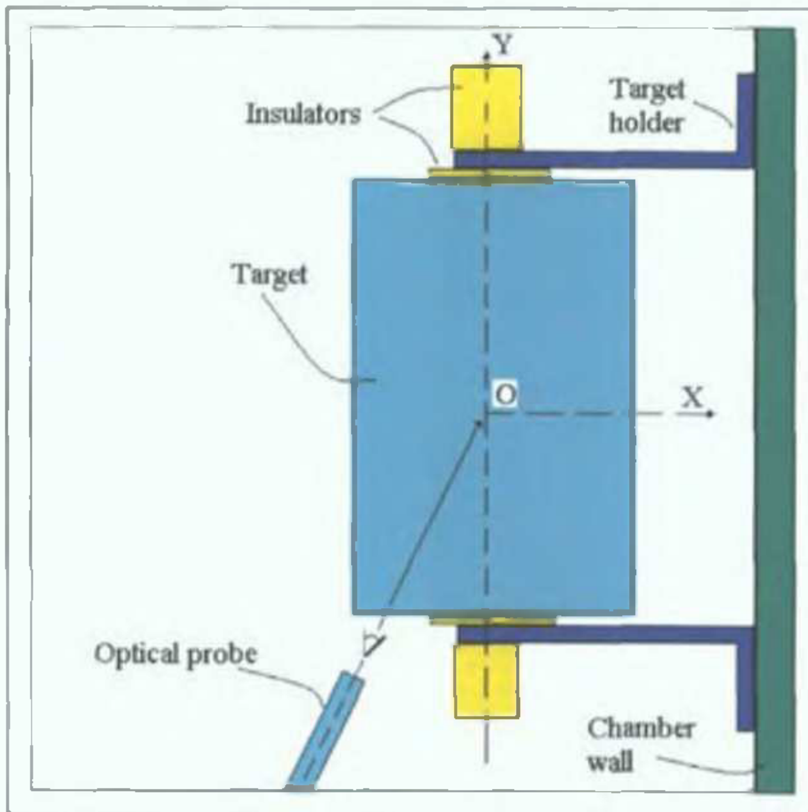

Fig.5.2.1: Cross-section view in the YOX plane with direction of OES observation. Probe positioning geometry A.

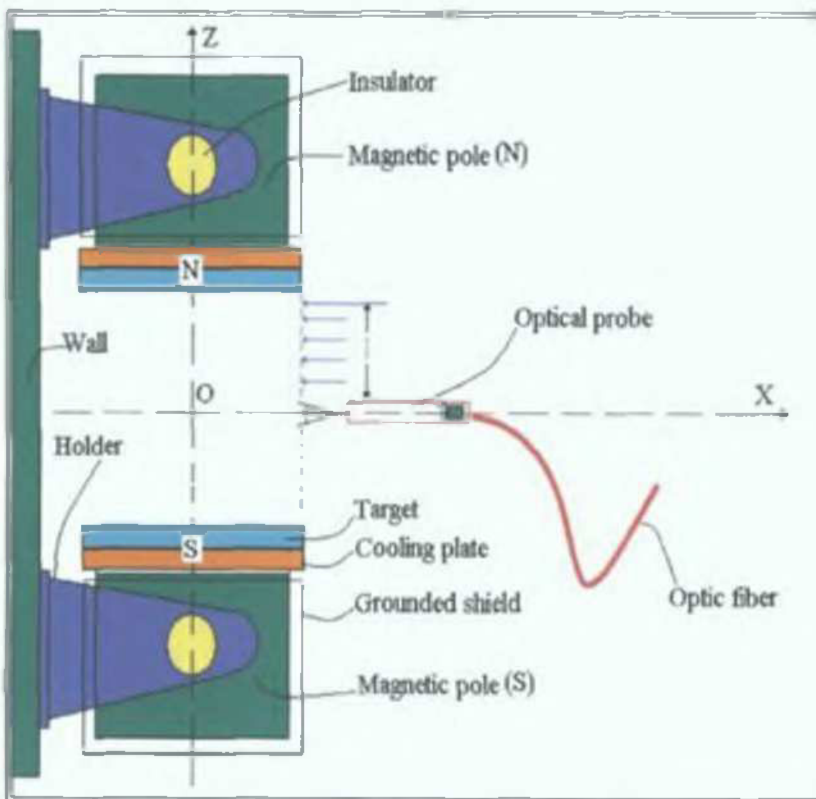

Fig. 5.2.2. Cross-section view in the ZOX plane with direction of OES observation. Probe positioning geometry

5.2.3. LINE SPECTRA

The observation of the discharge emission spectrum allows a basic analysis of the species present in the discharge process and of their evolution with the discharge parameters. In general, the observation and analysis of the line spectrum is the most basic plasma diagnostic method, providing information of major importance in the plasma diagnostic process. The main steps in this type of diagnostic are:

I) The identification and selection of emission lines for further analysis of their evolution;

II) The identification of continuum emission and its possible causes;

III) The observation of the evolution of emission lines' intensity with the discharge parameters (current, gas pressure, pulse-off time) in order to check the applicability of LTE assumptions.

I) The typical spectrum obtained for each target material configuration and the identification of the main emission lines involved are presented in Fig.5.2.3-Fig5.2.5 for the Cu targets and Fig.5.2.6 for the Fe targets. The lines selected for further analysis are presented in Table.5.2.3. The wavelengths and main parameters of the emission lines have been taken from the NIST Atomic Data Base.

Species	λ [nm]	E [eV] Upper level	E [eV] Lower level	$A_{ki}x10^8$ [s^{-1}]	gi - gk	Configurations	Ionization potential [eV]
Ar II	460.956	21.14308	18.45412	0.789	6 - 8	3s2.3p4 (1D)4s – 3s2.3p4 (1D)4p	27.629
Ar II	487.986	19.68005	17.14003	0.823	4 - 6	3s2.3p4 (3P)4s – 3s2.3p4 (3P)5s	27.629
Ar I	751.4651	13.27304	11.62359	0.402	3 - 1	3s2.3p5 (2P)4s - 3s2.3p5 (2P)4p	15.759
Ar I	763.510	13.17178	11.54835	0.245	5 - 5	3s2.3p5.(2P) 4s - 3s2.3p5.(2P)4p	15.759
Cu I	465.112	7.737028	5.072088	0.38	10 - 8	3d9 (2D) 4s.4p(3P*) – 3d9.4s (3D)5s	7.726
Cu I	521.820	6.192028	3.816692	0.75	4 - 6	3d10 (1S)4p - 3d10 (1S)4d	7.726
Cu II							20.292
Fe I	371.993	3.332020	0.00	0.162	9 - 11	3d6.4s2 – 3d6(5D)4s.4p(3P)	7.9024
Fe I	492.050	5.351572	2.832527	0.35	11 - 9	3d6(5D)4s.4p(3P)- 3d6(5D)4s(6D)5s	7.9024
Fe II							16.1877

Table.5.2.3.: Transition data for the observed lines.

For convenience, the lines will be named in the text using a round-up value of their wavelength: Ar II, 488nm; Ar II, 461nm, Ar I, 763nm, Cu I, 465nm, Cu I, 522nm, Fe I, 372nm and Fe I, 472nm. The higher levels of the Ar I and Ar II lines are generated through direct electron impact excitation and respectively ionization.

II) A continuum emission with a clearly defined edge at 473nm can be observed in Fig.5.2.5. Such a continuum emission is not observed in the Ar–Fe discharge, indicating that Ar recombination is not responsible for the above continuum emission observed in the Ar-Cu discharge.

The more probable process responsible for this continuum emission is the recombination of Cu ions (through one or several of the free–bound transitions described in Chapter (4.3.1)). The attached electron is usually found in a highly excited Cu I state from which it decays to the lower levels by radiative de-excitation.

The highly excited Cu I level *3d9.4s(3D)5s* with an energy of 7.737eV - above the ionization potential of Cu I (7.726eV) - can be directly obtained through recombination or by radiative cascade from higher excited Cu I levels. From this level, the strong Cu I 465nm line is emitted through a de-excitation transition to level *3d9 (2D) 4s.4p(3P*)*.

Such highly excited levels have a very low probability to be populated by direct electron impact excitation, as the required energy is higher than the ionization potential of Cu I. At energies above the ionization potential, the excitation cross-section reaches the lowest value while the ionization cross-section dominates (Chapter (4.3.1)). Therefore, the 465nm Cu I line is a result of Cu II recombination followed by radiative de-excitation.

Lewis et al. [9] has observed such high-energy electronic states (Cu I emission 368.74nm from 7.16eV to 3.82eV) predominate in the after-peak of a pulsed glow discharge, confirming that such lines are a result of the relaxation of highly excited Cu I atoms produced through Cu ions recombination.

A continuum emission with a clearly defined edge at 473nm (corresponding to the ionization potential of Cu I, 7.626 eV) can be observed. The most probable process responsible for this continuum emission is the recombination of Cu ions (through one or several of the free – bound transitions described in Chapter (4.3.1). The attached electron is usually found in a highly excited Cu I state (3d9.4s (3D)5s or above), and is performing a de-excitation transition to level 3d9 (2D) 4s.4p(3P*), emitting the strong Cu I 465nm line.

In the configuration with Fe targets, the Fe I 372nm line is a resonance line with a high level populated by a number of 386 transitions, most of which come from higher excited levels, with energies above the ionization potential for Fe I, thus states resulted from recombination.

Although in this case the higher level can be populated through either direct electron impact or radiative de-excitation (following recombination), its observation is interesting as it still provides collective information over a large number of possible transitions generated following recombination.

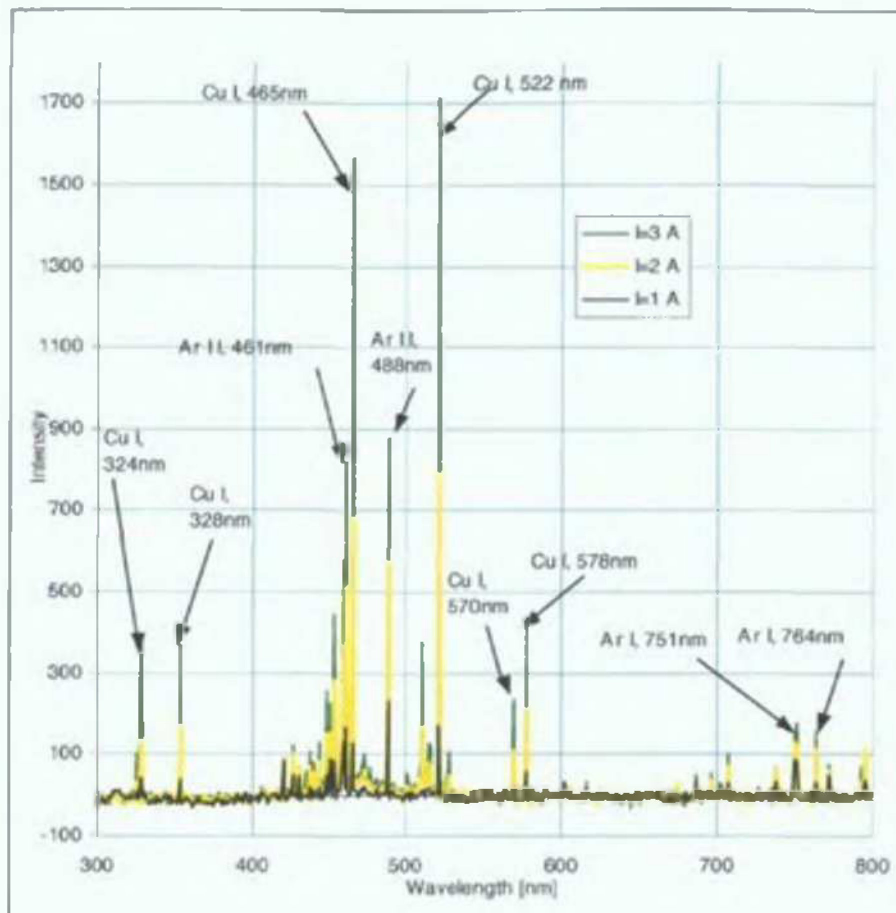

Fig.5.2.3. OES line Spectrum at 50KHz, w=496ns, pAr=1 mtorr

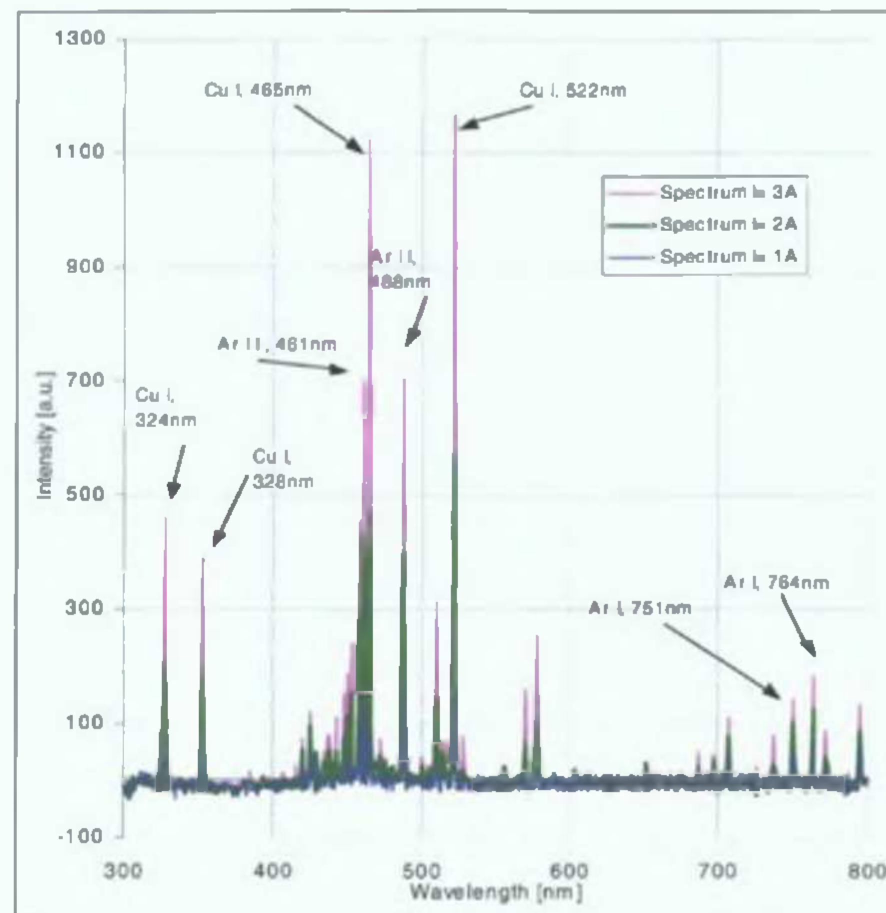

Fig.5.2.4. OES line spectrum at p=3mtorr, 50kHz, pulse-off time w=2016ns

Both measurements have been performed using cable A and a PMT potential of 600V. In these conditions the details of the continuum background cannot be observed. Nevertheless, the trend of the increase in the OES intensity with the current is not affected and can be clearly observed.

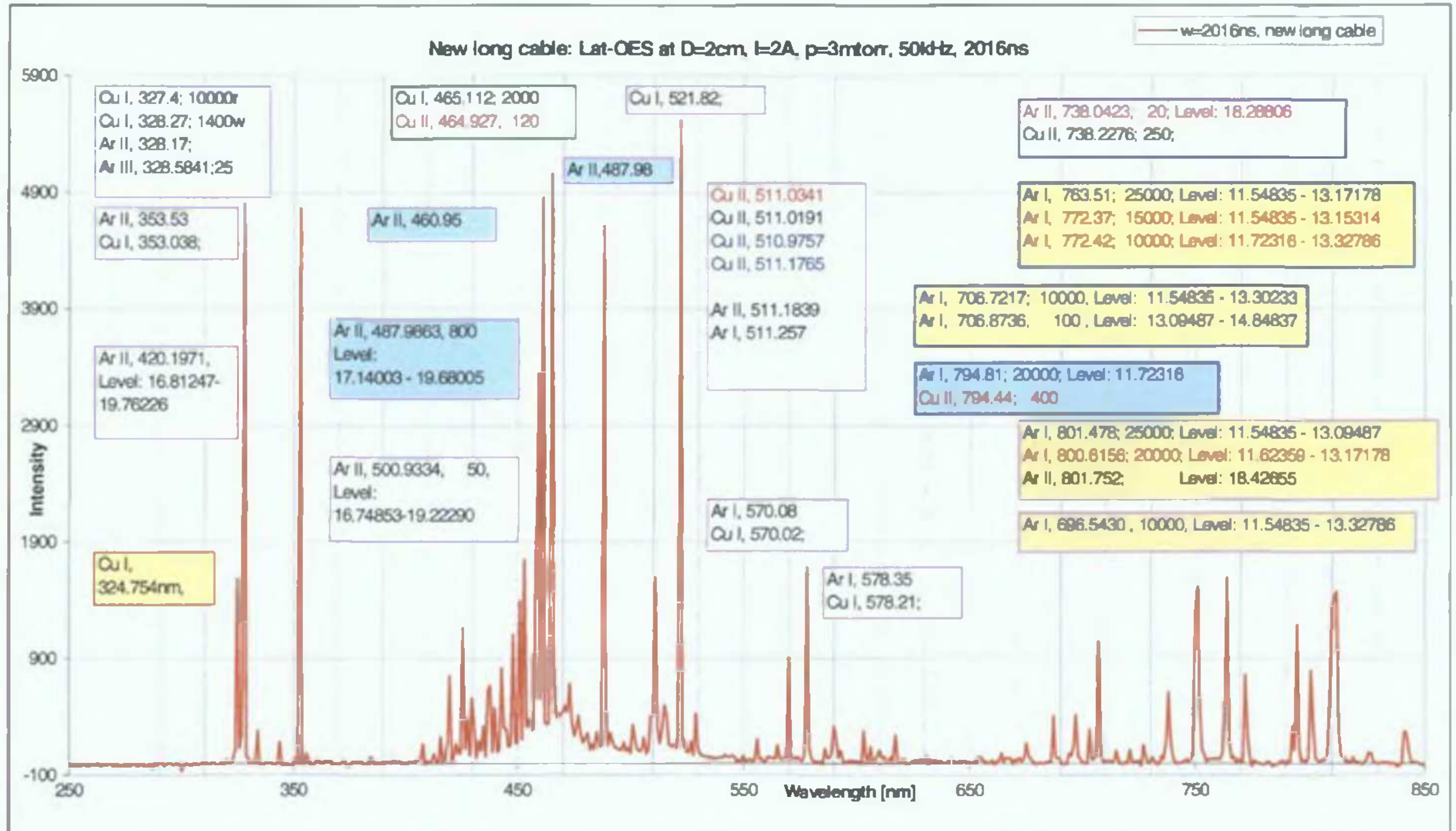

Fig.5.2.5. OES line spectrum for Cu targets at 50kHz, pulse-off time w=4016ns and Ar gas pressure p=3mtorr. The background has been subtracted for this graph. This line spectrum has been measured using cable B and a PMT voltage of 600V. The new cable allows observing the details of the continuum emission.

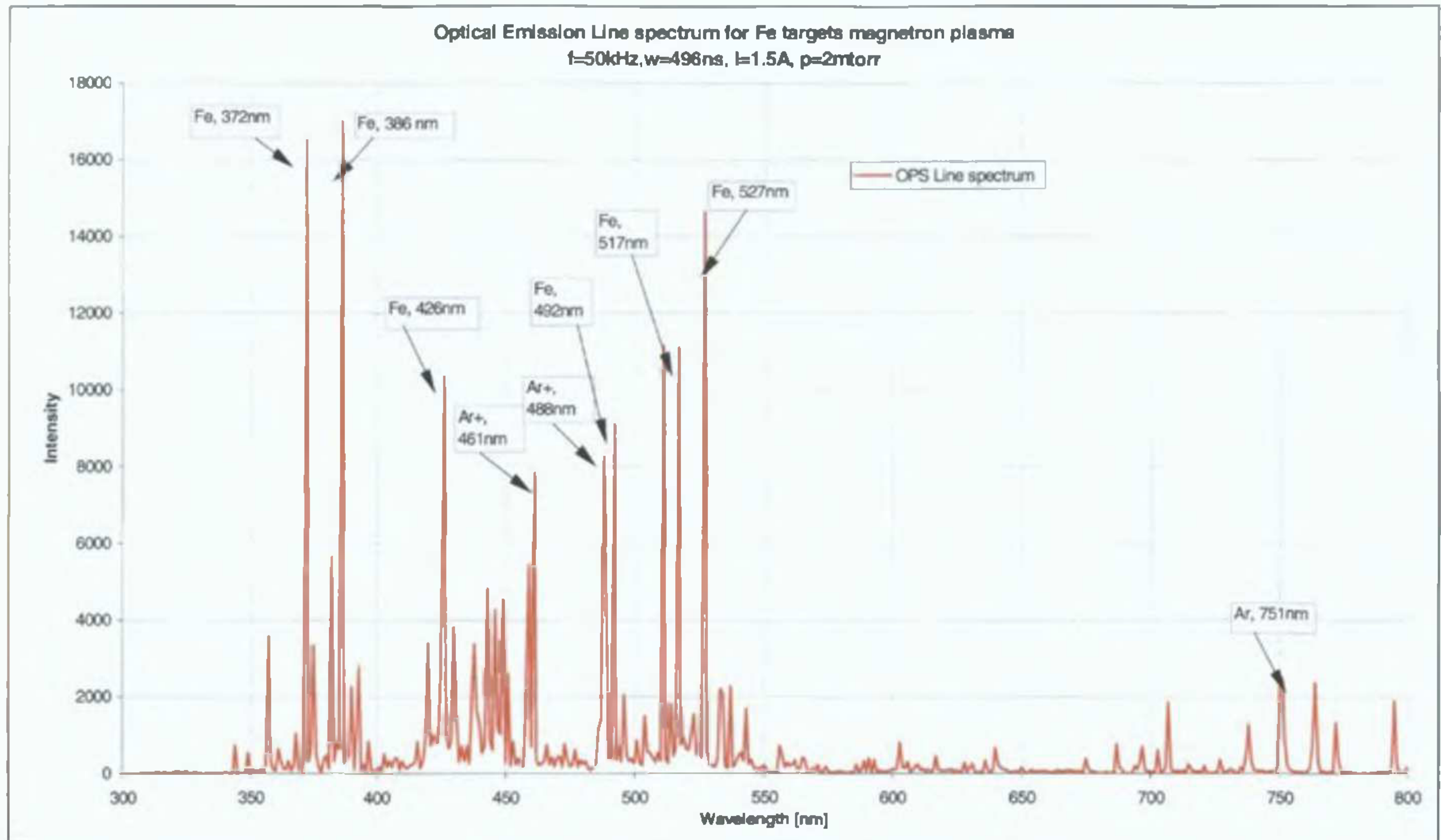

Fig.5.2.6. Optical Emission Line spectrum for Fe targets magnetron plasma f=50kHz,w=496ns, I=1.5A. p=2mtorr.

Measurement performed with cable B. The Fe II lines are all below 350nm and could not be observed. Fe III lines have very low intensities and could not be observed. The background has been subtracted for this graph.

III) One of the most important observation regarding the emission spectrum is to characterize the plasma from the point of view of its "transparency" that indicate appropriate conditions for OES line intensity measurements.

As shown in Chapter (4.3) optical spectrometry analysis provides direct information on the discharge parameters and allows determination of lines' intensities "along the line of sight" if the rate of radiative processes exceeds the rate of absorption process. This type of plasma is called "optically thin" and it is considered to be in LTE [39] allowing the application of statistical averaging under equilibrium conditions, meaning that the measured values are true averages of the processes involved and can be directly linked to the LTE statistics. A proof that the LTE or at least PLTE conditions occur is observing "optically thin" spectroscopic lines.

By definition, a plasma is "optically thin" when radiation absorption processes are negligible and the observed emission lines are "optically thin".

The emission lines are optically thin when their radiance (the area below the emission line, equal to the product between their FWHM, their height and a constant given by the line shape) increases proportional to the number of emitters (excited ions or atoms) at constant excitation temperature [76]. Here, the excitation temperature is the electron temperature.

To verify the proportionality, there are two methods to increase the number of emitters at constant excitation temperature [76]:

-to increase the gas density (the pressure) at the same excitation (electron) temperature (same excitation conditions) or,

-to increase the excitation (the current, thus the electron density) while keeping constant the gas density and plasma temperature.

The electron temperature is mainly determined by the average electron energy and thus by the cathode voltage which is independent of current (Chapter 5.1).

Thus, the electron temperature follows the cathode voltage behaviour and is independent of current as has been shown in Chapter (5.1) for both DC and pulsed DC discharges.

This behaviour has been observed in the evolution of all static I-V characteristics and Voltage waveforms (As an example, I-V characteristics for a discharge at 50kHz, 4016ns and 2016ns pulse-off time are presented in Fig.5.2.7 and Fig.5.2.8).

The I-V characteristics, display (Fig.5.2.7, Fig.5.2.8) constant voltage, practically independent of current in the range from 1A to 5A; and a strong dependence of the voltage on gas pressure, indicating that average electron temperature is constant with the increase in current but has strong variations with the increase in the gas pressure.

Therefore, the increase in the number of emitters at constant excitation temperature (electron temperature) can be obtained by increasing the discharge current.

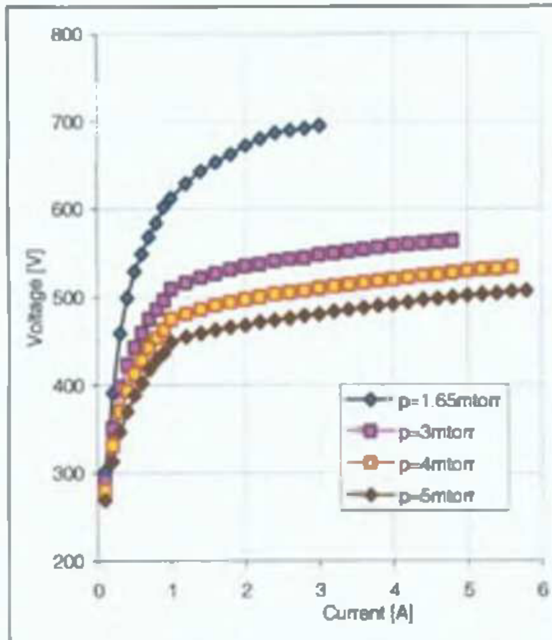

Fig.5.2.7. The IV characteristics with Ar gas pressure at 50kHz, w=4016ns pulse DC discharge.

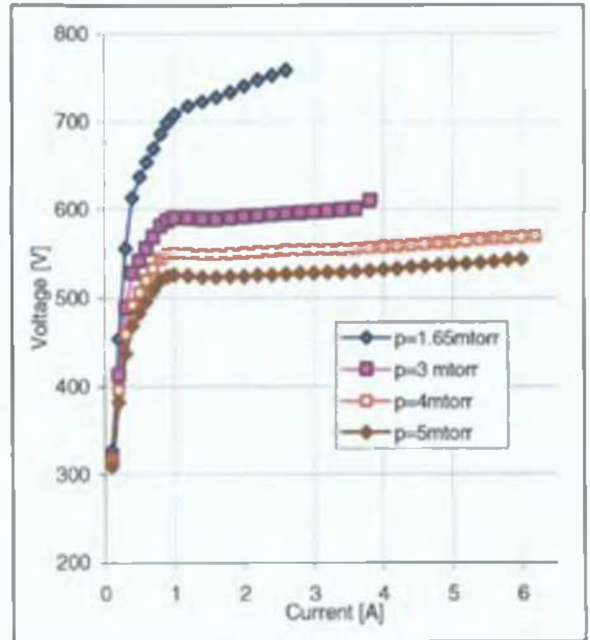

Fig.5.2.8. The IV characteristics with Ar gas pressure at 50kHz, w=2016ns pulse DC discharge.

A typical behaviour of lines radiances for the two Ar ionic lines is presented in Fig.5.2.9.

The behaviour of Ar ion emission lines' radiance with the increase in current presented in Fig.5.2.10 and Fig. 5.2.11, shows a linear trend at each position (z). This is a proof that the levels for the chosen emission lines are following the Boltzmann statistics and can be used for electron temperature estimations.

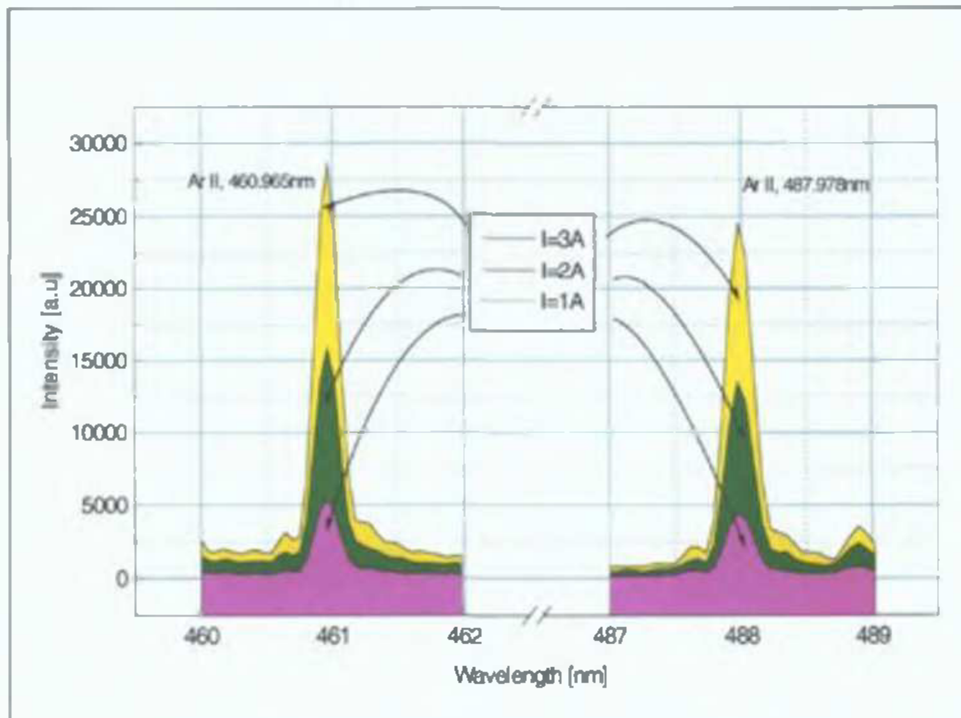

Fig.5.2.9: Typical evolution of lines' radiance with current for two Ar II emission lines: 460.965nm and 487.978nm at p=3mtorr, and 4016ns pulse-off time.

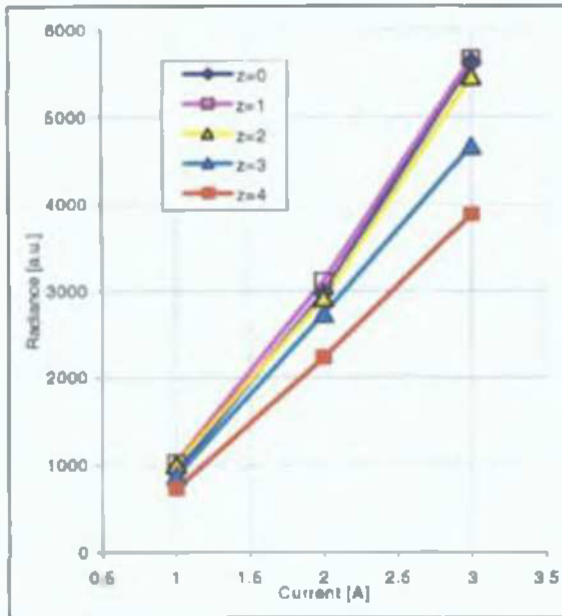

Fig.5.2.10. The evolution of the radiance for the Ar II 461nm line with current.

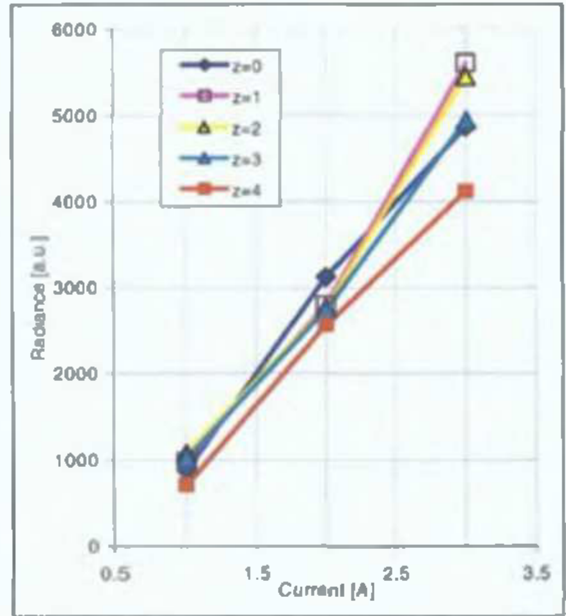

Fig.5.2.11. The evolution of the radiance for the Ar II 487nm line with current.

The similar behaviour of the IV characteristics for Fe targets and Cu targets (Figs. 5.2.7, 5.2.8 versus Fig.5.2.12) indicates that plasma temperature is constant for a given pressure and independent of the current, thus an increase in the number of excited species at constant plasma temperature can be obtained by an increase in the current.

The line spectrum for Fe targets (Fig.5.2.13.) also shows an increase in lines' intensities with current, indicating proportionality of the number of "emitters" with the current and thus optically thin lines.

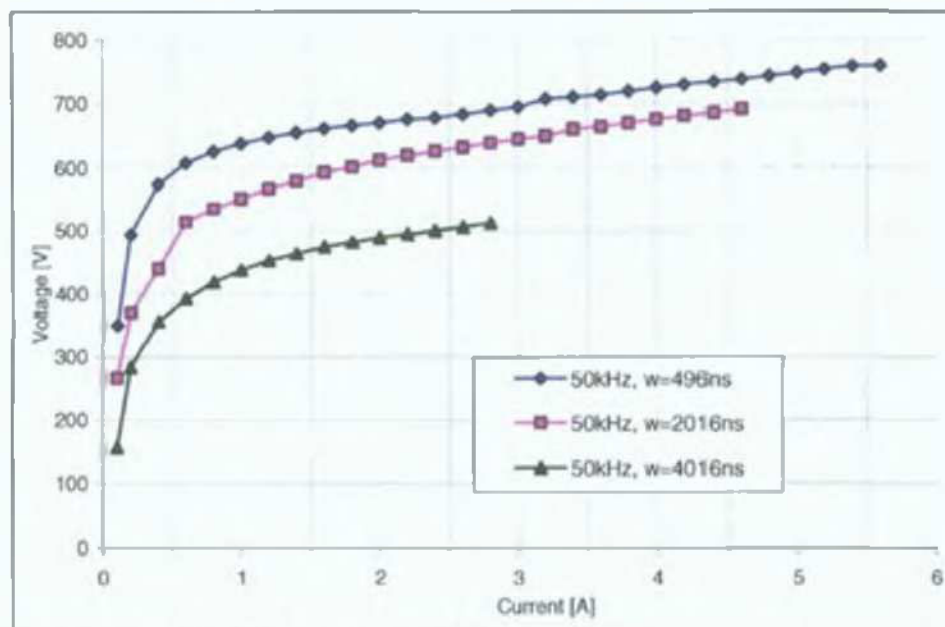

Fig.5.2.12. Typical IV waveforms for the Fe targets.

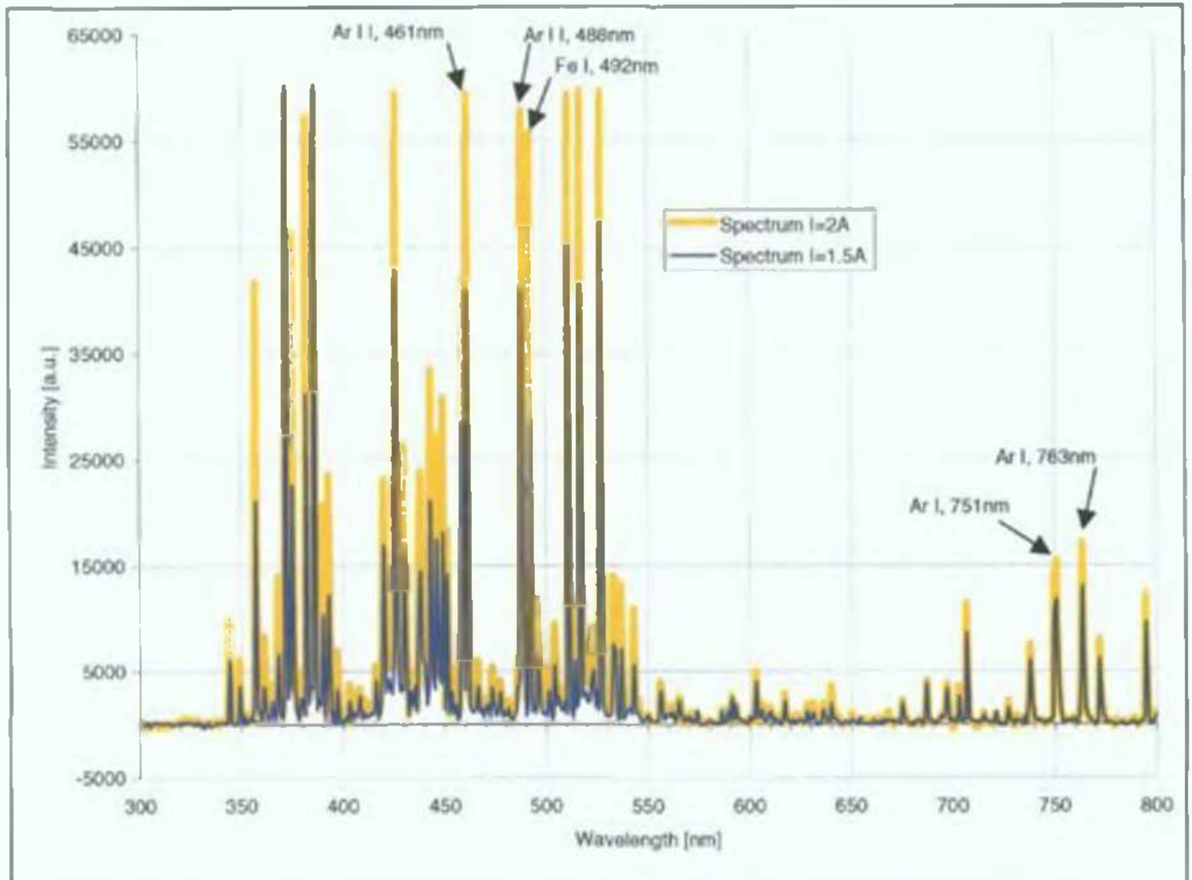

Fig.5.2.13. OES line spectra for Fe targets. OES Intensity with current at p=2mtorr, 50kHz, pulse-off time w=4016ns.

The Fe I resonance lines 372nm and 386nm show a different behaviour with current as their higher levels are filled through cascade transitions from higher excited levels and recombination levels and therefore they don't show a proportionality trend with current.

5.2.4. TIME-RESOLVED OES

5.2.4.1. THE Cu TARGETS CONFIGURATION

The main atomic processes leading to excitation and ionization processes in the magnetron discharge are due to direct electron impact excitation and ionization, balanced by their reverse processes, as discussed in Chapter (4.3).

Time-resolved OES provides information on the temporal evolution of different processes inside plasma, important as a diagnostic in pulse DC sputtering discharges. The observation of emission lines from different species allows a direct estimation of the time-scales for the beginning of the sputtering process.

The evolution of the sputtering process during the pulse has been observed by measuring the time-resolved OES intensity for the most intense lines observed in the line spectrum: Ar II, 488nm, Cu I, 522nm and Cu I, 465nm. Several examples and an analysis of the time-resolved data obtained with the probe viewing the discharge centre (configuration A, as explained in Section 5.2.1) follow.

In Fig.5.2.14 and Fig.5.2.15, the Ar ions start to be produced only after the first µs from the beginning of the pulse (the Ar II 488nm line). The applied power peak is followed by the Ar ion peak after a time delay. This delay can be related to the time needed to create new Ar ions that will return to the target, produce secondary electrons and new Ar ionization. The average value of this delay evaluated from the time-resolved OES data for different duty cycles gives a constant value of ~2.5µs at a pressure of 0.4Pa.

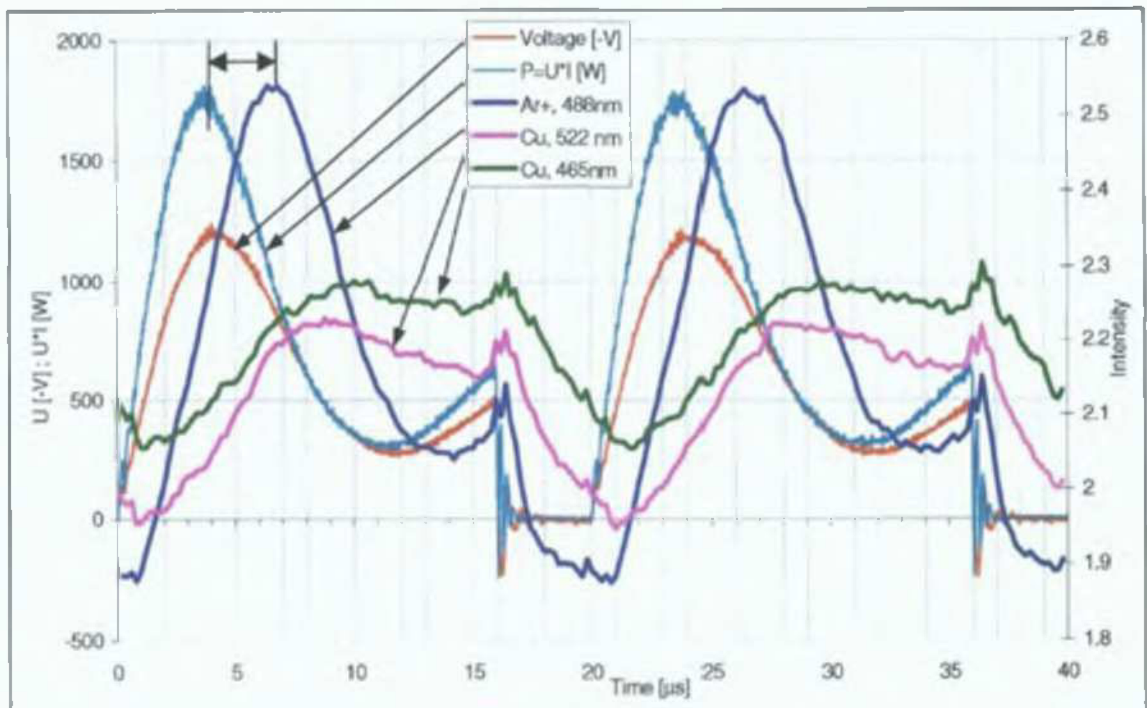

Fig.5.2.14. Voltage and power waveforms along with the time-resolved OES signal for Ar II (487.9nm) and Cu I (465nm and 522nm) for a discharge at I=2A, f=50kHz, w=4016ns, pAr=3mtorr.

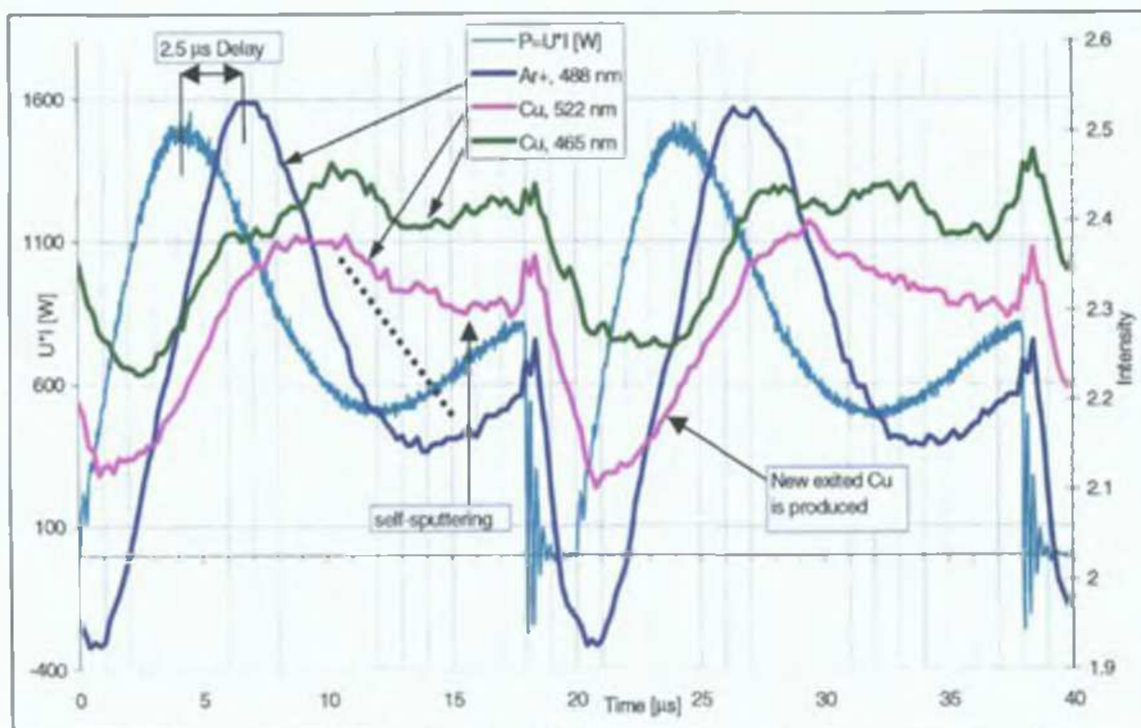

Fig. 5.2.15. Time resolved O.E.S. I=2A, f=50KHz, w=2016ns, pAr=3mtorr. The dotted line indicates the expected "fall" of the excited Cu peak.

New copper atoms are produced when the Ar ions reach the targets, so the above time constant can be also observed as the Cu I 522nm line emission peak follows the Ar line emission peak after ~2.5µs (fig.3A).

As the Ar ion peak is increasing and decreasing with symmetrical slopes following the applied power peak, we expect the sputtering process (Cu peak) to follow the same pattern if the sputtering is only due to the Ar ions. The expected "fall" in the Cu I line trend is indicated by a dotted line in Fig.5.2.15.

The fact that the trend of the Cu I line does not follow the decay of the Ar ion peak indicates that more Cu atoms are produced by other mechanisms, like self-sputtering, or that the efficiency in Cu atom excitation increases at later moments during the pulse. The latter assumption is contradicted by the observed shape of the excited Ar line (751nm) (and example is presented in Fig.5.219) that follows closely the shape of the Ar ion peak, indicating that excitation processes requiring lower electron energies are not increasing at later moments during the pulse. Therefore, Cu self-sputtering is expected to take place in such a discharge.

The 465nm Cu I line follows the trend of the Cu I 522nm line. From atomic spectroscopy data, as explained earlier, the 465nm line is expected to be due to a de-excitation process following Cu II recombination; and its evolution indicates the temporal evolution of the recombination rate during the pulse.

Therefore, the delay between the power peak and the Ar ion peak can be explained as the average time the Ar ions need to travel to the targets from the place of their production. Observing the evolution of the Ar ion line in relation to the power pulse we can get a deeper insight into the "heating" mechanism leading to the formation of the Ar ion peak: as the power

pulse increases, more Ar ions are produced. The Ar ions produced when the power pulse is at its maximum travel to the targets and produce secondary electrons that lead to the maximum of the Ar ion peak. As the electrons generated at the moment of maximum power (peak) will produce Ar ionization with maximum probability at a certain region in the discharge, the Ar ions thus created will have a well-defined average time to reach the targets and will produce a "wave" of secondary electrons that lead to the observed peak in Ar ionization, about 2.5μs later.

Thus, time-resolved observation of the plasma evolution brings information on the time-scale of the sputtering process that can be of high importance for the choice of the pulsed DC duty cycles.

Duty cycles with a pulse-on time shorter than the time required for the Ar ions to be produced and reach the targets will have a very low sputtering efficiency (for example, pulse-on times smaller than 5μs; or pulse frequencies higher than 100kHz). An example of the temporal evolution of the OES lines is presented in Fig.5.2.16 and indicates an insignificant variation in the emission of Cu lines, showing a poor efficiency of the direct sputtering process.

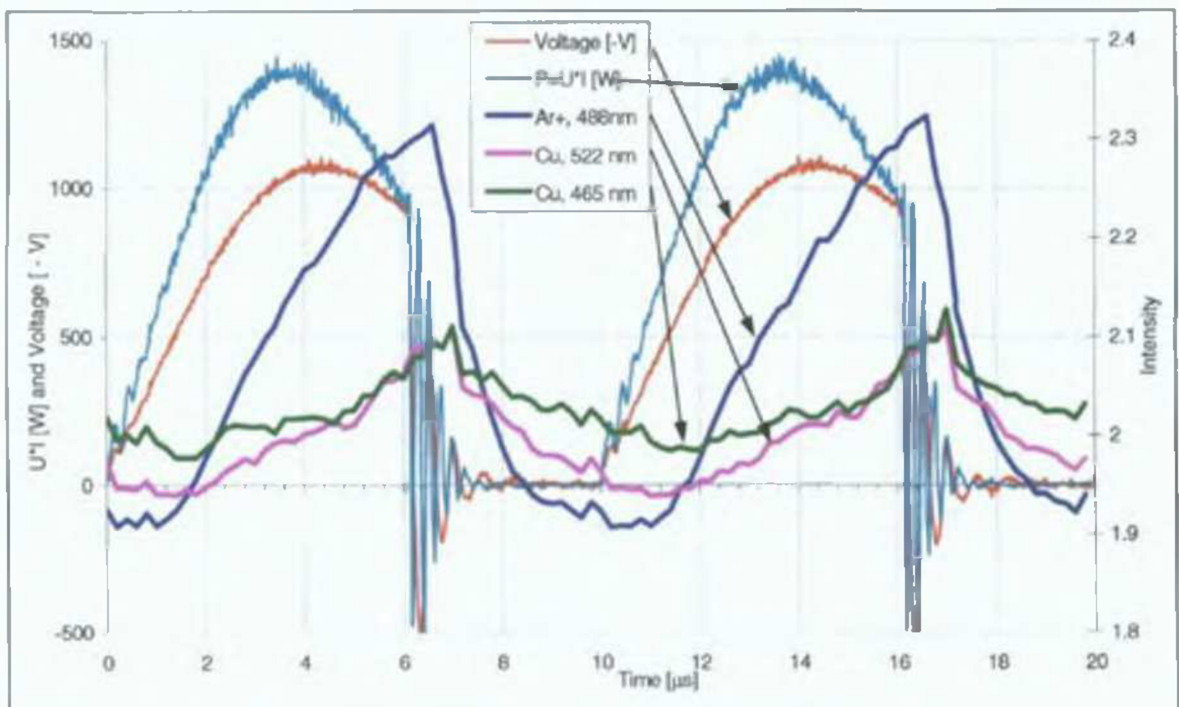

Fig.5.2.16. Time-resolved OES at I=2A, f=100kHz, w=4016ns, p=3mtorr

In Fig.5.2.16 we can see that the Ar ion peak is not complete, and it reaches a maximum at the end of the pulse-on time. These Ar ions don't have the time to reach the targets to produce more sputtering and are lost from the discharge during the next 4016ns pulse-off time. As a result, the excited Cu (522nm and 465nm) lines have a low intensity, indicating a low efficiency of the sputtering process.

Nevertheless, high frequency pulsed DC discharges can (under appropriate conditions) rely on the self-sputtering process as the slow Cu atoms may not leave the discharge during one duty cycle and will be ionized at the beginning of the next duty cycle.

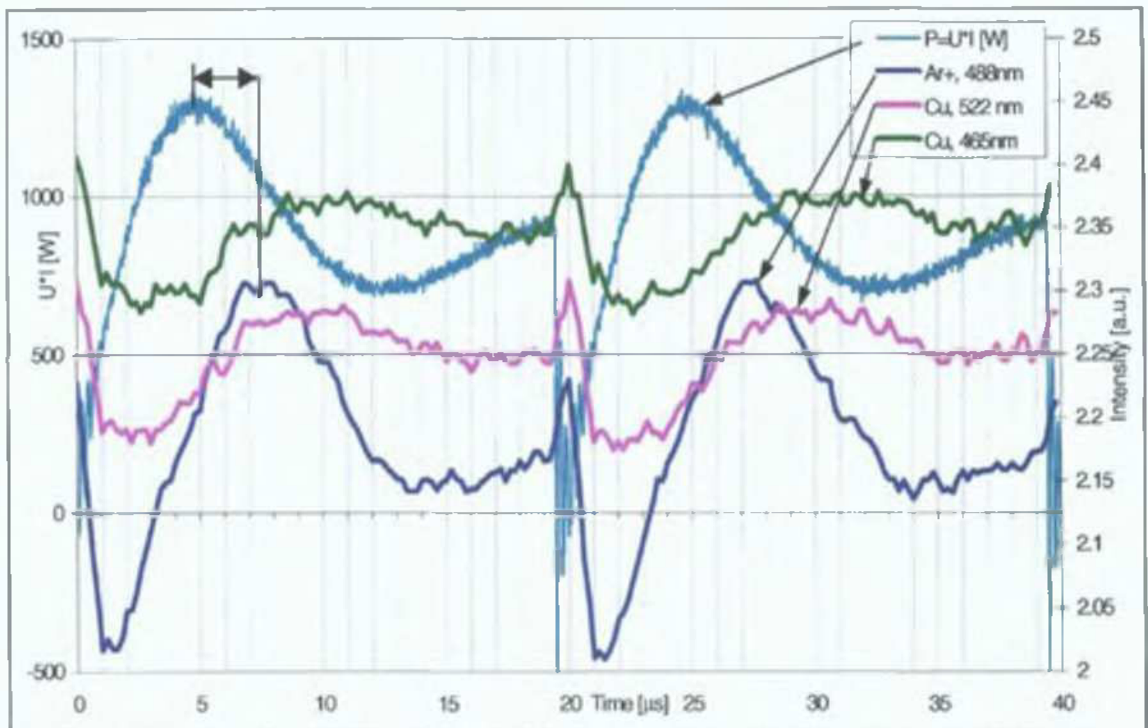

Fig.5.2.17. Time-resolved OES at I=2A, f=50kHz, w=496ns, pAr=3mtorr along with the power waveform.

Observing the relative intensity of the Cu I 465nm line (resulted from de-excitation following Cu ion recombination) and assuming LTE conditions, the relative Cu ionization density for different duty cycles can be observed.

For example, for a pulse-off time of 496ns (Fig.5.2.17) the 465nm Cu line has much higher values than those of Cu 522nm line, indicating that a higher percentage of Cu is ionized than excited on atomic levels. This process is strictly related to the evolution of electron temperature in pulsed DC plasmas, which will be analysed in Chapter 5.3.

This process can be also related to a "quenching" process [75] that occurs with high probability when electron energies are smaller than Ar ionization potential but higher that Cu ionization potential. In this process, once the Cu atoms are present in the discharge (after the Ar ions have initiated the sputtering process) the electron energy is no longer used for Ar ionization but for Cu ionization. This situation is enabled by the decrease in the voltage peak (thus lower electron energies) once the sputtering has started, due to a decrease in the discharge impedance. Such discharges are dominated by self-sputtering. This can be observed as an almost constant intensity of the Cu lines after the Ar ion peak fall (at t>10µs, Fig.5.2.17).

The self-sputtering is the dominant process in duty cycles with pulse-on times much longer than the time-scale for direct sputtering

5.2.4.2. THE Fe TARGETS CONFIGURATION

For the Fe targets, (Fig.5.2.18 and Fig.5.2.19) the temporal evolution of the sputtering process has a similar evolution to that for the Cu targets. A delay of ~2.5μs between the power peak and the Ar ion peak indicates the same time-scale for the travel time to targets of Ar ions.

While the trend for the excited Ar I line (751nm) follows the Ar ion peak, the trend of the excited Fe lines holds at high values after the Ar ion peak fall indicating an important contribution of the self-sputtering. For the Fe targets, once the discharge has been initiated by the Ar ions, the sputtered Fe atoms are ionized and can maintain an almost constant sputtering rate for the rest of the pulse-on time.

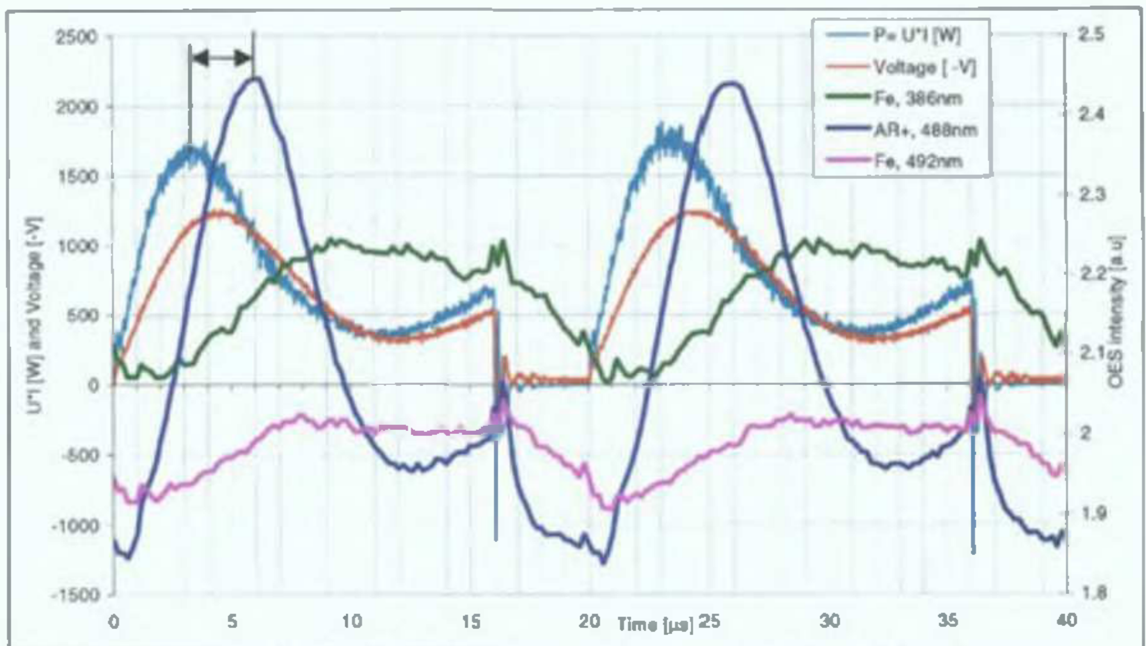

Fig. 5.2.18: Time -resolved OES for Fe targets at 50kHz, w=4016ns, I=1.5A, p=2 mtorr.

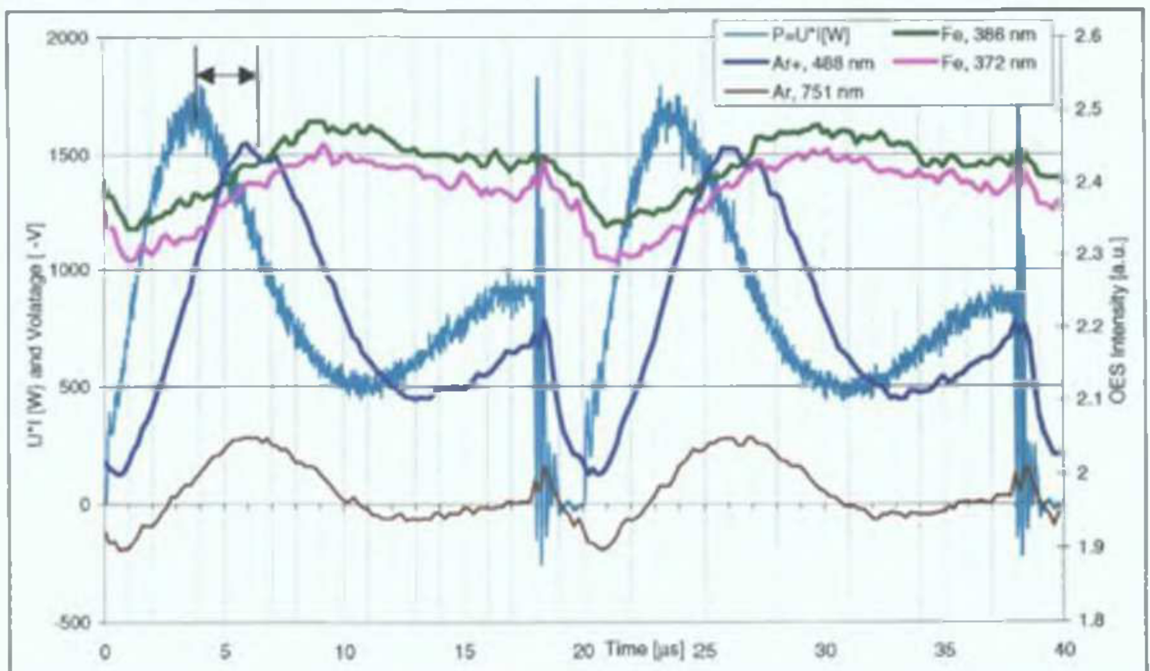

Fig.5.2.19. Time -resolved OES for Fe targets at 50kHz, w=2016ns, I=1.5A, p=2 mtorr.

5.2.4.3 CONCLUSIONS

The observation of the Cu I 465nm line is extremely interesting here due to its mechanism of production (through a de-excitation process following recombination) as it provides information on the rate of recombination processes and on the space and temporal distribution of Cu ions (assuming that LTE conditions apply).

Although the relative intensities of the two Cu I lines (the 465nm line produced following recombination and the 522nm line produced by direct electron impact excitation) cannot provide complete information on the ionization –recombination balance, their similar trend indicates that a constant equilibrium between excitation (and respectively direct impact electron ionization) and recombination processes is maintained during the pulse.

In the case of Fe targets, the relative intensity of the 492nm line (with a high level populated through direct electron impact excitation or de-excitation from levels populated through direct electron impact) is much lower that that of the 372nm line (resonance line with a lower high level that can be populated equally by direct electron impact and by radiative cascades following recombination).

The Fe I 492nm line populated mostly by direct electron impact excitation shows a strong dependence on the discharge current.

The fact that the 372m Fe I line intensity shows no dependence on the discharge current indicates that its high level is populated mostly by radiative recombination and less by direct impact processes. This can indicate that this line can provide an indication on the temporal and space distribution of recombination processes, therefore of the distribution of Fe ions in the discharge.

From the above, the lower intensity of the 492nm compared to that of the 372nm line could indicate that ionization-recombination processes have higher rate than direct impact excitation processes, therefore, the average electron temperature in the discharge is higher that the ionization potential of Fe I. This conclusion will be further analysed in connection with the observed electron temperatures in the discharge with Fe targets.

5.2.5 TIME AND SPACE-RESOLVED O.E.S.

5.2.5.1. TIME AND SPACE-RESOLVED O.E.S. FOR Cu TARGETS

The time and space-resolved OES data were recorded by an optical probe situated inside the discharge chamber, viewing the space between the targets at 5 positions, from the centre of the discharge at z=5 cm from the targets (d=0 cm from the discharge axis) to z=1cm from the targets (d=4cm form the discharge axis) as described for the OES positioning geometry B in the experimental set-up.

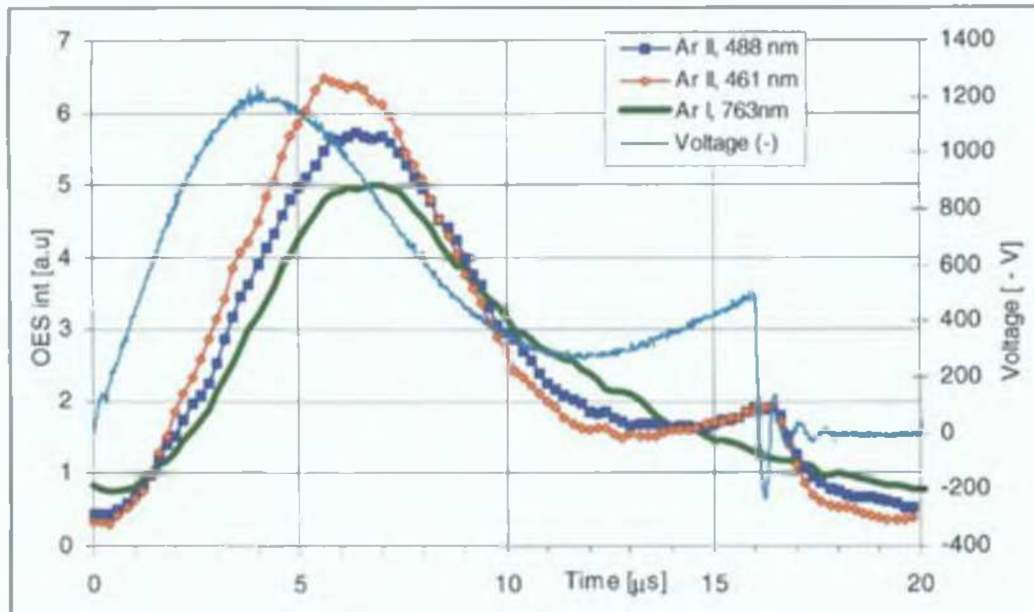

Fig.5.2.20. Time-resolved OES measurements at L=0 cm (discharge centre) for two Ar ion lines and one excited Ar atom line. The time-resolved voltage waveform is superimposed.

The typical temporal evolution of the Ar ion lines and excited atom lines intensity is presented in Fig.5.2.20, along with the voltage waveform. This graph allows observing the evolution of Ar ionization and excitation density during the pulse. The space and time-resolved relative distribution of Ar ion (487.9nm line) emission lines intensity from time and space-resolved OES at 50kHz, 2A, pulse-off time 2016ns and respectively for Cu I 465nm, with the Power waveform on the cathodes are presented in Fig.5.2.21 and Fig.5.2.22.

The observation of temporal and space distribution of ionization and excitation processes in the space between the targets provides information on the development of the discharge during the pulse-on time and information on the actual relative ionization density that can be used as start data for MC simulations of ions' trajectories in the pulsed DC discharge. This type of data have been used in Chapter (3.2).

The arrows in Fig.5.2.21 and Fig.5.2.22 indicate a possible start moment for the simulation and the relative OES intensities indicate the start relative ion/atom densities.

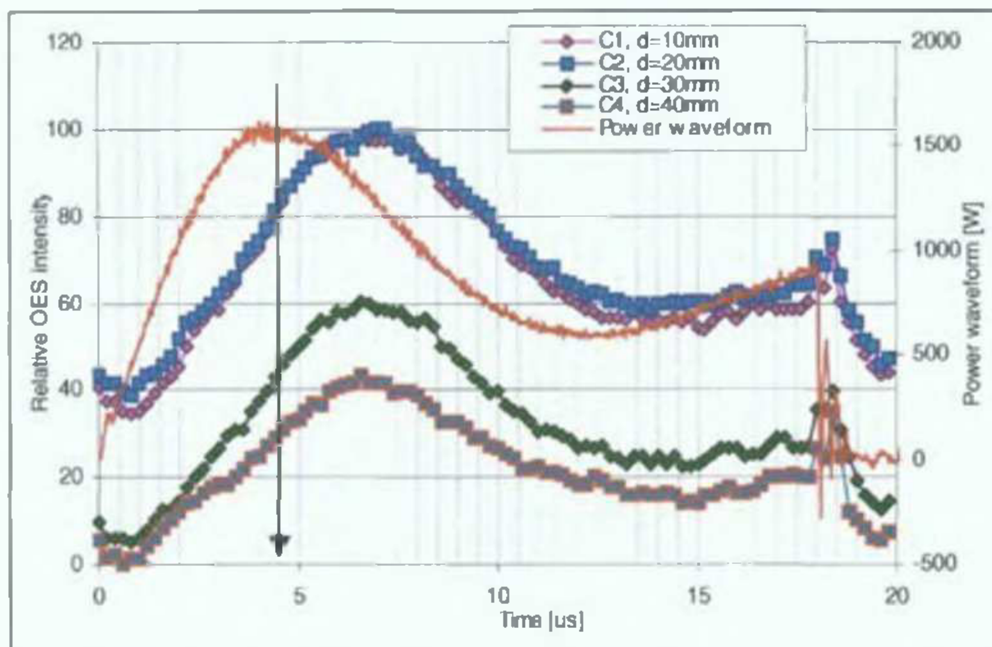

Fig.5.2.21.The relative Ar ion emission lines intensity from time and space-resolved OES at 50Khz, 2016ns, 2A and the Power waveform on the cathodes. Time resolution: 0.2μs, space resolution: 1mm.

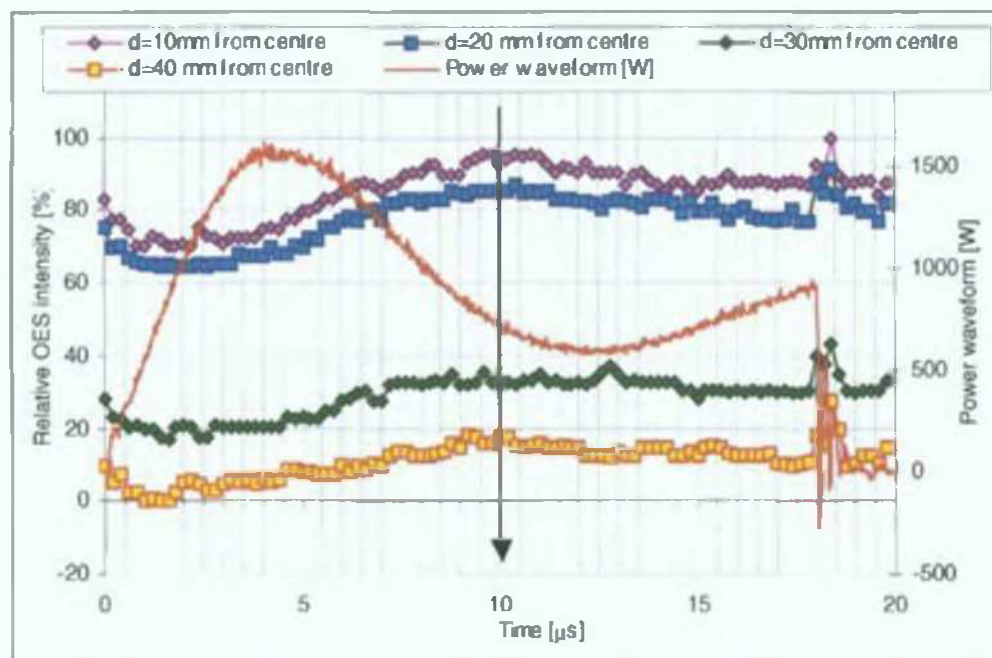

Fig.5.2.22. The relative (normalized) OES intensity for Cu I, 465nm line during the pulse, from time and space-resolved OES at 50Khz, 2016ns, 2A and the Power waveform on the cathodes. Time resolution: 0.2μs, space resolution: 1mm.

The time and space ionization density distributions allow observing the development of the sputtering process and the actual regions and moments in the discharge where the ions are produced.

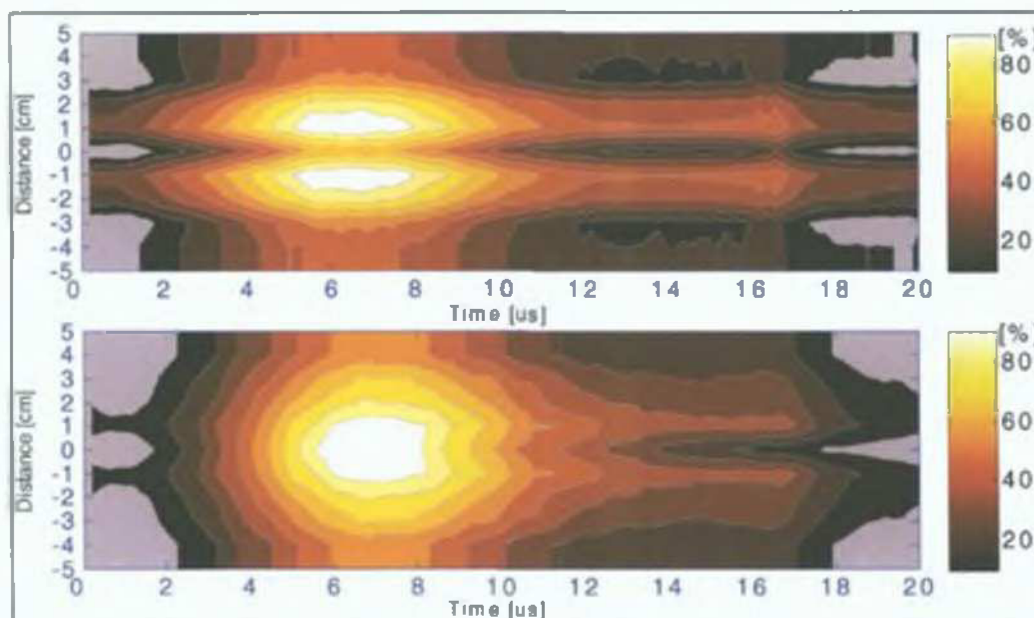

Fig.5.2.23. Normalized relative intensity for Ar II 488nm line (up) and for Ar I 763nm line (bottom), space and time-resolved at 50kHz , 4016ns and p=3mtorr, for the Cu targets.

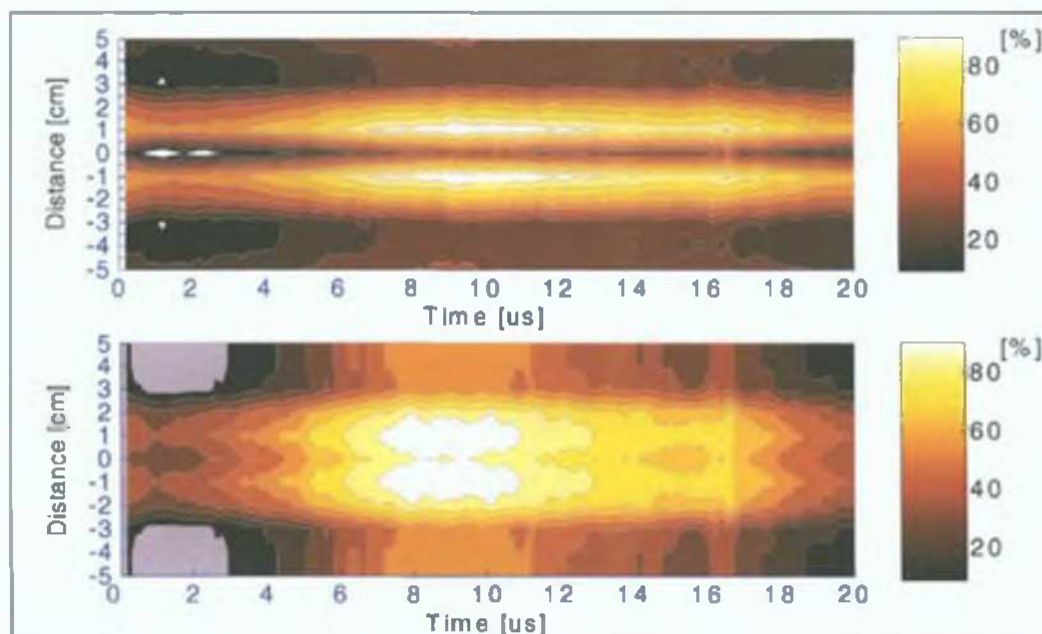

Fig.5.2.24. Normalized relative intensity for Cu I 465nm line (up) and for Cu I 522nm line (bottom), space and time-resolved at 50kHz, 4016ns and p=3mtorr.

Contour plots of the relative density distribution of Ar ions (488nm line) and excited Ar atoms (763nm line) are presented in Fig.5.2.23 and the excited Cu atoms distributions (lines 465nm and respectively 522nm) are presented in Fig.5.2.24.

The location of maximum Ar ion density confirms the observation that the value for the ~2.5μs time-delay between the applied power (voltage) waveform and the Ar ion peak can be attributed to the travel time to targets of Ar ions. From Fig.5.2.23, in the regions situated close to the targets (at less that 2cm) at the beginning of the pulse-on time (first 2μs), the relative Ar ion density is below 10%, indicating that sputtering will be insignificant at the beginning of the pulse-on time, as only few Ar ions are created at regions close to the targets.

The highest Ar ion density is produced at regions situated at about 4cm from the targets and therefore these ions need a certain time to travel to the targets in order to produce Cu atoms through sputtering. As the Ar ion distribution is localized, these ions will need in average the same time to travel to the targets, leading to the observed time-scale for the sputtering process. The excited Cu atom distribution is a convolution of the Cu atom density distribution from sputtering and that of electron temperature and density.

The Cu I 465nm line is most probably due to a de-excitation process following Cu ion recombination, therefore the relative distribution of this line is similar to the one of the Cu ions. This observation has been used in Chapter (3.2.4) as start data for the initial relative Cu ion density in MC calculations of Cu ions return time to targets, for the evaluation of the self-sputtering time-scale. As no Cu ion lines could be observed in the emission line spectrum (the most intense Cu II lines being below 250nm, the limit of the spectrometer wavelength range), the observation of the 465nm Cu I line has been the only possibility to evaluate the relative distribution of Cu ions.

The Ar and Cu ion distributions are mainly due to the distribution of electron temperature and density that allow intense ionization processes at those regions. The existence of an internal plasma field can also contribute to the symmetrical ion peaks distribution. As Ar ion and Cu ion distributions should follow both the same pattern located on each side of the discharge centre, this is another argument in favour of the above considerations regarding the 465nm line.

The excited atom species (Fig.5.2.24) have a more uniform distribution in the discharge space, following the temporal evolution of the power peak.

5.2.5.2. TIME AND SPACE-RESOLVED O.E.S. FOR Fe TARGETS

For the Fe targets, the relative Ar ion density has a more uniform distribution in the discharge space, with a marked peak at 6μs and quite high (60%) relative intensity at the targets (Fig.5.2.25). This indicates that Ar ionization can take place at regions situated close to the targets, leading to ionization of backscattered (post-sputtered) Ar atoms and to re-sputtering effects.

Practically no Ar ions are produced in the first 2μs at any region in the discharge. Thus the direct sputtering process starts only after the first 2μs and reaches a maximum at 6μs.

The temporal distribution of relative Ar ion density follows the power peak waveform, while the space distribution indicates that electron temperatures reach the highest direct impact ionization cross-section for Ar in the centre of the discharge.

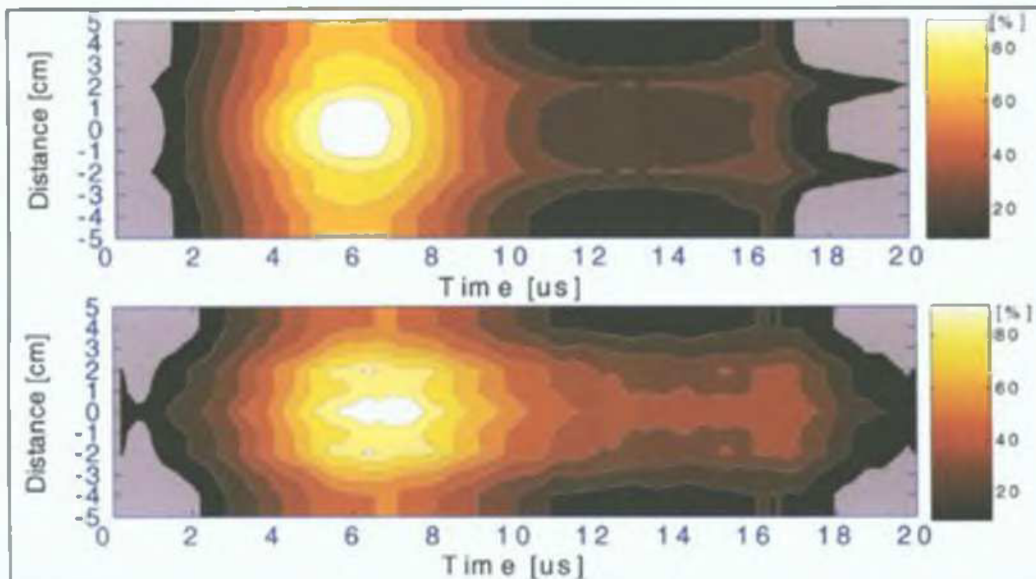

Fig.5.2.25. Normalized relative intensity for Ar II 488nm line (up) and for Ar I 763nm line (bottom), space and time-resolved at I=1.5A, 50kHz, 4016ns and p=2mtorr, for the Fe targets.

The distribution of excited Ar atoms is similar to that of Ar ions, with a maximum in the centre of the discharge.

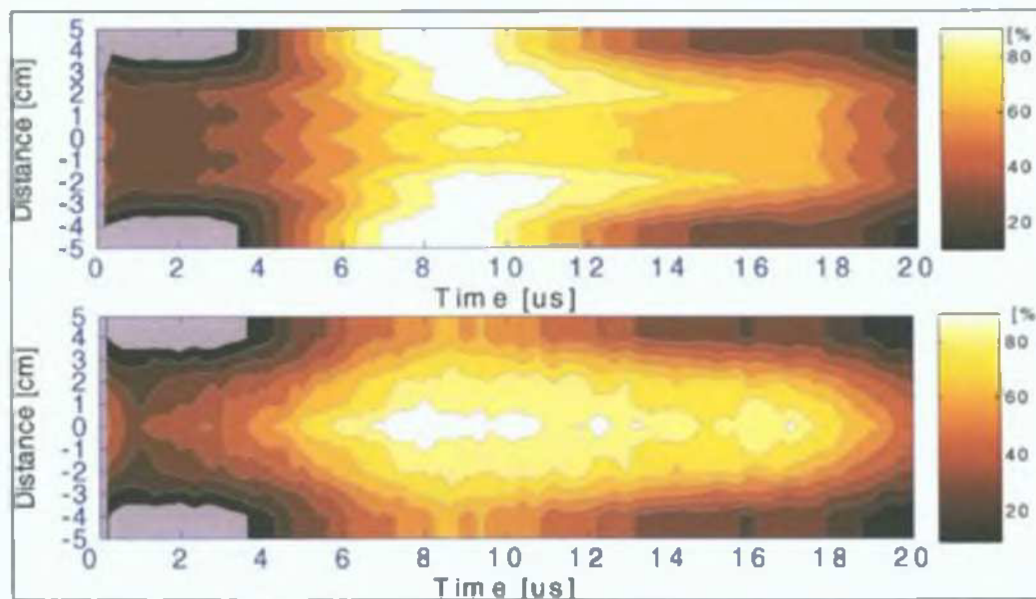

Fig.5.2.26. Normalized relative intensity for Fe I 372nm line (up) and for Fe I 492nm line (bottom), space and time-resolved at I=1.5A, 50kHz, 4016ns and p=2mtorr.

The observed relative intensity of the excited Fe lines is a convolution of the relative density of the Fe atoms and the distribution of electron temperature and density.

The strong difference between the distributions observed for the two excited Fe I lines (Fig.5.2.26) indicates that the two lines are generated through different processes. While the 492nm Fe I line is due to direct impact excitation of Fe atoms and has a distribution similar to that of excited Ar atoms, the 372nm Fe I resonance line has a totally different distribution.

The upper level of the 372nm Fe I line [$3d^6$(5D)4s.4p(3P)] is populated by a number of 368 transitions (NIST atomic database) from higher energy levels, most of them corresponding to highly excited configurations, characteristic to those resulted after ion recombination.

Considering that the 372nm Fe I line is mainly due to the de-excitation processes after Fe ion recombination, the relative density distribution of this line should be close to that of Fe ions. As Fe ion lines could not be directly observed in the line emission spectrum, the observation of the 372nm Fe I line is the only indication of the possible Fe ion distribution.

As seen in Fig.5.2.26, the 372nm line has high intensity at regions close to the targets, indicating a strong excitation and ionization of the sputtered material. Consequently, a high Fe ion density at regions close to the targets is expected, leading to intense self-sputtering. Both re-sputtering and self-sputtering effects generate intense ion bombardment of the targets and therefore intense heating of the targets.

The 3D images of the space and time resolved distributions for Cu targets and Fe targets are presented in Fig.5.2.27-Fig.5.2.34.

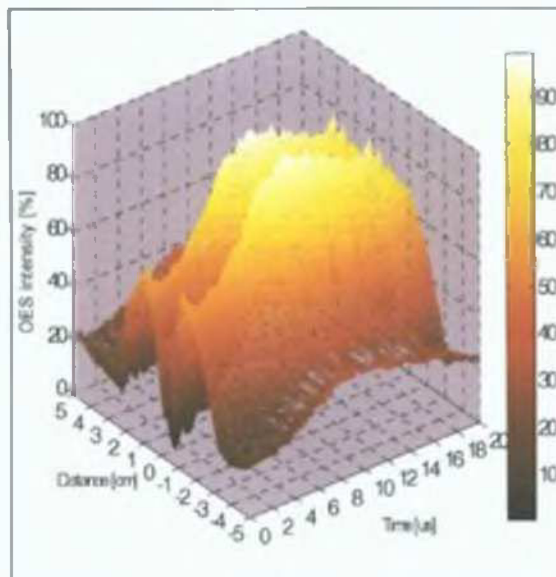

Fig.5.2.27: Cu I, 465nm line, space and time resolved, 3D image.

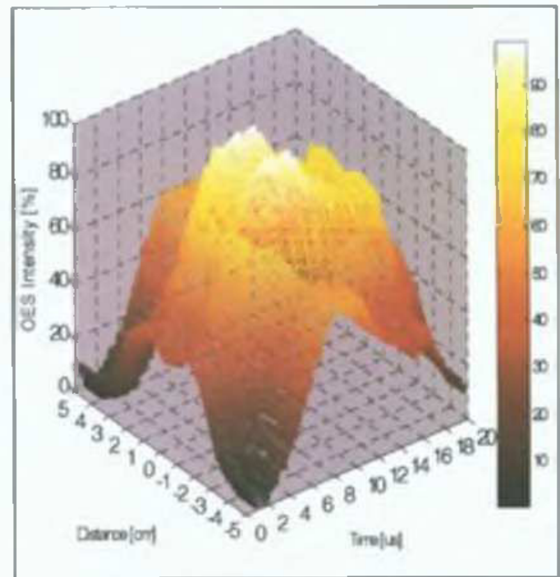

Fig.5.2.28: Cu I, 522nm line, space and time resolved, 3D image.

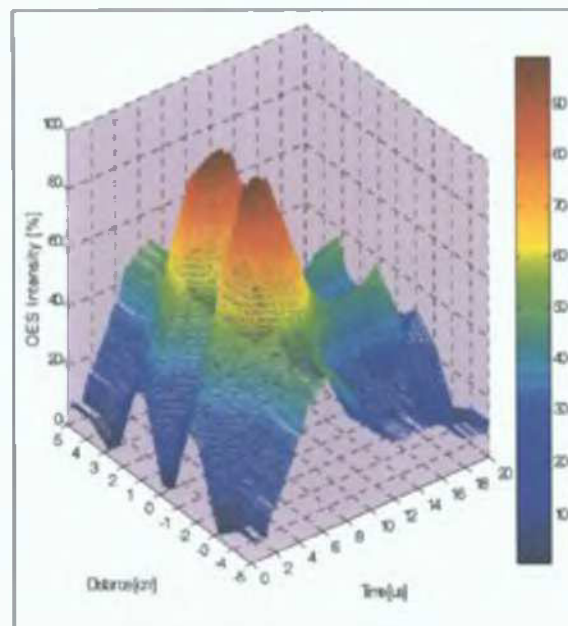

Fig.5.2.29. Ar II, 488nm line, space and time resolved, for Cu targets. 3D image.

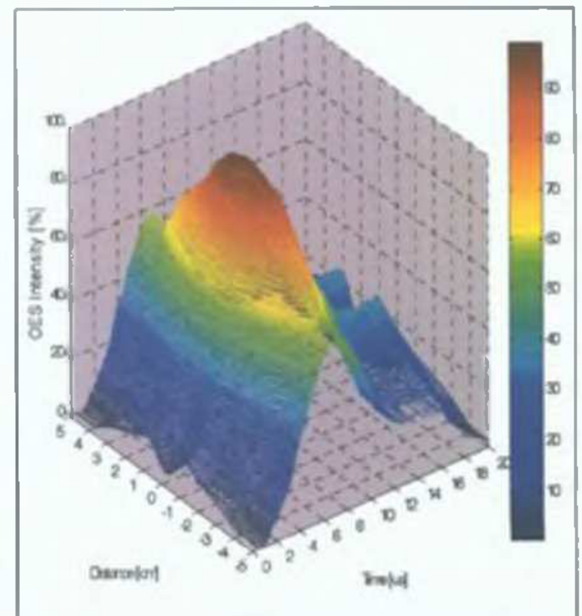

Fig.5.2.30. Ar I, 763nm line, space and time resolved for Cu targets. 3D image.

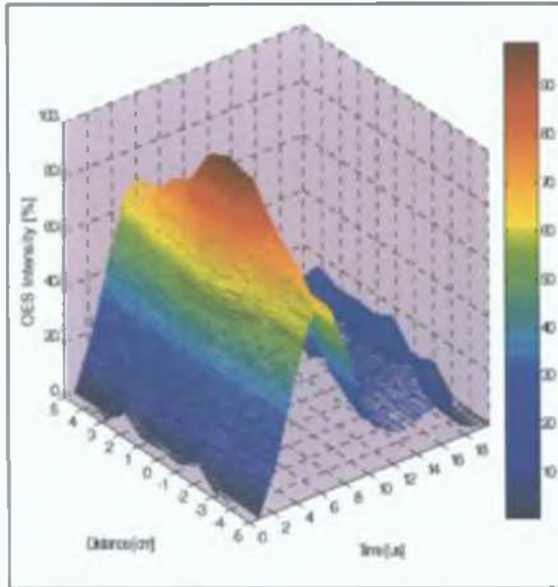

Fig.5.2.31. Ar II, 488nm for Fe targets, 3D image.

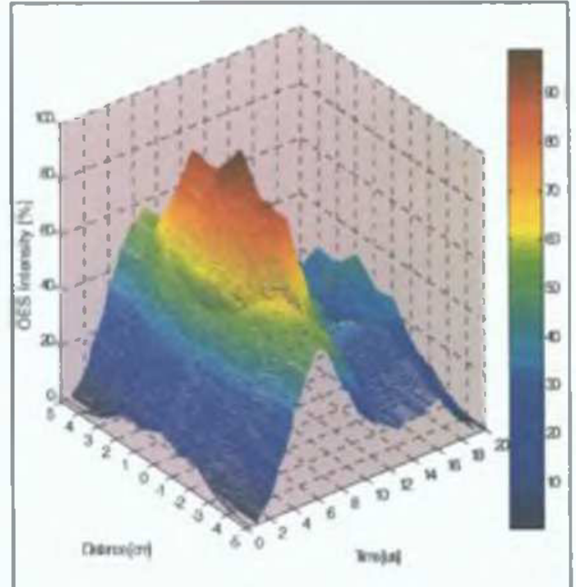

Fig.5.2.32. Ar I, 763nm for Fe targets, 3D image.

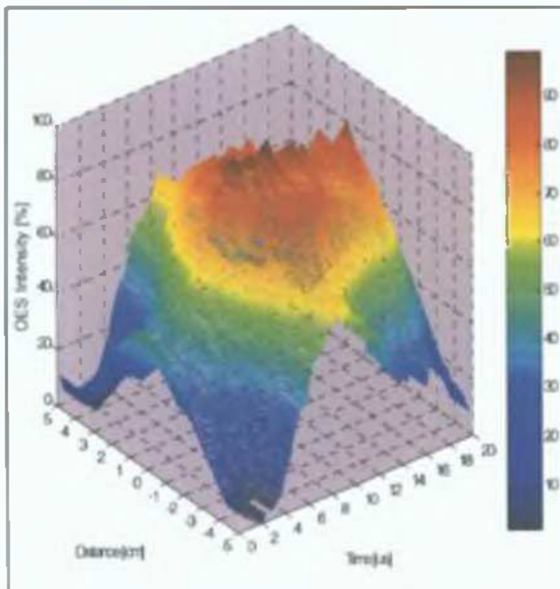

Fig.5.2.33. Fe I, 492nm, 3D image.

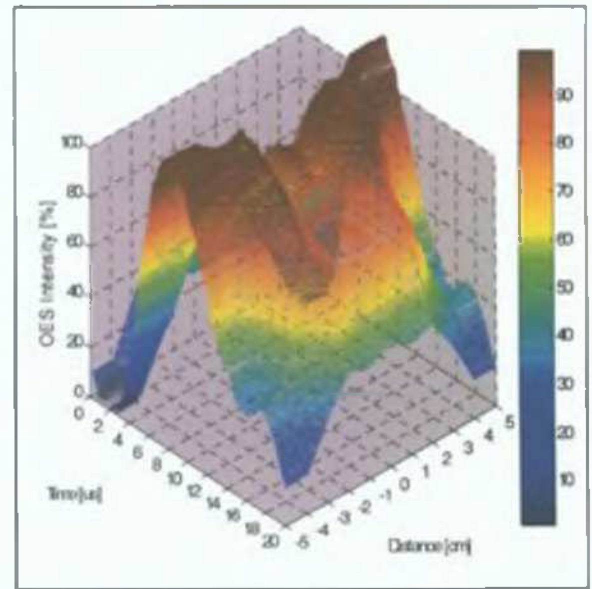

Fig.5.2.34. Fe I, 392nm, 3D image.

5.2.5.3. DISCUSSION AND CONCLUSIONS

1. Time-resolved OES data provide information on the connection between the applied pulsed DC power and the ionization efficiency and time-scales in the discharge development. The presented analysis indicates how this type of diagnostic can be used for choosing the optimum duty cycle from the point of view of direct-sputtering efficiency or self-sputtering effects.

2. The time and space resolved observation of emission lines from the Ar gas spectrum and sputtered metal spectrum allow an observation of the actual development of the discharge

and sputtering process during the pulse-on time. The region and moment where Ar ions are created plays an important role in the time-scale of the sputtering process, thus providing information on the direct sputtering process time-scale.

3. The analysis of the space and temporal distribution of sputtered material - excited atomic (or ionic) species - provides information on the self-sputtering effects and their time-scale and intensity.

4. The time-resolved and the time and space resolved OES diagnostic has a major importance in the study and understanding of the discharge behaviour, providing a non-invasive diagnostic means and direct information on phenomena taking place during the pulse-on time during the actual operating conditions of the magnetron.

5.3. TIME AND SPACE-RESOLVED ELECTRON TEMPERATURES

5.3.1 T_e CHARTS FOR CU TARGETS

The determination of electron temperatures has been performed using the method of ionic lines radiance ratios, described in Chapter (4.3.2.3).

All measurements are time and space resolved, based on the OES data presented in the previous chapter with the probe in the geometry configuration B of the experimental set-up.

As the theoretical basis for T_e evaluations from OES data require LTE or PLTE conditions and determination of lines radiances, these points will be examined next by presenting several parameters involved in the radiance measurement: the lines' widths and the resolution of the spectrometer, the lines' broadening and the observation process and lines intensity versus noise and background level.

5.3.1.1. LINE WIDTH AND INTENSITY MEASUREMENT

The AOS spectrometer [12] described in Chapter (2.3) has been used for the OES measurements. It calculates the emission line's wavelength using the formula:

$$\lambda = \frac{n_E - n_O}{f_0} v_0 ; \qquad (5.3.1)$$

where n_E, n_O are the refractive index of the bi-refringent crystal for the extra-ordinary and the ordinary wave, f_0 is the ultrasound frequency (RF) applied on the transducer and v_0 is the speed of the acoustic wave in the crystal.

As the filter pass-band (equivalent to the Instrumental Profile in conventional spectrometers) has not been defined by the manufacturer, it had to be determined using calibration lamps as shown in Chapter (2.3). The obtained bandwidth, along with the AOS resolution (provided by the manufacturer) and the widths for the observed Ar ion and atom lines are presented in Fig.5.3.1. The error bars indicate the maximum deviation in widths values obtained at the 5 positions in the discharge.

The Ar ion and atom line widths from the magnetron discharge are in the same range of values as the lines from the calibration lamps, indicating that they are mainly due to the pass-band (bandwidth) of the AOS and the broadening of the observed lines in the magnetron discharge is negligible.

The Intensity Response IR of the AOS with wavelength is mainly determined by the acoustic power applied to the crystal, the crystal's optical transmission and the spectral response of the photomultiplier (PMT). The relative intensity of lines situated at close wavelengths is only affected by the spectral response of the PMT. In the 450nm – 490nm range, the spectral response of the photocathode is expected to be constant, so the relative intensities will not be affected. Therefore the evolution (over time and space) of electron temperatures determined from intensity ratios of lines situated at close wavelengths will not be affected.

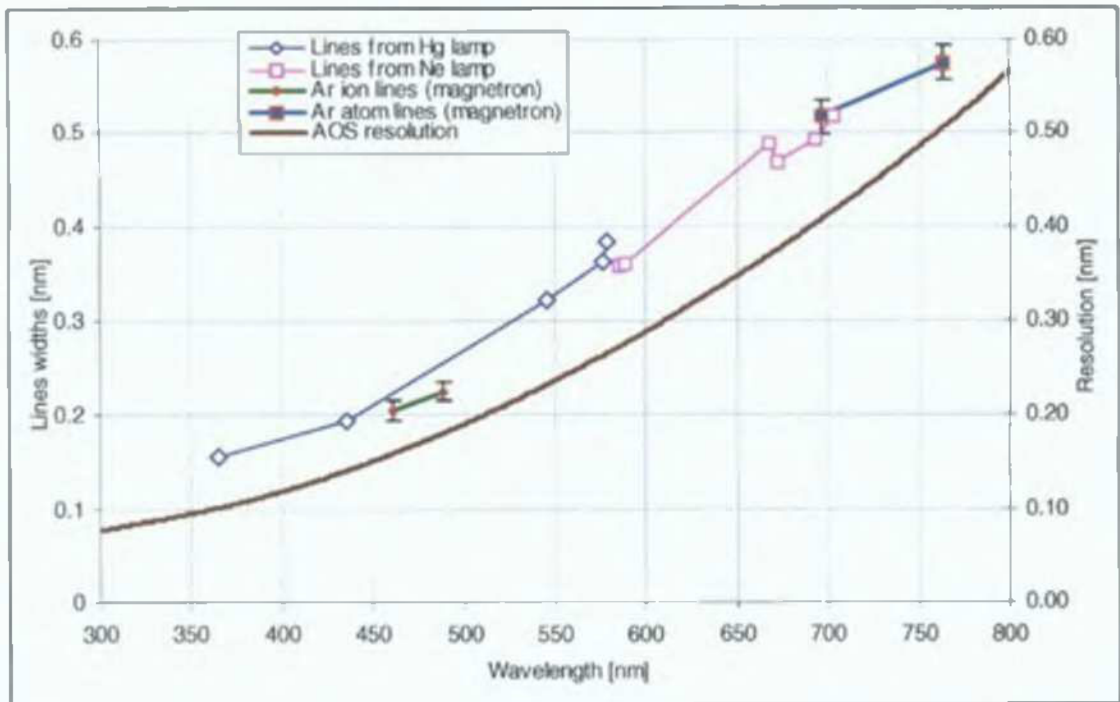

Fig.5.3.1: The AOS-4 Pass-band and Resolution and the experimental widths for the Ar ion and atom lines. The error bars indicate maximum deviation.

5.3.1.2. NOISE AND BACKGROUND DETERMINATIONS

In general, determination of electron temperature from lines radiance ratios requires accurate lines' radiance measurements while corrections for background noise, for continuum effects due to recombination and for lines superposition (overlapping) are necessary.

The background signal due to the electronic noise of the AOS-4 system can be considered independent of wavelength.

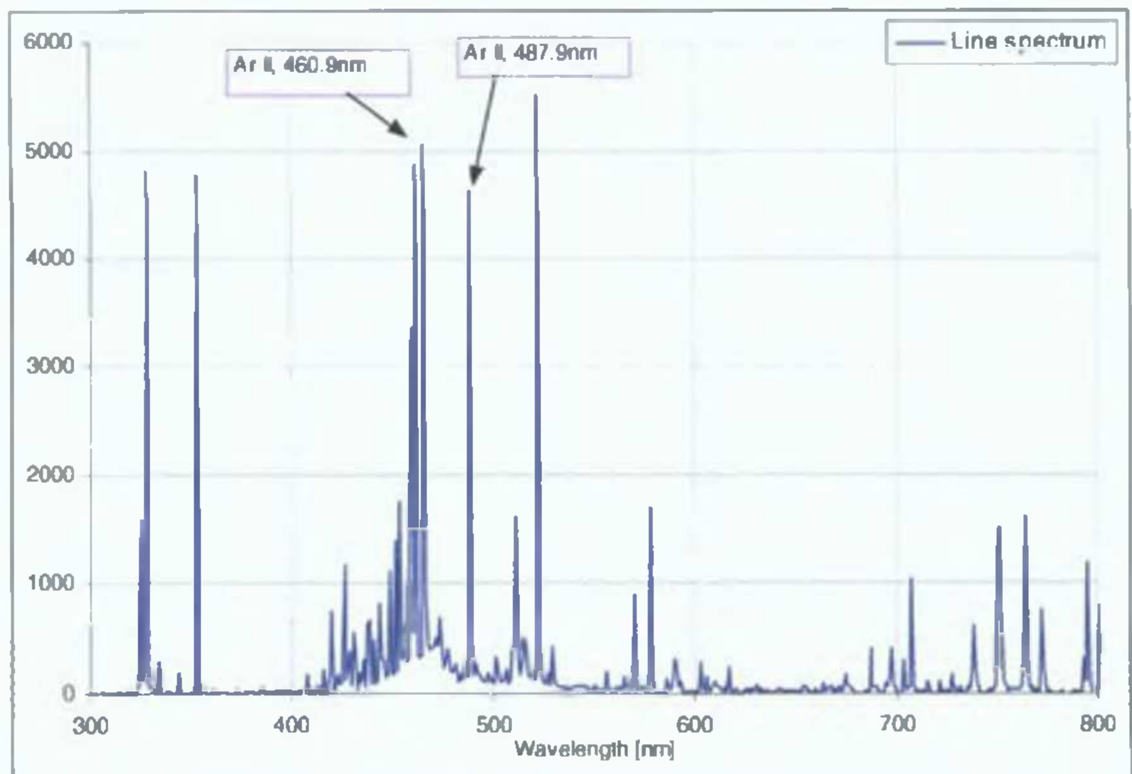

Fig.5.3.2: Typical emission line spectrum in the discharge with Cu targets.

The corrections for lines' superposition are not necessary, as the high resolution of the AOS spectrometer and the actual filter effect of the acousto-optic detection allow a high selectivity of the instrument for time-resolved measurements (the wavelength can be selected with a resolution of 0.01nm).

As discussed in the previous chapter, the line spectrum in the magnetron discharge with Cu targets (Fig. 5.3.2) shows a clear continuum region (400nm-473nm), with an edge at 473nm, most probably due to Cu II recombination. Therefore, corrections for continuum levels between emission lines situated in this region are necessary for this type of spectrum.

Measuring the noise levels on both sides of the lines situated in the continuum emission region and using these values as a correction for the intensity of the lines is used as a means for correcting the continuum noise.

The time-resolved noise signal has been measured at the following wavelengths: 460.698nm and 461.232nm for Ar II 460.965nm line (situated on the continuum emission region) and 495.00nm for the 487.978nm line (outside the continuum region). An average over three measurements for each position and noise wavelength has been used in order to improve the measurement precision.

In conclusion, Ar ion lines' intensities at 461nm have to be corrected for the continuum level at each side of the line, in the case of Cu targets. This induces a level of incertitude in the T_e evaluation as the lines will have different intensities according to the correction for the continuum level at each side. The values presented in the T_e chart for Cu targets are average values between the two values obtained after continuum corrections have been applied.

5.3.1.3. PROOFS FOR LTE (PLTE) CONDITIONS

The spectral lines' radiances used in the determination of T_e depend on level populations and radiative transfer processes.

The determination of T_e is based on the assumption of a Maxwellian distribution of free electrons and Boltzmann energy level distribution of ions, both valid only under LTE of PLTE conditions.

To ensure LTE for rapid time variations and steep space gradients requires the assumption of a high electron density, collisional - radiative relaxation times shorter than the time-scale of T_e or n_e variations and ion and atom diffusion time across plasma much longer than the relaxation times [40].

As the observed variations of the pulsed discharge input power occur over time-scales of 20ns, (coinciding with the time-resolution for optical measurements) the induced modifications in T_e and n_e will follow the same time-scale during the pulse-on time, thus longer than the radiative processes time-scale of a few ns. The atom and ion motion is also much slower than the time-scale of collisional and radiative processes.

The above considerations and the enhanced magnetic confinement provided by the opposed target geometry allows for high electron densities during the discharge and enables an analysis based on LTE conditions.

5.3.1.4. LINE BROADENING

The emission lines' radiance is defined as the integral of the emission intensity over the line's width and it is proportional to the product between the line's intensity and its width (FWHM).

For conventional spectrometers, corrections for the Instrumental Profile and the Intensity Response versus wavelength of the spectrometer have to be considered. The Instrumental Profile of AOS spectrometer is given by its pass-band and has very small values as shown previously (Fig.5.3.1).

Unlike slit spectrometers that are actually measuring lines' radiances, Acousto-Optic Spectrometers (AOS) are only measuring the light intensity signal, therefore only the line's height at the selected wavelength. Performing a high-resolution line spectrum can provide the line's width, but this width will not be time-resolved. The AOS time-resolved measurements only provide the time-resolved light intensity (the line's height).

So, in order to exploit the high resolution of the AOS (both as wavelength and temporal response) for electron temperature evaluations, an analysis of the possible temporal evolution of the lines' widths is required.

Observing emission lines of the same species at the same position and moment during the pulsed DC discharge ensures that the same conditions of electron temperature and density and same electric and magnetic fields apply for all lines.

The main factors influencing the line widths are:

- the natural (Lorentzian) line broadening, given by the natural widths of the emission levels, dependent only on electron temperature and having values well below 1Å.
- the Doppler thermal broadening, due to ions random movement along the direction of observation. (Its effects can be neglected for our situation as the ions move on parallel electric and magnetic field lines perpendicular to the direction of observation);
- the electron impact broadening, proportional to $\sim\frac{\sqrt{n_e}}{\sqrt{T_e}}$;
- the pressure broadening is encountered at high gas pressures or at electron densities higher than $10^{18}cm^{-3}$, much higher than the expected electron temperatures in the low pressure discharge.

In the opposed target magnetron geometry the electric and magnetic fields are parallel and the ions move practically in straight lines along the direction of the $\vec{E}$ and $\vec{B}$ field lines.

The initial thermal velocities of Ar ions are quickly overcome by the electric fields of the cathode pre-sheath and the ions' movement is perpendicular to the direction of observation, so the thermal Doppler broadening will not be observed.

So, the natural broadening, the Doppler broadening and the pressure broadening can be neglected as they are either negligibly small compared to the resolution of the spectrometer or simply do not apply to the observed plasma conditions. The line widths will only be affected by electron impact broadening.

As the ratio of line widths due to electron impact broadening (dependent only on electron density and temperature) is a constant at every moment during the pulse, there is no need for a time-resolved evaluation of the lines' width ratio. Only an evaluation of the average width ratio during the pulse (at each position in the discharge) may be required.

The above considerations allow time-resolved electron temperature measurements using Acousto-Optic spectrometers, as the lines' radiances at every moment during the pulse can be calculated as a product between their time-resolved heights and their FWHM widths.

The widths for the ionic lines 460.9nm and 487.9nm (Ar II) have been measured at the 5 positions in the discharge leading to values of 0.205 ± 0.07nm and respectively 0.225 ± 0.09nm, are close to the pass-band values of the spectrometer (presented in Fig.5.3.1).

As the lines' widths ratio affected mainly by electron impact broadening is a constant (independent of electron density or temperature) the ratio of lines radiances is equal to the ratio of lines intensities (heights) measured by the AOS spectrometer and the actual use of the determined lines widths is not necessary here.

In conclusion, for the observed magnetron configuration and while using an AOS spectrometer, the ratio of line's radiances is given directly by the ratio of lines' intensity (optical signal height as given by the AOS).

5.3.1.5. THE ELECTRON TEMPERATURE

Usual spectroscopic electron temperature measurements are based on the ratio of integrated lines radiances (of the same atom or ion), providing time-averaged T_e values in the discharge.

Using the ratio of time-resolved lines radiances (as shown in the previous considerations, here, only the time-resolved intensity of each line is necessary) provides a time-resolved T_e based on the same formula:

$$kT = \frac{E_{m2} - E_{m1}}{Ln(\lambda_{m1n1} g_{m2} A_{n2m2} \frac{I_{n1m1}}{I_{n2m2}} / \lambda_{m2n2} g_{m1} A_{n1m1})}; \tag{5.3.2}$$

where kT is the electron temperature T_e in [eV] and for each line (1) and (2) respectively, λ_{mn} is the line wavelength, I_{mn} is the radiance (line's height by its FWHM), g_m the statistical weight of the upper level, A_{nm} the transition probability and E_m the high energy level of each line.

Two Ar ionic lines (488nm and 461nm) have been used in order to determine the electron temperature for the magnetron configurations with Cu, respectively Fe targets. The characteristic emission parameters for the emission of each line are presented in Table 1 (Chapter 5.2.2)

Corrections for the continuum radiation are taken into account by deducting the noise level measured at a wavelength close to the emission line, in a region free from other lines as indicated in the previous chapter.

In order to increase precision (by minimizing the experimental error) lines intensities have been averaged over three sets of measurements at each position. The background measured at wavelengths just below and above each line has also been averaged over three sets of measurements. These averages include positioning errors as well as optical measurement errors due to low signal levels when measuring noise intensity.

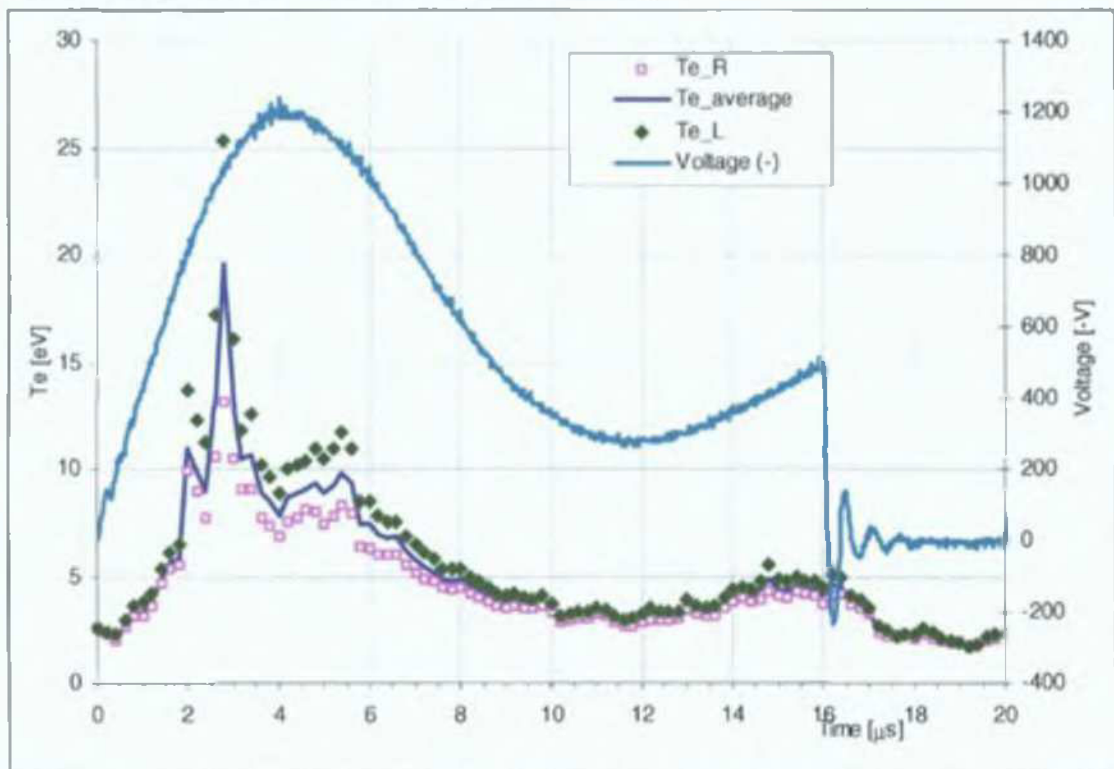

Fig.5.3.3: Typical T_e evolution, along with the voltage waveform. Values at z=0 (discharge centre).

The typical time-resolved evolution of the electron temperature from ionic lines is presented in Fig.5.3.3 for a pulsed DC discharge at 50kHz, 4016ns pulse-off time, 2A current run, at the centre of the discharge (z=0 cm).

In Fig.5.3.3, the T_e values are presented as an average between T_e values obtained taking into account the noise values to the left and right of each line (represented as green and pink dots). The electron temperature evolution during the discharge (Fig.5.3.3-Fig.5.3.5) allows direct observation of electron dynamics and of the different stages in the discharge evolution during the pulse. As can be seen from Fig.5.3.3, the electron temperature evolution follows the applied Voltage waveform on the cathodes.

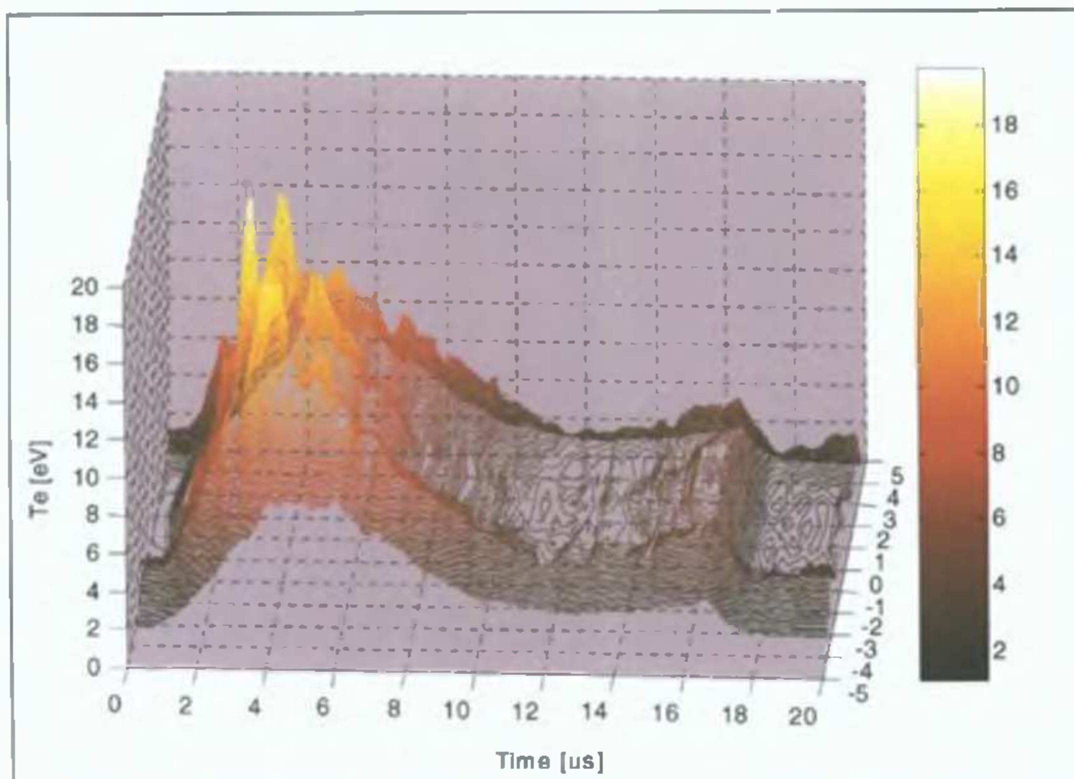

Fig.5.3.4. Space and time-resolved electron temperature (3D view) during the pulse at 50kHz, pulse off time 4016ns, set current I=2A, argon pressure p= 3mtorr.

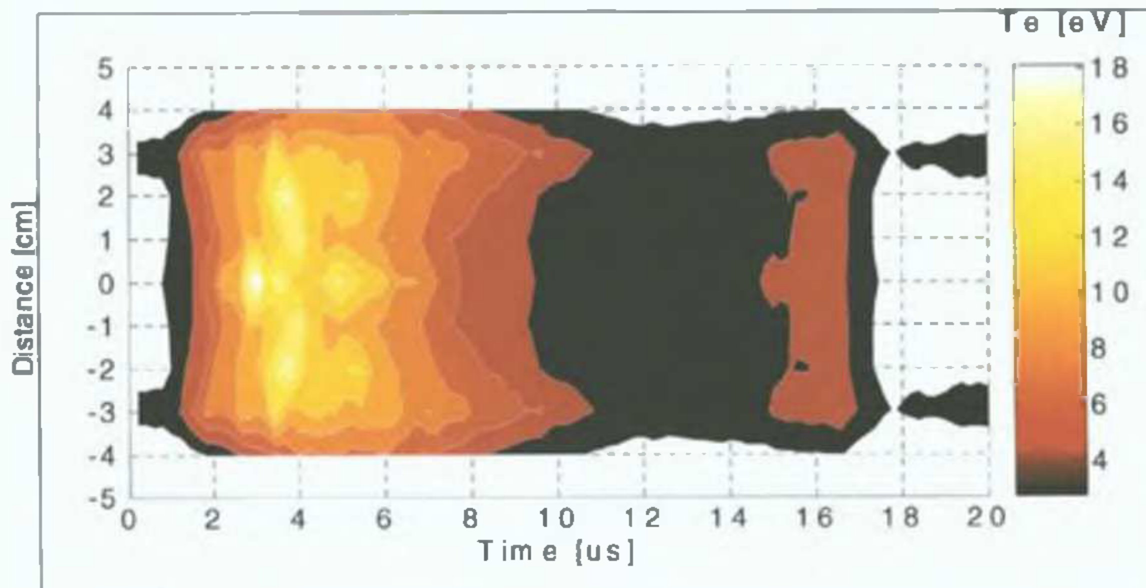

Fig.5.3.5. Electron temperature contour lines evolution during the pulse at 50kHz, pulse off time 4016ns, set current I=2A, argon pressure p= 3mtorr.

It can be noticed that maximum values for the electron temperature (T_e~18eV) are reached at regions close to the centre of the discharge (3cm to 5cm from the targets), at moments during the pulse between 3μs and 5μs. As these time and space intervals define the region with maximum Ar ionization probability, the development of the discharge can be inferred from it.

The sudden increase in T_e observed as high peaks (Fig.5.3.4) are a clear indication that a large number of ions reach the targets almost simultaneously, leading to a sudden increase in the number of secondary electrons and thus in the average electron energy.

The T_e values at regions closer to the targets (T_e<11eV) will not allow Ar ionization, therefore, re-sputtering effects will not encountered. A detailed discussion on the development of the sputtering process based on the results from the OES and T_e measurements will be presented in Chapter (6.1).

5.3.2 T_e CHARTS FOR Fe TARGETS

A typical line spectrum measured at z=0 (discharge centre) is presented along with a spectrum measured at z=4cm from the targets in Fig. 5.3.6.

We can observe that there are several regions with recombination edges (continuum emission) but the lines of interest (Ar II, 461nm and 488 nm) are situated in regions with a low background, with negligible continuum emission. The time and space distribution of Ar atoms Ar ions and exited Fe atoms have been presented in Chapter (5.2.4).

The strong Ar II lines at 461nm and 488nm with characteristics of the emission lines presented in Table.5.2.1 (Chapter 5.2.) are used for T_e determinations.

5.3.2.1. LINE BROADENING.

As explained in Chapter (4.3.2.1), the main line broadening effect in this type of magnetrons and operating conditions is due to Doppler (thermal) broadening and electron impact broadening.

For Fe targets (as in the case of Cu targets) the Ar ions move along the parallel electric (cathode pre-sheath) and magnetic field lines, on a direction perpendicular to the targets. These fields overcome the thermal movement of ions. The ion lines' widths in the Fe target configuration will not be affected by the Doppler effect broadening, as their main movement will be perpendicular to the direction of observation.

As in the case of the Cu targets configuration, the ratio of lines' widths affected only by electron impact broadening is a constant, as T_e and respectively n_e are the same for both lines at the same moment and position in the discharge.

So, in the case of Fe targets, the ratio of lines' radiances is also directly given by the ratio of the lines' intensities (signal height) as given by the AOS spectrometer.

5.3.2.2. CORRECTIONS

The determination of electron temperature from the lines' intensities ratio requires an estimation of the necessary corrections for the background noise, for continuum effects due to recombination and for lines superposition (overlapping).

The line spectrum (Fig.5.3.6) does not indicate a large discrepancy between background level of the two Ar ion lines (461nm and 488nm) chosen in for this study, so corrections for continuum levels between these two lines are not necessary.

As shown before, the corrections for lines superposition are not necessary due to the high resolution of the AOS, while the background signal due to the electronic noise of the AOS system can be neglected, being independent of wavelength.

Therefore, time-resolved background signal measurements for Fe (Ar) discharge have not been taken into account.

As shown in Chapter (2.3) the Intensity Response of the AOS can be considered constant for close lines (at 461nm and 488nm) and no further corrections of lines' intensities are necessary. Assuming that all noise at the required wavelength is only electronic noise (at the measured wavelength) the values obtained don't have to be corrected and the total intensity ratio can be used directly.

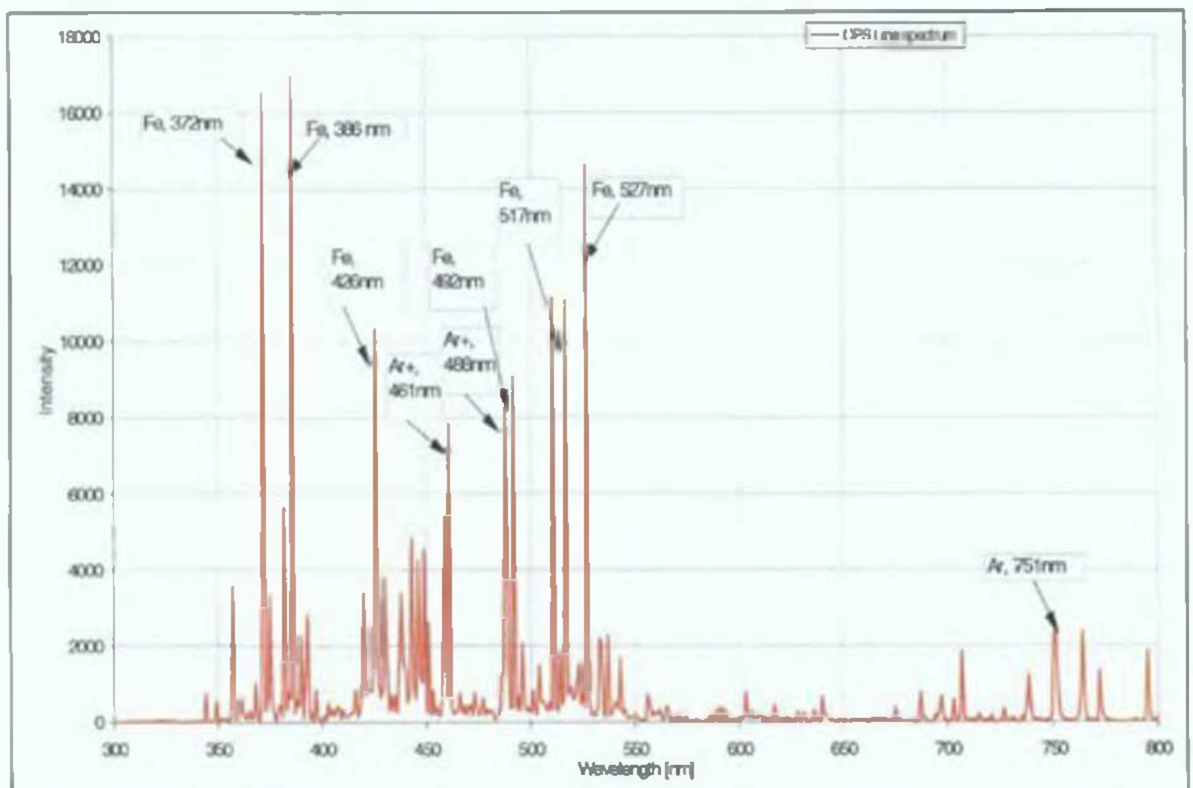

Fig.5.3.6: Optical Emission Line spectrum for Fe targets magnetron plasma at 50kHz,w=496ns, I=1.5A, p=2mtorr.

Therefore, in this case, the evolution of electron temperatures in the discharge is well described by the direct line intensity ratios (signal heights).

5.3.2.3. ELECTRON TEMPERATURE CHART

For Fe targets, the electron temperature has much higher values than those obtained for the Cu targets configuration (Fig.5.3.7 and Fig.5.3.8). These higher electron temperatures lead to a different space-temporal distribution for the Ar ions, with consequences on the discharge behaviour.

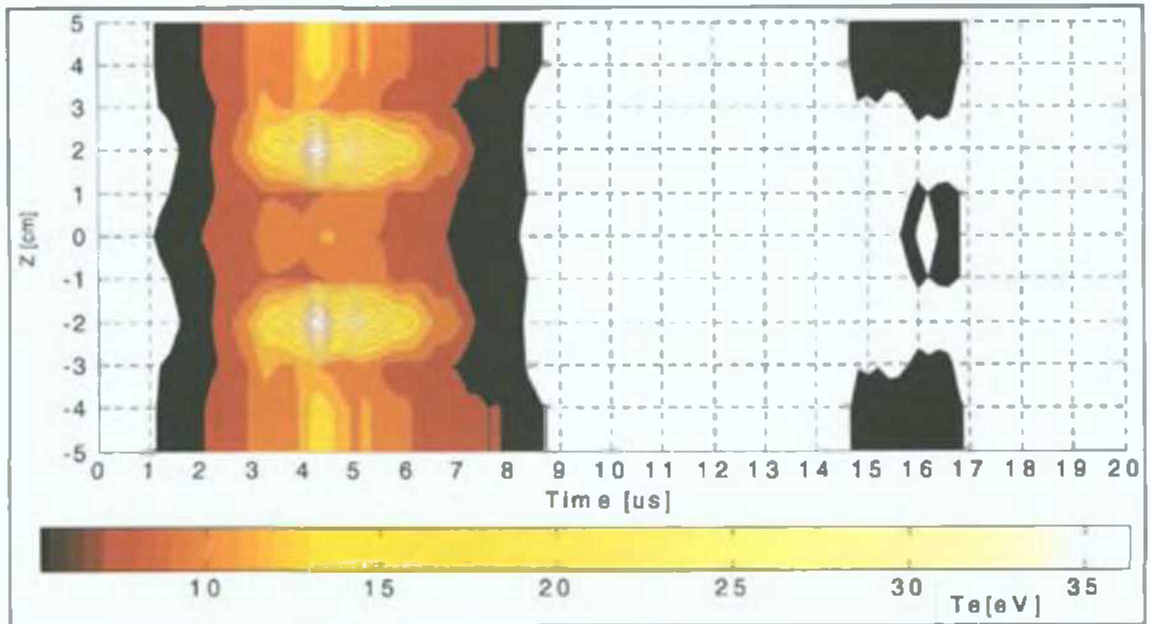

Fig.5.3.7: Contour lines for the space and time-resolved electron temperature distribution for Fe targets.

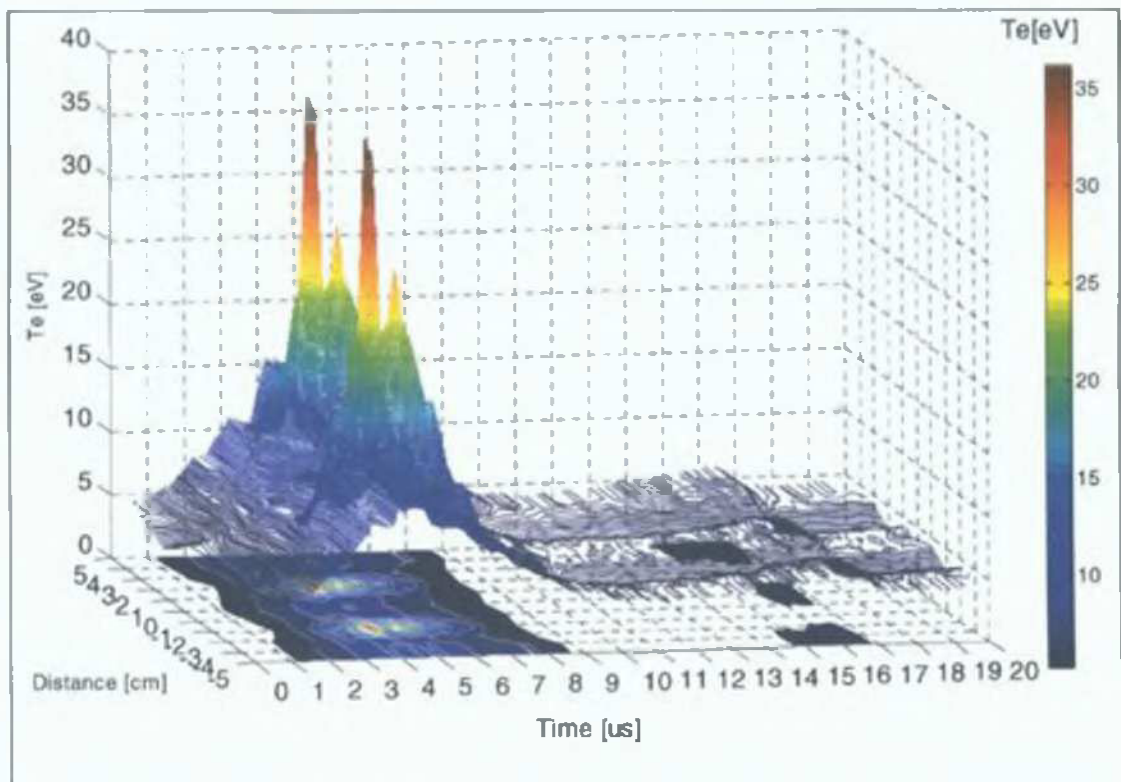

Fig.5.3.8: 3D view of the Space and time-resolved electron temperature distribution for Fe targets.

At moments between t=3μs and t=6μs during the pulse, in the regions close to the targets (1cm –2cm from the targets) the electron temperature reaches values above 11eV, thus electron energies above 16eV, allowing for Ar ionization (Fig.5.3.7).

A strong increase in T_e can be observed at t~4μs, (T_e~40eV) followed by a secondary peak at t=5μs (T_e~20eV). These high T_e peaks are formed due to the increase in the number of high-energy secondary electrons at the respective moments during the pulse.

As regions below 1cm from the targets have not been investigated by OES, the actual ion density at these regions could not be observed. A major difficulty in performing OES measurements in a region close to the targets is due to the reflected light from the targets.

5.3.3. CONCLUSIONS

The time and space-resolved determination of electron temperature, together with the distribution of exited and ionized species in the discharge allows a good understanding of the phenomena that take place during the pulse-on time in the pulsed-DC magnetron plasma.

The case of OES diagnostic for ferromagnetic targets is particularly interesting, both from practical point of view – providing an explanation of increased target heating and increased ion energies at the substrate – and as a model of physical phenomena that lead to these effects (Chapter 6.1).

This type of plasma has a certain particularity – the magnetic field distribution in the XOZ cross-section for Fe targets is concentrated in the centre of the discharge due to the absorption of the Bx component of the magnetic field in the ferromagnetic targets. Compared to the field for the Cu targets, for the Fe targets the magnetic field decreases fast in regions situated at 2cm from each end of the target cross-section (see Fig.3.1.8) leading to a loss of confinement at those regions, a lower electron density and higher electron temperatures.

This structure of the magnetic field leads to lower electron density in the discharge and to higher electron temperatures. Therefore, the magnetic field distribution has an important effect on the evolution of electron temperatures.

Some of the results presented in this Section have been included in a paper published in the SVC-48 proceedings [54].

5.4. TIME AND SPACE-RESOLVED ION ENERGY SPECTRA (IES)

5.4.1. INTRODUCTION

This chapter presents the experimental data obtained using the HIDEN mass-energy analyser, the space-resolved Ion Energy Spectra (IES), a discussion on the basic information provided by the IES and the method for obtaining time-resolved information from the energy distributions.

5.4.2. EXPERIMENTAL SET-UP

The Penning type [1, 2, 3] opposed target magnetron geometry is presented in Fig.5.4.1 and consists of two opposed, rectangular targets. This configuration is used for either copper or iron targets.

For the copper targets (99.99% purity) the dimensions are (120x180x9 mm), while for the iron targets (99.99% Fe) the dimensions are (120x180x11 mm). The working gas is Ar at a pressure of 0.4Pa (3×10^{-3} torr), after evacuating the chamber to 10^{-4}Pa (1×10^{-6} torr).

The ENI RPG-100 pulse generator has been used to provide the asymmetric pulsed DC bias of the targets at 50kHz and pulse-off times of 496ns to 8016ns. The high voltage is applied in parallel on the cathodes. The operation mode was set for a constant current run at 2A for Cu targets and respectively 1.5A for Fe targets. These operating conditions ensure a stable discharge for both configurations, at close operating parameters that allow a comparison of the experimental results.

The ion energy spectra were measured using the HIDEN Analytical EQP300 analyser (Chapter 1.4). The diameter of the probe orifice used was 50μm. The axial distance D of the EQP probe (Fig.5.4.1) to the targets edge can be adjusted from 1cm to 10cm from the targets edge. The EQP analyser has been tuned at D=10cm from the targets edge according to the description provided in Chapter (2.4).

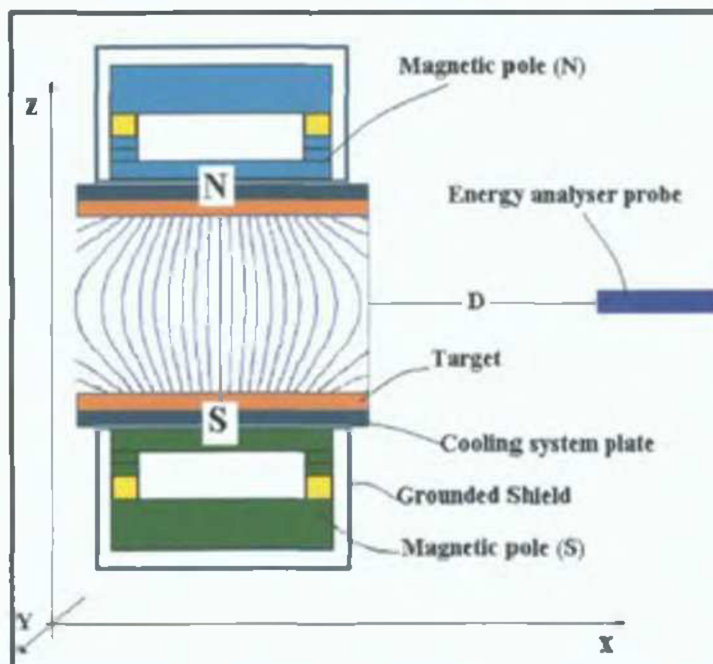

Fig.5.4.1. Geometry of the opposed target magnetron and the EQP probe.

5.4.3. THE ION ENERGY SPECTRA (IES)

The IES for Ar ions and respectively Cu ions and Fe ions measured at a distance D=10cm from the targets edge (Fig.5.4.1) for DC and pulsed DC operation are presented for several values of the pulse-off time (w) in Fig.5.4.2 - Fig.5.4.5.

During DC operation, the measured Cu ion spectrum has an energy distribution typical to the actual energy distribution of the metal atoms from the sputtering process. Similar energy distributions were obtained from simulations using the ACAT code for DC sputtering of Cu in Ar at 0.4Pa [21].

The Ar ions spectrum during DC operation has a peak at about 0.5eV and a higher energy tail in the same energy range as the Cu ions, most probably due to collisions between the gas atoms (ions) and the sputtered metal atoms (ions). The low energy peak represents the most probable energy of the Ar ions in the discharge bulk.

During pulsed DC operation the Ar and Cu ion spectra have a similar, wide energy distribution, with a peak at 40eV for pulse-off times longer than 4016ns. This indicates that both Ar and Cu ions are gaining energy in the same type of electric field during the pulse-off time.

The IES for Fe targets (Fig.5.4.4 for Ar ions and Fig.5.4.5 for Fe ions) show a similar behaviour with the pulse-off time but with higher intensity for the Ar ion spectra and a marked peak in the energy range 2eV-20eV, matching closely the energy distribution of sputtered Fe atoms and respectively post-sputtered (reflected) Ar atoms, as presented in [21].

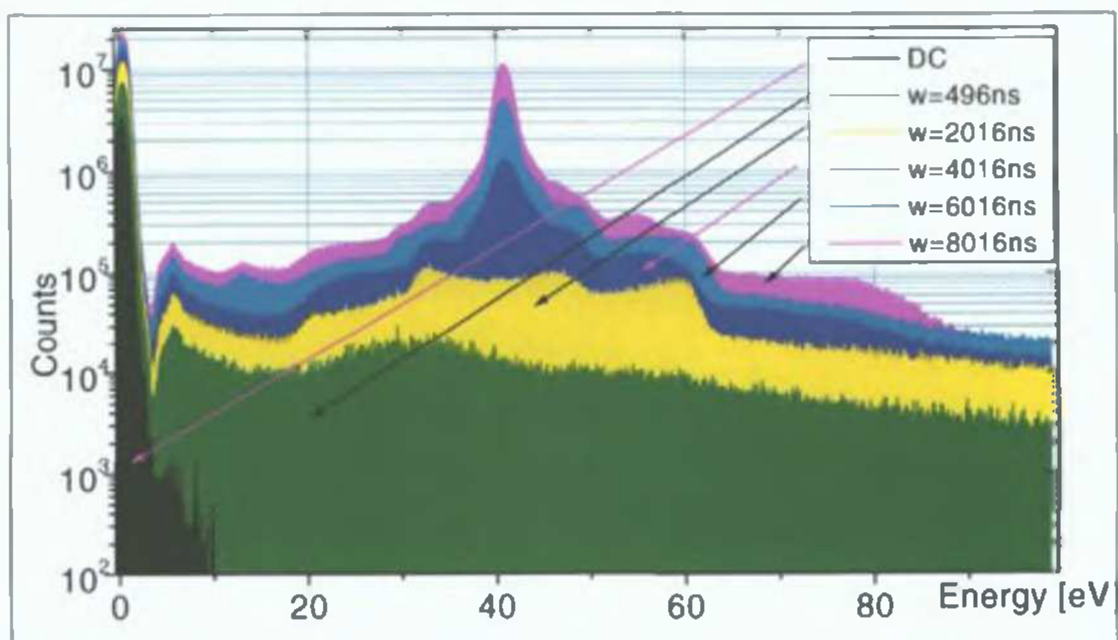

Fig.5.4.2: Ar ion energy spectra at 50kHz, I=2A, p=3mtorr, for different pulse-off time values for Cu targets.

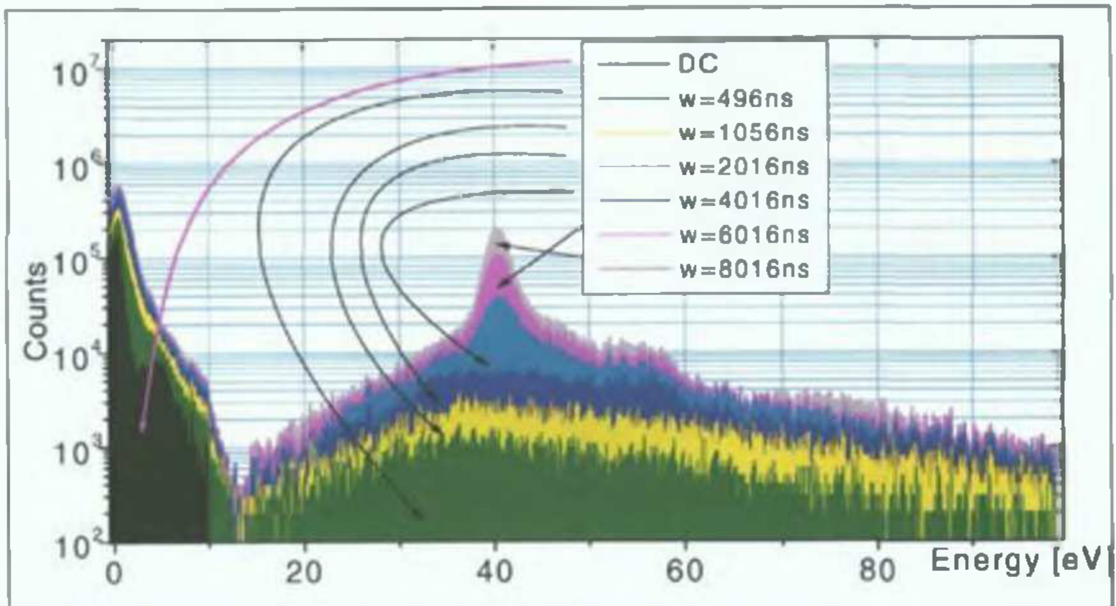

Fig.5.4.3: Cu ion energy spectra at f=50kHZ, I=2A, pAr=3mtorr, for different pulse-off time (w) values.

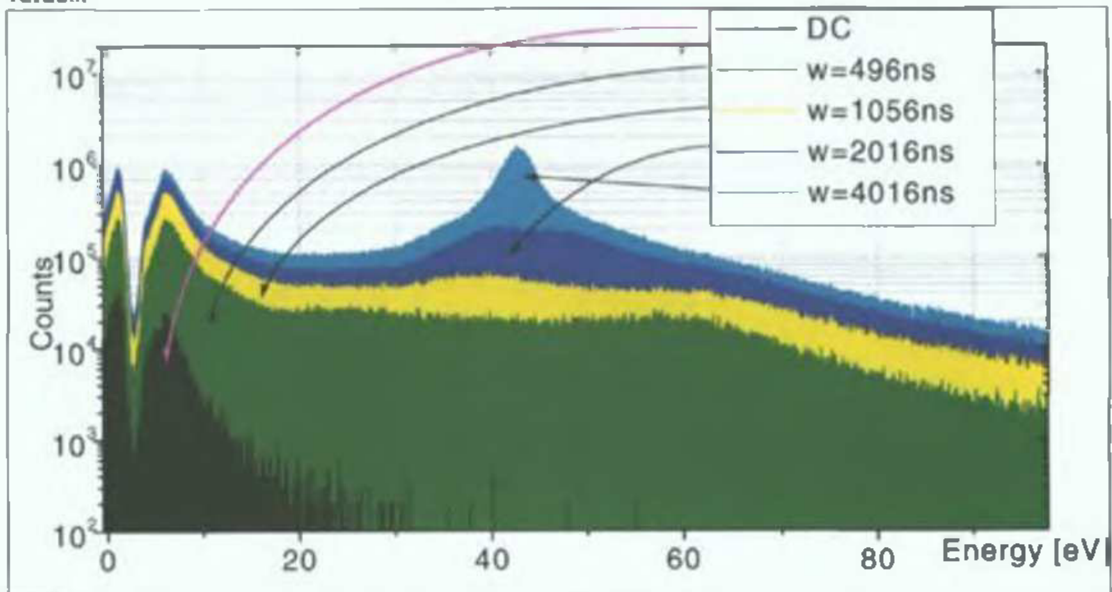

Fig.5.4.4:Ar ion energy spectra for Fe targets, for different pulse-off time (w) values.

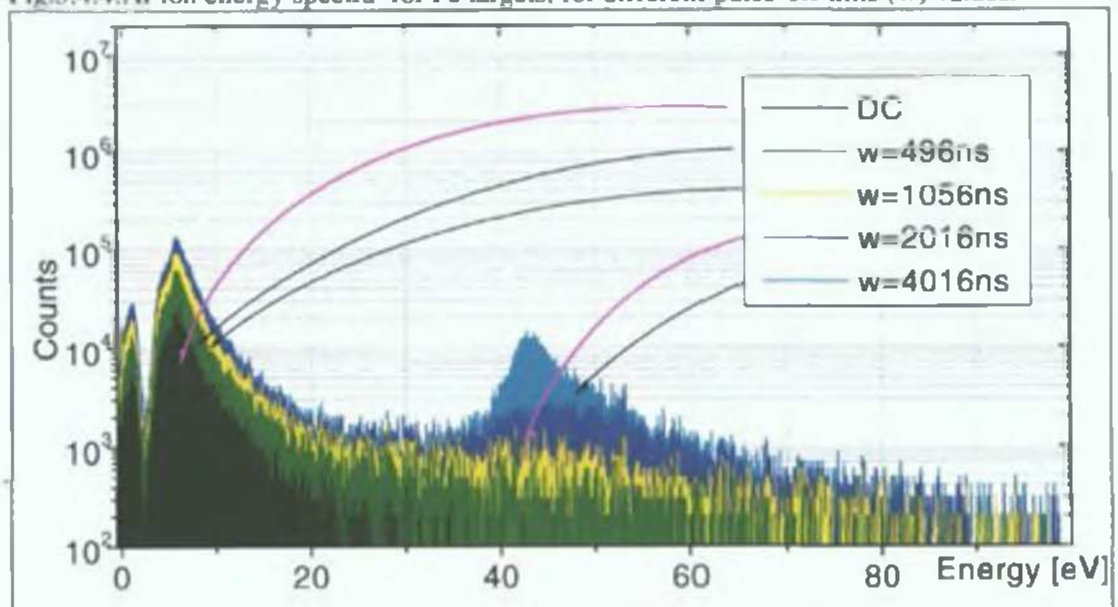

Fig.5.4.5: Fe ion energy spectra for Fe targets, for different pulse-off time (w) values.

5.4.4. DISCUSSION

A comparison between the IES obtained for Cu targets and for Fe targets is presented in Fig.5.4.6 for DC operation and respectively in Fig.5.4.7 for pulsed DC operation at 2016ns pulse-off time. The ion energy spectra during DC operation follow the existent ion energy distribution in the bulk, during the ON phase of the pulse.

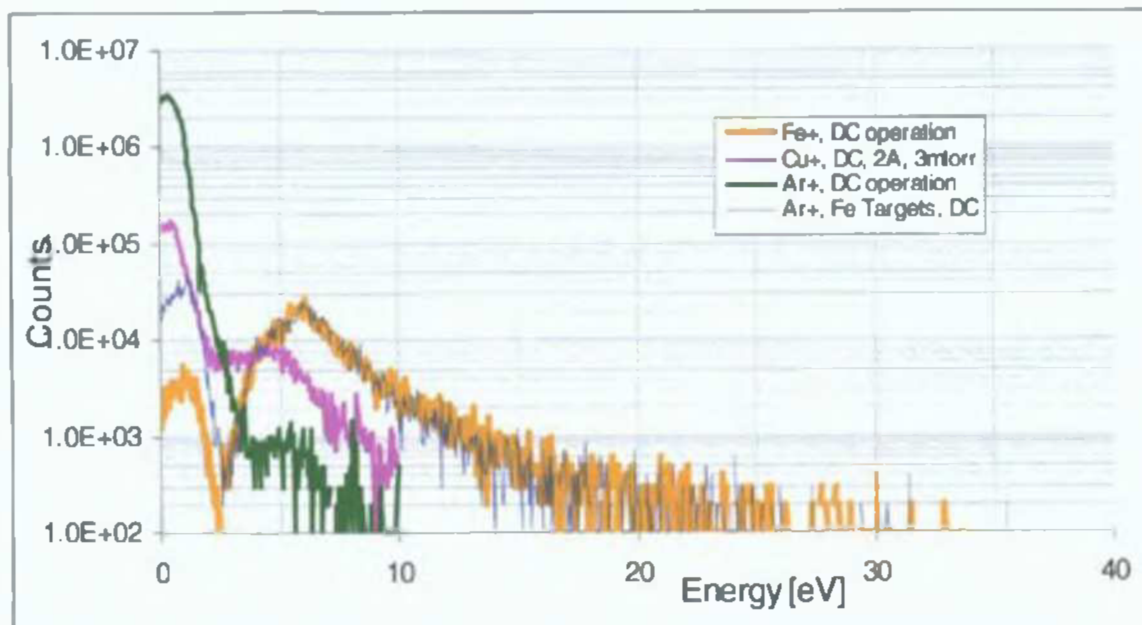

Fig.5.4.6: DC ion energy spectra for Cu and Fe targets.

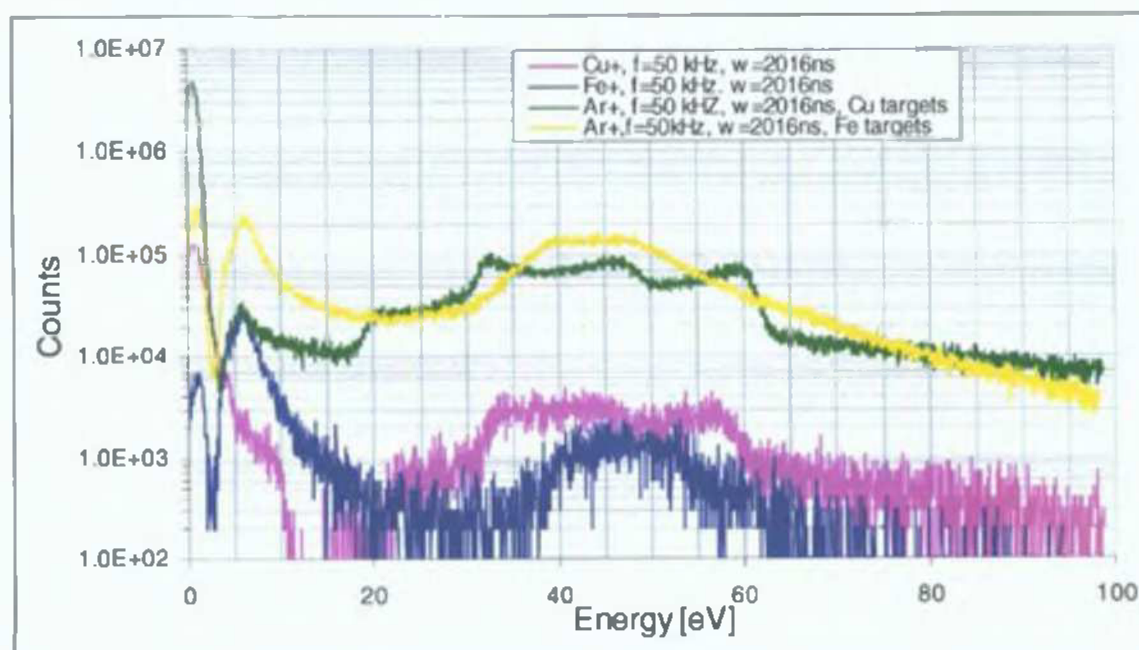

Fig.5.4.7: Pulsed DC ion energy spectra at f=50kHz, off time=2016ns, for Cu and Fe targets.

For Cu targets (Fig.5.4.6) both Cu ion and Ar ion energy spectrum display an energy distribution with two peaks (a thermal population and a higher energy population from the original sputtered atom energy distribution) as predicted [3] by simulations using the ACAT code for a DC planar magnetron discharge in Ar at 0.5Pa.

Differences in electron kinetics, confinement and electron temperature when using the Fe targets can be noticed (Fig.5.4.7):

- Both the Fe and Ar ions are leaving the bulk with the high energies from post-sputtering and backscattering indicating a high ionization efficiency at regions close to the targets;
- The low energy Ar gas is less ionized (the low energy Ar ion peak for Fe targets is 2 orders of magnitude smaller than the one for Cu targets), indicating a lower ionization efficiency at regions where gas atoms at thermal energy dominate.

The higher energies of the Fe (and Ar) ions can be explained through a higher degree of ionization for the post-sputtered and backscattered atoms (high energy Fe atoms are backscattered after Fe self-sputtering the same way as Ar atoms are backscattered after sputtering). The higher energy backscattered atoms [21] are ionized while crossing a region with high electron temperatures situated close to the targets, and can lead to self-sputtering and auto-sputtering.

The fact that the Ar ion energy distribution matches closely the one of the Fe ion indicates that both Ar and Fe ions (respectively atoms) originate from the same process: the backscattered (reflected) atoms after sputtering.

The occurrence of self-sputtering for Fe targets is also indicated by the presence of high-energy backscattered Fe ions.

The energy density of the total ion current (due to both Ar and metal ions during the whole pulse) at the substrate (measured for different pulse duty cycles and integrated over the total pulse duration, 20μs) is about twice for the Fe targets than for Cu targets (Fig.5.4.8).

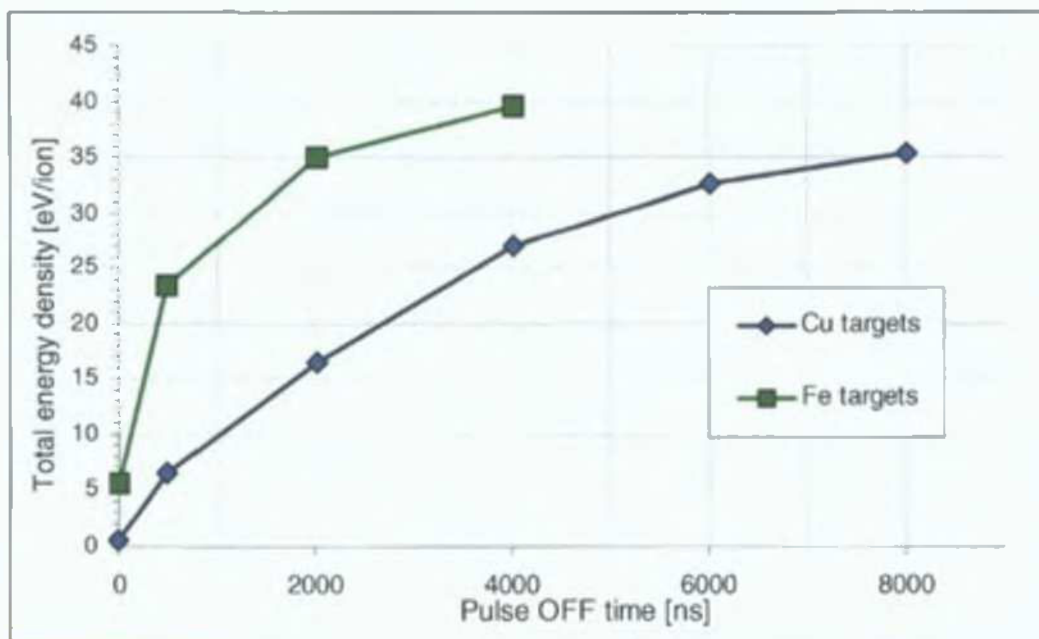

Fig.5.4.8: Comparison of the energy density of the total ion current at the probe (substrate) for Cu and Fe targets.

5.4.5. THE SPACE-RESOLVED ION ENERGY SPECTRA (IES)

The IES are observed as a function of the distance D (Fig.5.4.1) between the targets edge and the probe, for the Cu target configuration. The IES during a 50kHz, w=8016ns pulse-off time discharge at I=2A and 0.4Pa Ar gas pressure have been observed. The EQP tuning was performed with the probe situated at a distance D=10cm from targets edge, this tuning being used for all measurements.

The maximum IES energy value in Fig.5.4.9 and Fig.5.4.10 decreases as the probe distance to the targets increases. This is due to the plasma potential (Vp) values that are decreasing with distance from the targets.

The step-like edges in the energy distribution can be linked to the oscillations of the plasma potential during the pulse-off time. These occur at smaller energy values when increasing the distance from the targets as well. This leads to a narrower main peak for D=10 cm than those for D=8cm or D=6cm (Fig.5.4.9). For distances from the targets edge smaller than 5cm, the main peak width gets wider, while the maximum energy exceeds 100eV (Fig.5.4.10).

For distances very close to the targets edge, the measurement is perturbing the discharge - giving the large noise aspect of the spectrum - and can lead to an extinction of the discharge (Fig.5.4.10, for D=1cm).

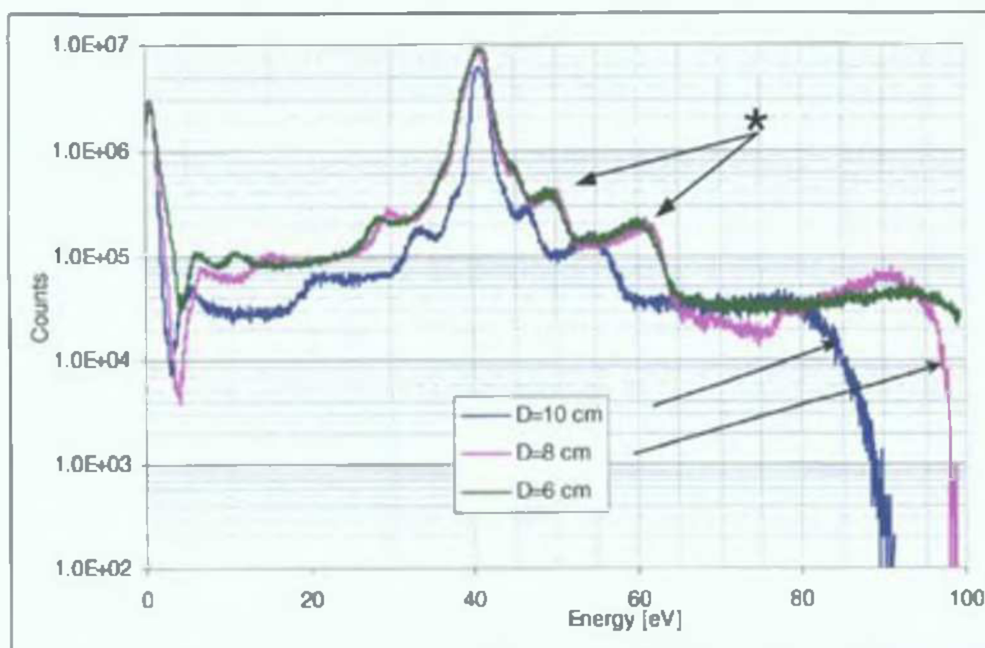

Fig.5.4.9: Ar IES as a function of the distance D of the probe from targets edge, for distances larger than 5cm. The (*) arrows indicate the "step-like" edges in the ion energy distribution.

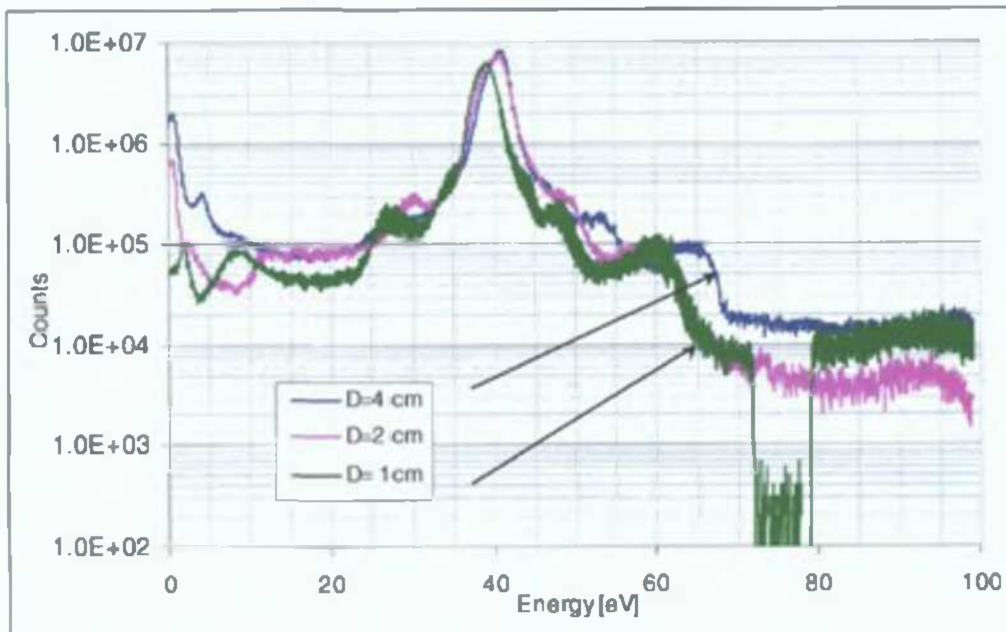

Fig.5.4.10: Ar IES as a function of the distance D of the probe from targets edge, for distances smaller than 5cm.

5.4.6. THE TIME-RESOLVED METHOD FOR I.E.S. ANALYSIS

Time-resolved IES can be obtained from the total integrated IES using simple de-convolution methods and a statistical analysis of the average number of counts integrated (during the pulse-off time) as a function of the pulse-off time, as it will be explained in the following.

Due to the obvious temporal dependence of phenomena taking place in the pulsed DC discharges, there is an increased interest in time-resolved IES data and significant work has been devoted to gated acquisition of counts at the detector, electronically shuttering the ions at the EQP entrance or through acceleration/deceleration methods [56, 78]. These methods are deficient from the point of view of temporal resolution (2µs to 4µs) and temporal sync between counted data and actual start moment of the pulse as the ions transit times through the spectrometer are of the order of 10µs (for Ar ions) and they are mass dependent.

In fact, real-time IES cannot be obtained with EQP analysers and the idea of a real-time measurement of the spectra is somehow meaningless as the required acquisition time (1ns – 1000ns) is generally less than the time the electronics needs to process the data! More, the number of counts integrated during very small time-intervals may be much smaller than the statistical measurement error, leading to very "noisy measurements" with data values smaller that the standard deviation.

This is why, the only reliable means to obtain the temporal information in particle counting systems is to acquire a number of counts during a measuring time interval, in order to allow for a certain statistics and precision level of the counting.

The EQP energy analyser provides the integrated number of counts during the 100ms dwell time of the EQP. At each energy point, the EQP will integrate the number of pulses acquired during a 100ms time interval.

So, at each energy point, the total number of ions collected over 100ms dwell time (over 5000 pulses of 20μs) is considered. This procedure allows a good precision of the counting (integration) and measurement. The temporal information can be derived by a statistical analysis of the acquired counts over the time interval of interest (characteristic for the observed process).

Any IES obtained during pulsed DC operation is a convolution of the spectrum obtained during the pulse-on time and the one obtained during the pulse-off time of the pulsed DC discharge.

As the DC spectrum (for both gas and metal ions) has a simple energy distribution that can be measured and observed during the DC operation of the magnetron, a similar energy distribution is expected for the pulse-on time operation. Observing pulsed DC spectra, we can see that the low energy part is similar to the one obtained during DC operation, indicating that the respective region of the IES is obtained during the pulse-on time. The higher energy regions of the IES are obviously obtained during the pulse-off time.

There is a clear separation in these distributions in the IES, indicating that they appear through different processes. This allows setting an energy threshold for the separation between pulse-on and pulse-off time counts. The error due to the choice of this threshold level is estimated to be below 5% when the threshold is chosen at the separation region.

The above approach represents the simplest de-convolution, given by the difference between two spectra (of which one has known causes and distribution) and it is extensively used in other fields of experimental physics: nuclear physics, atomic physics, radiation dosimetry. Therefore, the counts acquired during the pulse-on time and the pulse-off time can be de-convoluted by setting a threshold level in the pulsed DC spectra, while further analysis can be performed by temporal averaging over the characteristic time interval.

The obtained values are only averages and trends of the acquired number of counts, not absolute values. Nevertheless, the above-described time-resolved IES method allows an analysis of phenomena taking place at the EQP region.

The statistical analysis applied to the measured IES will be developed and discussed in relation to the "Physical model for the pulse-off time plasma", in Chapter 6.2.

5.4.7. THE IES STATISTICS

Some error (less than 5%) in calculating the ion number during the pulse-on and pulse-off duration arises from the choice of end, respectively start point of integration on the IES. This point was chosen at E=3.5eV for Ar ions and at E=11.5eV for Cu ions and it corresponds to a clear minimum in the energy spectra. These threshold values also correspond to the high-energy limit of the spectra obtained during DC operation.

The pulse-on time spectra were considered below 3.5eV for Ar ions, respectively below 11.5eV for Cu ions; and the pulse-off time spectra above these.

As the Cu ion density is about 100 times lower than that of Ar ions and it depends strongly on the sputtering process, the Cu ions are not included in the analysis of the ion flux and flux rate.

The number of ions collected during the pulse-on time decreases slightly with increasing the pulse-off time, as expected; while the number of ions collected during the pulse-off time has a strong increase with the pulse-off time (Fig.5.4.11). A similar behaviour is observed for both Cu and Ar ions. For pulse-off times longer than 4000ns, the ion number is increasing almost linearly with the pulse-off time.

The ion flux in Fig.5.4.12 has been calculated as the number of Ar ions collected during the pulse-on and pulse-off time, each per collection time. At 50kHz, the collection time for the pulse-on time is: 19504ns, 17984ns...11984ns and for the pulse-off time is respectively: 496ns, 2016ns...8016ns.

The obtained values for the ion flux are also "cumulative" values corresponding to the dwell time of the EQP and not absolute values of the real-time ion flux. Measuring the real-time values of the ion flux would lead to a very low count measurement and a poor precision of estimation. The "cumulative" ion flux calculated as above allows a good precision for temporal analysis and comparison purposes.

We can notice that the ion flux is constant with the duration of the pulse-on time, indicating a constant ion flux at the probe at any moment during the pulse-on time (or during DC operation). This proves that the plasma-probe sheath during the pulse-on time has a constant extent that is not influenced by the duration of the pulse-on time (i.e. it is independent of the duration of collection time). Also, the ion flux density at the probe region is independent of the pulse-off time duration.

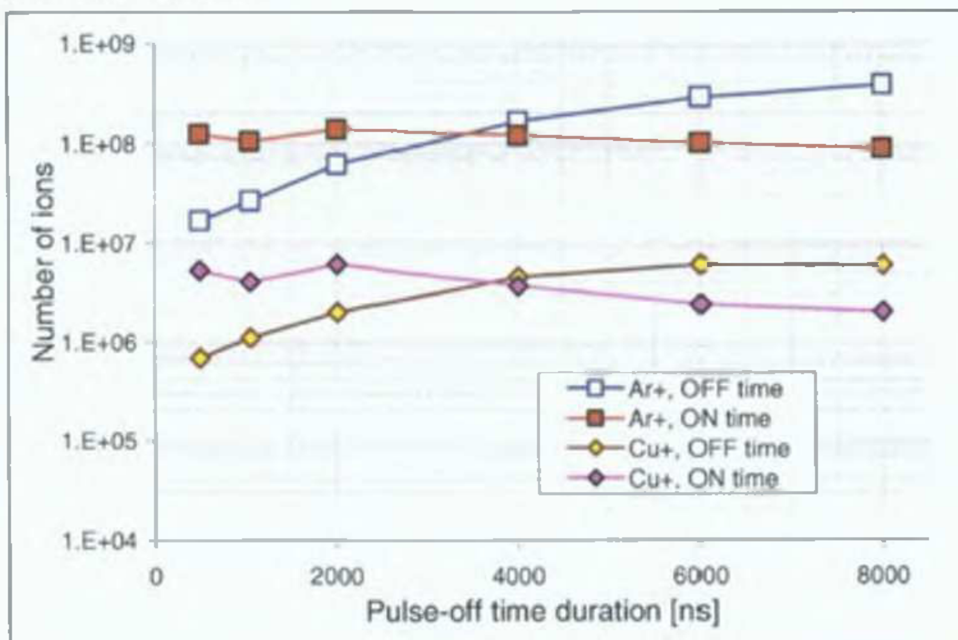

Fig.5.4.11: The number of Ar and Cu ions collected by the energy analyser probe during the pulse-on time and during the pulse-off time, as a function of the pulse-off time.

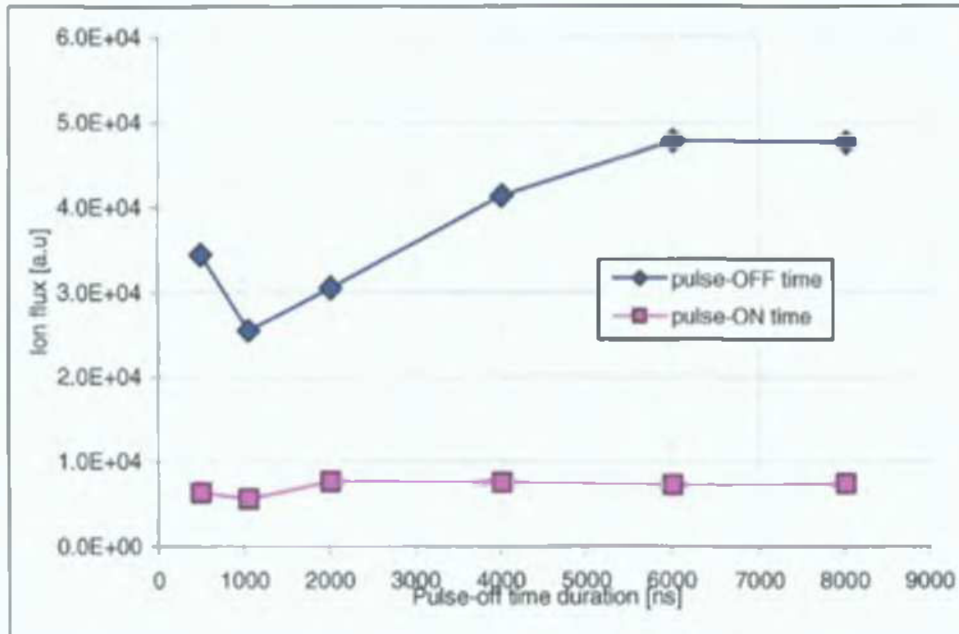

Fig.5.4.12: The Ar ion flux [Number of ions/collection time] collected by the probe during the pulse-on time and during pulse-off time as a function of the pulse-off time.

At the beginning of the pulse-off time, the ion flux at the probe is 3 times higher than the one during the pulse-on time, and continues to increase with the length of the pulse off time. This is a direct observation of the sudden increase in the ion flux at the probe (substrate region) during the pulsed DC operation and a proof that the extent of the pulse-off time has a direct implication in this effect. This observation is in good agreement with results from other experiments presented in literature [79, 80].

The ion flux rate values during the pulse-off time are calculated as the variation in ion flux values between consecutive pulse-off time durations, divided by the difference between these durations. This analysis is based on the assumption that for all pulse-off times the phenomena governing the ion transit and the plasma behaviour are similar. Again, the obtained values are only cumulative values over the measuring dwell time of the EQP analyser, and not real-time absolute values.

Representing the ion flux rate of change d^2N/dt^2 as a function of the pulse-off time, a strong maximum followed by a constant region can be observed (Fig.5.4.13). This behaviour of the rate of change in the ion flux at the probe during the pulse-off time will be examined in detail later, in Chapter 6.2.

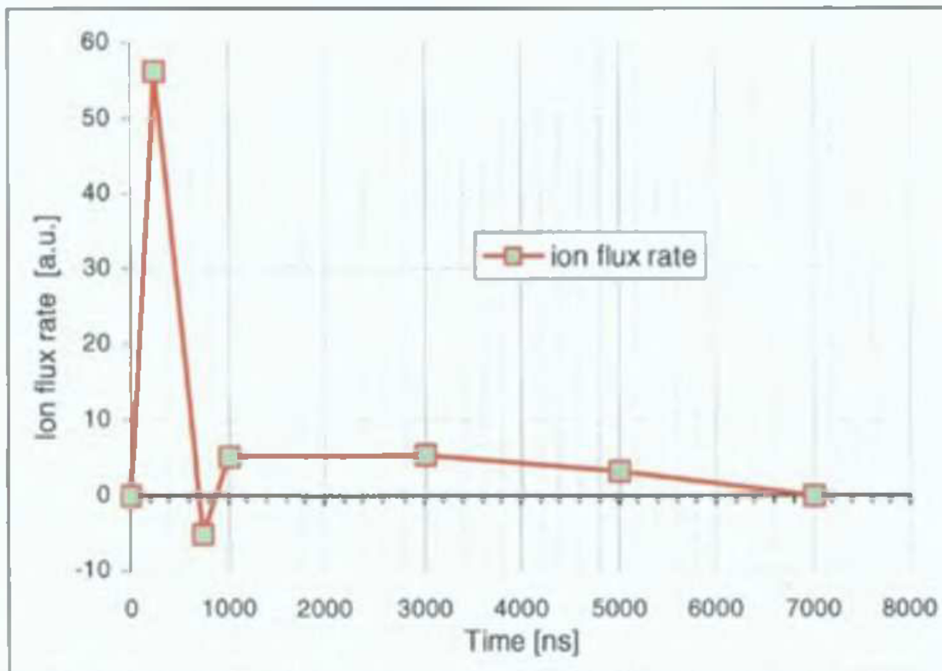

Fig.5.4.13: Typical ion flux rate variation during the pulse-off time, calculated as d^2N/dt^2 (the variation of the ion flux (dN/dt) between two consecutive values of the pulse-off time).

5.4.8. CONCLUSIONS

The IES obtained for a range of pulse-off times as well as the space-resolved IES at w=8016ns pulse-off time are presented, providing information on the energy distribution of ions reaching the substrate region.

The Ar, Cu and respectively Ar and Fe ions energy distributions during DC deposition are compared and explained though basic processes taking place in the sputtering discharge: sputtering and self-sputtering of the target material and backscattering and auto-sputtering of the gas ions (atoms) as well as collisions between the sputtered material and the gas.

A time-resolved method for analysing the IES during the pulsed-DC operation of the magnetron has been presented as a new method for plasma diagnostic. Its novelty consists in the fact that the actual IES measurements do not have to be time-resolved, as the data analysis can extract the temporal dependence of the main parameters characterizing the deposition during the pulse-on, respectively the pulse-off time: the ion number, flux and flux rate at the substrate region.

This temporal analysis provides an easy and effective means for plasma diagnostic of pulsed-DC discharges and allows further analysis of time-dependent phenomena taking place during the pulse-off time, as it will be shown in Chapter 6.2.

CHAPTER 6

TIME-RESOLVED PLASMA PHYSICAL MODELS OF THE PULSED DC DISCHARGE

Using the information gathered through the time-resolved plasma diagnostic methods presented in Chapter 5, a further analysis is presented here, liking the space-temporal evolution of several parameters to obtain physical models of the evolution of the discharge.

With the aim of developing a thorough understanding of pulsed DC discharges and phenomena governing the pulse-on and respectively the pulse-off time, two physical models of the pulsed discharge are presented:

- A time dependent physical model of the pulse-on time, based on the time and space evolution of electron temperature form OES data;
- A time dependent physical model of the pulse-off time, based on the time and space resolved IES at the substrate region.

6.1. MAGNETRON PLASMA MODEL FOR THE PULSE-ON TIME

6.1.1. INTRODUCTION

During the pulse-on time the discharge develops and produces sputtering in strong connection to the input parameters (input power and gas pressure). The complex phenomena taking place during this time can only be understood by observing the plasma parameters (electron temperature and density) and their evolution with regard to the input parameters.

Important work has been dedicated in the last decade to determination of electron temperature and density, especially related to studies on planar magnetrons. Early Langmuir probe measurements in the plasma bulk region close to the cathodes of a planar magnetron under DC operation have been performed by Rossnagel [47] and led to T_e values of about 5eV for low pressure (~mtorr) Ar gas plasmas. The concept of a two-temperature electron energy distribution in magnetron plasmas has been introduced by Sheridan et al [44] as a result of both Langmuir probe measurements and Monte Carlo simulations of magnetron plasmas.

The latest results, obtained by space and time-resolved Langmuir probe measurements at the substrate region of planar magnetrons under pulsed DC operation also led to the two-temperature electron energy distribution with high energies form 5eV up to 20eV and low energies around 0.5eV [7].

Opposed target (Penning type [1, 2, 3]) magnetrons with rectangular geometry present an interesting option for ferromagnetic material deposition in industrial applications [38]. Their configuration involves the use of parallel electric and magnetic fields between the opposed cathodes, leading to high efficiency sputtering of both ferromagnetic and non-ferromagnetic materials and the rectangular geometry allows on-line industrial applications.

Due to strong magnetic and electric interferences, Langmuir probes cannot be used in the opposed target magnetron configuration.

Although relying on the occurrence of LTE or PLTE conditions, Optical Emission Spectroscopy (OES) provides a non-invasive method for the evaluation of T_e inside the plasma bulk, at normal operating conditions of the opposed target magnetron.

Limitations of this method are related to the performances of the optical equipment (an accurate determination of the intensity throughput and instrumental profile of the spectrometer is required) and to line selection and background corrections, leading to possible high error levels [40]; but still providing reliable information on the overall space and temporal electron temperature evolution.

In this thesis, an assessment of the electron temperature based on time and space-resolved OES measurements in an opposed target magnetron plasma under pulsed DC operation is presented.

The novelty of the obtained results is manifold:

- OES electron temperature determinations in pulsed DC magnetrons have been obtained for the first time during this work;
- The Acousto-Optic spectrometer has been used here for the first time for evaluations of electron temperature, and a measuring method had to be designed and evaluated before use;
- The observed temporal and space evolution of the electron temperatures lead to a first time model of the behaviour of the plasma and discharge during the pulse-on time.

The observation of electron dynamics and plasma parameters throughout the pulse duration and the discharge space, allows explaining the evolution of the sputtering process as well as the distribution of ionized and excited species and their dynamics during the pulse.

6.1.2 THE PULSE-ON TIME PLASMA MODEL IN THE OPPOSED TARGET MAGNETRON DISCHARGE WITH Cu TARGETS.

Relying on the data acquired through time-resolved and time and space resolved OES diagnostic methods described in Chapter 5.2, coupled with the electrical diagnostic measurements (I-V characteristics and I-V waveforms presented in Chapter 5.1) a model for the phenomena taking place in the discharge can be inferred. The data obtained from the above diagnostic methods (for the configuration with Cu targets) have been presented in Chapter 5.1 and Chapter 5.2 and are shortly presented in the next graphs.

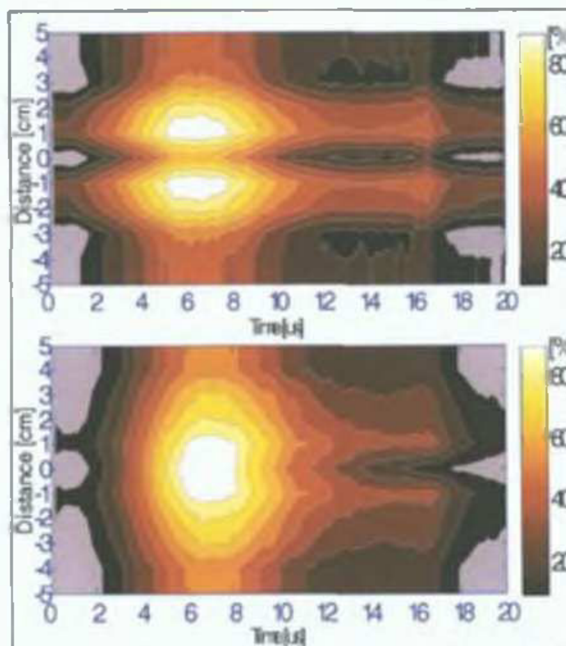

Fig.6.1.1. Normalized relative intensity for Ar II 488nm line (up) and for Ar I 763nm line (bottom), space and time-resolved at 50kHz, 4016ns and p=3mtorr, for the Cu targets.

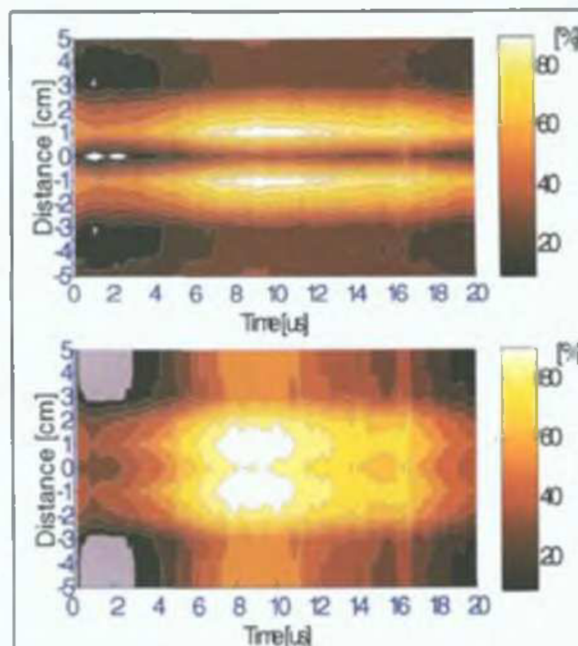

Fig.6.1.2. Normalized relative intensity for Cu I 465nm line (up) and for Cu I 522nm line (bottom), space and time-resolved at 50kHz, 4016ns and p=3mtorr.

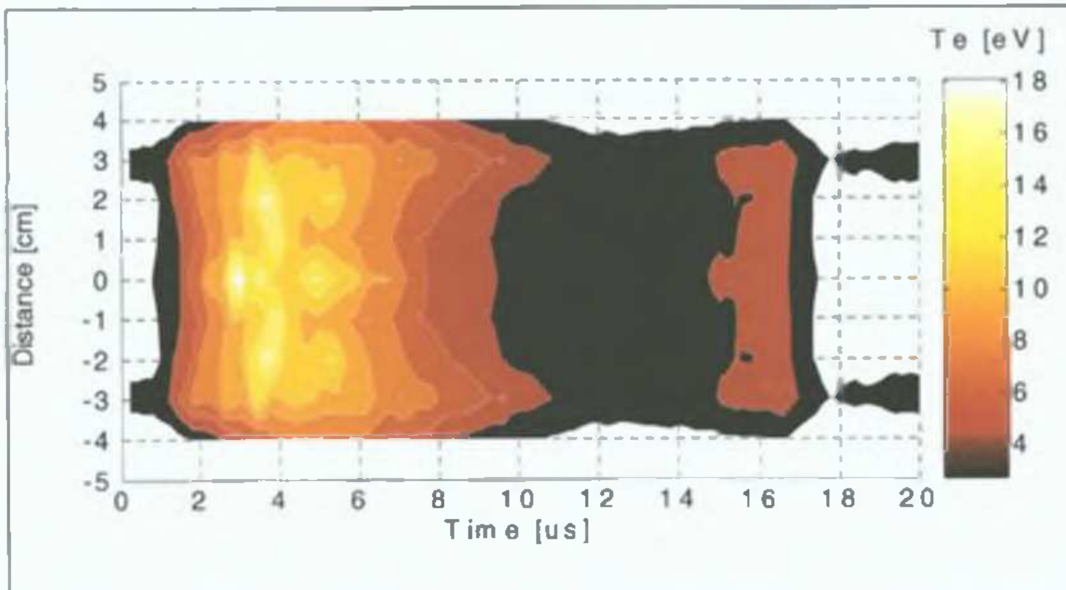

Fig.6.1.3: Electron temperature contour lines evolution during the pulse at 50kHz, pulse off time 4016ns, set current I=2A, argon pressure p= 3mtorr.

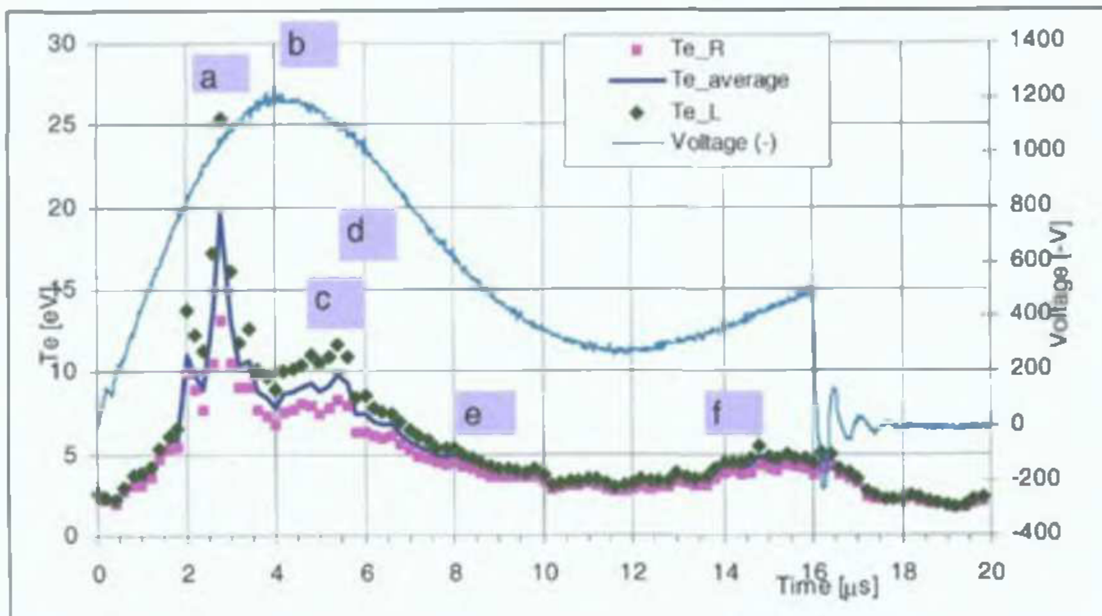

Fig.6.1.4: The time-resolved electron temperature during the pulse-on time at D=0 cm from the discharge centre along with the voltage waveform.

The time-resolved evolution of the electron temperature from ionic lines is presented in Fig.6.1.4 for a pulsed DC discharge at 50kHz, 4016ns pulse-off time, 2A current run, at a distance D=0.0 cm from the centre of the discharge, along with the voltage waveform. We can see that the time – resolved evolution of T_e during the pulse-on time allows for direct observation of electron dynamics and of the different stages in the discharge and sputtering process evolution during the pulse.

The Ar ions (produced by electron direct impact mainly in a region situated at D<3cm from the discharge centre, Fig.6.1.1) will travel to the targets in about 2.5 μs and lead to the start of the sputtering process. This event is marked by a sudden increase in electron temperature

(~20eV) due to the production of secondary electrons and the high accelerating potential at this moment (at t=2.5μs, V~1000V, Fig.6.1.3).

Meanwhile, secondary electron production as well as ions and free electrons from ionization processes lead to a strong decrease in the discharge impedance and consequently of the voltage. This is equivalent to a "breakdown" process (starting at t=4μs), leading to a steady decrease of the voltage during the next 8μs.

After t=6μs the potential on the targets has decreasing values and most of the electrons are loosing fast their energy in ionization (of metal atoms) and excitation processes, so the electron temperature has a steady decrease for most of the pulse duration, reaching ~2eV at t=12μs.

The electron temperature clearly indicates the evolution of discharge stages (points marked on Fig.6.1.4):

a) Start of sputtering marked by a high spike in T_e at t~2.5μs;

b) Start of "breakdown" (the target voltage decrease) due to the start of high-rate ionization processes and decrease in the discharge impedance, at t~4μs;

c) Start of self-sputtering marked by a second spike in T_e at t~5μs;

d) The Ar ion peak fall at t=6μs (when T_e becomes smaller that 11eV (Fig.6.1.4 and Fig.6.1.3);

e) Decrease in the ionization and sputtering efficiency;

f) The final increase in the discharge impedance.

The above described discharge stages form a model for the pulse-on time phenomena in the discharge. Although for different temperatures and time-scales for the sputtering and self-sputtering processes, this type of development is expected to occur in most pulsed DC discharges.

6.1.3 THE DISCHARGE BEHAVIOUR AND VALIDATION OF THE MODEL (Cu TARGETS)

The initial electron energy has values above 100eV, corresponding to the cathode potential. These electrons have a non-Maxwellian distribution given by the external (applied) electric field.

During the time interval between observation moments, the electrons are bouncing back and forth between the targets, along the magnetic field lines (about 20 times for 100eV electrons) and loose energy moving against the electric and magnetic field lines and in direct impact collisions with Ar atoms.

The observed T_e is the average EEDF over the time interval between measurements coinciding with the temporal resolution of the spectrometer (0.2μs).

At each measuring point, the observed electron temperature represents the mean temperature of the electrons that are producing the ionization and excitation processes at that position and moment during the pulse, according to their Maxwellian distribution.

At the beginning of the pulse, the electrons have relatively low mean energies corresponding to the low negative (accelerating) voltage on the targets. Their energy (and temperature) increases as the voltage increases. The space and time-resolved distribution of the electron temperatures can be observed in Fig.6.1.3.

The Ar ions produced during this time will travel to the targets in about ~2.5 μs and lead to the start of the sputtering process. This event is marked by a sudden increase in electron temperature (~20eV) due to the production of secondary electrons and the high accelerating potential at this moment (Fig.6.1.4. at t=2.5μs. V=-1000V). Once the sputtering has started, the production of metal atoms increases the rate of electron energy loss through ionization and excitation collisions with both gas and metal atoms, leading to a sudden fall in electron temperature.

The secondary electron production as well as ions and free electrons from ionization processes lead to a strong decrease in the discharge impedance, leading to a drop in the voltage at the targets, equivalent to a breakdown process (starting at t=~4μs), leading to a steady decrease of the voltage during the next 8μs.

While the electron temperature has values above 11eV (corresponding to electron energies of about 16eV, just above the Ar ionization potential of 15.7eV) the Ar ionization continues. Consequently, the Ar ion lines intensity increase until they reach a maximum at t=~6μs.

At t=~6μs, as T_e drops below 11eV and the one-step direct electron impact ionization of Ar atoms is no longer possible, the Ar ion intensity peak starts to fall.

After t=~6μs the potential on the targets has decreasing values and most of the electrons are loosing fast their energy in ionization (of metal atoms) and excitation processes, so the electron temperature has a steady decrease for most of the pulse duration, reaching ~2eV at t=~12μs. As the rate of ionization processes decreases in the second part of the pulse, the discharge impedance starts to increase, leading to higher voltage on the cathodes (targets) and to a slight increase in electron temperature (from about 2eV up to 5eV) in the last 2μs of the pulse-on time.

It is important to notice that the time–resolved observation of the high–energy electron temperature leads to a clear indication of the evolution of discharge stages, in good agreement with the expected electron energies required for one-step direct impact ionization processes. This can be seen by comparing the T_e chart and the ionization cross-sections (Fig.6.1.5):

a) Start of sputtering marked by a high spike in T_e (T_e~20eV) at t~2.5μs and E_e~30eV (a maximum in the ionization cross-section for Ar);

b) Start of "breakdown" due to the start of high-rate ionization processes (both gas and metal atoms are ionized) leading to a decrease in the discharge impedance, the power peak fall and a decrease in E_e at t~4μs;

c) Start of self-sputtering marked by a second peak in T_e at t~5μs (T_e>8eV and correspondingly Ee>12eV allow this process at maximum cross-section for Cu ionization);

d) Ar ion peak fall at t~6μs (T_e <11eV and E_e<16eV, Ar ionization is no longer possible in one-step processes);

e) Decrease in ionization and sputtering efficiency;

f) Final increase in the discharge impedance.

As seen in Fig.6.1.4, the maximum ionization cross-section by direct electron impact calculated from Thomson formula is achieved at electron energies of 30eV (T_e~20eV) for Ar and respectively at E~12eV (T_e~8eV) for Cu.

The high-energy electron temperature values are in good agreement with the required electron energies for Ar ionization and provide a direct insight on the temporal evolution and space distribution of ionization processes during the pulsed discharge.

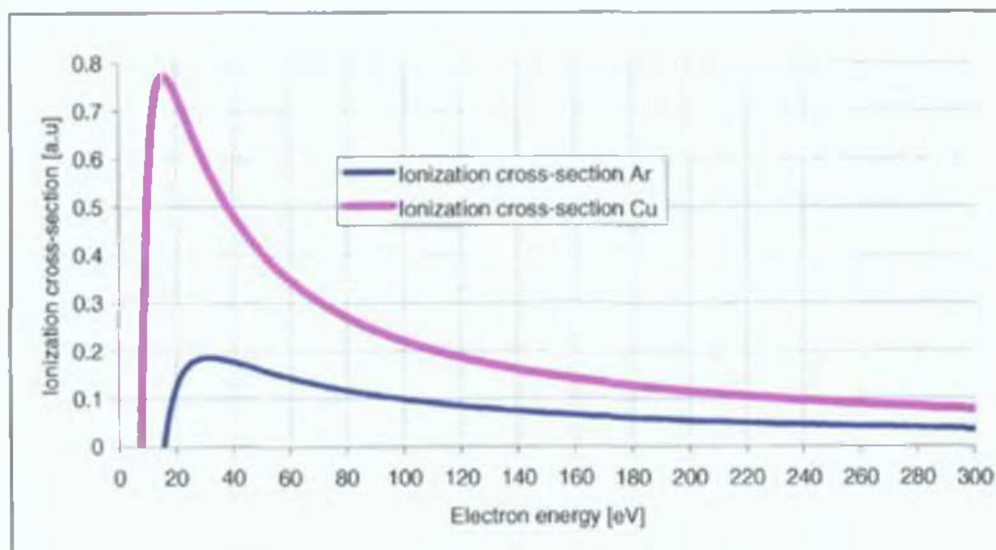

Fig.6.1.5. Calculation of Ar and Cu direct electron impact ionization cross-sections. Evolution with electron energy, using Thomson' formula presented in Chapter 4.3.1 [40].

In Fig.6.1.3, the regions with T_e >11eV (electron energies E_e>16eV) are characteristic for Ar ionization processes, while those with T_e > 5eV (electron energies E_e>7.5eV) are characteristic to ionization of Cu.

This indicates that Cu ion production takes place in the time region from t=~3μs to t=~10μs and in space regions closer to the targets that allow the apparition of self-sputtering (Fig.6.1.2). The delay between the two T_e peaks of about ~2μs also leads to the conclusion that the second peak is due to Cu ionized in a region close to targets (~1-2 cm).

The Ar ions are produced only in higher T_e regions closer to the centre of the discharge and need in average about ~2.5μs to reach the targets.

6.1.4. THE PULSE-ON TIME PLASMA MODEL IN THE OPPOSED TARGET MAGNETRON DISCHARGE WITH Fe TARGETS.

The case of OES diagnostic for ferromagnetic targets is interesting, both from practical point of view – providing an explanation of the increased target heating and increased ion energies at the substrate discussed in Chapter (5.4.4) and [58] and as a model for the physical phenomena that lead to these effects.

The time- and space-resolved evaluation of electron temperature, together with the distribution of excited and ionized species in the discharge (Fig.6.1.6 and Fig.6.1.7) provide the information for a good understanding of phenomena taking place during the pulse-on time in the pulsed-DC magnetron plasma, allowing the development of a physical model for the pulse-on time discharge.

The confinement for Fe targets has a particularity – the magnetic field distribution in the XOZ cross-section for Fe targets is concentrated in the centre of the target cross-section, with maximum magnetic field intensity achieved in a region close to the targets. This magnetic field distribution is due to the absorption of the Bx component of the magnetic field in the ferromagnetic targets. The magnetic field decreases fast in regions situated at 2cm from each end of the target (see Fig.3.1.8 along OX axis) leading to a loss of confinement at those regions, a lower electron density in the discharge and higher electron temperatures. This structure of the magnetic field leads therefore to higher electron temperatures in the discharge, while maximum electron density is achieved in the regions close to the targets.

The main data referring to the time and space resolved OES lines for Ar species and sputtered metal (Fe) are presented on the following page in order to allow the observation of phenomena taking place in the discharge related to time and apace resolved T_e and the Voltage waveform at the cathodes.

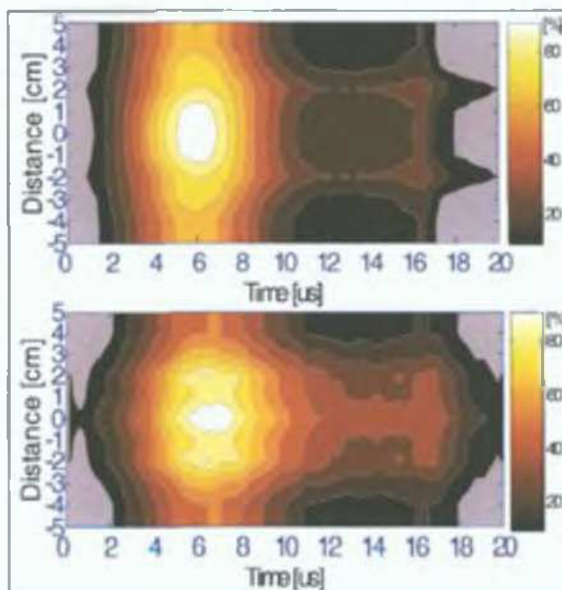

Fig.6.1.6. Normalized relative intensity for ArII 488nm line (up) and for Ar I 763nm line (bottom), space and time-resolved at I=1.5A, 50kHz,w=4016ns,p=2mtorr, for the Fe targets.

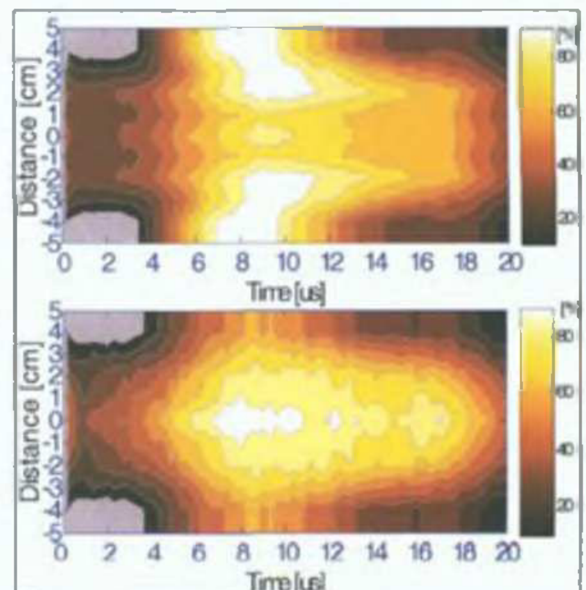

Fig.6.1.7. Normalized relative intensity for Fe I 372nm line (up) and for Fe I 492nm line (bottom), space and time-resolved at I=1.5A, 50kHz, w=4016ns and p=2mtorr.

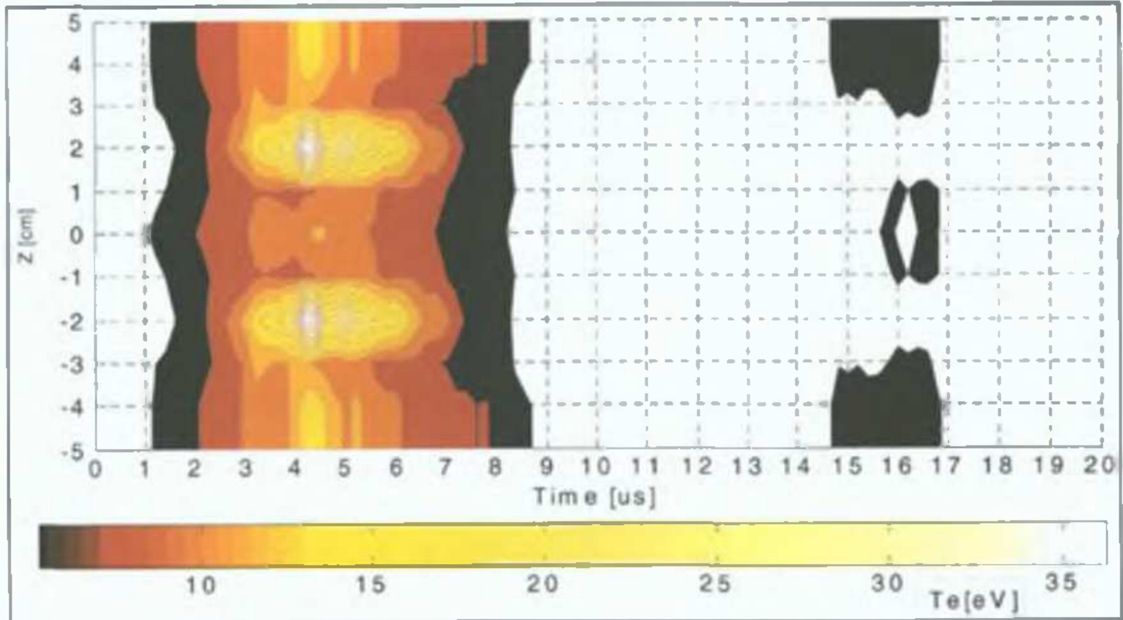

Fig.6.1.8. Electron temperature space and time-resolved at I=1.5A, 50kHz, w=4016ns and p=2mtorr, for the Fe targets. The values situated at distances below 1cm from the targets re extrapolated values.

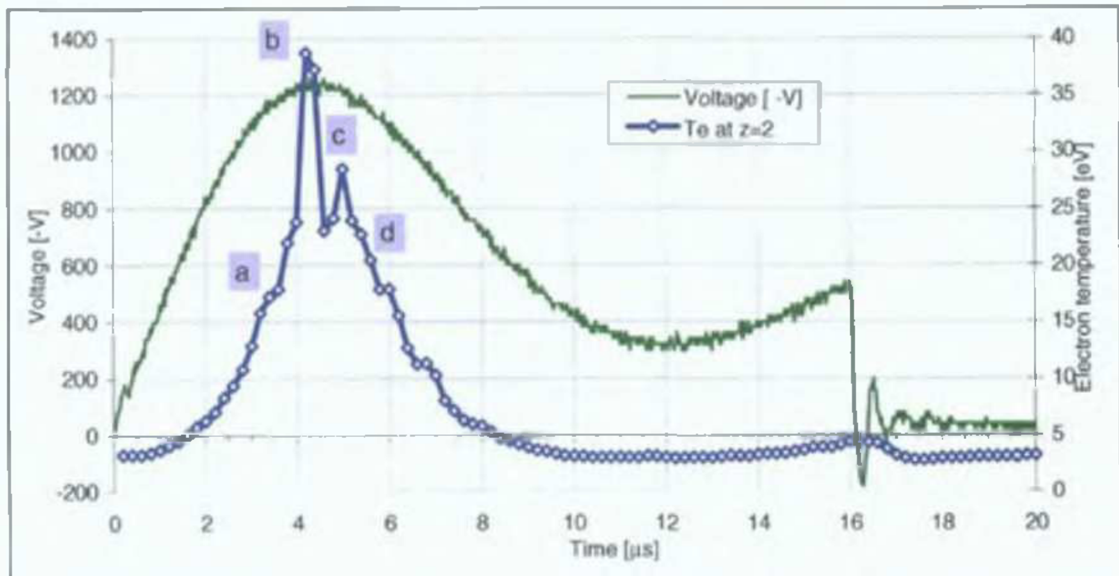

Fig.6.1.9. Te for Fe targets at D=3cm from the targets (z=2cm) along with the Voltage (-V) on the targets.

According to the evolution of time-resolved electron temperatures at the region with maximum T_e values (at D=2cm from the discharge centre, Fig. 6.1.8), the stages of the discharge can be identified as follows:

a) The start of intense one-step direct impact Ar ionization (OES relative intensity above 40%, Fig.6.1.6) starting at t~3µs (T_e>11eV). As Ar ionization occurs at all distances from the targets with the same probability (Ar ion distribution in Fig.6.1.6 is parallel to B lines) the start of sputtering does not have a clearly defined moment as the return time to targets is random, with large deviations from the average. Therefore, the "beginning of sputtering" cannot be observed in a similar way as for the Cu targets.

b) From the Fe distribution (Fig.6.1.7), we can see that new sputtered Fe starts to be created at t~4μs, mainly be direct sputtering. Also at t~4μs, a maximum in T_e~40eV, at a region situated at D=2cm from the targets is achieved. At this moment, a maximum in the sputtering process takes place mainly as a result of direct sputtering. This maximum coincides with the Voltage maximum at t~4μs.

   The Voltage starts to decrease slowly after t~4μs, due to the decrease in the discharge impedance caused by the intense ionization processes.

c) A second peak in T_e at t~5μs (T_e~20eV) can be observed. This peak is mainly due to the convolution of the voltage values at this moment and the rate of self-sputtering and target re-sputtering processes.

d) The maximum in the Ar ionization occurs at t=6μs. T_e decreases below 20eV (where the Ar ionization cross-section has a maximum) and Ar ionization rate starts to decrease along with T_e values.

6.1.5 DISCHARGE BEHAVIOUR AND VALIDATION OF THE MODEL (Fe TARGETS)

For Fe targets the higher electron temperatures lead to a different space-temporal distribution for the Ar ions, with consequences on the discharge behaviour.

At moments between t=3μs and t=6μs during the pulse, in the regions close to the targets (1cm from the targets) the electron temperature reaches values above 11eV, thus energies above ~16eV allowing for Ar ionization (Fig.6.1.8, Fig.6.1.9).

The ionization of reflected (post-sputtering) Ar atoms is enhanced in the opposed target geometry by the trajectory of these atoms that are reflected with highest probability in small angles relative to the normal to the targets [21, 22]. This implies that Ar atoms reflected from the targets will be ionized with high probability, as T_e maintains values above 20eV over a large space-temporal region of the discharge (Fig.6.1.8) and will return to the targets to produce target re-sputtering. (Target re-sputtering: sputtering produced by post-sputtering gas atoms that are ionized again after reflection off the targets).

The target re-sputtering leads to a higher density of ions on the targets, and thus a higher energy imparted to the targets, leading to targets heating.

The observed high electron temperatures also lead to sputtered Fe atoms ionization, also enhanced by the sputtered metal atom trajectories in an angle close to the normal to the targets. The ionization of sputtered metal in regions close to the targets (regions with Te~11eV, at maximum ionization cross-section) leads to intense self-sputtering effects, also with consequences on ion density bombarding the targets and increasing target heating.

The time-scale of the self-sputtering process can be evaluated by observing the moment of formation of the second peak in the T_e distribution, situated at about 1μs from the main peak.

Therefore, the above result allows an interpretation from the point of view of the discharge behaviour and confirms the findings from IES data: a high ionization density in a region close to the targets leads to sputtering, target re-sputtering, self-sputtering and to high ion flux density at the targets and target heating.

There is no precise moment for the beginning of sputtering because of the random arrival of ions at the targets (self sputtering and target re-sputtering). A strong maximum in the occurrence of sputtering can be observed at t~4μs, marked by a strong increase in T_e (~40eV), followed by a secondary peak at t~5μs (T_e~20eV) due to the combined target re-sputtering and self-sputtering effects (Fig.6.1.8). These high T_e peaks are formed due to the increase in the number of high-energy secondary electrons at the respective moments during the pulse.

The secondary T_e peak is a result of the strong increase in sputtering appeared at the first peak, as the large number of reflected Ar atoms and sputtered metal atoms are ionized in a region close to the targets producing target re-sputtering and self-sputtering.

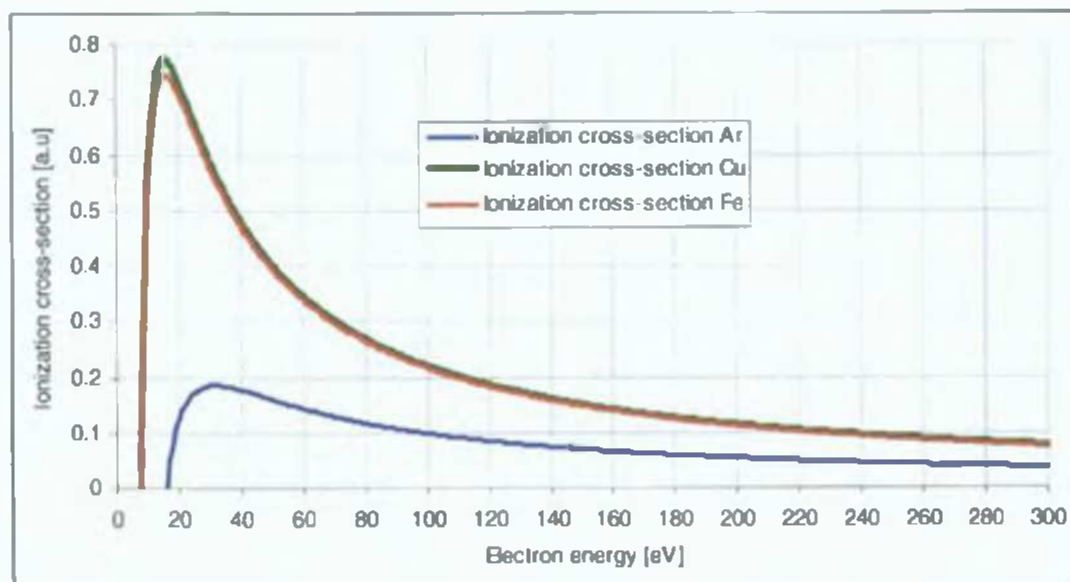

Fig.6.1.10. Relative direct electron impact ionization cross-sections for Ar and Cu and Fe atoms. Evolution with electron energy, using Thomson' formula [Chapter 4.3.1, Ref. 2].

From Fig.6.1.10 we can see that the direct impact ionization cross-section calculated from Thomson's formula has almost similar evolution for Cu and Fe atoms, due to their close ionization potential values (I_{Cu}=7.726eV and I_{Fe} =7.7870eV). The minimum electron temperature T_e that allows Fe ionization is T_e=5.2eV.

The maximum rate of direct electron impact ionization processes for Fe occurs at electron energies of E_e=16eV (T_e~11eV) while at moments between 3μs and 6μs, the electron energies are above 15eV, indicating a very efficient ionization of Fe atoms at regions close to targets. From Fig.6.1.8 we can see that Fe ionization can occur with maximum probability in the regions close to the targets (up to 2cm from the targets at moments during the pulse from t~3μs to t~6μs and the Fe ionization can continue until T_e ~7eV, at t~8μs.

The distribution of Fe I 372nm resonance line indicates the presence of Fe ions in the discharge and their recombination processes extending beyond t~10μs.

So, the study of space and time-resolved T_e for Fe targets can indicate the moments of highest sputtering rate occurrence and the moment of maximum self-sputtering and target re-sputtering processes.

6.1.6 CONCLUSIONS

The work described in this chapter presents a first time observation of electron temperature based on time and space – resolved OES in an opposed target magnetron discharge under pulsed DC operation.

The evaluation of T_e from time-resolved OES lines provides information on the dynamics of electrons directly involved in the excitation and ionization processes during the pulse-on discharge.

The time and space-resolved distribution of T_e provides important information on the evolution of discharge stages, indicating the start moment for the sputtering and self-sputtering processes as well as the most probable regions for the Ar and sputtered metal ionization (time and space-resolved).

The stages of the discharge development are similar for the magnetron configuration with Cu and Fe targets:

-The sputtering process starts at t~3μs and the self-sputtering process at t~5μs;

-The ionization process stops for Ar at t~6μs (T_e <11eV) and for metal at t~10μs (T_e <5eV);

-The second part of the pulse is dominated by self-sputtering.

The observed electron temperature (and energy) are in good agreement with Langmuir probe measurements in planar DC magnetrons [47], with results obtained by both Monte Carlo calculations and Langmuir probe measurements [44] as well as with time and space-resolved Langmuir probe measurements [7] (all giving T_e values in the range from 5eV to 20eV).

The obtained values for T_e are in good agreement with the expected T_e (and electron energy) values and can be used to explain directly the physical processes in the discharge, leading to the conclusion that the accuracy of the method is quite good, allowing its use for current plasma diagnostic in pulsed DC discharges.

Phenomena taking place during the pulse-on time in the pulse-DC magnetron discharge can be clearly identified from both points of view: their physical causes and their temporal development.

The time and space resolved OES data provide information on the production and location of Ar ions and sputtered metal atoms, indicating the moment of start of sputtering. As observed from the time-resolved evaluation of T_e, the start of sputtering is in generally accompanied by an increase (peak) in electron temperature. This peak in T_e cannot be seen in

discharges where the Ar ions are produced with equal probability at all distances from the targets, as in the case of Fe targets.

A second peak in T_e indicates secondary sputtering processes, usually self-sputtering. In the case of Fe targets, the high T_e in a region close to the targets also allows for ionization of back-sputtered material, thus for target re-sputtering.

The voltage decrease after the start of sputtering can be explained through the decrease in the discharge impedance due to an important increase in the electron density through intense sputtering and ionization processes.

The last 4μs of the pulse-on time are characterized by low T_e values and lower Voltage values indicating a lower direct sputtering rate. For the Fe targets, the Voltage values are still above 300V, allowing for self-sputtering effects.

The above physical phenomena and their evolution constitute a model for the discharge behaviour during the pulse-on time. The model is validated by relating the observed ionization and excitation processes to the direct electron impact ionization cross-section at the electron energies given by the evaluated T_e values. A good match of the electron energies required to produce these effects (Ar ionization) and the observed temporal and space distribution of Ar ions indicates the validity of the model.

The information provided by the pulse-on time model of the magnetron discharge can be used in magnetron design and for choosing the operating duty cycle.

6.2. MAGNETRON PLASMA MODEL FOR THE PULSE-OFF TIME

6.2.1. INTRODUCTION

Pulsed DC magnetron deposition improves significantly the physical properties of the deposited layers due to the increased ion bombardment of the substrate [79, 80].

Time and space-resolved Langmuir probe measurements [7, 55] have proven that the plasma potential during the pulse-off time reaches high positive values that can be linked to the ion energy gain during pulsed DC magnetron operation. As the energy distribution of this ion flux has a major influence on the deposited layer properties [55,80], it is important to know and control the relevant discharge parameters.

Although the temporal evolution of the ion flux to substrate has been investigated using time-resolved mass spectrometry [56, 81] the phenomena leading to increased ion energy and flux to the substrate during pulsed DC deposition have not been identified.

The phenomena taking place during the pulse-off time can be understood starting from basic theoretical models of charge-loss phenomena in equilibrium and non-equilibrium plasmas and using time-resolved diagnostic methods that provide information on plasma behaviour during the pulse-off time: the I-V waveforms and the time-resolved statistics of the IES.

In the following analysis I will present the most important experimental data leading to the development of a physical model that explains the increase in the ion flux and energy at the substrate region.

6.2.2. EXPERIMENTS AND DISCUSSION

6.2.2.1 CURRENT AND VOLTAGE WAVEFORMS

Typical Current and Voltage waveforms on the cathodes during a pulsed DC discharge at 50kHz, at 2A current run and 0.4Pa Ar gas pressure are presented for several pulse-off times values (w) in Fig.6.2.1, Fig.6.2.2a, and Fig.6.2.2b. From Fig.6.2.2a and Fig.6.2.2b we can observe the voltage and current behaviour only during the pulse-off time.

During the pulse-on time the voltage on the cathodes has negative values reaching –1200V. During the pulse-off time, the voltage has large oscillations between positive and negative values, reaching ±300V, especially for short pulse-off times. These voltage oscillations during the pulse-off time settle at a value of about 25V for pulse-off times longer than 4016ns.

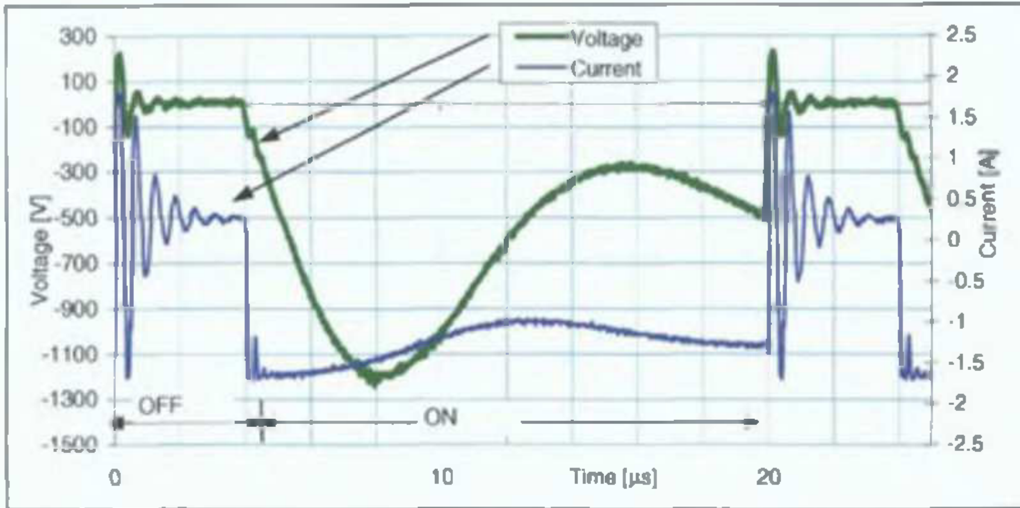

Fig.6.2.1 Typical Voltage and Current waveforms at the targets at Ar gas pressure of 0.4Pa, and a pulsed DC operation at 2A, 50Khz, and 4016ns pulse-off time.

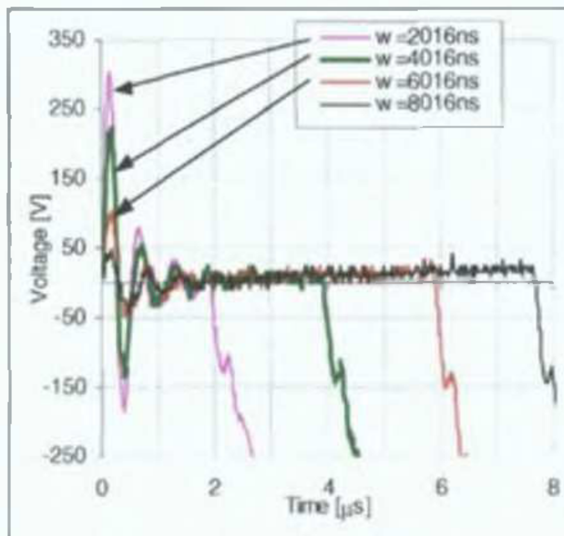

Fig.6.2.2a: Voltage waveforms during the pulse-off time.

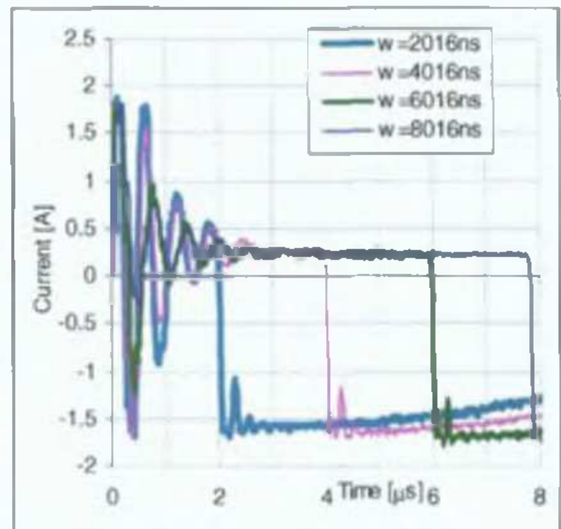

Fig.6.2.2b: Current waveforms during the pulse-off time.

The current waveforms also have large oscillations up to ±1.8A during the pulse-off time and settle at a value of 0.2A for pulse-off times larger than 4016ns. While during the pulse-on time the current is negative, consisting mainly of positive ions, the positive current on the cathodes during the pulse-off time is obviously due to the electron current drawn towards the cathodes.

The pulse-off time negative current spikes cannot be attributed to an ion current, as the slow ions will not be able to follow the fast voltage oscillations at the cathodes, over time intervals of 100-250ns (Fig.6.2.1, Fig.6.2.2a).

During pulsed DC operation in constant current mode, the power supply behaves like a large inductor [82] and the output voltage turns positive at the beginning of the pulse-off time. The high positive potential on the targets at the beginning of the pulse-off time leads to electron extraction from the plasma and a large electron current (up to 1.8A) - observed as a positive current - can be measured at the targets during the first 250ns of the pulse-off time (Fig.6.2.2b). This electron current drawn to the targets and through the power supply's large inductance

creates a negative supply output voltage - therefore a negative potential on the targets - causing the excess electrons to go back into the positive plasma (thus, a negative current at the targets).

This "oscillation" process repeats itself until the negative charge unbalance in the power supply-discharge circuit is spent through electron loss processes (mainly resistive losses). We can observe how the amplitude of the Current and Voltage "overshoots" decreases in time.

6.2.2.2. THE ION ENERGY SPECTRA (IES)

The IES for Ar and Cu ions measured at a distance D=10cm from the targets edge (Fig.5.4.1) for DC and pulsed DC operation are presented for several values of the pulse-off time (w) in Fig.6.2.3 and Fig.6.2.4.

During DC operation, the Cu ion spectrum has an energy distribution typical to the actual energy distribution of the metal atoms from the sputtering process. Similar energy distributions were obtained from simulations using the ACAT code for DC sputtering of Cu in Ar at 0.4Pa [21].

The Ar ions spectrum during DC operation has a peak at about 0.5eV and a higher energy tail in the same energy range as the Cu ions, most probably due to collisions between the gas atoms (ions) and the sputtered metal atoms (ions). The low energy peak represents the most probable energy of the Ar ions in the discharge bulk. During pulsed DC operation the Ar and Cu ion spectra have a similar, wide energy distribution, with a peak at 40eV for pulse-off times longer than 4016ns. This indicates that both Ar and Cu ions are gaining energy in the same type of electric field during the pulse-off time.

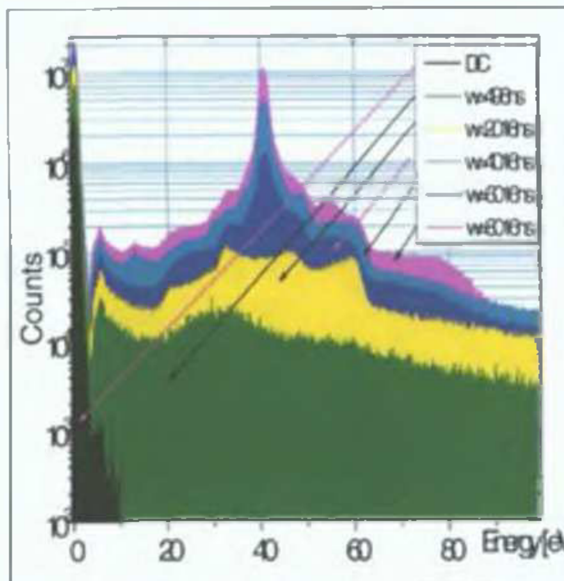

Fig.6.2.3: Ar ion energy spectra at 50kHz, I=2A, p=3mtorr, for different pulse-off time values.

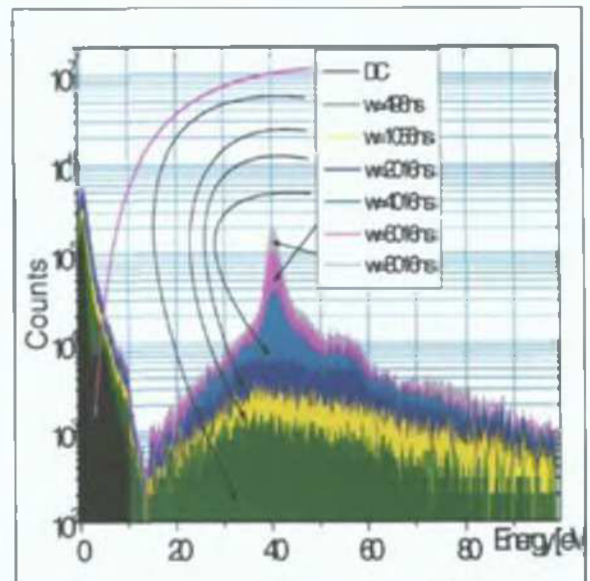

Fig.6.2.4: Cu ion energy spectra at f=50kHZ, I=2A, pAr=3mtorr, for different pulse-off time (w) values.

6.2.2.3. THE SPACE-RESOLVED ION ENERGY SPECTRA (IES)

The changes in the IES observed as a function of the distance D between the targets edge and the probe have been presented in Chapter 5.4.5 and are shown here again to enable the analysis.

The maximum IES energy value in Fig.6.2.5 and Fig.6.2.6 decreases with probe distance to the targets, due to the plasma potential (Vp) values that are decreasing with distance from the targets. The step-like edges in the energy distribution can be linked to the oscillations of the plasma potential during the pulse-off time.

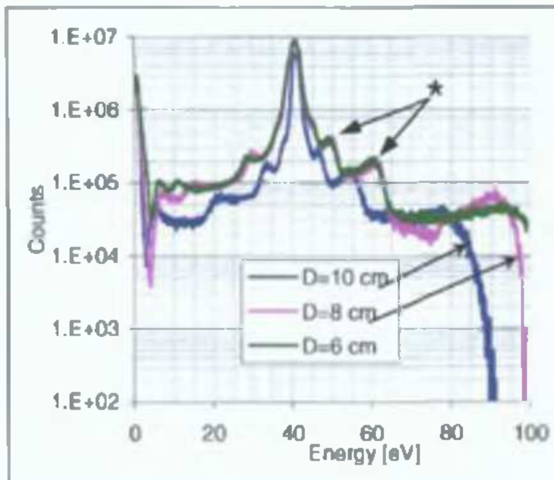

Fig.6.2.5: Ar IES as a function of the distance D of the probe from targets edge, for distances larger than 5cm. The (*) arrows indicate the "step-like" edges in the ion energy distribution.

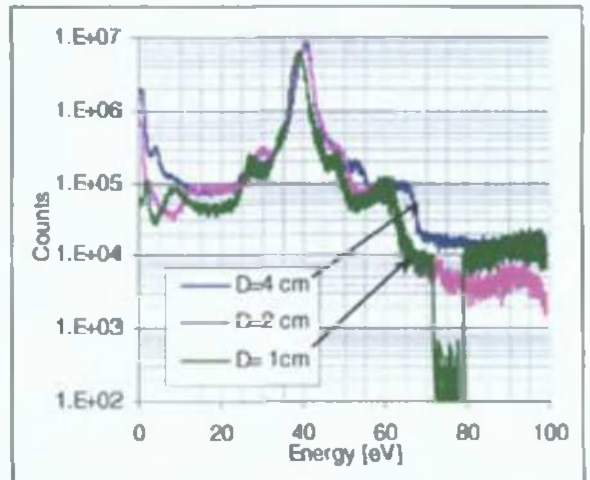

Fig.6.2.6: Ar IES as a function of the distance D of the probe from targets edge, for distances smaller than 5cm.

6.2.3 PHYSICAL MODEL FOR THE PULSE-OFF TIME ION FLUX AND ENERGY GAIN

6.2.3.1. THE PULSE-OFF TIME CHARGE DENSITY GRADIENTS

Due to the high positive potential on the cathodes at the start of the pulse-off time, a large electron current (up to 1.8A) is extracted from the plasma bulk. The equilibrium cannot be quickly re-established by ions' movement outside the bulk (due to the slow ion motion), so a negative charge density gradient (lack of electrons) and a positive charge density gradient (excess of ions) will be created at the plasma bulk region, along with a charge gradient.

Space and time-resolved Langmuir probe measurements in a planar magnetron [7, 8] show that the electron density has a sharp fall (by 60%) at the beginning of the pulse-off time (first 500ns), then it recovers (at 1μs) and is followed by a slow decrease with a time constant of the order of 40μs - this behaviour being observed at distances from 1mm, up to about 100mm away from the target, at the substrate (probe) position.

Assuming that the above electron density evolution is typical for all pulsed magnetron discharges, the phenomena leading to the observed behaviour will be examined next.

The strong decrease in electron density at the beginning of the pulse-off times at all regions in the discharge can be explained by electron re-distribution in order to compensate the negative charge density gradient created in the plasma bulk while the targets are at positive potential.

PIC-Monte Carlo simulations of a pulsed glow discharge [83] show that the electron re-distribution takes place by electron diffusion on a time scale of 4ns; while the plasma decay time-scale is reflecting the ion motion, being of the order of 4μs. As electron behaviour during pulse-off time is similar to non-magnetized electron dynamics [8, 56], similar electron redistribution times apply for magnetized discharges.

Therefore, the negative charge density gradient created inside the bulk at the beginning of the pulse-off time is fast compensated by electron diffusion from regions outside the bulk. This leads to overall electron redistribution and the strong fall in electron density at all regions (observed during the first ~500ns of the pulse-off time [7]).

While the targets are at negative potential, the electron density gradually recovers to its pulse-on time value, due to the electron current provided through the power supply (during several negative Current-Voltage oscillations). Thus, at the end of the first microsecond, the bulk charge quasi-neutrality is re-established and the electron density reaches again high values at all regions.

After the negative charge gradient has been compensated, the electron density has high values at all regions and the bulk has reached charge neutrality, only the positive charge density gradient (excess of ions in the bulk compared to outside the bulk) is still uncompensated. The electric field created by the positive charge density gradient leads the ions to drift outside the bulk, while the excess electrons are lost at the targets. This leads to a slow, continuous loss of electrons from the regions situated at the bulk boundary, generated and maintained by the positive charge density gradient. The electrons outside the bulk will re-establish (redistribution by diffusion) the overall plasma quasi-neutrality at every moment, leading to an overall slow decrease in electron density.

The ion drift continues, until the positive charge density gradient at the bulk boundary is compensated and the excess electrons in the bulk are lost at the targets through resistive losses.

The ion drift outside the bulk and the electron loss at the bulk establish an ambipolar flow of particles with a speed dictated by the ion average speed. The term ambipolar flow is used here to replace the misnomer "ambipolar diffusion" [45] in the sense of equal loss rates of ions and electrons from the bulk (ions leave the bulk and electrons are lost at the targets).

The observed (Fig.6.2.1, Fig.6.2.2a, b) Current and Voltage oscillations at the targets allow the plasma to reach quasi-neutrality (n_i~n_e) towards a lower density, as electrons are lost at the targets through resistive losses, while the ions leave the bulk. The ambipolar flow process restores plasma quasi-neutrality, but not to the original plasma density [6].

The above considerations indicate an overall (bulk and outside bulk) decrease in electron density during the pulse-off time, taking place in two steps:

- a sudden, marked decrease due to the formation of negative charge density gradients and overall electron re-distribution, dictated by the time-scale of electron motion (tens – hundreds of ns);
- a slow decrease given by the rate of the ambipolar flow, over a time-scale dictated by the ion average speed and compensation of positive charge density gradients leading to plasma equilibrium (several μs).

6.2.3.2. THE PLASMA-PROBE SHEATH MODEL

The space-resolved IES (Fig.6.2.5, Fig.6.2.6) clearly indicate that pulse-off time ions are accelerated in a sheath that moves along with the probe: the energy values increase as the probe is closer to the targets, due to higher plasma potential values. Obviously, if this sheath would be at the targets region, its position would be fixed, so ion energy (and the IES) would be independent of the EQP probe position.

The increase in ion energy during pulsed DC operation has been attributed before to the formation of a sheath at the substrate (or EQP probe) region [56, 78, 79].

The initial plasma-probe sheath is the "Debye-length" sheath created at the "contact" between the plasma and the grounded probe and this space does not contain electrons [4]. Due to the sudden decrease of electron density and sharp increase in electron temperature at the probe region at the beginning of the pulse-off time [7], the length of the contact sheath will increase, as the Debye length is proportional to the square root of electron temperature to density ratio:

$$\lambda_D = \sqrt{\frac{kT_e}{4\pi e^2 n_e}} \qquad (6.2.1)$$

where: k is Boltzmann's constant, e the electron charge, T_e the electron temperature and n_e the electron density at the probe (substrate) region.

Considering a decrease in electron density by ~60% [7] at the start of the pulse-off time, λ_D will be ~1.6 times larger at constant T_e. As the electron temperature at the beginning of the pulse-off time at the probe region has been reported to increase up to twice the pulse-on time value [7], the extent of the plasma-probe sheath can be enhanced up to about 3 times the value at the beginning of the pulse-off time.

The positive plasma potential values across the plasma-probe sheath will prevent electrons leaking towards the grounded probe, thus preventing (along with the decrease in electron density) the sheath's contraction. Only during a short time interval the sheath will stop its expansion (and may even contract shortly), due to the sudden increase in electron density at all regions when the negative charge gradient is compensated.

After the sudden increase and sudden stop in its expansion, the sheath will continue to expand at a slower rate, corresponding to the decrease rate of electron density dictated by the ambipolar flow. During this time, the electron temperature has slowly decreasing values that can be considered constant: so, the decrease in electron density is the main factor in the sheath expansion.

From the I-V waveforms, we can estimate that the plasma reaches equilibrium after 4μs, once the current and voltage oscillations at the targets are extinct. This will mark the end of the ambipolar flow process and the moment when the plasma-probe sheath expansion stops.
The ions that have left the bulk just before this moment will continue to move (inertia) towards the probe.

Considering the ion average speed ~1500m/s, with a ±500m/s spread in the distribution (an average energy of 0.5eV±0.25eV in the bulk) the ions need ~65±20μs to cross the 10cm distance to the probe. So, only a small decrease in the ion flux density due to the end of the diffusion process will be observed at the probe region, as a new "wave" of ions will start their diffusion towards the probe every 20μs. Therefore, the ion flux density values at the probe region are practically constant and independent of the pulse-off time.

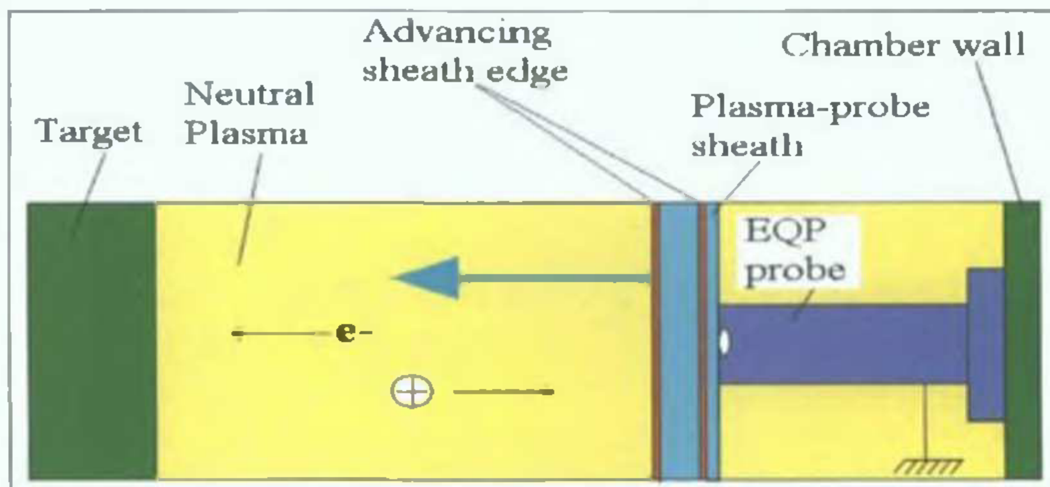

Fig.6.2.7. Schematics of the plasma-probe sheath model. Cross-section view of discharge chamber in plane XOY.

The average expansion speed of the sheath is dictated by the ambipolar flow and thus by the ion average speed. For an ion average energy of 0.5eV (average speed ~1500m/s) and a duration of the expansion process of ~3μs, the extent of the plasma-probe sheath resulted from ambipolar flow can be approximated to about 4.5mm.

From the Debye length formula, the 4.5mm extent corresponds to a decrease in electron density of about one order of magnitude during the ambipolar flow process.
So, the formation and expansion of the plasma-probe sheath is due to the expansion of the Debye-length contact sheath at the probe, controlled by the evolution of plasma parameters (n_e, T_e) during the pulse-off time at the probe region.

The plasma-probe sheath expansion has a three-step evolution:

- a sudden expansion in the first ~500ns, due to the sudden decrease of electron density and a sharp rise in the electron temperature at the beginning of the pulse-off time;

-a sudden slow-down and stop of the expansion due to an increase in the electron density at all regions (at about 1μs);

- a slow expansion for ~3μs (starting at ~1μs and ending at ~4μs) due to the slow decrease in electron density dictated mainly by the ambipolar flow.

Once the overall plasma has reached neutrality (at a lower plasma density), the expansion of the sheath stops and the sheath width remains constant until the end of the pulse-off time.

Therefore, during most of the pulse-off time, the plasma-probe sheath will not contract - like the cathode sheath during pulse-off time - as there are less electrons available to restore the plasma density in the plasma-probe sheath and the positive potential on the sheath prevents the electrons to leak to the grounded probe.

Explaining the plasma behaviour during pulse-off time through diffusion of charges is justified here, as this is the main charge-loss mechanism for the regions outside the bulk.

Other charge-loss mechanisms like recombination, although neglected in this basic model, appear as a consequence in our further analysis.

I have to emphasize that in the above considerations for the formation of the plasma-probe sheath, the presence of an electric field over the neutral plasma is not accounted for, or assumed, at any moment. The electric fields leading to electron diffusion (and ion drift) are plasma generated fields due to charge density gradients and are a direct consequence of plasma non-neutrality in the respective regions.

The above analysis is in good agreement with Franklin [45] who has shown that for magnetized discharges, the ions movement is mainly due to drift (generated by local ambipolar electric fields) and the electron movement is mainly a diffusion process.

6.2.3.3. THE PLASMA-PROBE SHEATH BEHAVIOUR AND THE IES

Measurements of the temporal evolution of the plasma potential during the pulse-off time indicate that at distances of 10cm from the targets this potential follows closely the voltage oscillations at the cathodes, with smaller, but positive values [57].

So, at the beginning of the pulse-off time, the plasma potential at the probe (substrate) region will be more positive than the probe (at ground level) and the ions will be accelerated over the plasma-probe sheath.

After a large electron current has been drawn to the cathodes (first 250ns, Fig.3) the electron density at the probe region has a sudden decrease (while the electron temperature rises) and as a result, the edge of the plasma-probe sheath will move away from the probe creating a larger plasma-probe sheath (Fig.6.2.7). This leads to an increase in the measured ion current at the probe (Fig.6.2.3, Fig.6.2.4). The resulting IES (Fig.6.2.3, Fig.6.2.4 at w=496ns) are

distributed over a wide energy range (0eV up to above 100eV) as the plasma potential values are large.

The fast expansion of the plasma-probe sheath stops when the electron density recovers to high values at ~1µs; then, it continues to expand slowly as long as there is an uncompensated positive charge density gradient leading to ambipolar flow.

After 4µs (as shown by the I-V waveforms) the plasma reaches equilibrium and the voltage and current oscillations at the cathodes are extinguished (Fig.6.2.1). The potential on the cathodes settles at a value of about 25V but the plasma potential will have a higher value. We can identify this value as 40V from the shape of the ion energy distributions we measure (Fig.6.2.3, Fig.6.2.4). The ions continue to arrive at the sheath edge and are accelerated, but their most probable energy is 40eV, resulting in a high 40eV peak in the energy distribution.

The temporal behaviour of the plasma-probe sheath expansion explains the increase in the ion flux at the probe, while the shape of the IES are given by the convolution of the plasma potential values on the sheath edge and the temporal evolution of its extent.

6.2.4. VALIDATION OF THE MODEL

6.2.4.1. FROM THE SPACE –RESOLVED IES

The geometry of the opposed target magnetron does not allow for direct measurement of the plasma potential (Vp) in the bulk.

It was shown [7, 57] that pulse-on time Vp values are generally small, (a few Volts) and decrease significantly with the distance from the targets, reaching Vp ≈ 1V at D=10cm from the targets for a planar magnetron discharge. Assuming the same behaviour in our magnetron, at the EQP probe position (situated at D=10 cm from the targets edge) the plasma potential during the pulse-on time can be considered close to zero. As the exterior plate of the EQP probe is in direct contact with the chamber's wall and set to ground, there is practically no potential difference between the probe and the plasma potential. Thus, the ions are not accelerated across the contact sheath at the plasma – probe boundary. This is essential as an energy calibration for any IES measurement.

Measuring the ion energy distribution at closer distances to the targets actually perturbs the measurement, as there will be a larger Vp over the sheath at the plasma-probe boundary. We can observe this in our data from the IES analysis with distance (Fig.6.2.5 and Fig.6.2.6) where the energy distribution during the pulse-on time (the low energy peak) changes its shape.

At small distances between the probe and the targets, the low energy peak loses intensity towards other energies as the plasma potential on the plasma-probe sheath edge has values above zero. The high-energy edge of the IES is also perturbed. As the probe is closer to the targets, the high-energy limit shifts towards higher values: 90eV at D=10cm, 98eV at D=8cm, and above 100eV for D<8cm. This corresponds to an increase in Vp in regions closer to the targets, during the pulse-off time.

The change in the maximum energy values with distance indicate that the sheath is situated at the probe and follows its position, the potential on the plasma-probe sheath changing according to the plasma potential values at the respective probe position. A similar situation occurs when the EQP probe is replaced by a grounded substrate.

The fact that the 40eV ion peak height (Fig.6.2.5 and Fig. 6.2.6) does not change significantly with the distance from the targets proves that the number of ions collected depends mainly on the plasma-probe sheath volume (that is achieved after the plasma bulk has reached equilibrium).

The formation of the 40eV peak for w>4016ns and the fact that its 40eV energy value does not depend on the axial distance D are proofs that this peak is due to the plasma potential (Vp~40V) values attained after the plasma has reached equilibrium (for w>4016ns).

6.2.4.2. FROM THE IES STATISTICS

The total ion number, flux and flux rate is calculated by integration over the measured IES as explained in Chapter 3.4.

The pulse-on spectra were considered below 3.5eV for Ar ions, respectively below 11.5eV for Cu ions; and the pulse-off spectra above these.

As the Cu ion density is about 100 times lower than that of Ar ions and it depends strongly on the sputtering process, the Cu ions are not included in the analysis of the ion flux and flux rate.

The number of ions collected during the pulse-on time decreases slightly with increasing the pulse-off time, as expected; while the number of ions collected during the pulse-off time has a strong increase with the pulse-off time (Fig.6.2.8). A similar behaviour is observed for both Cu and Ar ions. For pulse-off times longer than 4000ns, the ion number is increasing almost linearly with the pulse-off time – a proof that at 4000ns the plasma-probe sheath is formed and has a stable volume.

We can notice that the ion flux is constant with the duration of the pulse-on time, indicating a constant ion flux at the plasma-probe sheath edge (Fig.6.2.9) during the pulse-on time. This proves that the plasma-probe sheath during the pulse-on time has a constant extent that is not influenced by the duration of the pulse-on time (i.e. it is independent of the duration of collection time). Also, the ion flux density at the probe region is independent of the pulse-off time duration.

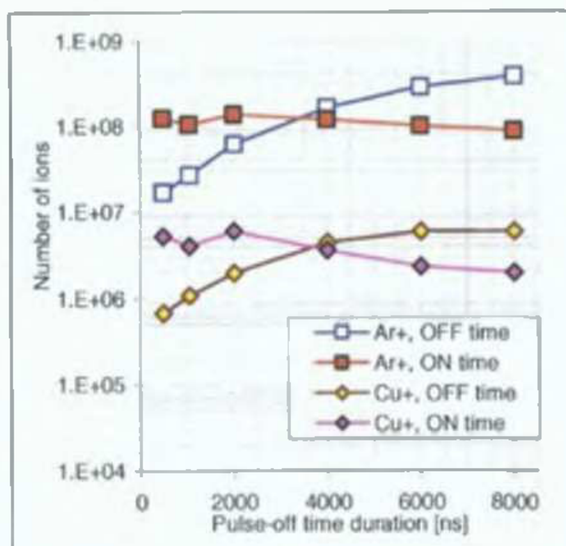

Fig.6.2.8: The number of Ar and Cu ions collected by the energy analyser probe during the pulse-on time and during the pulse-off time, as a function of the pulse-off time.

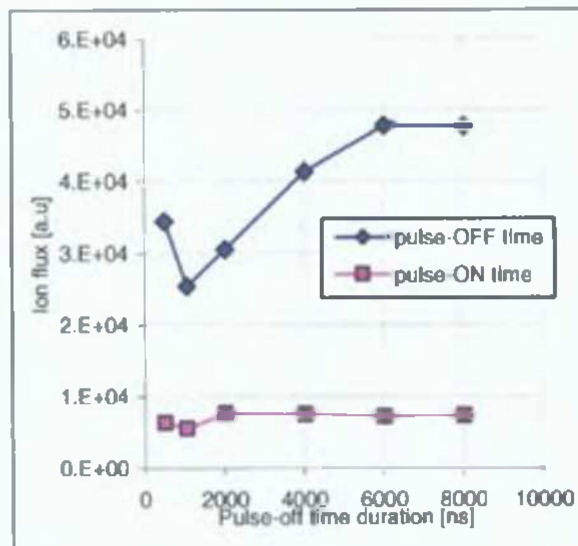

Fig.6.2.9: The Ar ion flux [Number of ions/collection time] collected by the probe during the pulse-on time and during pulse-off time as a function of the pulse-off time.

At the beginning of the pulse-off time, due to the sudden expansion of the plasma-probe sheath and the positive Vp across the sheath, the ion flux at the probe is 3 times higher than the one during the pulse-on time. This is in good agreement with the 3–fold expansion of the plasma-probe sheath evaluated in Section 6.2.3.2.

While the plasma–probe sheath expands slowly (during the next 4000ns) the ion flux doubles, and then it stays constant, at the highest value, during the last 2000ns. This shows that after the sheath has reached full extent it remains constant for another 2000ns. The plasma-probe sheath is still present at 8000ns, about 4000ns after the oscillations of the potential on the cathodes have reached a stable value.

6.2.4.3. THE ION FLUX RATE ANALYSIS

The ion flux rate values during the pulse-off time are calculated as the variation in ion flux values between consecutive pulse-off time durations, divided by the difference between these durations. This analysis is based on the assumption that for all pulse-off times the phenomena governing the ion transit and the plasma behaviour are similar. Again, the obtained values are only cumulative values over the measuring dwell time of the EQP analyser, and not real-time absolute values.

Considering the situation during the pulse-off time, the number of ions dN that are collected by the probe during the time interval dt is:

$$dN = \Gamma_i \cdot V \cdot dt \qquad (6.2.2)$$

where Γ_i [ions.s^{-1}cm^{-3}] is the ion flux density at the plasma-probe sheath edge and V is the plasma-probe sheath volume. The ion flux at the probe in dt is:

$$dN / dt = \Gamma_i \cdot V \qquad (6.2.3)$$

The ion flux rate of change with time is:

$$d^2N/dt^2 = d/dt(\Gamma_i \cdot V) \qquad (6.2.4)$$

and can be developed as:

$$\frac{d^2N}{dt^2} = \Gamma_i\frac{dV}{dt} + V\frac{d\Gamma_i}{dt}; \qquad (6.2.5)$$

So, when the ion flux density Γ_i at the sheath edge is constant ($\frac{d\Gamma_i}{dt} = 0$) the ion flux rate at the probe depends only on the change in the volume of the sheath; and when the volume V is constant ($\frac{dV}{dt} = 0$) the ion flux rate only depends on the change in Γ_i.

Representing the ion flux rate of change d^2N/dt^2 as a function of the pulse-off time, a strong maximum followed by a constant region can be observed (Fig.6.2.10).

During the first 250ns the sudden decrease in electron density accompanied by a strong increase in electron temperature leads to a fast expansion of the plasma-probe sheath. As a result, a sharp increase in the ion flux rate appears at the beginning of the pulse-off time (or for short off times) while Γ_i at the sheath edge stays constant and the sheath volume increases suddenly. Between ~250ns and ~800ns, a slow-down and even stop of the expansion of the plasma-probe sheath is observed as a sharp fall in the ion flux rate (Fig.6.2.10).

We can notice that the flux rate indicates a stop of the sheath expansion at ~1000ns (when the plasma bulk reaches neutrality) proving that our data and analysis are in good agreement with the experimental results obtained by Bradley et al. [7].

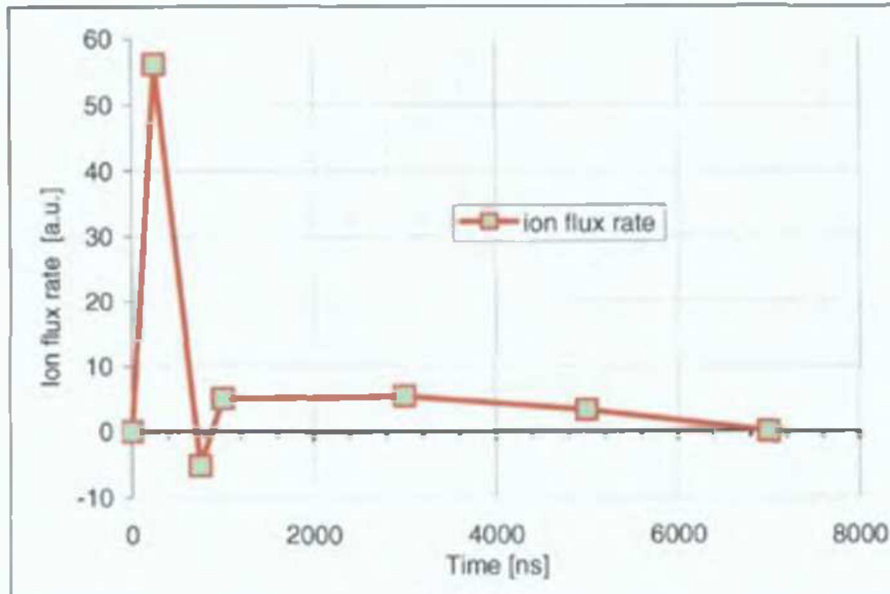

Fig.6.2.10: Typical ion flux rate variation during the pulse-off time, calculated as d^2N/dt^2 (the variation of the ion flux (dN/dt) between two consecutive values of the pulse-off time).

Once the ambipolar flow dominates and the decrease rate of the electron density is quasi-constant being controlled by the decrease in the ion density in the bulk, the ion flux rate at the probe is dominated by the slow expansion rate of the sheath (*dV/dt* term). The sheath expansion speed will equal the average speed of the ions leaving the bulk. A steady increase in the measured ion flux (Fig.6.2.9) and a positive, almost constant ion flux rate (Fig.6.2.10) can be observed at this stage.

The constant ion flux rate between 1000ns and 4000ns indicates a constant expansion speed of the plasma-probe sheath.

Beyond 4000ns, after the plasma has reached neutrality and the sheath expansion has stopped ($dV/dt=0$), the ion flux rate at the probe only depends on the change in the ion flux density with time. Here, d^2N/dt^2 is dominated by the second term in equation (5). The ion flux rate at the probe slowly decreases (in Fig.6.2.10, above 4000ns) as Γ_i at the sheath edge decreases, probably, mainly due to recombination processes.

In conclusion, the information given by the analysis of the ion flux rate during pulse-off time confirms the proposed plasma-probe sheath model and its temporal evolution.

6.2.5. CONCLUSIONS

A model for the phenomena leading to the increase in the ion flux and energy during the pulse-off time at the substrate region of a pulsed DC magnetron discharge has been presented and validated using measurements of the IES at the substrate region and the I and V waveforms at the cathodes.

This model enables a control over the pulsed DC discharge parameters in order to obtain the desired ion flux level and to evaluate the ion energy distribution only from basic knowledge of the I-V waveforms. The proposed model is based on the formation and expansion of a plasma-probe (or respectively, a plasma-substrate) sheath, due to the positive plasma potential Vp values and changes in the plasma parameters (electron density and temperature) in the pulse-off time plasma.

A "contact" sheath of small (Debye length) thickness is always present at the plasma-probe boundary. During the pulse-off time, a potential difference is created across this sheath, between the plasma potential (at the probe location) and the probe (at ground) while the sheath expands. The ions are accelerated in this sheath at high energies corresponding to the (oscillating) plasma potential values at the sheath edge.

The expansion of the plasma-probe sheath is due to the two-step decrease in electron density during the pulse-off time. As the plasma-probe sheath expands, a higher number of ions will be accelerated towards the probe with different energies depending on their position in this sheath and the plasma potential values.

According to the model, the Debye-length of the plasma-probe sheath will first expand due to a sudden overall drop in electron density and rise in electron temperature that characterize the plasma at the beginning of the pulse-off time. The sudden drop in electron density at the substrate region is initiated by the bulk plasma negative charge density gradient and enabled by the fast electron dynamics.

The expansion slows down and stops at around 1μs, when the electron density reaches uniform distribution over the plasma and the bulk reaches charge neutrality.

After ~1μs, the sheath will continue to expand slowly due to an ambipolar flow (ion drift outside the bulk and electron loss at the bulk at the same rate), until the positive charge density gradient is compensated, leading to a stop in expansion after 4μs. The expansion speed of the sheath is given here by the speed of the ambipolar flow, which is dictated by the ion average speed. After 4μs, the plasma-probe sheath extent stays constant until the end of the pulse-off time. The plasma-probe sheath is rapidly compensated and disappears at the beginning of the following pulse-on time.

The formation of the plasma-probe sheath and its behaviour during the pulse-off time explains the ion flux and energy gain as well as the observed IES at the substrate region. The validation of the model is given by space-resolved IES experimental data and the analysis of ion number, flux and flux rate evolution with the pulse-off time.

Although the model is initially explained through the evolution of plasma parameters like T_e and n_e that have not been directly measured in this experiment, the fact that our IES experimental data match closely the proposed model proves that the model can be generalized to all pulsed DC discharges. The above analysis in terms of charge-loss phenomena is justified, as these are governing the plasma behaviour during pulse-off time.

The time intervals chosen for the IES measurements presented in this paper allow the observation of the general trend of the plasma-probe formation and behaviour during pulsed DC sputtering and provide a good validation for the proposed model.

The analysis of ion flux evolution at the substrate region for different values of the pulse-off time indicates the optimum pulse-off time values that provide the maximum number of ions at the substrate. This pulse-off time value should be close to the time needed by the plasma to reach equilibrium (4μs in our case) coinciding to the moment when the plasma-probe sheath reaches a maximum extent. The pulse-off time value can be easily determined from the I-V waveforms that provide in this case, a direct result for such plasma diagnostic problems.

The results presented in this chapter have been included in a recent paper [84].

CHAPTER 7:

FINAL CONCLUSIONS

This chapter presents a summary of the work performed and the most important results.
A few important issues for pulsed DC magnetron operation and design are discussed as direct consequences of the proposed time-resolved plasma physical models and diagnostic results.

7.1. SUMMARY OF THE WORK

The work described in this thesis aims at providing a global understanding of the major processes taking place during pulsed DC magnetron sputtering and the links between the main macroscopic parameters of the discharge (gas pressure, pulsed target bias) the inner magnetron design (discharge geometry and magnetic confinement) and the plasma parameters characterizing its dynamics. Identifying these links would allow the design of a magnetron with the required performances as well as the correct choice of discharge parameters to obtain the desired quality of the films.

In this work, all fields of plasma physics (theoretical, computational and experimental/diagnostic methods) have been approached and employed to various degrees of depth in order to infer a complete, time-resolved physical model of the sputtering process:

-a time-dependent physical model of the pulse-on time, indicating the temporal evolution of the electron kinetics, based on time and space-resolved OES electron temperature determinations (Chapter 6.1);

-a time-dependent physical model of the pulse-off time, providing a physical model and explanation for the increase in ion flux and energy at the substrate region, based on time-resolved ion energy spectra analysis and charge-loss phenomena (Chapter 6.2);

- a physical model of the sputtering process by Monte Carlo simulations of ion transit times in the discharge (Chapter 2.2).

As the temporal analysis of pulsed DC discharges required the use of time-resolved plasma diagnostic methods, several time-dependent diagnostic methods have been designed and used to characterize the pulsed DC plasma:

- the I and V waveforms combined with time-resolved OES ion lines provide information on the average travel time to targets of ions, defining the time-scale for the sputtering process (Chapter 5.1);
- the determination of time-resolved electron temperatures using an acousto-optic spectrometer has been tested and used for a mapping of the electron temperatures through-out the discharge space during the pulse-on time (Chapter 5.3);
- the time-resolved analysis of time averaged ion energy spectra at the substrate region linked with information on the electron density leads to a simple physical model of phenomena responsible for the increase in ion flux and energy at the substrate during pulsed DC discharges (Chapter 5.4).

Each chapter (Chapter 5 and Chapter 6) presents the experimental (or computational) method, the results and a detailed discussion on the observed phenomena with indication on the use of the designed diagnostic method and guidelines for the choice of pulsed DC duty cycle for obtaining a stable discharge or certain sputter effects.

The description of the opposed target magnetron construction and insulating shields as well as the associated measuring equipment are presented in Chapter 2. The "current sheet" method to calculate the magnetic field, the developed algorithm and the actual distribution of the magnetic field are presented in Chapter 3. In Chapter 4, a short theoretical basis for the plasma physics concepts and methods is provided as a background for the examination of experimental work validity under different plasma conditions (pulse-on, respectively pulse-off time).

7.2. SUMMARY OF THE EXPERIMENTAL RESULTS

7.2.1. The IV characteristics and the Current and Voltage waveforms are a direct indicator of the temporal evolution of the power delivered to the discharge as well as of phenomena taking place in the plasma during the pulse-on and pulse–off time.

The behaviour of the I-V characteristics indicate that this type of rectangular, opposed target geometry allows magnetron operation at high currents without an increase in the applied voltage, ensuring a stable discharge for currents from 1A up to 6A and working gas (Ar) at pressures from 1mtorr up to 5mtorr, for target power density in the range 1.5W/cm^2 – 10W/cm^2.

The I-V characteristics and Current and Voltage waveforms have almost identical trends for the Cu and Fe targets and are strongly affected by changes in the gas pressure, but practically independent of the current run. The Current waveforms are independent of gas pressure. Both Current and Voltage waveforms are strongly affected by the duration of pulse-off time.

The Current and Voltage waveforms are equivalent to a time-resolved measurement of the IV characteristics indicating:

-the moment of "breakdown" during each pulse (maximum of the voltage waveform, when the discharge conduction level turns from that of an insulator to that of a conductor);

-the moment when the plasma density has the highest level (minimum in the voltage waveform);

-the pulse-off time oscillations of the voltage give an estimation of the temporal evolution of the plasma potential during the off time;

-the moment when the Current and Voltage oscillations are extinct (at around 4μs after the start of the pulse-off time) indicate the moment when the plasma bulk has reached quasi-neutrality.

This time-resolved diagnostic method -although under-estimated- is extremely useful on its own and in connection to other time-resolved diagnostic methods as a base for building physical models of pulsed sputtering discharges.

7.2.2. Time-resolved OES data provide information on the ionization density distribution. The region and moment where the ions are created plays an important role in the time-scale of the sputtering process. For the Ar-Cu discharge, the maximum ionization density is situated in the central regions of the discharge, while for the Ar-Fe discharge, it is situated in a region close to the targets.

7.2.3. Time-and space-resolved electron temperatures have been evaluated for both Cu and Fe target configuration.

In both cases, the time-resolved Te values follow closely the Voltage waveform evolution during the pulse-on time with maximum values of about 20eV (at t~2.5μs) for the Ar-Cu discharge and 40eV (at t~4.5μs) for the Ar-Fe discharge.

The evaluation of T_e from space and time-resolved OES lines provides information on the dynamics of electrons directly involved in the excitation and ionization processes during the pulse-on discharge and the evolution of discharge stages.

A pulse-on time model of the Cu discharge and sputtering process has been inferred, having the following stages:

a) Start of sputtering marked by a high spike in T_e (~20eV) at t~2.5μs and E_e~30eV (a maximum in the ionization cross-section for Ar);

b) Start of "breakdown" due to start of high-rate ionization processes (both gas and metal atoms are ionized) and decrease in the discharge impedance, the power peak at t~4μs and a decrease in E_e;

c) Start of self-sputtering marked by a second peak in T_e at t~5μs: Te>8eV (Ee>12eV) allow this process at maximum cross-section for Cu ionization;

d) Ar ion peak fall at t~6μs (T_e <11eV and E_e<16eV. Ar ionization is no longer possible in one-step processes);

e) Decrease in ionization and sputtering efficiency;

f) Final increase in the discharge impedance.

Cu ion production takes place in the time region from t~3μs to t~10μs and in space regions closer to the targets that allow the apparition of self-sputtering. The Ar ions are produced only in higher T_e regions closer to the centre of the discharge and need in average about ~2.5μs to reach the targets defining this as the time-scale for the sputtering process.

For Fe targets, the electron temperature has higher values than those obtained for the Cu targets configuration, leading to a different space-temporal distribution for the Ar ions, with consequences on the discharge behaviour. The observed higher Te values in the regions close to the targets lead to sputtering, target re-sputtering, self-sputtering, high ion flux density at the targets and target heating.

A strong maximum in Te (~40eV) can be observed at t~4μs, followed by a secondary peak at t~5μs (Te~20eV) due to the combined target re-sputtering and self-sputtering effects.

The stages of the discharge and the pulse-on time model for the discharge with Fe targets has been identified as follows:

a) The start of intense one-step direct impact Ar ionization at t~3μs (T_e>11eV).

   The start of sputtering does not have a clearly defined moment, as the return time to targets is random, with large deviations from the average. Therefore, the "beginning of sputtering" cannot be observed in a similar way as for the Cu targets.

b) From the Fe I distribution we can see that new sputtered Fe starts to be created at t~4μs, mainly be direct sputtering. Also at t~4μs, a maximum in T_e~40eV, at a region situated at D=2cm from the targets is achieved. At this moment, a maximum in the sputtering process takes place mainly as a result of direct sputtering. This maximum coincides with the Voltage maximum at t~4μs. The Voltage starts to decrease slowly after t~4μs, due to the decrease in the discharge impedance caused by the intense ionization processes.

c) A second peak in T_e at t~5μs (T_e~20eV) can be observed. This peak is mainly due to the convolution of the voltage values at this moment and the rate of self-sputtering and target re-sputtering processes.

d) The maximum in the Ar ionization occurs at t=6μs. T_e decreases below 20eV (where the Ar ionization cross-section has a maximum) and Ar ionization rate starts to decrease along with T_e values.

7.2.4. A physical model for the phenomena leading to the increase in the ion flux and energy during the pulse-off time at the substrate region of a pulsed DC magnetron discharge has been presented and validated using measurements of the IES at the substrate region and the I and V waveforms at the cathodes.

The proposed model is based on the formation and expansion of a plasma-probe (or respectively, a plasma-substrate) sheath, due to changes in the plasma parameters (electron density and temperature) during the pulse-off time.

The ions are accelerated in this sheath at high energies corresponding to the (oscillating) plasma potential values at the sheath edge. As the plasma-probe sheath expands, a higher number of ions will be accelerated towards the probe thus explaining the increase in the ion flux.

According to the model, the Debye-length of the plasma-probe sheath will first expand due to a sudden overall drop in electron density and rise in electron temperature that characterize the plasma at the beginning of the pulse-off time.

The expansion slows down and stops at around 1μs, when the electron density reaches uniform distribution over the plasma and the bulk reaches charge neutrality. After ~1μs, the sheath will continue to expand slowly due to an ambipolar flow (ion drift outside the bulk and electron loss at the bulk, at the same rate), until the positive charge density gradient is compensated, leading to a stop in expansion after ~4μs. After 4μs, the plasma-probe sheath extent stays constant until the end of the pulse-off time. The plasma-probe sheath is rapidly compensated and disappears at the beginning of the following pulse-on time.

The formation of the plasma-probe sheath and its behaviour during the pulse-off time explains the ion flux and energy gain as well as the observed IES at the substrate region.

This optimum pulse-off time value (for a maximum increase in ion flux) should be close to the time needed by the plasma to reach equilibrium (~4μs in our case) coinciding to the moment when the plasma-probe sheath reaches a maximum extent. The pulse-off time value can be easily determined from the I-V waveforms that provide in this case, a direct result for such plasma diagnostic problems.

7.3 CONSIDERATIONS DERIVED FROM THE PROPOSED MODELS

7.3.1. THE PRE-SHEATH ELECTRIC FIELD

The electron kinetics examined through time and space OES methods provided information on the space and temporal distribution of the excited and ionized species allowing to understand the connection between the input power wave during the pulse-on time, the electron temperatures and discharge evolution at various moments during the pulse.

While the electron kinetics has been examined using experimental plasma diagnostic methods, the ion kinetics, respectively the transport history from their formation inside the discharge to their arrival at the targets have been investigated using Monte Carlo simulations (Chapter 2.2).

This study required the development of an original algorithm and code for charged particle transport in complex, time and space dependent electric and magnetic fields. The developed code is based on a non-Runge-Kutta routine and calculates at each step the value of the magnetic field using a current sheath method, while the electric field in the plasma sheath is calculated using the Child Langmuir formula and the I and V waveforms.

Although the time and space-resolved OES data provide the initial relative ion densities, the physical model is incomplete, as an important piece of information is missing: the intensity of the pre-sheath electric field.

As Langmuir probes could not be used in this configuration of magnetic confinement, no direct information was available about the intensity and space dependence of the electric field in the discharge pre-sheath.

The importance of the pre-sheath electric field during pulsed DC discharges has lately been observed by several authors, but no physical model for its space distribution and intensity has yet been developed for pulsed DC discharges.

The pre-sheath electric field brings the ions to the targets in order to produce sputtering, and has a major importance in the development of the sputtering process, as its intensity and space distribution dictates the amount of ions that produce sputtering. From this point of view, the pre-sheath electric field can be considered the "motor" of the sputtering discharge and it is an essential piece of information in designing a model of the sputtering process.

In this case, the pre-sheath electric field has been a "missing link" and the only means to estimate its intensity was through Monte Carlo simulations, based on the estimation of the travel time to targets of Ar ions from the time-resolved OES data. Several possible functions

describing the electric field evolution in the pre-sheath have been used in MC simulations of Ar ions travel time to targets in order to determine the function that provides the best match to the experimental value of the delay between the observed power peak and the Ar ion OES peak that accounts for the average transit time of Ar ions.

Once the pre-sheath field has been evaluated, more information on the sputtering process can be extracted through MC simulations: the time scale and intensity of the sputtering and self-sputtering processes and the bombarding ions energies at the targets (Chapters 2.2, 2.3).

The ions reach the targets at different moments during the pulse and with significant spread in their energy values, related to the voltage values on the plasma sheath. It can be noticed that for the considered pre-sheath functions, a significant proportion of ions (60% -70%) do not participate in the sputtering process. These ions are trapped in the discharge due to the strong magnetic confinement and magnetic mirror effects. For longer pulse-on times or for DC deposition they may reach the targets after long transit times, or can simply accumulate in the discharge, leading to arcs. Therefore, during the pulse-off time the plasma has to release the accumulated charges in order to re-establish the charge quasi-neutrality.

The simulation results also indicate that ions starting at different distances from the target have significantly different transit times and consequently, reach the target with different energies, dependent on the variable electric field on the cathode sheath. Although this leads to a continuous sputtering process, the sputtering yield and rate are variable during the pulse.

The conditions that enable an optimization of the sputtering process leading to maximum sputtering rates as a function of the pulsed DC duty cycle could make the subject for further investigation.

The self-sputtering process can be important for long pulse-on times and high electron temperatures near the targets and the choice of the duty cycle can be made according to whether the self-sputtering has to be reduced or enhanced.

7.3.2. MAGNETIC FIELD GEOMETRY AND PLASMA PARAMETERS

Another important issue to be addressed here is the connection between the geometry of the magnetic field and its influence on the plasma parameters.

Working with both non-ferromagnetic (Cu) and ferromagnetic (Fe) target material that brings changes in the magnetic field between the targets, allowed the comparison of discharge parameters for the two types of magnetic field and the observation of modifications in plasma parameters and dynamics induced by such changes in the magnetic field.

For Fe targets, the magnetic field distribution in the XOZ cross-section for Fe targets is concentrated in the centre of the target due to the absorption of the Bx component of the magnetic field in the ferromagnetic targets. Compared to the field for the Cu targets, for the Fe targets the magnetic field decreases much faster at regions situated at 2cm from each end of the

target cross-section (see Fig.3.1.8), leading to a loss of confinement, a lower electron density and higher electron temperatures.

These higher temperatures lead to a different distribution of the regions with high ionization probability for both Ar gas atoms and metal atoms (Fe), increasing the ion density in the regions close to the targets and leading to intense self-sputtering and target re-sputtering effects and the observed excess heating of the targets.

As the sputtered (metal) and reflected (gas) atoms have higher energies with a distribution around 10eV, when ionized in the Fe target discharge, their higher energy will be observed in the IES at the substrate as well as in the ion fluxes and will double the energy density at the substrate compared to the situation with Cu targets (Chapter 5.4). Thus, the loss of confinement leads to an increase in electron temperature with consequences on the sputtering process, target and substrate heating.

For the Cu targets, larger confinement region leads to lower electron temperatures, a different ionization density distribution and a smaller thermal load of the targets and substrate. Therefore, the magnetic field distribution has an important contribution to the development of the discharge, sputtering and deposition processes and designing the magnetic field should be taken into account when certain plasma parameters should be reached.

7.3.3. THE MAGNETIC FIELD AND CHARGE-LOSS EFFECTS

Other consequences on the discharge behaviour can be inferred from the plasma behaviour during the pulse-off time.

As the charge-loss phenomena during the pulse-off time are governed by the time-scale of electron, respectively ion redistribution processes, the electron kinetics along and across magnetic field lines should be considered.

While the duration of electron redistribution takes place on short time-scales: 10-100ns, the ion redistribution through drifts and ambipolar flow processes is much longer and can be influenced by the distribution of the magnetic field.

In general, for ambipolar processes to occur, both the ions and electrons should move together, across magnetic field lines. In the case of strong magnetic fields, the electron motion across magnetic field lines will be slowed down, leading to the same average mobility of both species.

As the ambipolar flow coefficient across magnetic field lines is inversely proportional to the square of the magnetic field, the electron mobility increases fast as the magnetic field decreases. Therefore, ambipolar flow processes can occur at regions of the discharge where the magnetic field is weak (at the boundaries of the magnetic confinement and centre line between the magnets). Discharges that cannot allow for any charge–loss effects will generally become unstable turning into arcs; so, such gaps in the magnetic field should be allowed when designing

the magnetic field distribution of the discharge. The electron diffusion along the magnetic field lines will ensure the electron re-distribution in the first ~100ns of the pulse-off time.

So, the un-balanced type magnetrons with magnetic field lines extending far towards the substrate will enable a fast diffusion of electrons towards the bulk during the pulse-off time and a stronger decrease in electron density at the substrate region, leading to a larger plasma sheath at the substrate and consequently a higher ion flux at the substrate.

Therefore, along with the pulsed bias and power on the targets, the distribution of the magnetic field has a major influence on the plasma parameters, sputtering process and the quality of the deposited layers.

Some assumptions made in designing the different models presented in this thesis are still to be verified:

-the assumption of a time-independent pre-sheath electric field;

-the detailed mechanism for the obvious ambipolar flow type process during the pulse-off time;

-the accuracy of the designed Monte Carlo code and trajectory algorithm;

-the metal ion relative densities in the Cu ion simulations.

7.4 NEW AND ORIGINAL RESULTS PRESENTED IN THIS THESIS

The following results have been obtained and presented for the first time in this thesis:

- OES electron temperature determinations in pulsed DC magnetrons have been obtained for the first time during this work;
- The Acousto-Optic spectrometer has been used here for the first time for evaluations of electron temperature, and a measuring method had to be designed and evaluated before use;
- The observed temporal and space evolution of the electron temperatures lead to a first time model of the behaviour of the plasma and discharge during the pulse-on time;
- A new method for temporal analysis of time-averaged IES spectra has been presented;
- An original physical model explaining the increase in ion flux and energy at substrate, during pulsed DC magnetron operation;
- The possible evolution of the electric field in the pre-sheath of a pulsed DC discharge has been estimated for the first time, using Monte Carlo simulations.

7.5. POSSIBLE DIRECTIONS FOR CONTINUATION OF THE WORK

The proposed physical models for the pulse-on and respectively pulse-off time plasma can be further tested through the study of different other discharges, pulse-off time values and even different configurations of the magnetic field.

Nevertheless, the proposed time-resolved plasma physical models as well as the time-resolved methods of diagnostic developed and tested through-out the work for this thesis can be easily used and provide the necessary tools for the control of plasma parameters and layers properties during pulsed DC deposition.

The experimental study of electron densities during both pulse-on and pulse-off time for the same magnetron will provide further insight into the phenomena governing the discharge and will allow an increase in the accuracy of the presented models. More experimental data are necessary in order to understand the actual mechanism of the ambipolar flow taking place during the pulse-off time, so time-resolved and space –resolved measurements of electron density and temperature may provide an answer.

Viewing the importance of the magnetic field distribution, further research in the field of magnetron design should approach the study of opposed target magnetrons with pre-designed magnetic field distribution and its consequences on the behaviour of the discharge, the plasma parameters, the ion flux and energy at the substrate and ultimately, the layers properties. Such research could aim at developing a physical model of the magnetic field influence on the plasma parameters and the sputtering process.

CHAPTER 8:

REFERENCES

The references include the papers that I have published during the work on this thesis as they are referenced in the text.

A short list of the papers published during thesis preparation and the presentations at conferences follows.

8.1. REFERENCES

1. F.M. Penning, U.S Patent, 2.146.025, 7 Feb. 1939;

2 B. Window, F. Sharpless and N. Savides, "Magnetically Confined Sputter Source with High Ion Flux", J. Vac.Sci. Technol. A3(6), Nov/Dec 1985, 10-13;

3. B. Window and F. Sharpless, "Magnetron Sputtering Sources for Ferromagnetic Material", J. Vac. Sci. Technol. A3(1), Jan/Feb 1985, 2368-2372;

4. M.A. Lieberman, A. J. Lichtenberg, "Principles of Plasma Discharges and Materials Processing", Wiley, New York, 1994;

5. B. Chapman, "Glow discharge Processes", John Wiley & Sons, New York, 1980;

6. A. Anders, "Fundamentals of Pulsed Plasmas for Materials Processing", Surface and Coatings Technology, 183(2004) 301-311;

7. J.W. Bradley, H. Backer, P.J. Kelly, R.D. Arnell, "Space and Time-Resolved Langmuir Probe Measurements in a 100kHz Pulsed Rectangular Magnetron System", Surface and Coatings Technology 142-144(2001) 337-341;

8. J.W. Bradley, H. Backer, P.J. Kelly, R.D. Arnell, "Time-Resolved Langmuir Probe Measurements at the Substrate Position in a Pulsed Mid-frequency DC Magnetron Plasma", Surface and Coating Technology 135(2001) 221-228;

9. M.A. Lieberman, "Model of Plasma Immersion Ion Implantation", J. Appl. Phys. 66(7) 2986, 1 October, 1989;

10. J.D. Jackson, "Classical Electrodynamics", Wiley, New York, 1980;

12. ENI Operation Manual: "RPG-50 Family of Pulsed DC Plasma Generators", 1997, ENI;

13. Time Resolving Acoustooptic UV/VIS – Spectrometer AOS 4-1 µchron 02", Technical Description and User's Guide, IfU GmbH.

14. "Acousto-Optic Signal Processing: Theory and Implementation", Edited by Norman J. Berg and John N. Lee, Marcel Dekker, Inc. New York and Basel, 1983.

14. Electrostatic Quadrupole Plasma (EQP 300) Mass-Energy Analyser Manual, 1998, Hiden Analitical Ltd.;

15. S. Ramo, J. R. Whinnery, T.van Duzer, "Fields and Waves in Communication Electronics", Wiley International, New York, London, 1965;

16. W. Baumjohann, R.A. Treumann, "Basic Space Plasma Physics", Imperial College Press, 1999;

17. C.K. Birdsall, A.B. Langdon, "Plasma Physics via Computer Simulation", Adam Hilger Series on Plasma Physics, Bristol, Philadelphia and New York, IOP Publishing Ltd 1991;

18. C.H. Shon, J.K. Lee, "Modelling of Magnetron Sputtering plasmas", Applied Surface Science 192 (2002) 258-269;

19. M.J. Goeckner, J.A. Goree and T.E. Sheridan Jr., "Monte Carlo Simulation of Ions in a Magnetron Plasma", IEEE Transactions On Plasma Science, Vol.19, No. 2, April 1991;

20. M.J. Goecker, J. Goree and T.E. Sheridan, "Laser Induced Fluorescence Characterisation of Ions in a Magnetron Plasma", J. Vac. Sci. Technol. A8(6), Nov/Dec 1990;

21. Y. Yamamura, M. Ishida, "Monte Carlo simulation of the Thermalization of Sputtered Atoms and Reflected Atoms in the Magnetron Sputtering Discharge", J. Vac. Sci. Technol. A13(1), Jan/Feb 1995, pp.101-112;

22. G. M. Turner, "Monte Carlo Simulations of Gas Rarefaction in a Magnetron Sputtering Discharge", J. Vac. Sci. Technol. A13(4), Jul/Aug 1995, pp.2161-2169;

23. A. Bogaerts and R. Gijbels, "Role of Sputtered Cu Atoms and Ions in a Direct Current Glow Discharge: Combined Fluid and Monte Carlo Model", J. Appl. Phys. 79 (3), 1 February 1996, pp. 1279-1286;

24. J.T. Scheuer, M. Shamim and J.R. Conrad, "Model of Plasma Source ion implantation in Planar, Cylindrical, and Spherical Geometries", J. Appl. Phys. 67(3), 1 February 1990;

25. R. Günzel, J. Brutscher, "Sheath Dynamics in Plasma Immersion Ion Implantation", Surface Coatings Technology 85(196) 98-104;

26. M.H. Cho, N. Hershkowitz and T. Intrator, "Temporal Evolution of Collisionless Sheaths", J. Vac. Sci. Technol. A6(5), Sep/Oct 1988;

27. Boris Briehl and Herbert M. Urbassek, "Pre-sheath Dynamics Induced by Sudden Electrode Voltage Jumps", J. Phys. D: Appl. Phys. 33(2000) 3066-3072;

28. W.H. Cramer, "Elastic and Inelastic Scattering of Low-Energy Ions: Ne+ in A, A+ in Ne and A+ in A", J. Chem. Phys., vol 30, pp.641-642, Mar. 1959;

29. Shuji Sakabe and Yasukazu Izawa, "Simple formula for the cross-sections of resonant charge transfer between atoms and their positive ions at low impact velocity", Physical Review A, Vol. 45, No.3, 2086-2089, 1 February 1992;

30. D. Rapp and W.E. Francis, "Charge Exchange between Gaseous Ions and Atoms", J. Chem. Phys., 37, 2631 (1962);

31. I. Popescu Iovitsu and N. Ionescu-Pallas, "Resonant Charge-Exchange and the Kinetics of Ions", Sov. Phys.-Tech.Phys., vol.4, pp.781-791, Jan.1960;

32. M. Gryzinski, "Two-Particle Collisions. I. General Relations for Collisions in the Laboratory System", Phys. Rev. 138, A305-321 (1965);

33. Encyclopedia of Physics. Principles of Classical Mechanics and Field Theory. Berlin: Springer-Verlag, 1956-1962;

34. Xiu Zou, Jin-Yuan Liu, Ye Gong, Zheng-Xiong Wang, Yue Liu, Xiao-Gang Wang, "Plasma sheath in a Magnetic Field", Vacuum 73 (2004) 681-685;

35. A.V. Phelps and Z. Lj. Petrović, "Cold Cathode Discharges and Breakdown in Argon: Surface and Gas Phase Production of Secondary Electrons", Plasma Sources Sci. Technol. 8(1999) R-21-R44;

36. S.M. Rossnagel, H.R. Kaufman, "Charge transport in Magnetrons", J. Vac. Sci. Technol. A5(4), Jul/Aug 1987, pp.2276-2279;

37. W. En and N.W. Cheung, "Analytical Model of Plasma Immersion Ion Implantation Target Current Using the SPICE Circuit Simulator J. Vac. Sci. Technol. B, 12 (1994) 833].

38. T. Moiseev and D.C. Cameron, "Pulsed DC Operation of a Penning Type Opposed Target Magnetron", J.Vac. Sci. Technol. A(23(10), Jan/Feb 2005, 66-71;

39. A. Friedmann and L.A. Kennedy, "Plasma Physics and Engineering", Taylor & Francis Inc, 2004;

40. H. R. Griem, "Principles of Plasma Spectroscopy", pp.281, pp.191, pp.167, Cambridge University Press, 1977;

41. David Salzmann, "Atomic Physics in Hot Plasmas", New York, Oxford, Oxford University Press, 1988;

42. Xi Chen and Peng Han, "On the Thermodynamic Derivation of the Saha Equation Modified to a Two-Temperature Plasma", J. Phys. D: Appl. Phys. Vol. **32**, 1711, (1999);

43. S.M. Rossnagel and H.R. Kaufman, "Langmuir Probe Characterization of Magnetron Operation", J. Vac. Sci. Technol. A (43), 1822, May/June 1986;

44. T.E. Sheridan, M.J. Goekner and J. Goree, "Observation of Two-Temperature Electrons in a Sputtering Magnetron Plasma", J. Vac. Sci. Technol. A (93), 688, May/June 1991;

45. R.N. Franklin, "Ambipolar Diffusion is a Misnomer", J. Phys. D: Appl. Phys. **36**(2003), pp.828-831.

46. S.M. Rossnagel, H.R. Kaufman, "Current voltage relations in magnetrons", J. Vac. Sci. Technol. A6(2), Mar/Apr 1988, pp. 223-229;

47. S.M. Rossnagel, H.R. Kaufman, "Langmuir probe characterization of magnetron operation", J. Vac. Sci. Technol. A4(3), May/Jun 1986, pp. 1822-1825;

48. S.M. Rossnagel, "Gas density reduction effects in magnetrons", J. Vac. Sci. Technol. A6(1), Jan/Feb 1988, pp. 19-24;

49. A.P. Ehiasarian, R. New, W.-D. Munz, L. Hultmann, U. Helmersson, V. Kouznetsov, "Influence of high power densities on the composition of pulsed magnetron plasmas", Vacuum 65(2002) pp.147-154;

50. A. Thornthon and A. Penfold, "Thin Film Processes", edited by J. Vossen and W. Kern (Academic, New York, 1978);

51. Richard A Sholl, Advanced Energy Industries Inc., "Power Supplies of Pulsed Plasma Technologies: State of the Art and Outlook", http:// www.advanced-energy.com/ , May 2005;

52. W.M. Posadowski, Z. Radzimski, "Sustained self-sputtering using a direct-current magnetron source", J. Vac. Sci. Technol. A 11(1993) 2980-2984;

53. W.M. Posadowski, "Sustained self-sputtering of different materials using DC magnetron", Vacuum 46(8-10)(1995) 1017-1020;

54. S. Kadlec, J. Musil, "Low pressure magnetron sputtering and self-sputtering discharges", Vacuum 47(3) (1996) 307-315;

55. H. Backer, P.S. Henderson, J.W. Bradley, P.J. Kelly, "Time-resolved investigation of plasma parameters during deposition of Ti and TiO2 thin films", Surface and Coating Technology, 174-175(2003) 909-913;

56. M. Misina, J.W. Bradley, H. Backer, Y. Aranda-Gonzalvo, S.K. Karkari, D. Forber, "Investigation of the pulsed magnetron discharge by time-and energy-resolved mass-spectrometry", Vacuum 68 (2003) 171-181;

57. J.W. Bradley, S.K. Karkari and A. Vetushka, "A Study of the transient Plasma Potential in a Pulsed Bi-Polar DC Magnetron Discharge", Plasma Sources Sci. and Technol. **13**(2004) 189-198;

58. T. Moiseev, D.C. Cameron, "Comparison of the Operating Characteristics of an Opposed Target Magnetron using Ferromagnetic and Non-Ferromagnetic Targets", Surface and Coatings Technology, Volume 200, Issues 1-4, 1 October 2005, Pages 644-648.

59. F. Guimaraes, J. B. Almeida and J. Bretagne, "Study of an Argon Magnetron Discharge used for Molibdenum Sputtering. II. Spectroscopic Analysis and Comparison with the Model", Plasma Sources Sci. Technol. 2(1993) 138-144;

60. Yi-Kang Pu, Zhi_Gang Guo, Zheng-De Kang, Jie Ma, Zhi-Chang Guan, Guang-Yu Zhang and En-Ge Wang, "Comparative Characterization of High Density Plasma Reactors using Emission Spectroscopy from VUV to NIR", Pure Appl. Chem., Vol. 74, No. 3, pp. 459-464, 2002;

61. F. Clénet, Ph. Briaud, G. Turban, "Experimental Study of an RF magnetron Discharge for Thin-Film Deposition", Surface and Coatings Technology, 97(1997) 528-532;

62. B. Yotsombat, S. Davydov, P. Poolcharuansin, T. Vilaithong and I. G. Brown, "Optical Emission Spectra of a Copper Plasma Produced by a Metal Vapour Vacuum Arc Plasma Source", J. Phys. D: Appl.Phys 34(2001)1928-1932;

63. Takeo Nakano, Noriyuki Ohnuki and Shigeru Baba, "Pressure Dependence of Optical Emission from DC Magnetron Sputtering Plasma Observed with Spatial Resolution", Vacuum 59(2000)581-585;

64. K. Macak, V. Kouznetsov, J.Scheider, I. Petrov and U. Helmersson, "Ionized Sputter Deposition using an Extremely High Plasma Density Pulsed Magnetron Discharge", J. Vac. Sci. Technol. A 18(4) Jul/Aug/2000;

65. A.D. Pajdarová, J. Vlček, P. Bělsky and B. Musil, "Time-Resolved Optical Emission Spectroscopy of Pulsed Dc Magnetron Sputtering Plasmas";

66. M. Dickson and J. Hopwood, "Axially-resolved Study of Highly Ionized Physical Vapour Deposition", J. Vac. Sci. Technol. A15(4), pp. 2307 –2312, Jul/Aug 1997;

67. A.E. Wendt and M. A. Lieberman, "Spatial Structure of a Planar Magnetron Discharge", J. Vac. Sci. Technol. A8(2), Mar/Apr 1990;

68. F. Debal, M. Wautelet, J. Bretagne, J. P. Dauchot and M. Hecq, "Spatially –resolved Spectroscopic Optical Emission of DC magnetron Sputtering Discharges in Ar-Nitrogen Mixtures", Plasma Sources Sci. Technol. 9(2000) 152-160;

69. Annemie Bogaerts and Renaat Gijbels, "Argon and Copper Optical Emission Spectra in a Grimm Glow Discharge Source: Mathematical Simulations and Comparison with the Experiment, Journal of Analytical Atomic Spectrometry, Aug.1998, Vol.13(721-726);

70. Cris L. Lewis, Glen P. Jackson, Stephen K. Doorn, Vahid Majidi, Fred L. King, "Spectral, Spatial, and Temporal Characterization of a Millisecond Pulsed Glow Discharge: Copper Analyte Emission and Ionization", Spectrochimica Acta Part B56 (2001)487-501;

71. Glen P. Jackson and Fred L. King, "Bulk Plasma properties in the Pulsed Glow Discharge", Spectrochimica Acta Part B 58(2003) 1417-1433;

72. A. Descoeudres, Ch. Hollenstein, R.Demellayer and G. Wälder, "Optical Emission Spectroscopy of Electrical Discharge Machining Plasma", J. Phys. D: Appl. Phys. **37**(2004) 875-882;

73. B. Clarenbach, B. Lorenz, M. Krämer and N. Sadeghi, "Time-Dependent Gas Density and Temperature Measurements in Pulsed Helicon Discharges in Argon", Plasma Sources Sci. and Technol. 12(2003)345-357;

74. G. Zambrano, H Riascos, P. Prieto, E. Restrepo, A. Devia, C. Rincón, "Optical Emission Spectroscopy Study of RF Magnetron Sputtering Discharge used for Multilayers Thin Film Deposition", Surface and coatings Technology 172(2003) 144-149;

75. M. Dickson, F. Qian and J. Hopwood, "Quenching of Electron Temperature and electron Density in Ionized Physical Vapour Deposition", J. Vac. Sci. Technol. A 15(2) Mar/Apr 1997;

76. J.B. Tatum, "Stellar Atmospheres", http://orca.phys.uvic.ca/~tatum/stellatm.html, May2005.

77. T. Moiseev and D.C. Cameron, "Estimation of the Electron Temperature and Density from Space and Time-Resolved O.E.S. during Pulsed DC Operation of an Opposed Target Magnetron" – oral presentation at the 48th Annual Society of Vacuum Coaters (SVC) Conference, Denver, Colorado USA, April 23-28, 2005; paper accepted for publication in the SVC proceedings;

78. S. K. Karkari, H. Backer, D. Forder and J.W. Bradley, "A Techniques for Obtaining Time-and Energy Resolved Mass Spectroscopic Measurements on Pulsed Plasmas", Meas. Sci. Technol. **13** (2002) 1431-1436;

79. H. Bartzsch, P. Frach, K. Goedicke, "Anode Effects on Energetic Particle Bombardment of the Substrate in Pulsed Magnetron Sputtering", Surface and Coating Technology 132(2000) 244-250;

80. P.J. Kelly, C.F. Beevers, P.S. Henderson, R. D. Arnell, J.W. Bradley, H. Bäcker, "A Comparison of the Properties of Ti –based Films Produced by Pulsed and Continuous DC Magnetron Sputtering", Surface and Coating Technology 174-175(2003) 795-800.

81. C. Muratore, J. J. Moore and J. A. Rees, "Electrostatic quadrupole plasma mass spectrometer and Langmuir probe measurements of mid-frequency pulsed DC magnetron discharges", Surface and Coatings Technology, 163-164(2003) 12-18;

82. Richard A. Scholl, Advanced Energy Industries Inc., "Power supplies for pulsed plasma technologies: state of the art and outlook", www.advanced-energy.com;

83. C.V. Budtz-Jørgensen, J. Bøttiger, P. Kringhøj, "Energetic In Bombardment of the Grounded Anode in Pulsed DC Glow Discharges", Surface and Coating Technology 137(2001) 104-110;

84. T. Moiseev and D.C. Cameron, "On the ion flux and energy gain during pulsed DC operation of an opposed target magnetron", Surface and Coatings Technology, In Press, Corrected Proof, Available online 2 August 2005;

8.2. LIST OF PUBLISHED PAPERS DURING THESIS PREPARATION

1. T. Moiseev and D.C. Cameron, "On the ion flux and energy gain during pulsed DC operation of an opposed target magnetron", Surface and Coatings Technology, In Press, Corrected Proof, Available online 2 August 2005;

2. T. Moiseev and D.C. Cameron "A 3-Step Algorithm for Solving 2D Inverse Magnetostatic Problems for Magnetron Design Applications", Inverse Problems in Engineering, Vol. 13, No. 3, June 2005, 279-297;

3. T. Moiseev and D.C. Cameron, "Pulsed DC Operation of a Penning-Type Opposed Target Magnetron", J. Vac. Sci. Technol. A 23(1), Jan/Feb 2005, 66-71;

4. T. Moiseev and D.C. Cameron, "Comparison of the Operating Characteristics of an Opposed Target Magnetron using Ferromagnetic and Non-Ferromagnetic Targets", Surface and Coatings Technology, Volume 200, Issues 1-4, 1 October 2005, Pages 644-648;

5. T. Moiseev and D.C. Cameron, "Estimation of the Electron Temperature and Density from Space and Time-Resolved O.E.S. during Pulsed DC Operation of an Opposed Target Magnetron"- accepted for publication in the SVC-48 Proceedings;

8.3. LIST OF PRESENTATIONS AT CONFERENCES DURING THESIS PREPARATION

1. T. Moiseev and D.C. Cameron "Design and Characterization of a Penning-type Opposed Target Magnetron"; -oral presentation at The 15th Annual Conference of the Irish Plasma and Beam Processing Group in conjunction with 13th Symposium on Fusion Research in Ireland, Dublin City University, 23rd-24th June 2004 - presented by Tamara Moiseev;

2. T. Moiseev and D.C. Cameron, "Pulsed DC Operation of a Penning-Type Opposed Target Magnetron" - oral presentation at The International Conference on Metallurgical Coatings and Thin Films, ICMCTF 2004, San Diego, May 2004; - presented by Prof. D.C. Cameron.

3. T. Moiseev and D.C. Cameron, "Comparison of the Operating Characteristics of an Opposed Target Magnetron using Ferromagnetic and Non-Ferromagnetic Targets" - poster presentation at the 9th Conference on Plasma Surface Engineering, Garmisch-Partenkirchen, Germany, Sept.12-17, 2004; - presented by Tamara Moiseev.

4. T. Moiseev and D.C. Cameron, "Estimation of the Electron Temperature and Density from Space and Time-Resolved O.E.S. during Pulsed DC Operation of an Opposed Target Magnetron" – oral presentation at the 48th Annual Society of Vacuum Coaters (SVC) Conference, Denver, Colorado USA, April 23-28, 2005; - presented by Prof. D.C. Cameron;

5. T. Moiseev and D.C. Cameron, "Evaluation of a Plasma Pre-Sheath Model for Pulsed DC Magnetron Discharges" - poster presentation at the 47th Gaseous Electronics Conference, Bunratty, Ireland, Sept 26-29, 2004; - presented by Tamara Moiseev.

6. T. Moiseev and D.C. Cameron, "Evaluation of Self-Sputtering Time-Scale in Pulsed Magnetrons Using Time-Resolved O.E.S. and Monte Carlo Simulations" – oral presentation at the 47th Gaseous Electronics Conference, Bunratty, Ireland, Sept 26-29, 2004; - presented by Tamara Moiseev.